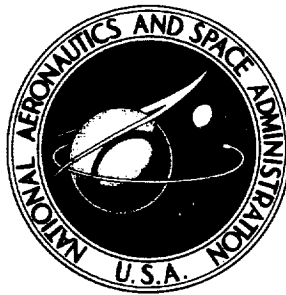


**NASA CONTRACTOR
REPORT**



NASA CR-1960

NASA CR-1960

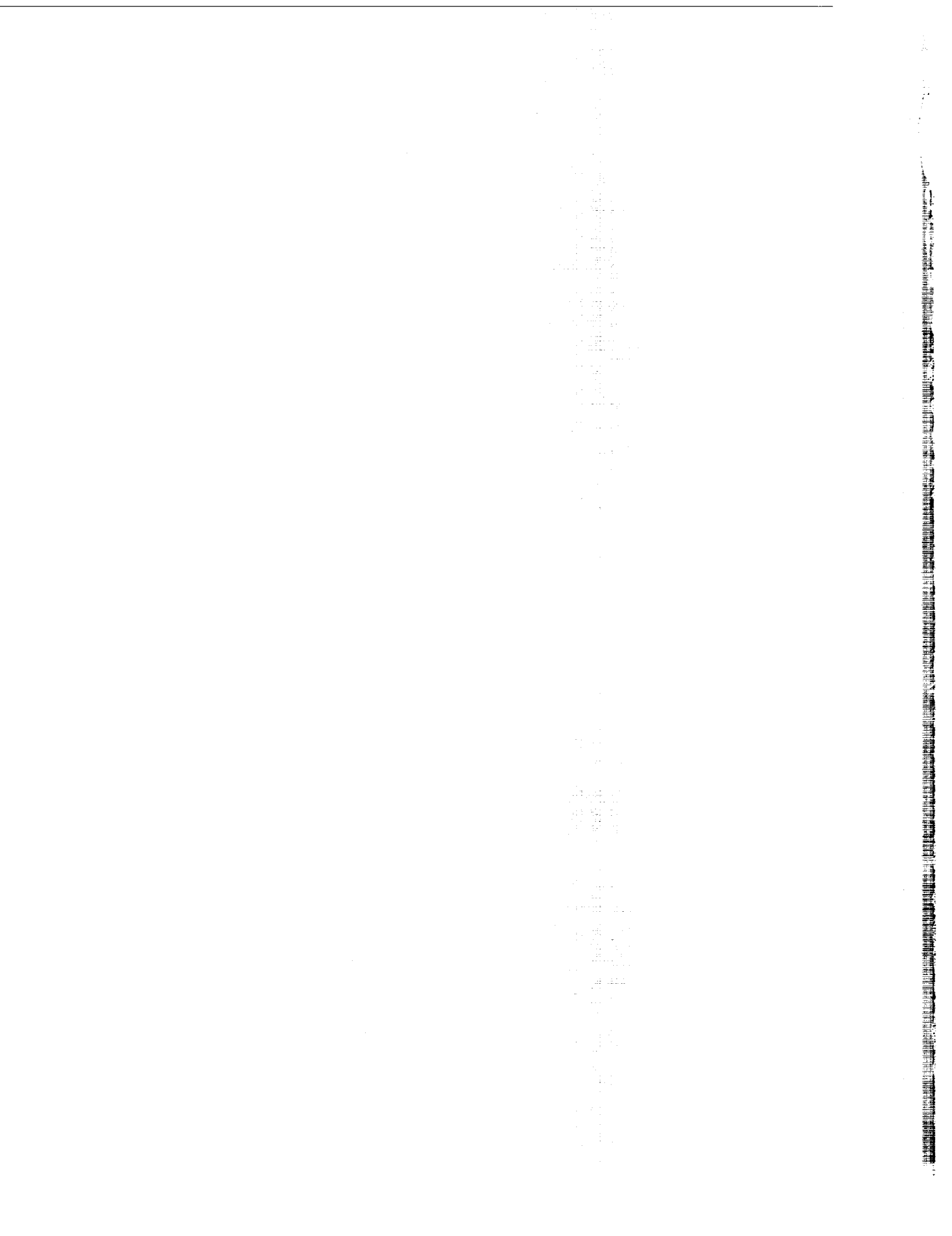
**CASE FILE
COPY**

**DEVELOPMENT OF A
SATELLITE MICROWAVE RADIOMETER
TO SENSE THE SURFACE TEMPERATURE
OF THE WORLD OCEANS**

*by G. M. Hidy, W. F. Hall, W. N. Hardy, W. W. Ho,
A. C. Jones, A. W. Love, M. J. Van Melle,
H. H. Wang, and A. E. Wheeler*

Prepared by
NORTH AMERICAN ROCKWELL CORPORATION
Downey, Calif. 90241
for Langley Research Center

NATIONAL AERONAUTICS AND SPACE ADMINISTRATION • WASHINGTON, D. C. • FEBRUARY 1972



1. Report No. NASA CR-1460		2. Government Accession No.		3. Recipient's Catalog No.	
4. Title and Subtitle DEVELOPMENT OF A SATELLITE MICROWAVE RADIOMETER TO MEASURE THE SURFACE TEMPERATURE OF THE WORLD OCEANS				5. Report Date February 1972	
				6. Performing Organization Code	
7. Author(s) G. M. Hidy, W. F. Hall, W. N. Hardy, W. W. Ho, A. C. Jones, A. W. Love, M. J. Van Melle, H. H. Wang, and A. E. Weisberg				8. Performing Organization Report No.	
				10. Work Unit No.	
9. Performing Organization Name and Address North American Rockwell Science Center Thousand Oaks CA Space Division, Downey, California				11. Contract or Grant No. NAG 1-10100	
				13. Type of Report and Period Covered Contractor Report	
12. Sponsoring Agency Name and Address National Aeronautics and Space Administration Washington, D.C. 20546				14. Sponsoring Agency Code	
15. Supplementary Notes This report describes the first phase of a satellite prototype S-band radiometer development under the AAFE-program of NASA.					
16. Abstract The determination of the ocean-surface temperature with an absolute accuracy of ± 1 Kelvin and a resolution of $\pm .1$ Kelvin from a satellite on a global, all-weather, and day-night basis is of vital importance to the fishery industry, the marine transport industry, the oceanographers and marine meteorologists. A proposed S-band-radiometer measurement from SMMRS for this purpose was judged to have scientific and practical merits and was placed under the Advanced Applications Flight Experiment (AAFE) program of NASA for further advancement into the satellite readiness state. As the first phase under the AAFE program this report describes the investigation results to assess for S-band radiometry the (1) effects due to the state of the sea surface, (2) effects caused by the intervening atmosphere, and (3) instrumental effects associated with imperfections in the instrument itself. The report also describes an instrument design for better than $\pm .1$ Kelvin temperature resolution under unattended condition. The investigation of the emissivity of sea water revealed that the global temporal change of salinity causes a maximum uncertainty of $\pm .2$ Kelvin and that a possible error of salinity level of 1 percent causes another uncertainty of $\pm .2$ Kelvin. The surface roughness effect for circular polarization at nadir is according to the theory a few tenth Kelvin. Measurements indicated much larger effects especially if the sun is within 30° degrees of the zenith. The effect of foam depending on coverage may introduce several Kelvins uncertainty and represents a problem in the data analysis since foam and cloud coverage exist mostly simultaneously preventing auxiliary remote foam detection. The influence of spray and of natural oil slicks is very small on the measurement accuracy and may be neglected. The effect of oxygen, of water vapor in a clear atmosphere, and of the extra terrestrial sources has been determined to be $\pm .3$ Kelvins. This value is changed only slightly by cloud coverage according to the theory. Experimental verification is still required. An extensive sea-truth program is described for future correlation of aircraft-test flight measurements or of satellite remote measurement to in-situ data. The improved S-band radiometer design is a modified Dicke-switch type with temperature stabilized, microwave-integrated-circuit front-end and with a pulsed injection-noise nulling-system. The radiometer has a multimode rectangular horn antenna with very low ohmic losses and a beam efficiency ($\frac{1}{2}$ times the $\frac{1}{2}$ dB beam angle) of 90 percent or better.					
17. Key Words (Suggested by Author(s)) Radiometer Sea-surface-temperature Emissivity, salinity, roughness Atmospheric effects, sky emission Satellite-radiometer-design Sea-truth-program			18. Distribution Statement Unclassified - Unlimited		
19. Security Classif. (of this report) Unclassified		20. Security Classif. (of this page) Unclassified		21. No. of Pages 278	22. Price* \$3.00

|

FOREWORD

This document represents the final report of a twelve month study for the development of a satellite microwave radiometer to sense the surface temperature of the world oceans. This study was performed under Contract NAS 1-10106, issued by the National Aeronautics and Space Administration, Advanced Applications Flight Experiments Office, Langley Research Center, Hampton, Va. Accomplished in this study were theoretical analyses, experimental investigations, system design studies, mathematical modeling and the engineering development required to establish the conceptual design and performance capabilities of a S-Band radiometer for utilization in aircraft and satellite applications.

The following North American Rockwell staff members rendered invaluable technical assistance, without which this work could not have been accomplished: L. A. Ahlberg, R. M. Govan, K. W. Gray, D. H. Hengstenberg, D. H. Hern, A. J. Lewin, W. Morris and E. P. Parry.

|

CONTENTS

Section		Page
1.0	SUMMARY AND CONCLUSIONS	1
2.0	INTRODUCTION	9
3.0	USER NEEDS AND REQUIREMENTS	13
	3.1 Principal Users of Sea Surface	
	Temperature Data	13
	3.2 Measurement Requirements	14
	3.2.1 Oceanographic Research	19
	3.2.2 Thermal Mapping and Charting	19
	3.2.3 Fisheries Applications	21
	3.2.4 Pollution Applications	24
	3.2.5 Meteorological Applications	24
	3.2.6 Weather Forecasting	28
	3.3 Requirements Summary	31
4.0	EMISSIVITY OF SMOOTH SEA WATER	35
	4.1 Introduction	35
	4.2 Theoretical Considerations	36
	4.2.1 Dielectric Theory of Polar Liquids	
	and Their Frequency Dependence	36
	4.2.2 Relationships Between Emissivity	
	and Dielectric Constant	37
	4.2.3 Influence of Salinity and	
	Frequency	38
	4.3 Salinity Variation in the Oceans	40
	4.3.1 Geographical Variations	40
	4.3.2 Temporal Variations	40
	4.3.3 Summary and Conclusion	45
	4.4 Laboratory Measurements of the	
	Dielectric Properties of Distilled Water,	
	NaCl Solutions, and Sea Water	45
	4.4.1 Experimental Method	51
	4.4.2 Experimental Results	61
	4.5 Conclusions	77

Section		Page
5.0	ATMOSPHERIC EFFECTS AND SKY EMISSION	79
5.1	Cosmic Background Radiation	79
5.2	Microwave Absorption in the Clear Atmosphere	81
5.2.1	Absorption by Oxygen Gas	82
5.2.2	Absorption by Water Vapor	84
5.3	Attenuation by Rain Clouds	85
5.3.1	Attenuation by Non-Precipitating Clouds	87
5.3.2	Attenuation by Non-Precipitating Hydrometeors	90
5.4	Calculation of the Brightness Temperature of the Earth's Cloudless Atmosphere	90
5.5	Correction to the Radiometer Measurements	92
5.6	Experimental Verification of the Theory	100
5.6.1	Measurements in a Cloudless Atmosphere	100
5.6.2	Aircraft Measurements	107
5.6.3	Observations of Attenuation by Clouds	109
5.7	Summary of Atmospheric Effects and the Satellite Instrument	113
6.0	EMISSION FROM A ROUGH SEA	119
6.1	Introduction	119
6.2	The Geometrical Optics Model	122
6.3	An Integral Equation Solution for the Scattering Problem	128
6.4	An Experiment on the Effect of Surface Roughness	131
7.0	MICROSCALE SURFACE DISTURBANCES	139
7.1	Types of Surface Disturbances	139
7.2	Theoretical Models and Their Predictions	139
7.3	Experimental Study	144
7.3.1	Set-up and Operation	144
7.3.2	Results of Experiments	157
7.4	Summary and Conclusions	162

Section		Page
8.0	INTERPRETATION OF 1969 EXPERIMENTAL FLIGHTS	165
8.1	Introduction	165
8.2	Test Programs	165
8.2.1	Morris Dam Experiments	165
8.3	Aircraft Flight Test Program	167
8.3.1	Measurement of the Apparent Sea Temperature	172
8.3.2	Instrument Tests	174
8.3.3	External Load Design and Applications	174
8.3.4	Re-Interpretation of the DC-3 Flight Observation	178
8.3.5	The Effect of Surface Roughness and Sun Glitter	179
8.4	Summary and Conclusions	180
9.0	CONCEPTUAL DESIGN FOR SATELLITE PROTOTYPE INSTRUMENT	183
9.1	Introduction	183
9.2	Candidate Radiometers	187
9.2.1	Resolution	192
9.2.2	Sensitivity to Non-Ideality of the Circulator Switches	193
9.2.3	Suitability for Satellite Use	194
9.2.4	Waveguide vs Coaxial or Microstrip Transmission Line	198
9.3	Conceptual Design of Satellite Radiometer	200
9.3.1	Introduction	200
9.3.2	Need for Square Law Detection for Pulsed Mode	205
9.3.3	Radiometer Sensitivity	206
9.3.4	Radiometer Calibration	207
9.4	Practical Design	207
9.4.1	RF and IF Amplifiers	207
9.4.2	Electronics Subsystem	210
9.4.3	Noise Injection Subsystem	210
9.4.4	Quantitative Analysis of Square Law Detector	211
9.5	Frequency Selection	219
9.6	Radiometer Antenna Configuration	220
9.6.1	Fundamental Requirements	220
9.6.2	Comparison of Antenna Types	222

Section		Page
	9.6.3 Antenna Selection	226
	9.6.4 Multimode Horn Analysis	230
	9.6.5 Effect of Change in Frequency	237
10.0	SEA TRUTH PROGRAM	241
	10.1 Requirements for Radiometry Tests	241
	10.2 Development of a Sea Truth Program	243
	10.3 Test Programs	247
	10.4 Availability of Sea Truth Instrumentation	248
	10.5 Summary and Conclusions	248
11.0	FUTURE DEVELOPMENT PLANS	259
	11.1 Data Interpretation and Utilization	259
	11.1.1 Roughness and Foaming	259
	11.1.2 Data Analysis and Interpretation	259
	11.1.3 Integration With Other Remote Sensors	260
	11.1.4 Oceanographic and Meteorological Utilization	260
	11.2 Satellite Instrument Development	260
	11.3 Flight Applications Survey	262
	11.3.1 Aircraft	262
	11.3.2 Satellite Applications	263
APPENDIX: MAJOR USERS OF SEA SURFACE TEMPERATURE DATA		265

ILLUSTRATIONS

Figure		Page
3.1	Example of Typical Sea Surface Temperature Chart	25
3.2	Typical Sea Surface Temperature Chart, Showing Deviations From Long Term Mean	26
4.1	Uncertainty in the Molecular Temperature T_g Measured at 2.65 GHz by the Radiometer Due to Changes in Salinity for the World Oceans	39
4.2	Average Distribution of Sea Surface Salinity and Temperature for the Pacific Ocean	41
4.3	Average Sea-Surface Salinity (‰) of the World Oceans (From Defant, 1961).	42
4.4	Daily Fluctuation of Sea Surface Salinity and Temperature in Northwest Pacific Ocean	44
4.5	Annual Fluctuation in Sea Surface Salinity for the California Coastal Region	44
4.6	ϵ' for Distilled Water as a Function of Temperature at 2.653 GHz	46
4.7	ϵ'' for Distilled Water as a Function of Temperature at 2.653 GHz	47
4.8	ϵ' for 0.5N NaCl Solution as a Function of Temperature at 2.653 GHz	49
4.9	ϵ'' for 0.5N NaCl Solution as a Function of Temperature at 2.653 GHz	50
4.10	Cross-Sectional Diagram of 2.653 GHz Cavity	58
4.11	Block Diagram of Microwave and Electronic Components Used to Measure the Cavity Characteristics in the Experiment	60
4.12	Cavity Response as Measured by X-Y Recorder With and Without Sample in the Cavity	62
4.13	Differentiated Cavity Response as Measured by X-Y Recorder and Phase Sensitive Detection	63
4.14	Values of $\epsilon' - 1$ Relative to That for Distilled Water as a Function of Salinity at 5°C for NaCl Solutions and Sea Water Samples at 2.653 GHz	65
4.15	Values of $\epsilon' - 1$ Relative to That for Distilled Water as a Function of Salinity at 15°C for NaCl Solutions and Sea Water Samples at 2.653 GHz	66

Figure		Page
4.16	Values of $\epsilon' - 1$ Relative to that for Distilled Water as a Function of Salinity at 24.5°C and 30°C for NaCl Solutions and Sea Water Samples at 2.653 GHz	67
4.17	Cavity Response for the Empty Sample Holder at 15°C	69
4.18	Cavity Response for Distilled Water in Sample Holder at 15°C	70
4.19	Cavity Response for 0.5N NaCl Solution in Sample Holder at 15°C	71
4.20	$\epsilon''/(\epsilon' - 1)$ for NaCl Solutions and Sea Water Samples at 5°C and 2.653 GHz	72
4.21	$\epsilon''/(\epsilon' - 1)$ for NaCl Solutions and Sea Water Samples at 15°C and 2.653 GHz	73
4.22	$\epsilon''/(\epsilon' - 1)$ for NaCl Solutions and Sea Water Samples at 24.5°C and 2.653 GHz	74
4.23	$\epsilon''/(\epsilon' - 1)$ for NaCl Solutions and Sea Water Samples at 30°C and 2.653 GHz	75
5.1	Comparison between Antenna Temperature Contributions from Absorption by Oxygen and Water Vapor with Galactic Background	80
5.2	Parallel Polarized Sky Temperature as a Function of Frequency for Clear and Cloudy Skies	86
5.3	Relationship Between Integrated Absorption in db and Radiometer Frequency for Liquid and Ice Clouds with liquid water content of 10 gm m^{-3} (From Lhermitte, 1968)	89
5.4	Zenith Brightness Temperature of the Earth's Atmosphere due to Oxygen Absorption as a Function of Frequency (from Ho, 1969)	93
5.5	Sketch of Terms in Radiometer Equation	94
5.6	Downward Atmospheric Opacity as a Function of Altitude for the Frequency of 2.65 GHz	96
5.7	Emission from a Layer of Air Between the Ground and Altitude h at the Frequency of 2.65 GHz	98
5.8	Correction in Apparent Temperature seen by an Airborne Radiometer as Calculated for $r = 0.65$, $T_s = 280^\circ\text{K}$, $T_c = 3.0^\circ\text{K}$ at the Frequency of 2.65 GHz	99
5.9	Sketch of the Science Center Rooftop Experiment to Observe the Sky Temperature as a Function of Viewing Angle, θ	102
5.10	Sky Temperature as a Function of Viewing Angle	104

Figure		Page
5.11	Experimentally Measured Pattern for Potter Horn Antenna	105
5.12	Comparison between Van Vleck Model and Changes in Brightness Temperature of the Sea from the 1971 Convair 990 Flights	108
5.13	Effect of Clouds on the Apparent Temperature of the Sea	112
6.1	Polarization Averaged Brightness Temperature of the Rough Sea in the Geometrical Optics Model	126
6.2	Geometry of the Rooftop Pool Experiments	132
6.3	Antenna Temperature vs Equivalent Slope	133
6.4	Antenna Temperature vs Wave Length	134
7.1	Wind Dependence of Whitecap Coverage and Spray Concentration (Monahan, 1968)	140
7.2	Latitudinal Variations of the World Ocean Whitecap Distribution (Blanchard, 1963)	141
7.3	Variation of Emissivity with Composition for a 10 cm Thick Foam Layer on Sea Water	143
7.4	Front View of Rooftop Pool, Horn Lowered for Calibration	145
7.5	Side View of Rooftop Pool, Horn in Operating Position	146
7.6	Back View of Rooftop Pool Showing Air Hose Used in Foam Simulation	150
7.7	Surface of Pool at Maximum Air Flow Rate (Foam Simulation)	151
7.8	View of Bubbles Rising From Air Hose to Water Surface	152
7.9	Surface of Pool at Air Flow Rate of 0.94 Liters per Second or 3% Coverage	153
7.10	Surface of Pool at Air Flow Rate of 1.88 Liters per Second or 6% Coverage	154
7.11	Surface of Pool at Air Flow Rate of 2.83 Liters per Second or 12.3% Coverage	155
7.12	Surface of Pool at Air Flow Rate of 3.77 Liters per Second or 20% Coverage	156
7.13	Transient Response of Oil on Water Surface (10 minute period)	158
7.14	Transient Response of Crude Oil Poured on Fresh Water over 12 Minutes	159
7.15	Transient Response of Crude Oil on Salt Water After Stirring	160
7.16	Effect of Bubble Formation on Antenna Temperature	161

Figure		Page
8.1	Radiometer Arrangement in SIO DC-3	168
8.2	Flight Trajectories over Pacific Ocean	171
8.3	Antenna Temperature During a Circular Flight Path	175
8.4	Schematic Diagram of Cryogenic Load for Aircraft Calibration	176
8.5	Equilibrium Amplitude Spectra for Gravity-Capillary Waves on the Sea and in the Laboratory (from Hess <i>et al.</i> , 1970)	181
9.1	Candidate Radiometer Configurations	188
9.2	Schematic of Test Setup for Measuring Noise Diode Stability	197
9.3	Simplified Block Diagram of Precision Comparator Concept	201
9.4	Simplified Block Diagram of Precision Nulling Radiometer	203
9.5	Input to Precision Comparator in Pulsed Mode	206
9.6	Three Different Calibration Techniques	208
9.7	Detailed Block Diagram of Practical Design for Proposed Radiometer	209
9.8	Detector Diode Circuit	212
9.9	Effective Power Input to Square Law Detector	216
9.10	Horn Compensation	227
9.11	Multimode Horn Pattern	234
9.12	Multiple Modes in Square Aperture	236
9.13	Beam Efficiency, Multimode Square Horn	238
10.1	Conceptual Sea Truth Facility	244

TABLES

Table		Page
1.1	Frequency Selection Criteria for Measurement of Sea Temperature by an S-Band Radiometer at 2.5-4.2 GHz	6
3.1	Principal Users of Satellite-Derived Sea Surface Temperature Data	15
3.2	Sea Surface Temperature Measurement Requirements - Oceanographic Research	20
3.3	Sea Surface Temperature Measurement Requirements - Thermal Mapping and Charting	22
3.4	Sea Surface Temperature Measurement Requirements - Fisheries Applications	23
3.5	Sea Surface Temperature Measurement Requirements - Pollution Applications	27
3.6	Sea Surface Temperature Measurement Requirements - Meteorological Research	29
3.7	Sea Surface Temperature Measurement Requirements - Weather Forecasting	30
3.8	User Needs and Requirements Summary	33
4.1	Variations From Year to Year in Surface Salinity at 24°20'N, 153°58'W Taken in Mid-August (After Muromstev, 1963)	45
4.2	ϵ' and ϵ'' for Distilled Water as a Function of Temperature	76
5.1	Attenuation by Non-Precipitating Cloud (One-Way) in db km^{-1} (From Gunn and East, 1954)	88
5.2	Attenuation Resulting From Precipitating Clouds in db km^{-1} (From Gunn and East, 1954)	91
5.3	Preliminary Evaluation of Attenuation at 2.7 GHz from Clouds Observed on the 1971 NASA Convair 990 Flights, Ground Data, and 1969 DC-3 Flights	111
5.4	Summary of Effects on Radiometric Observation of Sea Temperature Associated with Sky Background and Atmospheric Attenuation at 2.69 GHz	113
7.1	Smooth Water Observations on the Rooftop Pool	148
7.2	Oil Film Effect on Brightness Temperature of Salt Water	163
7.3	Oil Film Effect on Brightness Temperature of Fresh Water	163

Table		Page
8.1	Weather and Sea Conditions During the San Diego Flight	170
8.2	Typical Data From DC-3 Flights	173
9.1	Correction Factors and Errors for Cooled Terminations	186
9.2	Characteristics of Selected Radiometers	191
9.3	Performance of Noise Sources	196
9.4	Characteristics of High Quality Waveguide, Stripline and Microstrip Latching Circulators	199
9.5	Antenna Comparison Chart	225
9.6	Phase Error in Horns of Various Flare Angles	228
9.7	Lens Loss for Horns of Various Flare Angles	229
9.8	Multimode Horn Pattern Characteristics, $\beta = 0.465$	233
10.1	Projected Needs for S-Band Radiometer Sea Truth Program	242
10.2	Summary of Instrumentation and Techniques for Sea Truth Program	250

DEVELOPMENT OF A SATELLITE MICROWAVE RADIOMETER
TO SENSE THE SURFACE TEMPERATURE OF THE
WORLD OCEANS

by

G. M. Hidy, W. F. Hall, W. N. Hardy, W. W. Ho, A. C. Jones,
A. W. Love, M. J. Van Melle, H. H. Wang and A. E. Wheeler

Members of the Technical Staff
North American Rockwell Corporation

1.0 SUMMARY AND RECOMMENDATIONS

S-band microwave radiometers developed to perform absolute measurement of sea surface temperature have in the past been subjected to limited laboratory, field and aircraft flight test programs. The results of these test programs and theoretical analyses had provided convincing data as to the feasibility of using this type of radiometer as a future remote sensor system. However, there remained problems associated with the separation of uncertainties caused by the atmosphere and sea-surface conditions, for which further investigation was required, and the instrumental limitations needed to be better understood. This contracted study was undertaken to resolve these uncertainties, to establish the feasibility of developing such an instrument, and to prepare the conceptual design of a satellite-type radiometer system.

By means of theoretical analysis and experimentation several factors were investigated in this study that contribute to the uncertainties in interpretation of radiometric observations. These included: (1) establishing an analytical model for the deduction of the molecular sea-surface temperature from the measured data which contain the error effects of (a) the atmosphere, (b) the sea-surface condition and, (c) the radiometer system with a tentative absolute temperature accuracy of 1°K and a tentative temperature resolution of 0.1°K in the frequency domain 2.5-4.2 GHz; (2) designing a prototype space satellite oriented microwave radiometer; and (3) selection of the optimum frequency for use by the radiometer system. Hardware development and flight testing were not a part of this study.

The results of this study have contributed significant information to the evaluation and application of satellite microwave radiometry for use in the remote measurement of sea surface temperature. Factors were identified that are crucial to the design of an airborne instrument and to the interpretation of radiometric observations of thermal emission from the sea as molecular temperature. No insurmountable conceptual or instrumental difficulties developed as the result of these investigations. The conclusions of the study are summarized in the following remarks.

User Needs. A survey of current user requirements has indicated that there is a broad range of applications of radiometric data regarding thermal radiation from the oceans. Currently routine surface temperature data are not available for most of the open ocean areas particularly in the Southern Hemisphere. To be most widely useful for applications to sea temperature observation, satellite observations of the world ocean are desirable from one to two times a week, with an absolute accuracy of order $\pm 1^\circ\text{K}$ molecular temperature, averaged over a 100 km diameter area.

Implications of Salinity Change. Since the emissivity of water from 2.5-4.2 GHz is somewhat sensitive to salinity changes, the impact of surface salinity differences at sea had to be evaluated. The survey of geographical and temporal variations in salinity indicates that uncertainties resulting from such changes do not exceed a few tenths of a degree, except under extreme conditions. The climatological, averaged spatial variations can be corrected for using current knowledge of the global distribution of surface salinity. Temporal changes are more difficult to allow for because of lack of oceanographic data. However, without correction, these fluctuations are not expected to create uncertainties greater than $\pm 0.2^\circ\text{K}$ in molecular temperature.

Laboratory measurements of the dielectric properties of dilute salt solutions and sea water samples were made in this study to absolute accuracies comparable with those in the literature available for fresh water. These measurements have shown that sea water cannot be modeled accurately by simple sodium chloride solutions alone. However, the experimental results indicate that the dielectric properties of sea water can be predicted to high accuracy solely by measurement of the salinity of the water. Using measurements of the dielectric properties, the emissivity of smooth sea water can be calculated with absolute accuracy equivalent to $\pm 0.2^\circ\text{K}$ molecular sea temperature. To maintain this accuracy in the radiometric application, the average salinity of the world ocean should be known to an accuracy of at least $\pm 1\%$.

Atmospheric Effects and Sky Background. An analysis was made in this study of the various effects contributing to the sky background radiation, and the atmospheric attenuation at 2.5-4.2 GHz. Available ground based

and aircraft observations were used to assess the validity of the conclusions derived from the analysis. In the atmosphere, a major absorber of microwave energy over the frequency range of interest is oxygen, whose concentration is essentially constant. The major variable constituents are water in condensed and vapor states. Water vapor absorbs an order of magnitude less energy at 3 GHz than oxygen. However, water clouds and precipitation scatter, absorb, or emit sufficient radiation to be a significant factor in radiometric observations of the sea surface. Their interference depends on cloud thickness, liquid water content, and precipitation rate. Ice is a weaker factor than liquid water in the atmosphere.

In the clear atmosphere, past measurements have left the magnitude of the total atmospheric contribution to sky temperature uncertain. Some evidence supports a 2°K contribution to the zenith sky temperature while other results point to 4°K at 2.69 GHz. Theoretical models for oxygen absorption support the lower value.

Two new, independent experiments were conducted by the Science Center that confirm the atmospheric contribution to sky temperature estimated from theory. The first experiment was a ground based study of the variation in brightness temperature as a function of viewing angle from zenith to that approaching the horizon. The second investigation involved interpretation of aircraft measurements of the brightness temperature of the sea at various altitudes to approximately 11 km. The results of these studies support the Van Vleck-Weisskopf model for oxygen absorption to estimate the contribution of the clear atmosphere to the sky background.

Limited experimental observations suggest that the contribution of clouds is small, as expected from predictions of simple theory. The cloud interference is expected to be intermittent for satellite observation, but will have to be accounted for in interpretation of the instrumental observations. The available experimental results are inadequate for verifying the applicability of available theoretical models of cloud attenuation. It is important for the success of the oceanographic applications to further pursue the cloud interference experimentally. It is recommended that ground based aircraft observation of clouds be attempted in the range of 2.5-4.2 GHz with high priority while simultaneous direct measurements are made of cloud thickness, liquid water content, and precipitation rate.

The radio noise contributions from extraterrestrial sources and that of the clear atmosphere at 2.69 GHz are now believed to be known to high accuracy equivalent to a brightness temperature less than $\pm 0.5^\circ\text{K}$.

Surface Roughness. The investigation of the influence of surface roughness was aimed at improving the theoretical framework for predicting such effects. Existing theoretical models for the effect of surface roughness

on the observed brightness temperature are open to question and hence their predictions are of doubtful value. The analysis conducted in this study classified the relationship between different models currently being evaluated. The classical geometrical optics calculations was extended to include the effect of multiple reflections. This modification produced a significant increase in surface emissivity over the simpler case for very large wave slopes equivalent to hurricane force winds.

Limited exploratory experiments were conducted to test the theoretical predictions. The results are essentially qualitative in nature, but indicate that the roughness contribution to the surface emissivity is substantially greater than expected from available theory.

To improve the state of theoretical development, a new analytical theory has been developed that can be shown to yield results of arbitrarily high accuracy in calculation, using adequate computational models of the sea surface topography. Although the new model has been formulated, the equations have not been investigated numerically for results relevant to the radiometer application.

Evaluation of the influence of reflection of solar radiation from a rough surface has indicated that this may be a potentially significant contribution to the apparent sea temperature observed at 2.5-4.2 GHz for a downward looking instrument; a 1°C contribution to brightness temperature may be expected from solar energy reflection when the sun is within 20° of the zenith.

Aside from foaming, the contribution of roughness to the emissivity of the ocean surface at 2.69 GHz is the principal phenomenon presently unaccounted for in interpretation of the radiometer antenna temperature. Therefore, the theoretical work initiated in this part of the program should be pursued to its logical conclusion. Because of the apparent sensitivity to roughness of circularly polarized reception of thermal emission from the sea, this work should be continued at high priority.

Microscale Surface Disturbances. There has been controversy about the magnitude of interference expected from microscale disturbances at the air-sea interface. The main identified contributors are sea spray, foam, and oil slicks. Both experimental results and theoretical analyses derived from this study have indicated that neither sea spray nor natural oil slicks will have a significant influence on the brightness temperature of the sea. Oil pollution may become locally severe enough to make a noticeable contribution, but only if film thickness exceeds 0.5 mm. Indirectly, there may be an effect due to oil slicks by their inhibition of wind waves.

Potentially, the microscale effect of greatest concern is that resulting from sea foam. The magnitude of the effect depends on the extent of surface coverage as well as the thickness, density, and composition of the bubble

layer. Little quantitative information is available about the nature of sea foams. However, our investigation of simulated foam has indicated that this effect can contribute as much as several degrees Kelvin to brightness temperature under intense storm conditions with high winds where foam coverage exceeds 10-20 percent of the surface. Taking into consideration the available climatological information on foam coverage, the extent of surface coverage should be well below five percent in middle latitudes and tropical areas where sea temperature surveillance is of interest. If such extrapolations are reliable, foam formation should present a major interpretation problem only during limited periods over areas in stormy weather, where clouds may obscure the surface. To evaluate more quantitatively the role of foam in degrading sea temperature measurement accuracy, an extensive study of the properties of foam, as they effect radiometry, is recommended at high priority.

Interpretation of DC-3 Flight Results. The studies conducted in flight programs, with the independent development of a new calibration technique, have enabled further evaluation to be made of airborne radiometric observations of the sea taken in 1969. Results indicate that the observed brightness temperature of the Eastern Pacific Ocean coastal waters up to 1 km altitude were systematically warmer by 4°K than that calculated for a smooth sea. This discrepancy is now tentatively assigned to the effect of surface roughness and associated sun glitter. The fact that the discrepancy remained constant for somewhat varying sea state conditions and is approximately the same as observed in 1971 Convair 990 flights over markedly different sea state conditions suggests that a constant correction for roughness may be justifiable. Such a constant factor may be associated with the tendency of the sea surface to achieve an equilibrium configuration at relatively short water wavelengths.

Cosmic background is effectively a constant (small) correction at a given frequency, and the salinity variation can be accounted for with current knowledge of the world ocean to first order. Despite the drawback of larger antenna sizes, we recommend that the frequency of instrument operation for oceanographic applications be selected at or near 2.69 GHz.

Antenna requirements for a satellite-borne instrument are considered and enumerated and various generic antenna types are compared in the light of these requirements. As a result of these comparisons the recommended antenna for radiometric sea surface temperature measurement is the horn. The simple horn, however, is inadequate and requires some modification to its aperture field distribution. Two methods of achieving this are discussed; use of corrugations on the inside walls, and creation of certain higher order modes within the horn to modify the field of the dominant mode. An analysis of the radiation patterns of such multimode horns has been carried out. Computation shows that beam efficiency can be as high as 98 percent for the multimode horn.

It is recommended that further flight programs be designed and conducted at the earliest possible opportunity since they provide important experience for guiding identification of problem areas in the application of the instrument (see also Sea Truth).

Conceptual Design of Airborne Radiometer. Bearing in mind the limitations and constraints placed upon any eventual satellite-borne instrument, a new radiometer design concept was evolved in which the long term high absolute accuracy of measurement is not compromised. Resulting from a survey of many possible and proposed radiometer configurations, the recommended system uses a signal-modulated (Dicke) receiver with noise injection in the signal arm so that the system operates in the nulling mode. The question of stability of the noise injection source has been studied and it is concluded that the avalanche diode best meets the needs of the system.

The preliminary survey of the requirements placed on minimization of physical effects and hardware for optimum operational frequency in the range 2.5-4.2 GHz can be summarized in Table 1.1.

Table 1.1. Frequency Selection Criteria for Measurement of Sea Temperature by an S-Band Radiometer at 2.5-4.2 GHz

Effect	Recommended Frequency	Relative Significance
Salinity	As High as Possible	Correctable to 1st Order
Galactic Noise	As High as Possible	Small Contribution through entire region
Clear Atmosphere	Approximately Independent of Frequency	--
Clouds and Precipitation	As Low as Possible	Corrections uncertain & difficult to evaluate with single instrument
Surface Roughness	Uncertain	--
Foaming and Spray	As Low as Possible	Foaming a crucial factor
Oil Slicks	As Low as Possible	
Instrument Hardware	As High as Possible (particularly for antenna)	Not a critical factor

From a practical standpoint of operational capability on a worldwide basis, consideration also has to be given to the optimum frequency for minimizing interference from radio and radar transmission. From this point of view, the radio astronomy band centered at 2.695 GHz is best. Taking into account this conclusion in the light of the data in Table 1.1, a recommended operational frequency is made.

Sea Truth Program. It is vital to the further development of microwave radiometry for oceanographic applications to compare the observations by remote sensors with suitable direct measurements of ocean water properties. A study of possible alternatives for a sea truth facility has been made. A useful, but economical system appears to begin with a well instrumented tower or oceanographic ship as a base point. For spatial coverage, the moored vessel should be supplemented with throwaway buoys launched from the instrumented aircraft. Minimum instruments on the buoys should include water temperature and electrical conductivity. To be most effective, radiometers should be mounted on the moored vessel and operated simultaneously with similar airborne instruments flown overhead. To expedite the further development of methods for interpretation of observations of thermal emission from the sea temperature, a sea truth facility should be designed and built as soon as possible.

Utilization and Engineering Development. A preliminary review of potential applications to planned aircraft and satellite programs has been made. There appear to be ample opportunities in the coming years to exploit the potential benefit of S-Band radiometers for oceanographic applications. Every effort should be made at this time to integrate this instrument into aircraft experiments so that its performance and usefulness can be determined.

The development of instrumentation for aircraft applications is now feasible. Further work will be required to develop high precision radiometers compatible with orbiting satellite requirements. Particular attention to problems of calibration and miniaturization of critical electronics components and system long term stability will be needed. Development of the radiometer system for ultimate satellite use is recommended for initiation as soon as possible.

Further attention is needed on the critical factors affecting the potential limitation of the widespread applicability of S-Band radiometry for oceanographic applications. To parallel with further investigations of the class described here, effort must be made to consider integration of multi-instrument packages to optimize the information to be obtained from remote

sensing of the sea surface. In the case of microwave radiometry, particular attention is required to identify the most efficient methods of deriving both temperature and surface roughness from instrument configurations.

Perhaps the best way, at this stage, to further develop the usefulness of microwave radiometry for oceanographic applications is to more actively seek the participation of interested scientists in such programs. Early participation by users will create a self-stimulating atmosphere to influence the science and applications of oceanography for the possible benefits of this type of experimental capability. By such interaction, it should be possible to use directly the radiometric observations of thermal radiation rather than force such data "unnaturally" into a pattern relying on more classical instrumentation.

2.0 INTRODUCTION

Until recently most of the effort aimed at the development of remote sensors for Earth Applications have been concentrated on those for measurement of atmospheric properties. However, improved instrumental techniques and a better understanding of the transmission properties of the atmosphere have led to much more interest in viewing quantitatively the properties of the Earth's surface. One of the more significant and practical global measurements that can be made from a satellite is the absolute ocean surface temperature. A preliminary rationale for the importance of such observations to the meteorological and oceanographic community was reported a few years ago by a panel of the National Academy of Sciences (1969).

Measurement of sea surface temperature from satellite borne instruments has already been performed with some success using infrared radiometers wavelength on Nimbus vehicles (Smith, et al., 1970). Experiments to deduce sea temperature from infrared detectors at other wavelengths are being planned, and some success has been achieved for measuring gradients of temperature at the sea surface by aircraft borne infrared radiometers (McAlister and McLeish, 1969). These infrared experiments have demonstrated important capability by achieving useful observations of sea surface temperature. However, they suffer severe degradation when operated at high altitudes by rain cloud interference, and sun glitter from the water surface. It is possible to avoid these difficulties, in principle, by using microwave radiometry to determine sea temperature with a 24 hour, all weather operational capability.

To investigate the feasibility of passive measurement of sea temperature at microwave frequencies, a study program was instituted at the North American Rockwell Corporation (NR) in 1966. The objectives of the project were: (1) to develop microwave radiometers for observing quantitatively the thermal emission from the sea, (2) to interpret the instrumental observations in terms of sea surface temperature and other important physical properties of the sea, and (3) to deduce the practical limitations on measurement of absolute sea surface temperature by microwave radiometry from aircraft and satellite altitudes.

The initial results achieved in the program are discussed by Hidy, et al (1969). The first stage of the study demonstrated the feasibility of

constructing an S-Band radiometer with a capability for absolute measurement of the thermal emission from the sea to about $\pm 1^\circ\text{K}$. Observations of lake water and of the Pacific Ocean suggested that the following uncertainties in such experiments seriously limited relating the measured antenna temperatures to the molecular temperature of the natural waters: (1) the dielectric properties of sea water were not known to high enough accuracy to evaluate the error in the radiometric measurements, (2) the role of atmospheric attenuation by oxygen gas, and rain clouds were not well enough known to correct the instrumental measurements, (3) the influence of roughness of the sea on the water emissivity and other surface effects such as oil slicks could not be calculated quantitatively. Nevertheless, with the use of rather crude information the limited measurements of the brightness temperature for the Pacific Ocean from an airborne radiometer could be corrected to agree within about $.4^\circ\text{K}$ without accounting for surface waves. Such a result was sufficiently promising to encourage continuing the development of a satellite compatible instrument system.

The radiometer used in the preliminary NR investigations was of simple Dicke design, and used a boiling cryogenic termination load for calibration. The application of boiling liquids for aircraft or satellite systems is unsuitable, so it was necessary to design a new configuration more compatible with airborne applications.

A serious problem in evaluating the limitations of remote sensors for sea temperature is the lack of adequate direct measurements of ocean surface properties. Our experience in flying the first prototype microwave radiometer emphasized this point, and presents a continued unresolved problem in further development of remote sensors for oceanographic applications.

Discussions in late 1969 with staff of the National Aeronautics and Space Administration (NASA) - Advanced Applications Flight Experiment (AAFE) Program indicated that NASA sponsorship was appropriate for continuing the NR study program. This report is a discussion of further progress on the development of a satellite borne microwave radiometer to measure sea temperature as sponsored under NASA Contract NAS 1-10106. The principal objectives of this study contract were: (a) to investigate further those aspects of atmospheric and ocean physics listed above that inherently limit the interpretation of radiometric data, (b) to design a new instrument configuration that is compatible with airborne constraints, but is aimed at achieving high absolute accuracy ($\pm 0.1^\circ\text{K}$) of detection of thermal emission from the sea, and (c) the design of a sea truth program to provide an adequate test facility for microwave radiometry applied to sea temperature detection.

The following text describes the study results to date, and discusses recommendations for further studies to develop a useful satellite system. Before undertaking such discussion, it is appropriate to reemphasize the applications of remote detection of sea temperature by reviewing and updating the user needs and requirements.

REFERENCES

Hidy, G.M., K.W. Gray, W.N. Hardy, W.F. Hall, W.W. Ho, A.W. Love, and E.J. Thompson, Dec. 1969, "S-Band Radiometer for Measurement of Sea Temperature," North American Rockwell Science Center Report SCTR-69-31, p. 60.

McAlister, E.D. and W. McLeish, "Heat Transfer in the Top Millimeter of the Ocean," J. Geophys. Res. 74, 3408-3414 (1969).

Smith, W.L., P.K. Rao, R. Koffler, and W.R. Curtis, "Determination of sea surface temperature from satellite hi-resolution infrared window radiation measurement," Monthly Weather Review 98, 604-611 (1970).

Summer Study on Space Applications, Panel 5, 1969: Useful Applications of Earth Oriented Satellites National Academy of Science, Washington, D.C., p. 27-37.

3.0 USER NEEDS AND REQUIREMENTS

One of the objectives of this study was to establish the tentative design and operational parameters for an S-Band Microwave Radiometer that will provide the greatest amount of useful sea surface temperature data commensurate with user needs and requirements. A survey of potential users and an analysis of their requirements and applications of microwave radiometer data were conducted to define the current needs of the oceanographic and meteorological communities. These needs are used to provide a basis for the establishment of the design and performance parameters.

Potential applications for satellite or airborne measurements of sea surface temperature may be grouped as follows:

- Oceanographic Research
- Thermal Mapping and Charting
- Fisheries Applications
- Pollution Applications
- Meteorological Research
- Weather Forecasting

3.1 Principal Users of Sea Surface Temperature Data

As an initial step in the determination of user requirements, an investigation was conducted to identify the various agencies, institutions, international cooperative associations, etc. engaged in activities directly related to these applications. The identification of these user groups was accomplished by an investigation consisting of a literature search, supplemented by pre-existing personal knowledge of the investigators working on the study program, and confirmed by discussions with typical representatives in each of the categories noted above. In the case of international organizations, an effort was made to contact either specific individuals participating in these activities or having working knowledge of their operational requirements. A listing of typical user agencies and the individual contacted to ascertain requirements is presented in the Appendix.

A tabulation of the principal user groups is presented in Table 3.1, in which the using agencies are listed as (1) Federal Agencies (other than Department of Defense); (2) Department of Defense; (3) Educational Institutions; (4) International Organizations. For each user agency identified in these listings the areas of application, corresponding to those previously noted, are indicated by a solid (●).

To avoid needless detail, specific potential commercial users of data are not included in these listings. Examples would be the shipping companies who would find sea surface temperature of interest in route planning and ice avoidance, and the small local fisheries advisory groups who relay data to fishing fleets.

3.2 Measurement Requirements

A survey of typical representatives of each of the user groups disclosed a number of specific applications of sea surface temperature data, covering a broad range of specific needs. These vary according to the nature of the application, and even according to the specific needs of specialists working in a given application area. The general nature of the data and measurements requirements in each of the major areas are discussed in the following paragraphs, and the specific needs are summarized in Tables 3.2 through 3.7, which present the requirements in terms of temperature accuracy, temperature measurement range required, surface resolution, geographic areas of interest, and the most commonly requested frequencies of observation. Due to the broad range of the requirements as determined during the user survey, it is not possible to give specific overall requirements as to the temperature accuracies required, the desired surface resolution, and the required frequency of observation. During the discussions and in the subsequent analyses of the stated needs, the requirements were evaluated in terms of (1) optimal values, designated as "O", which provide information fully meeting the present and anticipated needs for remote sensing measurements; (2) acceptable values, designated as "A", which will provide a large portion of the needs; and (3) marginal values, shown as "M", which will provide useful information not fully meeting the needs of the user, but still of considerable value.

Table 3.1 Principal Users of Satellite-Derived Seas Surface Temperature Data (Cont)

		Oceanographic Research	Oceanog. Mapping & Charting	Meteorological Research	Weather Predictions	Fisheries Applications	Pollution Applications	Data Handling	Other Applications
Natl Center for Atmospheric Research	Boulder, Colo.	•	•	•	•			•	
U.S. Coast Guard									
Marine Sciences Div.	Washington, D. C.	•	•			•		•	
Department of Defense									
Naval Oceanographic Office	Washington, D. C.								
Oceanographic Surveys Dept.		•							
Oceanographic Analysis Div.		•							
Spacecraft Oceanographic Project		•							•
Research, Develop. Div.		•							
Oceanographic Plans Office		•							
Oceanographer of the Navy	Alexandria, Va.								
Ocean Science Dept.		•							•
Environmental Prediction Service									•
Fleet Numerical Weather Central	Monterey, Ca.	•	•						
Fleet Weather Facility	San Diego, Ca.	•	•	•	•				•

3.2.1 Oceanographic Research

In the various educational and research institutions and governmental agencies engaged in oceanographic research, a broad spectrum of types of oceanographic research is represented, presenting varied and widely differing sea surface temperature measurement requirements. Data which fully meet the needs for a specific type of investigation, such as ocean-wide current and circulation studies, will be of virtually no value in the investigation of thermal microstructures of phenomena of limited temporal duration and spatial extent. An analysis of measurement requirements presenting the overall requirements in terms of ranges (i. e., temperature accuracy of 0.1°C to 2°C, surface resolution of 60 m to 100 km, etc.) would only observe the development of performance requirements, application areas, and operational parameters for the microwave radiometer system. Similarly, a tabulation of the requirements for specific on-going or planned programs would yield an unworkable mass of conflicting data. For the purpose of analyzing and evaluating the requirements to develop useful criteria, the types of oceanographic research have been categorized as follows:

Thermal Mapping - Ocean-Wide

Thermal Structures and Anomalies - Ocean-Wide

Thermal Mapping - Regional (i. e., major currents, upwelling areas)

Thermal Mapping - Coastal

Thermal Studies - Microstructures

Arctic Studies - (Sea Ice, Water-Ice Boundaries)

The requirements in each of these areas, as determined from extensive literature surveys and personal contacts with representative user groups and agencies, are summarized in Table 3.2.

3.2.2 Thermal Mapping and Charting

One of the principal uses of sea surface temperature as derived from future satellite and aircraft sensor systems is the preparation of sea surface temperature maps and charts on an oceanwide or global scale. Mapping of this type, for the purpose of preparing monthly, seasonal, and annual sea surface temperature charts, is accomplished by the Naval Oceanographic Office, with data collected from a variety of sources, including oceanographic research ships, ships of opportunity, buoy systems, and survey-type aircraft equipped with remote sensing devices. Satellite systems will provide much

Table 3.2. Sea Surface Temperature Measurement Requirements
Oceanographic Research

Application	Temp. Accuracy	Temp. Range	Surface Resolution	Area of Interest	Frequency
Thermal Mapping - Ocean Wide	±1° C (O)	-10° C to +30° C	100-200 KM(O) 200-400 KM(A)	No. Pac. So. Pac. No. Atl. So. Atl.	1 WK (A) 2 WK (A) 1 MO (M)
Thermal Structures and Anomaly Studies - Ocean Wide	±1° C (O)	-10° C to +30° C	100-400 KM(O) 200-400 KM(A)	No. Pac. So. Pac. No. Atl. So. Atl.	4 D (O) 1 WK (A) 1 MO (M)
Thermal Mapping - Regional (Major Currents, Upwelling Areas)	±0.5° C (O) ±1° C (A)	-10° C to +30° C	10-20 KM(O) 20-50 KM(A) 50-100KM(M)	No. Pac. So. Pac. No. Atl. So. Atl.	1 D (O) 4 D (A) 1 WK (M)
Thermal Mapping - Coastal	±0.1° C (O) ±0.5° C (A)	0° C to +30° C	5-10 KM(O) 10-20 KM(A) 20-50 KM(M)	No. Amer. Seas. Arctic Coastal Areas	1 D (O) 4 D (A) 1 WK (M)
Thermal Studies - Microstructures	±0.1° C (O) ±0.5° C (A) ±1° C (M)	-10° C to +30° C	5-10 KM(O) 10-20 KM(A) 20-50 KM(M)	No. Atl. No. Pac.	1 D (O) 4 D (A)
Arctic Studies	0.5° C (O) 1.0° C (A)	-10 to 20° C	5-10 KM(O) 10-50 KM(M) 50-100 KM()	60° to 90° N and S	4 D (O) 1 WK (A) 1 MO (M)

(O) Optimal (A) Acceptable (M) Marginal

more reliable data, in a timely manner, and on a global basis. Sea surface temperature maps are also prepared by the National Marine Fisheries Service (NMFS) on a routine basis for the Pacific Ocean, and by the Coast and Geodetic Survey for coastal waters. The U. S. Coast Guard issues some sea surface temperature maps of restricted areas.

The basic requirement for ocean-wide or global sea surface temperature mapping is generally accepted as an accuracy of 1°C , and a spatial resolution on the order of 400 km is adequate to meet requirements. For regional mapping, such as the Gulf Stream area and in the vicinity of other major currents and in upwelling areas, a temperature measurement accuracy of 1°C is regarded as adequate, although some researchers would prefer an accuracy of 0.5° or better; a surface resolution of 100 km is acceptable, with 20 to 50 km being desired. The most stringent requirements arise from special purpose studies, involving thermal micro-structures, current, or anomalies of short temporal duration, for which the requirements may be as severe as 0.1°C on a 4 hour to one day basis, and with a surface resolution of four to twenty kilometers.

The requirements for thermal mapping and charting are summarized in Table 3.3.

3.2.3 Fisheries Applications

The principal application of satellite-derived sea surface temperature data to the fisheries community is the preparation of periodic advisories, including sea surface temperature charts and other data related to the distribution and probable abundance of commercially-catchable fish types in the oceans. As an aid to the fisheries industry, synoptic sea-surface temperature charts for the global oceans are issued on a monthly and bi-monthly basis (principally by NAVOCEANO and the National Marine Fisheries Service). In addition, daily fisheries advisories bulletins are issued, conveying sea surface temperature data of timely interest, including information regarding the distribution and characteristics of significant ocean currents and upwelling zones and areas.

The measurement requirements for these various types of charts and advisories are summarized in Table 3.4.

At the present time, the ocean-wide sea surface temperature maps are prepared from all available information, including oceanographic research vessels, buoys, and ships of opportunity. The reliability of the data derived from ships of opportunity leaves much to be desired, with different observers reporting temperatures varying as much as several

Table 3.3. Sea Surface Temperature Measurement Requirements
Thermal Mapping and Charting

Application	Temp. Accuracy	Temp. Range	Surface Resolution	Area of Interest	Frequency
Sea-Surface Temperature Charting - Ocean Wide	±0.5° C (O) ±1° C (A) ±2° C (M)	-10° C to +30° C	100-200 KM(O) 200-400 KM(A)	No. Pac. So. Pac. No. Atl. So. Atl.	1 WK (O) 2 WK (A) 1 MO (M)
Sea-Surface Temperature Charting - Coastal Areas;	±0.1° (O) ±0.5° (A) ±1° C (M)	0° C to + 30° C	10-20 KM (O) 20-50 KM (A) 50-100KM (M)	Coastal to 500 Mile N and S America 15°N-15°S	4 D (O) 1 WK (A) 2 WK (M)
Tropics	±0.1° (O) ±0.5° (A) ±1° C (M)	0° C to + 30° C	10-20 KM (O) 20-50 KM (A) 50-100KM (M)		4 D (O) 1 WK (A) 2 WK (M)
Sea-Surface Temperature Charting - Regional					
Ocean Currents	±0.2° C (O) ±0.5° C (A) ±1.0° C (M)	-10° C to + 30° C	10-20 KM(O) 20-50 KM(A) 50-100 KM(M)		4 D (O) 1 WK (A) 2 WK (M)
Upwelling Zones	±0.2° C (O) ±0.5° C (A) ±1.0° C (M)	0° C to + 30° C	10-20 KM (O) 20-50 KM (A) 50-100 KM(M)		1 D (O) 4 D (A) 1 WK (M)

(O) Optimal (A) Acceptable (M) Marginal

Table 3.4. Sea Surface Temperature Measurement Requirements
Fisheries Applications

Application	Temp. Accuracy	Temp. Range	Surface Resolution	Area of Interest	Frequency
Monthly Sea Surface Temperature Charts (Synoptic)	1° C	-10° C to +30° C	200 KM (O) 400 KM (A)	No. Pac. So. Pac. No. Atl. So. Atl.	2 WK (O) 1 MO (A)
Bi-Weekly Sea Surface Temperature Charts (Synoptic)	1° C	-10° C to +30° C	100-200 KM(A) 200-400 KM(A)	No. Pac. So. Pac. No. Atl. So. Atl.	1 WK (O) 2 WK (A)
Daily Fisheries Advisories (Synoptic/Predictive)	1° C	-10° C to +30° C	100-200 KM(O) 200-400 KM(A)	30° N to 5° S (Pacific)	1 Day
Ocean Current Monitoring	0.2° C (O) 0.5° C (A) 1.0° C (M)	-10° C to +30° C	20-50 KM (O) 50-100 KM (A)	Specific Areas	1 D (O) 4 D (A) 1 WK (M)
Upwelling Detection and Monitoring	0.2° C (O) 0.5° C (A) 1.0° C (M)	0° C to +30° C	10-20 KM (O) 20-50 KM (A) 50-100 KM(M)	Specific Zones	1 D (O) 4 D (A) 1 WK (M)

(O) Optimal (A) Acceptable (M) Marginal

degrees as observed at approximately the same time in close proximity. Also, the data derived from ships of opportunity are for the most part restricted to the customer shipping lanes, leaving large areas of the oceans with sparse or no data. The effects of this are indicated in the NMFS maps shown in Figures 3.1 and 3.2.

It is of considerable interest to note in Figures 3.1 and 3.2 how limited the sea surface temperature data is in the Southern Pacific Ocean. The NMFS feels that the currently available data are completely inadequate to estimate any surface temperature anomalies over the entire Southern Pacific Ocean. The application of satellite instrumentation could supply a broad coverage of this area on a routine basis.

3.2.4 Pollution Applications

Because of social and economic considerations, the major emphasis on the application of remote sensing techniques to the problems of pollution detection and monitoring has been concentrated on the coastal and in-shore environments. The characteristic short-term and restricted spatial features of these pollution problems result in rather severe measurement requirements, as is shown in Table 3.5. To date, the major emphasis has been directed toward coastal problems resulting from oil spills, with some attention to potential thermal pollution from coastal power plants and to other types of industrial pollution. A survey of potential users of open ocean pollution data has been unrewarding, with the principal comments being directed toward the possibility of major oil spills resulting from the use of super-tankers to transport crude oils and other petroleum products. The summary of the potential requirements for pollution applications is given in Table 3.5.

3.2.5 Meteorological Applications

As the science of meteorology becomes more concerned with the controlling effects of the masses of the ocean waters upon atmospheric circulation and weather phenomena, more attention is being directed toward the need for means to measure sea surface temperature reliably and quickly on a global basis. Present atmospheric research ranges broadly in scope, from studies of the effects of small structural features of limited temporal duration (e.g., upwelling areas near coasts) to those major features such as general oceanic circulation patterns and energy exchange mechanisms at and near the air-water interface.

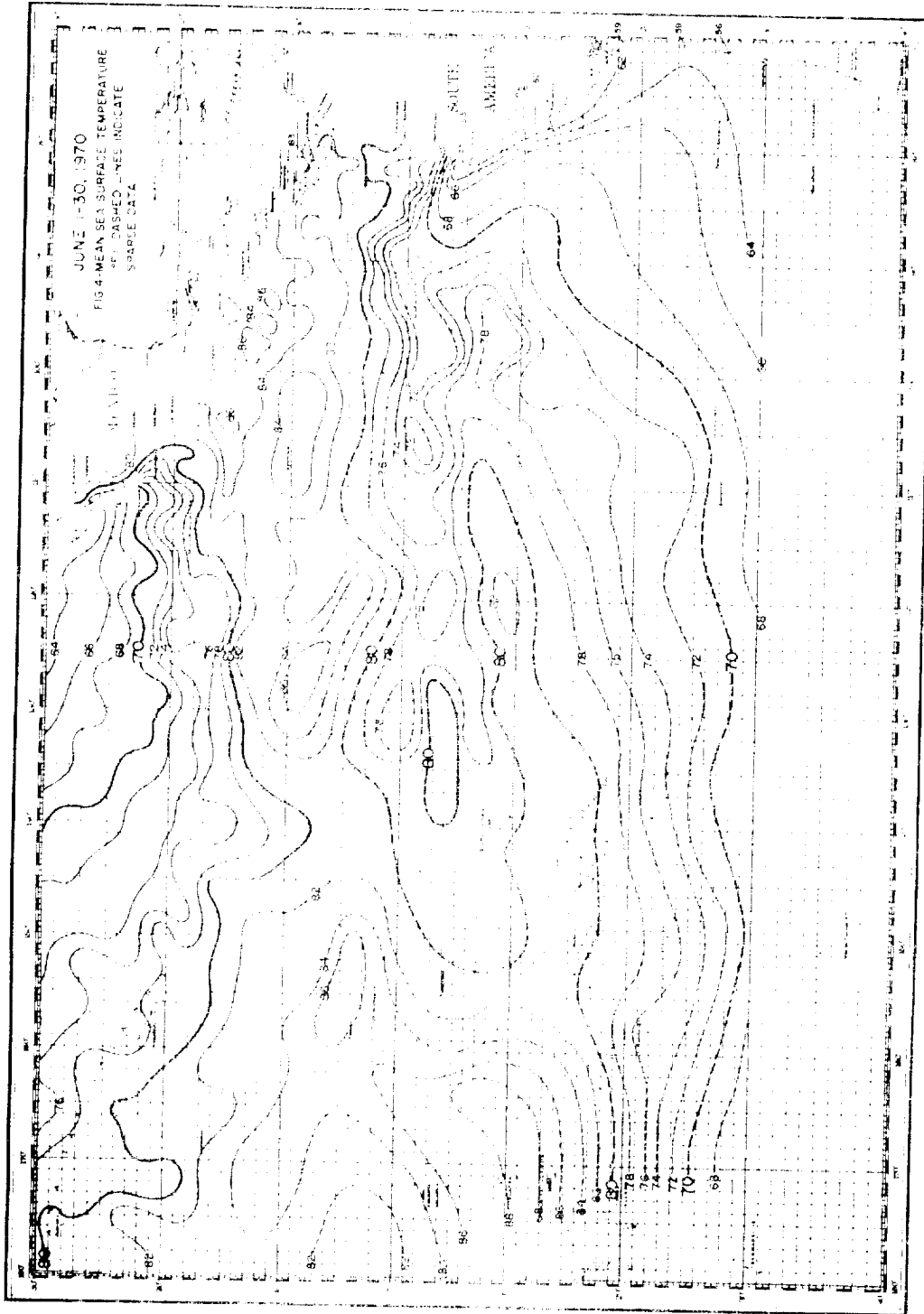


Figure 3. 1 Example of Typical Sea Surface Temperature Chart

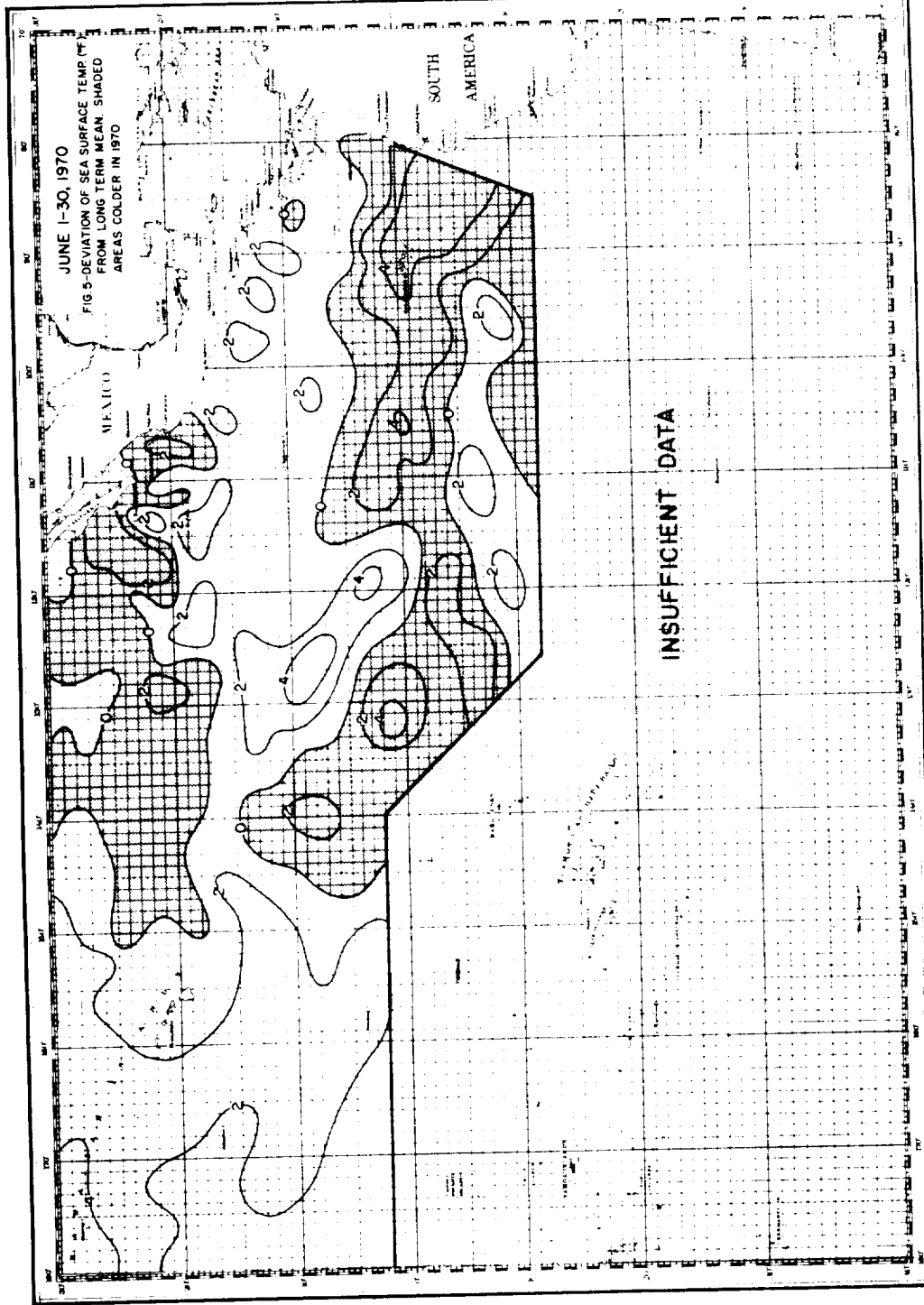


Figure 3.2 Typical Sea Surface Temperature Chart, Showing Deviations from Long Term Mean

Table 3.5. Sea Surface Temperature Measurement Pollution Applications

Application	Temp. Accuracy	Temp. Range	Surface Resolution	Area of Interest	Frequency	Requirements
Thermal Pollution (Coastal)	0.5° C (O) 1.0° C (A)	0° C to +30° C	10-50 KM	Coastal Areas of U.S. (to 200 KM)	1 WK	Requirements not definitely established
Industrial Pollution, Oil Spills, Wash Disposal (Coastal)	0.1° C to 0.5° C (O) 1.0° C (A)	0° C to +30° C	10-50 KM	As Above	1 WK (1 Day During Oil Spill Activity)	Requirements not definitely established
Oil Spills (Open Ocean)	0.5° C (O) 1.0° C (A)	-10° C to +30° C	50-100 KM	No. Atl. No. Pac.	1 WK	Requirements not definitely established

(O) Optimal (A) Acceptable (M) Marginal

The planned programs of the Global Atmospheric Research Program exemplify the needs for ocean-wide measurement of sea surface temperature for atmospheric research programs. Observations on a 200 to 400 km grid, with a surface resolution of 200 to 400 km will provide much needed data. Similar data are required by the universities engaged in large-scale meteorological research, as well as by the National Weather Service. Smaller-scale programs, such as the studies of the NWS on the relationship of small coastal thermal anomalies to fog formation require data on a much finer grid, and to a higher degree of precision. The requirements for sea surface temperature as applicable to meteorologic research are summarized in Table 3.6.

3.2.6 Weather Forecasting

The basic sea surface temperature measurement requirement for long range (4 to 7 days) weather forecasting is the detection of thermal anomalies and changes of such temporal duration and spatial extent as to result in significant energy-exchange transfers between the ocean and the atmosphere. These oceanic phenomena which will affect weather sufficiently to permit long-range forecasts will in general extend over areas of hundreds of kilometers. Marine meteorologists can profitably use sea surface temperature data providing surface resolutions of 400 to 600 km, and absolute accuracies of 1.0°C . For some specific types of forecasting, accuracies of 0.5°C to 0.1°C may be desired. For shorter range forecasts (1 to 4 days), the same considerations pertain as to measurement accuracy, but smaller areas are of interest, resulting in a somewhat smaller surface resolution requirement, on the order of 200 to 400 km. In both cases, a one-day measurement interval is optimum, but for the long-range forecasts a 2 to 4 day interval would produce useful data. For short range (12 hours to 2 days) predictions of local and/or short term phenomena (fogs, squalls, etc.), and for some types of military applications, accuracy of 0.1 to 1.0°C is required, with surface resolutions varying from 10 to 100 km.

Frequent, periodic and accurate measurements of sea surface temperature could greatly improve the reliability of weather forecasts. Present coverage of the Northern Hemisphere will be improved, both by providing data from areas not presently well sampled (e. g., away from shipping lanes) and by repetitive average on a routine basis. Predictive data will also be available for the southern hemisphere, not presently feasible.

The measurement requirements for weather forecasting are summarized in Table 3.7.

Table 3.6. Sea Surface Temperature Measurement Requirements
 Meteorological Research

Application	Temp. Accuracy	Temp. Range	Surface Resolution	Area of Interest	Frequency
Energy-Exchange Studies; Temporal and Spatial Structures, Anomalies, Global	0.5°C (O) 1.0°C (A)	-10°C to +30°C	200 to 400 KM	No. Pac. So. Pac. No. Atl. So. Atl.	1 Week
Circulation Studies; Temporal, Spatial Structures Anomalies; Global	0.5°C (O) 1.0°C (A)	-10°C to +30°C	200-400 KM	No. Pac. So. Pac. No. Atl. So. Atl.	1 Week 1 Week 1 Week 1 Week
Fog Formation Studies	0.5°C (O) 1.0°C (A)	0°C to +30°C	20-50 KM	Pacific Coast to 200 Mi.	1 Day
Integrated Global Studies (GHRP)	±0.1°C (O) 1°C (M)	-10°C to +30°C	100 to 200 KM	Atl. O., , 10°S to 20°N	1 to 4 Per Day
Special-Purpose Research	0.2°C to 0.5°C (O) 1°C (M)	-10°C to +30°C	20-100 KM	No. Pac., No. Atl., Tropics (±15° Lat)	1 Per Day to 1 Per Week

(O) Optimal (A) Acceptable (M) Marginal

Table 3.7. Sea Surface Temperature Measurement Requirements
Weather Forecasting

Application	Temp. Accuracy	Temp. Range	Surface Resolution	Area of Interest	Frequency
Long-Range Predictions (4 to 7 Days)	±0.1 (O) 1°C (M)	-10°C to +30°C	400 to 600 KM	Global Oceans	1 Day (O) 2 Days (A) 4 Days (M)
Short-Range Forecasts (1 to 4 Days)	±0.1°C (O) 1°C (M)	-10°C to +30°C	200 to 400 KM	Atl. & Pac. to Mid-Ocean	1 Day
Fog Predictions	±0.1°C (O) 1°C (A)	-10°C to +30°C	50-100 KM	No. Atl. No. Pac.	1 Day
Special Purpose Predictions	0.1°C to 0.5°C	-10°C to +30°C	10-50 KM	No. Atl. No. Pac. Tropics	1 Day to 1 Week

(O) Optimal (A) Acceptable (M) Marginal

Numerical Predictive Services; Some Military Applications

3.3 Requirements Summary

The identified needs of the various user-group communities represent a broad range of measurement requirements for remote sea surface temperature determinations, including required accuracy, surface "foot-print" size, frequency of measurement, and desired geographic coverage. Studies ranging from global oceanographic to thermal microstructure investigations have established the requirements for both aircraft and spacecraft derived measurements. In the preceding paragraphs, the specific requirements in each application area have been defined, and quantitative values assigned, based upon the consensus among the representative users contacted. The requirements in the various application areas are summarized in Table 3.8.

The most frequently requested values are indicated by the solid bars on the chart. In certain instances, certain users have expressed needs which vary somewhat from the general requirements, due to the peculiar nature of the application. These are indicated by the broken lines on the chart.

In general, the requirements as stated represent the best attainable data, using current technology. Because of sparse observations in some areas, however, the data are not always complete. This is particularly true in the case of measurements in the Southern Hemisphere. The previously cited Sea Surface Temperature charts of the NMFS exemplify this (Figures 3.1 and 3.2). The FNWC data, further, are confined for the most part to the Northern Hemisphere.

The following statements may be made regarding temperature measurement accuracy:

- (1) For ocean-wide, global, or regional applications, a temperature accuracy of 1°C is adequate for most applications.
- (2) For mapping and monitoring of phenomena of limited temporal or spatial extent, an accuracy of 0.2 to 0.5°C may be required.
- (3) For special purpose applications involving small anomalous thermal structures or restricted areas, an accuracy of 0.1 to 0.5° may be required. For these, aircraft borne systems may be satisfactory.

Surface resolution requirements may be summarized as follows:

- (1) For ocean-wide applications, a surface resolution element of approximately 400 km will provide large amounts of data not available by other techniques.

- (2) Some special applications involving ocean-wide survey require resolution of 100-200 km.
- (3) Research, mapping, etc. involving regional areas 900-1800 km resolution of 50-100 km is required.
- (4) Special applications involving coastal areas of studies of thermal microstructures require resolutions of 10 to 50 km. For the most part, these can best be served by aircraft borne systems.

The frequencies of observation as required for the various applications range from 1 per day to 1 per month. Daily observations are probably impossible with a single satellite, assuming a near-polar orbit; weekly observations would be difficult.

The temperature extremes as postulated for a sea surface temperature measuring system are -10°C to $+30^{\circ}\text{C}$. Most of the measurement requirements fall within the range of 0° to $+30^{\circ}\text{C}$, hence these should be considered the minimum required extremes. However, several important applications involve polar area mapping for temperature, hence the overall range should be considered as highly desirable.

From the assessment presented here, it is felt that the S-Band radiometer system would have wide usefulness by aiming for surveillance of the world ocean at a frequency of one or two times per week, with an absolute accuracy of surface temperature measurement $<\pm 1^{\circ}\text{K}$, averaged over a 100 km diameter area.

Table 3.8 User Needs and Requirements Summary

Representative User Requirements Application	Temperature °C				Surf. Resolution km						Frequency					Temp. Range °C					
	0.1-0.2	0.2-0.5	0.5-1.0	~ 1.0	1-2	10-20	20-50	50-100	~ 100	100-200	200-400	1 Day	4 Days	1 Wk	2 Wks	1 Mo.	-10 to 0	0 - 10	10-20	20-30	
Oceanographic Research Thermal Mapping - Ocean-wide, Global Thermal Structures, Anomalies Thermal Mapping - Regional Coastal Thermal Microstructures Studies Arctic Studies																					
Oceanographic Mapping and Charting Thermal Mapping - Ocean-wide, Global - Coastal Areas - Tropics Thermal Mapping - Currents - Upwellings																					
Fisheries - Applications Synoptic SST Mapping - Monthly - Bi-weekly - Daily																					
Current Monitoring Upwelling Monitoring Pollution Applications Thermal Pollution - Coastal Industrial Pollution - Coastal Oil Spills - Open Ocean																					

The quantities, ϵ' and ϵ'' are the real and imaginary parts of the complex dielectric constant ϵ , and $\mu = \cos \theta$, θ being the angle of incidence of observations. The parameters p and q are

$$p = \frac{1}{\sqrt{2}} \left\{ \left[(\epsilon' + \mu^2 - 1)^2 + \epsilon''^2 \right]^{1/2} + (\epsilon' + \mu^2 - 1) \right\}^{1/2}; \quad (4.4)$$

$$q = \frac{1}{\sqrt{2}} \left\{ \left[(\epsilon' + \mu^2 - 1)^2 + \epsilon''^2 \right]^{1/2} - (\epsilon' + \mu^2 - 1) \right\}^{1/2}.$$

Once the quantities ϵ' and ϵ'' are determined in terms of temperature and sea water composition, then the measurement of T_B by the radiometer uniquely determines the molecular temperature of the sea surface T_s .

4.2 THEORETICAL CONSIDERATIONS

4.2.1 Dielectric Theory of Polar Liquids and Their Frequency Dependence

The dielectric properties of pure water and NaCl solutions, to a very good approximation, may be described by the Debye theory of polar liquids in terms of a single relaxation time. The real and imaginary parts of the dielectric constant are accordingly given by,

$$\epsilon' = \frac{\epsilon_s - \epsilon_\infty}{1 + x^2} + \epsilon_\infty$$

$$\epsilon'' = \frac{(\epsilon_s - \epsilon_\infty)x}{1 + x^2} + \frac{4\pi\sigma_1}{\omega} \quad (4.5)$$

where ϵ_s is the static dielectric constant, ϵ_∞ is the dielectric constant due to the sum of electronic and atomic polarizations, ω is the angular frequency, σ_1 is the DC ionic conductivity, and $x = \omega\tau$ where τ is the relaxation time characteristic of a particular temperature and composition. ϵ_∞ is a constant whose value has been determined by Saxton and Lane (1952) to be 4.9 and σ_1 , ϵ_s and τ are, in general, functions of temperature and salinity.

The values for ϵ' and ϵ'' at two different frequencies are related to each other by,

$$\epsilon'_{\omega_2} = \epsilon_{\infty} + \left(\frac{\epsilon_s - \epsilon_{\infty}}{1 + x_1^2} \right) \left(\frac{1 + x_1^2}{1 + x_2^2} \right) \quad (4.6)$$

$$\epsilon''_{\omega_2} = \frac{4\pi\sigma_i}{\omega_1} \left(\frac{\omega_1}{\omega_2} \right) + \frac{(\epsilon_s - \epsilon_{\infty}) (x_1)}{(1 + x_1^2)} \left(\frac{\omega_2}{\omega_1} \right) \left(\frac{1 + x_1^2}{1 + x_2^2} \right)$$

where $x_1 = \omega_1\tau$ and $x_2 = \omega_2\tau$.

Typical values for τ in the temperature range from 0°C to 40°C and for salinities up to 1.0N range from 5×10^{-12} to 1.8×10^{-11} sec, corresponding to a range for x in the S-band frequency region from 0.1 to 0.3. Consequently, the factor $1 + x^2$ is close to unity (1.01 to 1.09) and $x^2 \ll 1$. As the conductivity σ is well known for different salinities and ϵ_{∞} is small compared to ϵ_s (approximately 5 versus 80) and reasonably well known, it can be seen that when ϵ' and ϵ'' are measured accurately at one frequency, their values at another frequency can be deduced accurately via the above expression even though the various τ are not well known. When the two frequencies are within 20% of each other, the extrapolation can be done to within a tenth of a percent accuracy for values of τ which are known only to a few percent. One can therefore make a precise measurement at a single frequency and then use the values of τ obtained by Saxton and Lane (1952) to generate accurate values for ϵ' and ϵ'' for a $\pm 20\%$ frequency range about the measured frequency.

The present experiment was performed at a frequency of 2.653 GHz and the results can be used with the above procedure to extrapolate values of ϵ' and ϵ'' over the frequency region from 2.0 to 3.0 GHz with negligible error.

4.2.2 Relationships Between Emissivity and Dielectric Constant

The emissivity for normal incidence is given by Equations (4.2), and (4.4) with $\mu = 1$, i. e. ,

$$e = 1 - \left| \frac{1 - \sqrt{\epsilon}}{1 + \sqrt{\epsilon}} \right|^2 \quad (4.7)$$

It is now possible to evaluate the uncertainty introduced in the measured surface temperature due to changes in ϵ . Differentiating Equation (4.7),

$$\frac{de}{e} = 2 \operatorname{Re} \left[\frac{d\epsilon}{\sqrt{\epsilon} (1-\epsilon)} \right] \quad (4.8)$$

where ϵ is complex, and $\epsilon = \epsilon' + i\epsilon''$. Expressing $\epsilon - 1$ as $a + ib$ and $\sqrt{\epsilon}$ as $c + id$, then

$$\frac{de}{e} = \frac{2}{(cb+ad)^2 + (ac-bd)^2} \left[(ac-bd) d\epsilon' + (cb+ad) d\epsilon'' \right]$$

or (4.9)

$$\frac{de}{e} = A d\epsilon' + B d\epsilon''$$

The uncertainty resulting in the molecular temperature T_S is then given by,

$$dT_S = \left[A d\epsilon' + B d\epsilon'' \right] T_S \quad (4.10)$$

Taking a typical ϵ' of 70 and ϵ'' of 40, roughly the values for sea water at 10°C , and evaluating the constants A and B, one obtains,

$$\frac{dT_S}{T_S} \approx 2 \times 10^{-3} (d\epsilon' + d\epsilon'') \quad (4.11)$$

For $T_S = 283^\circ\text{K}$, then

$$\Delta T_S \approx 0.6 (\Delta\epsilon' + \Delta\epsilon'')^\circ\text{K} \quad (4.12)$$

It is immediately apparent that for ΔT_S to be less than 0.5°K , $\Delta\epsilon' + \Delta\epsilon''$ must be less than 0.8. For $\Delta T_S < 0.1^\circ\text{K}$, ϵ' (which is ~ 70) and ϵ'' (which is ~ 40) must be measured to an accuracy of 0.15%.

A more detailed application of the above analysis of ΔT_S in terms of expected daily, seasonal and annual fluctuations in salinity of sea surface at a particular locality is given in Section 4.2.

4.2.3 Influence of Salinity and Frequency

The variation in salinity at the ocean surface is potentially a significant factor in the uncertainty of interpretation of molecular temperature as a brightness sea temperature. The significance of this effect can be estimated readily from knowledge of salinity variation at sea and the relationship of

sea water composition to its electrical properties. Using the equation for the reflectivity in terms of the complex dielectric constant of sea water, a set of uncertainty curves can be derived. Such a set of curves calculated from Equation 4.12, is shown in Figure 4.1. Here the uncertainty in the measured molecular temperature due to variation in salinity is shown for different water temperatures, and the calculations were made using the values of ϵ' and ϵ'' at 2.65 GHz. The results can be scaled in frequency since, as can be seen from Equation (4.6), the effect on the emissivity in the S-band region due to a change in salinity is given mainly by the conductivity term in ϵ'' . Since this term varies inversely as the frequency, the change ΔT_S due to changes in salinity at some other frequency, f , is related to ΔT_S given in Figure 4.1 by,

$$\Delta T_S(f) \approx \Delta T_S(2.65 \text{ GHz}) \times \frac{2.65 \text{ GHz}}{f} \quad (4.13)$$

By doubling the frequency, the uncertainty is reduced by roughly a factor of 2, and therefore, on the basis of considering salinity variation alone, the frequency of operation of the radiometer in the S-band region should be chosen as high as possible. However, the study of other competing effects such as atmospheric attenuation and radar interference

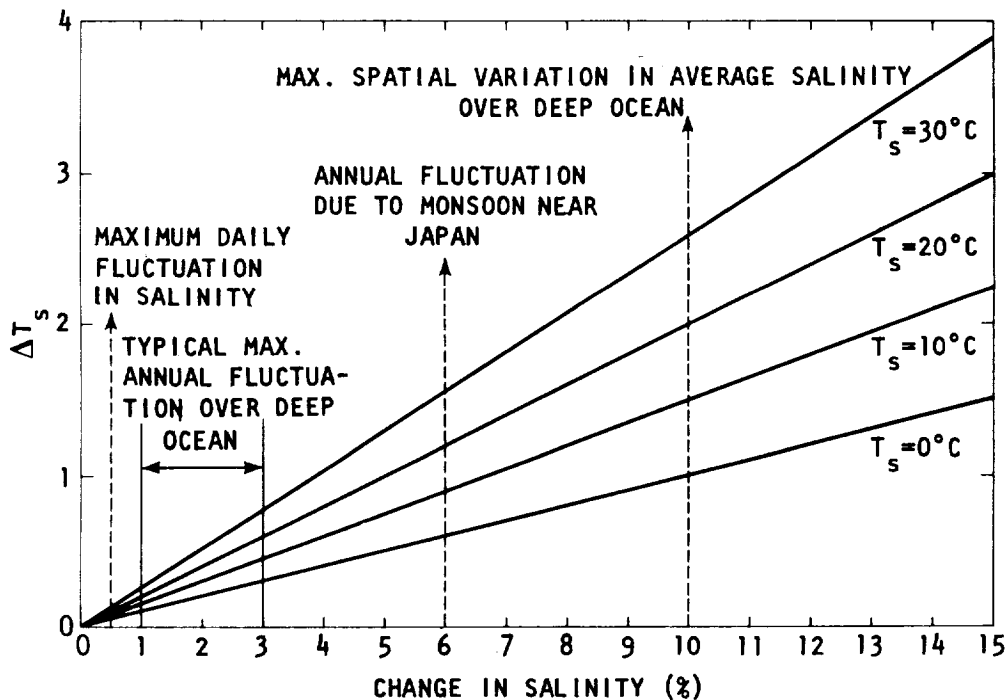


Figure 4.1. Uncertainty in the Molecular Temperature T_S Measured at 2.65 GHz by the Radiometer Due to Changes in Salinity for the World Oceans

indicate that the best operating frequency range be approximately from 2.55-2.7 GHz. The advantages gained by operating at a higher frequency due to salinity variation are largely offset by these other effects.

4.3 SALINITY VARIATION IN THE OCEANS

A study of the geographical and temporal variation in salinity over the world's oceans was undertaken in order to show that, at least to first order, these variations can be accounted for and the resulting uncertainty in the measured sea surface temperature can be kept small enough to render going to higher frequencies unnecessary.

4.3.1 Geographical Variations.

The variations in salinity of the world ocean may be classified in terms of spatial and temporal changes. The average distribution of surface salinity has been established and is reported in available oceanography texts (see, for example, Defant, 1961). The average distribution of surface salinity is shown in Figure 4.2 for the Pacific Ocean, with the average temperature distribution for comparison. An idea of the uncertainty in average geographical variations can be obtained by comparing Defant's (1961) worldwide distribution in Figure 4.3 with the summer Pacific Ocean in Figure 4.2. From this comparison can be seen that zonal and meridional variations are similar in both oceans.

For a polar orbiting satellite, a microwave radiometer viewing the sea surface would "see" a change in salinity of about 10‰ from pole to equator over the mid-oceans, corresponding to an apparent molecular temperature change of 3°K. This is to be compared to a sea temperature change of 35°K from pole to equator. Thus, the geographical variation in sea temperature is expected to far exceed that of the effect of salinity in a meridional trajectory. Without correction for salinity, however, one would find a maximum uncertainty in measured sea temperature of 1-3°K based on the curves in Figure 4.2. The effect of the geographical changes on average salinity can be corrected to at least first order. And one would expect that such a correction would reduce the uncertainty in molecular temperature estimates to be comparable with error associated with temporal variations on a scale of days to a week.

4.3.2 Temporal Variations

The temporal variations of surface salinity are much less well known than the geographical differences. The time scales for differences generally have been classed in terms of diurnal changes, seasonal changes and year to year changes. The diurnal variations in salinity that have been measured in the Atlantic and Pacific Oceans appear to be about 0.5‰ or less in the

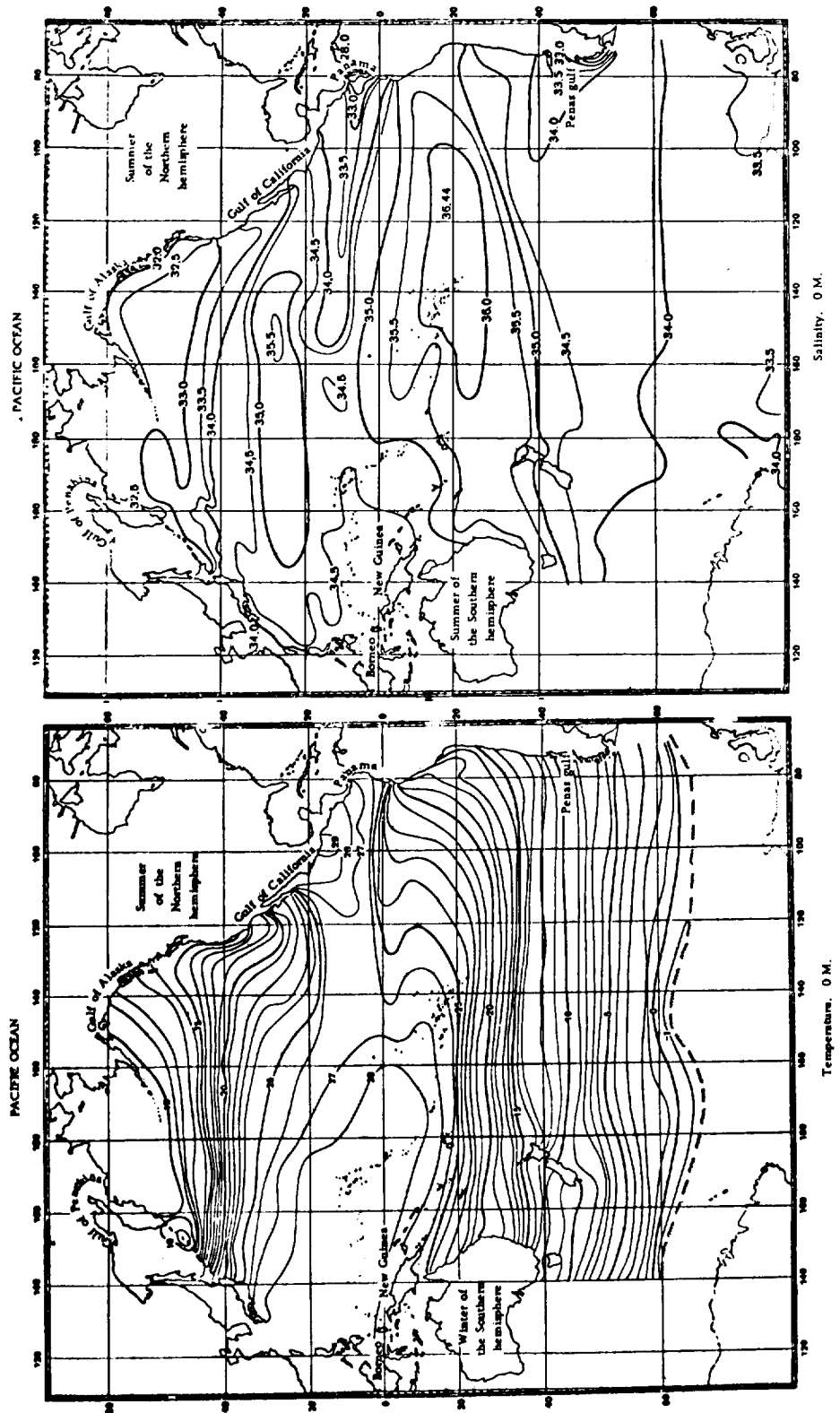


Figure 4.2. Average Distribution of Sea Surface Salinity and Temperature for the Pacific Ocean (From Muromtsev, 1963)

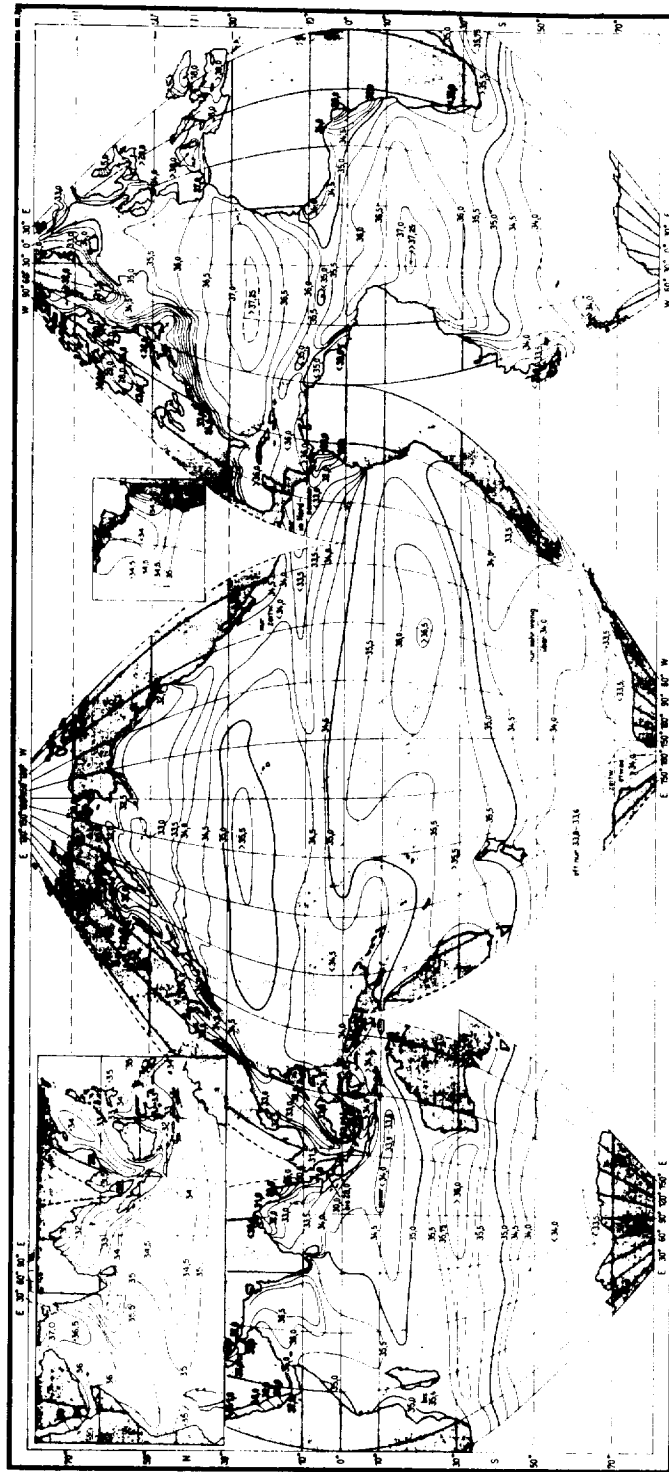


Figure 4.3 Average Sea-Surface Salinity (‰) of the World Oceans
(from Defant, 1961)

mid-ocean (Defant, 1961; Neuman and Pierson, 1966), and the main perturbations in surface salinity are associated with evaporation in combination with precipitation. In coastal waters, disturbances in salinity have been identified with tidal flow of fresh and salt water out of partially closed areas with strong river effluents. An example of a diurnal salinity pattern is shown with a corresponding diurnal temperature change for the northwest Pacific Ocean in Figure 4.4. Muromtsev (1963) has suggested that this kind of variation is more or less typical of the surface of the deep ocean in the absence of precipitation. Here the temperature is seen to go down at night with conductive cooling of the surface and rise during the day by solar warming. The salinity change reveals a maximum at night, with oscillations about 180° out of phase with the temperature changes. In this case, the diurnal temperature variation is about three times as great as the apparent temperature change due to salinity change that would be inferred by remote sensing. Since the salinity and temperature variations are in opposition they tend to cancel one another.

The data shown in Figure 4.4 do not appear to be typical in salinity variation. For example, other fractional diurnal changes in salinity for the mid-Atlantic reported by Defant (1961) are less, but the salinity peaks late in the afternoon, as a result of surface evaporation. Since little is currently known about the broad patterns of daily salinity variation, one must anticipate a resulting uncertainty in molecular temperature reading of $0.1-0.2^\circ\text{K}$. However, it is expected that this could be corrected to first order considering the daily-geographical heat exchange and precipitation process influencing the surface properties.

Monthly Variations. The seasonal changes in salinity at the ocean vary widely geographically. An extreme example for the California Coastal region and the mid-Atlantic are shown in Figure 4.5. The known seasonal fractional changes in salinity amount to typically a maximum of 1-3%, considerably larger than the diurnal variations. More normally, at least in the Atlantic, the range of salinity variation in the middle latitudes in the open ocean is less than 0.5%, usually less than 0.25% (Defant, 1961). However, there exists a zone with more than 0.5% and a core of more than 1%-1.5%, across the Atlantic from South America to Africa between 5° and 15°N , and includes the area of the equatorial countercurrent. There is another zone with changes greater than 0.5% and several cores $\geq 1\%$, in the Gulf Stream region extending to the southeast of the Newfoundland banks. Other strong maxima and minima are observed at river mouths under conditions of spring runoff, etc. These seasonal variations are evidently closely linked with climatological changes and changes in currents such as increased evaporation during the summer months so that they are correctable to an uncertainty in molecular temperature equivalent seasonally to less than 0.5°K .

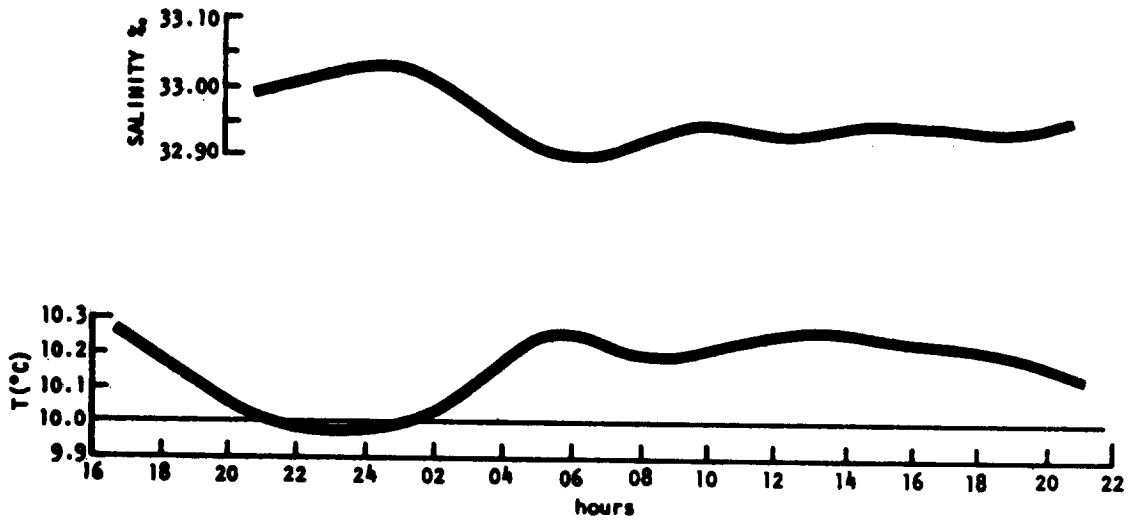


Figure 4.4. Daily Fluctuation of Sea Surface Salinity and Temperature in Northwest Pacific Ocean (From Muromtsev, 1963)

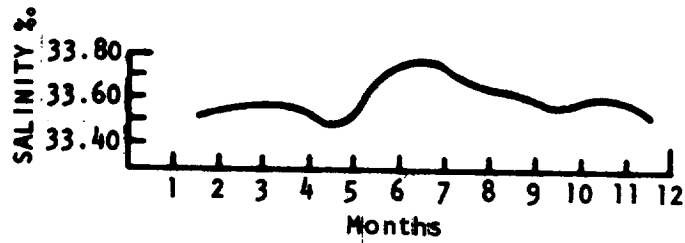


Figure 4.5. Annual Fluctuation in Sea Surface Salinity for the California Coastal Region (From Muromtsev, 1963)

There are cases of more extreme variations that are associated with regular climatological fluctuations. For example, the annual fractional change in salinity resulting from the monsoon near Japan is about 6%, corresponding in Figure 4.1 to an uncertainty in measured molecular temperature of as much as 1.5°K. Again such cases can be corrected for salinity to $\Delta T_S \leq 0.5^\circ\text{K}$, however, by taking into account these severe climatological disturbances.

Year to Year Variations. Relatively little information is available on the year to year changes in salinity. An example of recorded changes for the Pacific Ocean are indicated in Table 4.1. If these slow variations are typical of the mid-ocean, their fractional changes is quite small, of the order of 2-3%. These will produce a long term uncertainty in molecular surface temperature of $\pm 0.5^\circ\text{K}$ over several years of satellite operation.

Table 4.1 Variations From Year to Year in Surface Salinity at 24°20'N, 153°58'W Taken in Middle August (From Muromtsev, 1963)

Year	Salinity	Year	Salinity
1933	35.03	1938	-
1934	34.40	1939	34.96
1935	35.14	1940	34.90
1936	35.10	1941	34.93
1937	34.22		

4.3.3 Summary and Conclusions.

Geographical and temporal salinity variation in the world ocean represent a small but significant, uncertainty in interpreting S-Band radiometer observations for sea surface temperature. However, the largest changes in salinity are seasonal ones, and are correctable to first order with known geographical variation to yield an uncertainty in molecular temperature of $\leq \pm 0.5^\circ\text{K}$, as inferred from microwave radiometry.

4.4 LABORATORY MEASUREMENTS OF THE DIELECTRIC PROPERTIES OF SEA WATER, NaCl SOLUTIONS AND DISTILLED WATER

The dielectric properties of distilled water have been measured in the S-band frequency region by many workers over the temperature range from 0°C to 40°C. These measurements are summarized in Figures 4.6 and 4.7

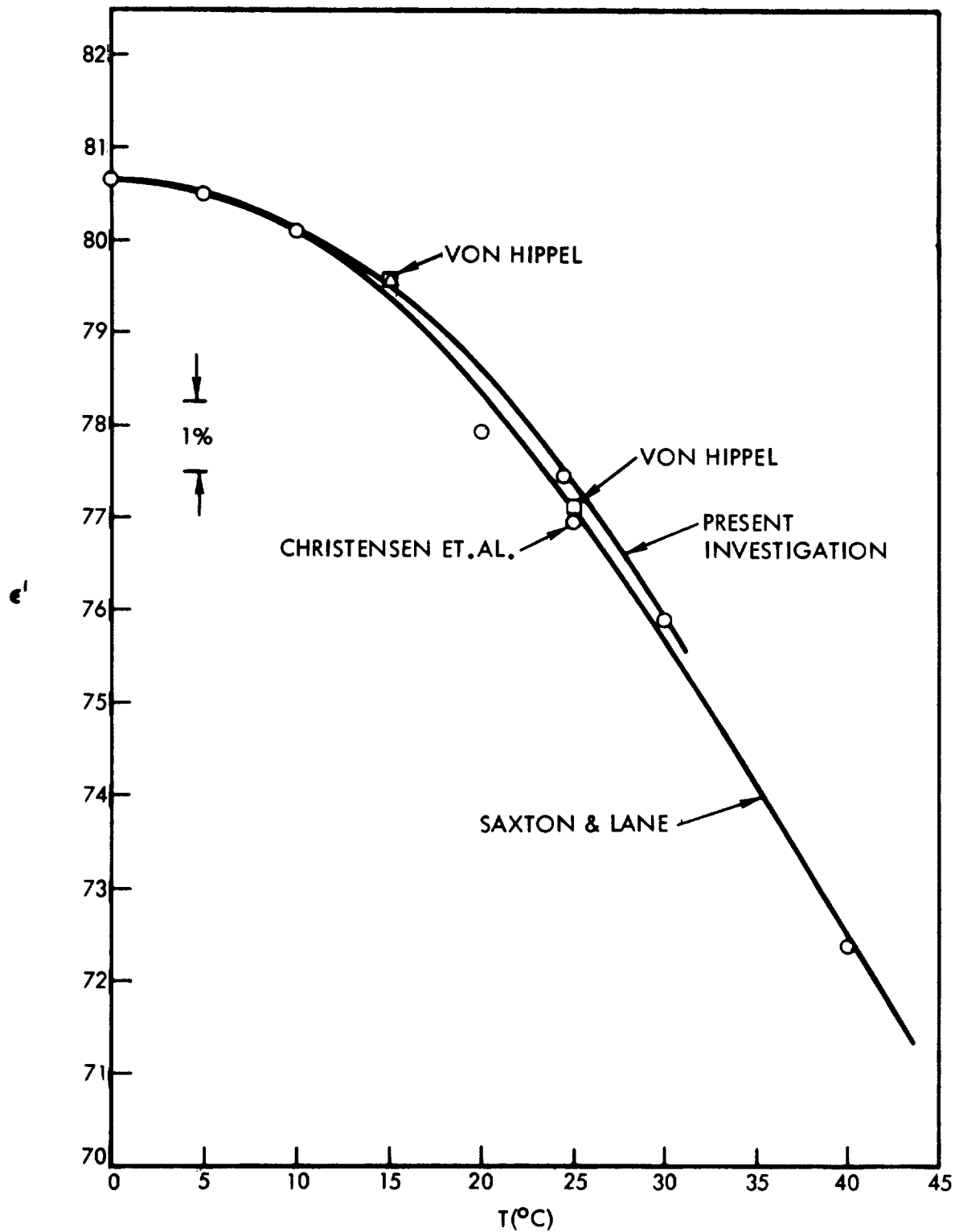


Figure 4.6. ϵ' for Distilled Water as a Function of Temperature at 2.653 GHz

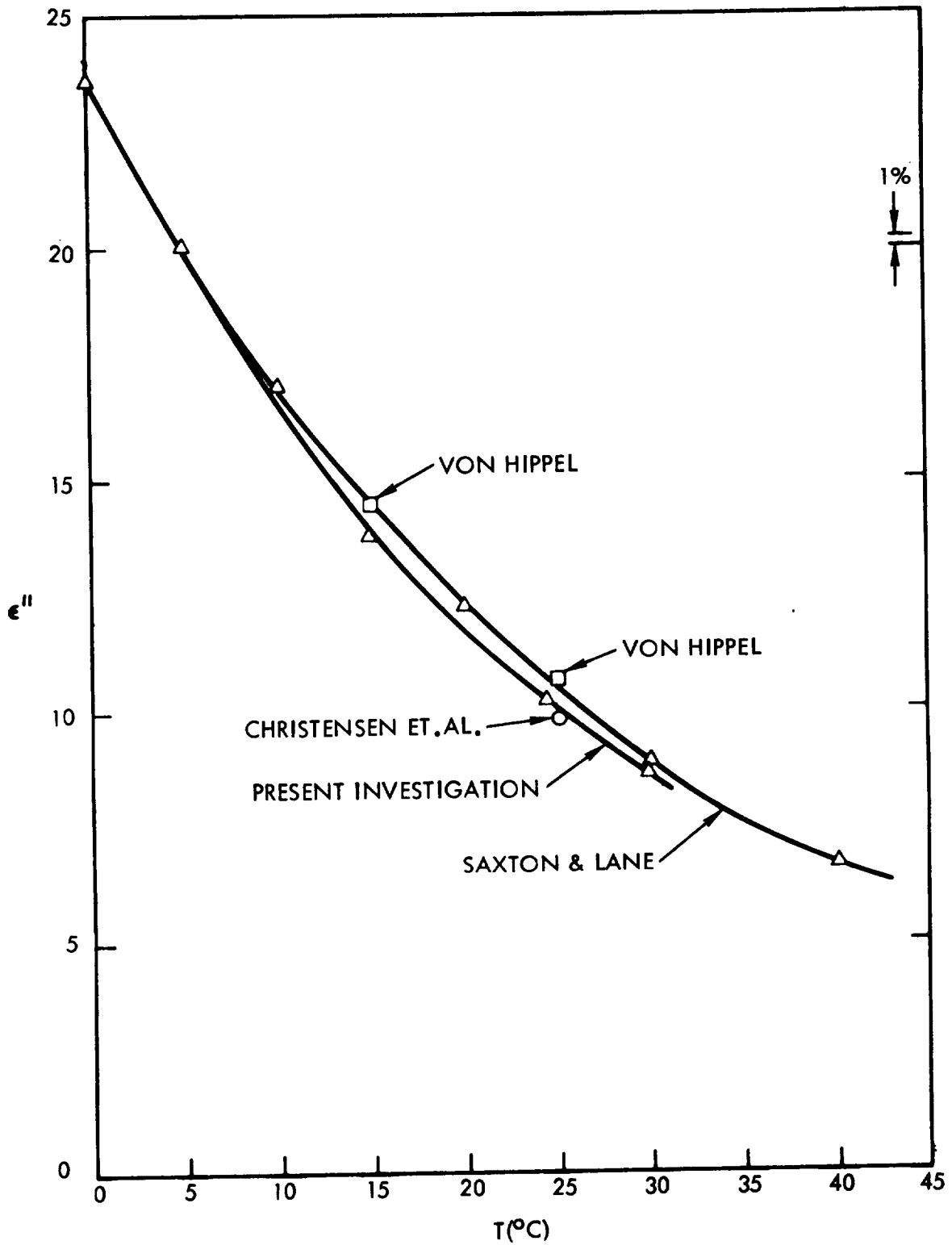


Figure 4.7. ϵ'' for Distilled Water as a Function of Temperature at 2.653 GHz

where it may be seen that agreement between the various measurements is well within 0.5%. Various measurements have also been performed for NaCl solutions for molar concentrations up to several normal over a more limited temperature range. As seen by Figures 4.8 and 4.9, which summarize the available data at 0.5N (approximately that of sea water) and at 24.5°C, there is considerable disagreement among the various results. We note that not all the measurements shown in Figures 4.6 through 4.9 were performed at the frequency of 2.653 GHz which is the frequency at which the present investigation was conducted. However, as was shown, the Debye theory for polar liquid can be used to predict values for ϵ' and ϵ'' for approximately a 20% change in frequency with essentially negligible error (~0.1%) and the data shown in the figures were accordingly deduced from the data in the literature by the use of the Debye expression.

There are no published measurements of ϵ' and ϵ'' for actual sea water samples at any temperature, nor has any extensive theoretical work been done on the dielectric properties of a multi-electrolyte solution such as sea water. Until now it has generally been assumed that the dielectric properties of sea water can be approximated by that for a 3.35 wt. percent NaCl solution; however, this assumption has little justification, as will be shown. It is well known that the salinity of the world ocean changes by as much as 10% in spatial variation over the open sea and therefore for any precision application such as that projected in this study, the assumption of a uniform average value for the salinity is clearly inadequate. In addition, it has never been demonstrated that the dielectric properties of a complex solution such as sea water can indeed be simply related to its chloride concentration since the presence of other salts and dissolved organics could conceivably make a significant contribution. Indeed, the validity of data from the satellite radiometer system under consideration as an absolute temperature measuring device would be in serious doubt if the dielectric properties and emissivity of the world's ocean surface cannot be related to a physical parameter which is well measured in terms of spatial and temporal variations such as the salinity (or chlorinity). It is impossible to determine, by measuring T_B with the radiometer, which part of the change in T_B is due to an actual change in the molecular temperature of the ocean's surface and which is due to changes in the emissivity unless the changes in the dielectric properties of the world ocean can be predicted beforehand both spatially and temporally.

The present investigation therefore has two basic goals. Firstly, to measure the dielectric properties of NaCl solutions and sea water samples to a sufficient relative and absolute accuracy such that the ocean surface temperature can be extracted from the radiometer measurements to better than $\pm 0.5^\circ\text{K}$, and secondly to prove that the variation in the dielectric properties of the world ocean can be related uniquely to the sodium chloride concentration alone and therefore can be predicted from existing sea truth data.

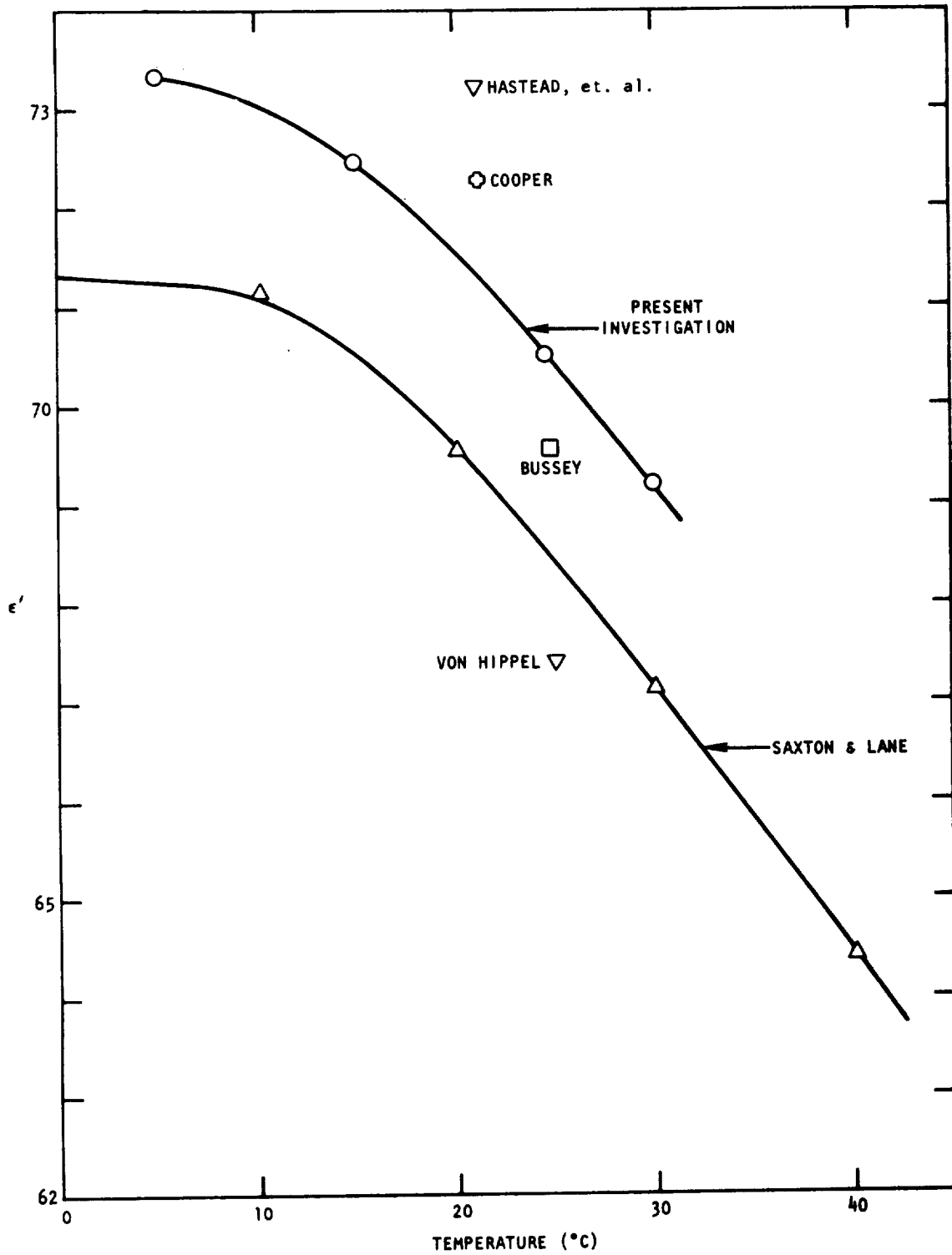


Figure 4.8 ϵ' for 0.5N NaCl Solution as a Function of Temperature at 2.653 GHz

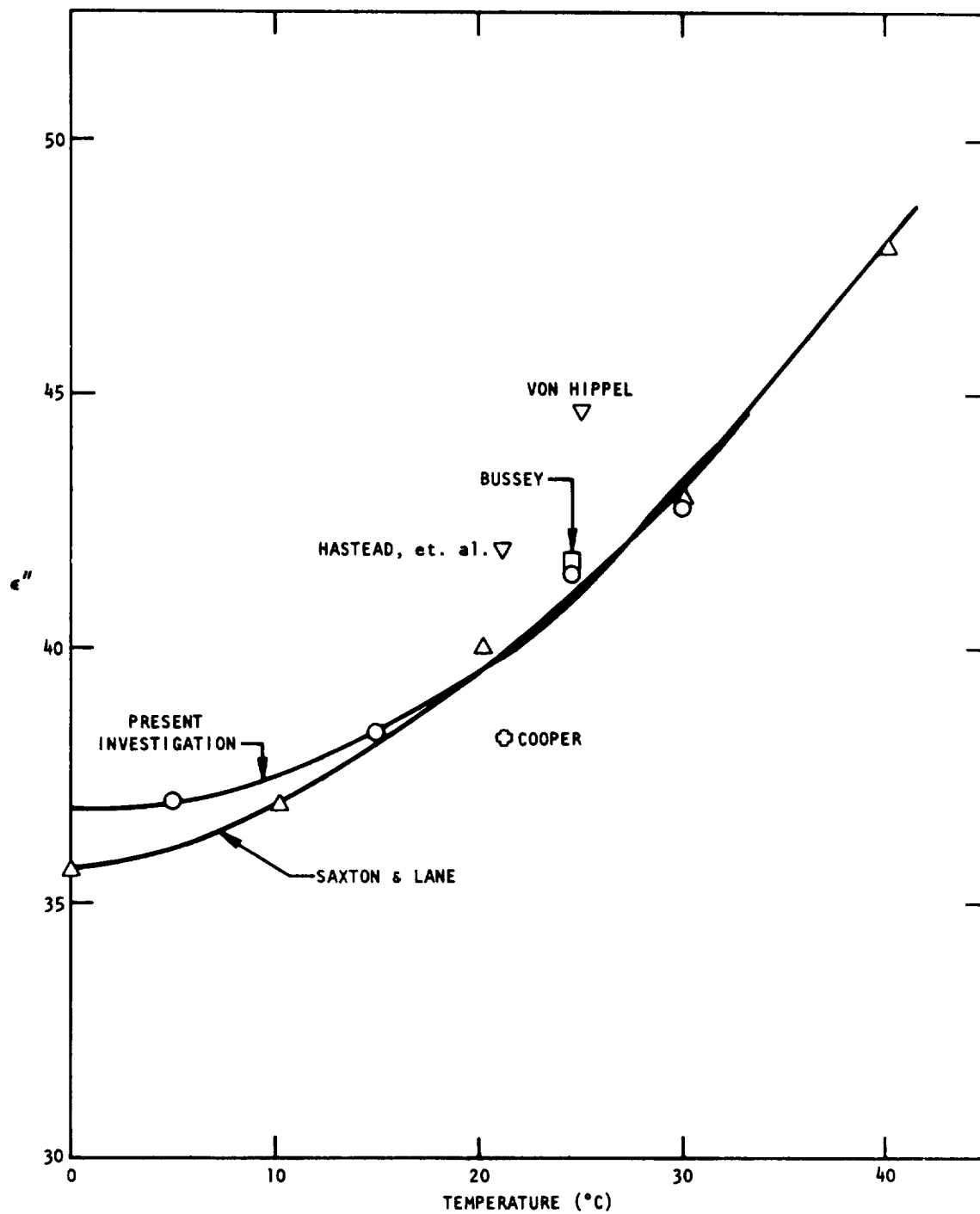


Figure 4.9 ϵ'' for 0.5N NaCl Solution as a Function of Temperature at 2.653 GHz

4.4.1 Experimental Method

After an investigation of the various alternative methods for measuring the dielectric property of solutions, it was decided that the cavity perturbation technique currently used by the National Bureau of Standards was most suitable for the present measurements. A sample of known volume is introduced into a high Q resonant cavity and the dielectric constants ϵ' and ϵ'' are measured by determining respectively the shift in the cavity resonance and the change in the quality factor Q of the cavity. If the perturbation due to the sample is kept sufficiently small, then the effects of ϵ' and ϵ'' on the cavity resonance are essentially decoupled and each can be determined independently. We shall now summarize the pertinent properties of a reflection-type resonant cavity and give the relevant relationships used in the subsequent work.

Choice of Operating Mode

After careful consideration, it was decided that the TM_{010} mode for a right circular cylinder resonant cavity is ideally suited for measurements of the type under consideration. The electric field in this mode is axially symmetric and is a maximum at the center, along the axis of the cavity. Cylindrical symmetry can therefore be maintained throughout by introducing the sample in a cylindrical tube along the axis at the center of the cavity. The electric fields at the walls of the cavity are therefore expected to change very little due to the perturbation introduced by the sample tube and higher-ordered effects can be kept to a minimum. The resonant frequency for this mode depends only on the diameters of the cavity and sample tube and is independent of their lengths so long as the sample tube extends beyond the end walls. The only pertinent parameters that then enter the calculations are the ratios of the various diameters. The behavior of this resonant mode has been investigated extensively by other workers in the field and used in precise measurements of dielectric properties of materials so that small corrections in the measurements by effects such as those due to the extension of the sample tubes beyond the end walls of the cavity are well determined. In addition, although the quality factor Q that can be obtained in principle for the TM_{010} mode is less than that obtainable at the same frequency for other modes such as the TE_{011} mode, it has the overwhelming advantage that it is not degenerate in frequency with any other excitable resonances and that for the S-band frequency region, the dimensions for the cavity can be chosen such that other mode resonances will occur only at frequencies very far away from the resonance frequency of the TM_{010} mode. For the final design in the present case, for instance, the next nearest mode in frequency (TE_{111}) occurs at a frequency whose separation from the TM_{010} mode is several orders of magnitude larger than the width of the resonance. Therefore, no mode mixing exists and the actual field configuration within the cavity is expected to be very close to that obtained from theory for the boundary

conditions given. It is expected, then, that the theoretical calculations for the properties of the TM_{010} mode are applicable to a high precision, a conclusion subsequently verified by test measurements.

Properties of Microwave Resonant Cavities. The electric and magnetic fields inside a cavity filled with a homogeneous, isotropic dielectric are given by the solution of Maxwell's source-free equations with the appropriate boundary conditions. The general approach of Borgnis and Papas (1958) will be followed here.

The electric field solutions for a cavity of infinite conductivity consist of a set of complex eigenvectors, \vec{E}_p which satisfies the following condition:

$$\begin{aligned} (\nabla^2 + K_p^2) \vec{E}_p &= 0 \\ \nabla \cdot \vec{E}_p &= 0 \end{aligned} \quad (4.14)$$

throughout the interior region of the cavity, and

$$\vec{n} \times \vec{E}_p = 0 \quad (4.15)$$

on the boundary walls.

A finite but high conductivity for the cavity surfaces represents a small perturbation on the modes as calculated on the assumption that the wall losses are zero. The only change that occurs in the spatial dependence of the electric and magnetic fields is that the tangential component of the electric field is no longer zero at the walls. The fields penetrate into the enclosure walls by the skin depth. The conductivity of copper or silver is about 6×10^7 mho/meter which at a frequency of 3 Gc/sec gives a skin depth of 10^{-4} cm. This dimension is small with respect to the free-space wavelength, and therefore the dimensions of any resonant cavity in the microwave region. Consequently the electric and magnetic fields are only very slightly perturbed from the values for lossless cavities.

When the cavity is slightly lossy, the eigenfrequencies become complex and can be represented in the form $\omega_p (1 - i\delta)$, where $\delta = 1/2 Q_p$ by definition, and Q_p is the quality factor or Q of the p^{th} normal mode. For typical skin depths and skin conductivities in the microwave region, Q_p is in the range 10^4 to 10^5 and therefore δ is in the range 10^{-4} to 10^{-5} . The electric and magnetic fields are now slowly attenuated in time and are,

$$\begin{aligned} \vec{E}_p(r, t) &= \vec{E}_p(r) e^{-\omega_p t / 2Q_p} \\ \vec{H}_p(r, t) &= \vec{H}_p(r) e^{-i\omega_p t / 2Q_p} \end{aligned} \quad (4.16)$$

When the quality factor is very large compared to unity, as is nearly always the case, the average energy of the p^{th} mode as a function of time is given by,

$$\bar{W}_p(t) = \bar{W}_p e^{-\omega_p t/Q_p} \quad (4.17)$$

Therefore,

$$Q_p = \omega_p \bar{W}_p \bigg/ \frac{d}{dt} \bar{W}_p(t) \quad (4.18)$$

or

$$Q_p = \omega_p \left(\frac{\text{Total time average of energy stored}}{\text{Time average of power dissipated}} \right)$$

This is the usual definition for the Q of a cavity.

If the individual ω_p 's are sufficiently far apart, such that the modes are non-interacting, then individual modes may be excited separately. By measuring the resonant response of the cavity, the quality factor Q_p and hence the wall losses inside the cavity can be determined for the p^{th} mode, if it is the only mode excited. Consequently, by measuring the Q for a given mode before and after the introduction of a lossy material into the cavity, the microwave absorption properties of the material may be obtained.

In practice, microwave power is coupled into a cavity via an iris hole or a loop. For our case where microwave power is propagated by means of waveguides, the iris hole method is more convenient. The cavity now is no longer totally enclosed as energy is also being returned to the system by the cavity through the coupling hole. This additional loss in energy is taken into account by defining the total Q of the cavity for a given mode as,

$$\frac{1}{Q_T} = \frac{1}{Q_o} + \frac{1}{Q_c} \quad (4.19)$$

where Q_c is referred to as the coupling Q and is proportional to the energy loss through the coupling hole.

The fields inside the cavity are in general difficult to measure, and in practice, the usual procedure is to measure the power transmitted or reflected by the cavity as a function of frequency for a given mode. Because of the resonant behavior of the fields inside the cavity, the relationship between the

cavity Q , the reflected power, and the frequency for a cavity can be derived by means of equivalent circuit elements. Detailed treatment of this problem has been presented by Montgomery (1947) and only the results will be given here.

It can be shown in general that for a reflection cavity, i. e., a cavity for which power is introduced and extracted by the same coupling hole, the relationship between Q_o , Q_c , the incident power P_o , the reflected power P_r , the frequency ν and the resonant frequency ν_o , is given by

$$P_r/P_o = \frac{1/4 \left(\frac{1}{Q_o} - \frac{1}{Q_c} \right)^2 + \left(\nu - \nu_o \right)^2 / \nu_o^2}{1/4 \left(\frac{1}{Q_o} + \frac{1}{Q_c} \right)^2 + \left(\nu - \nu_o \right)^2 / \nu_o^2} \quad (4.20)$$

At the resonant frequency, the ratio of the reflected power to incident power is defined as the reflection coefficient for the cavity

$$(P_r/P_o)_{\nu=\nu_o} = r = (Q_c - Q_o)^2 / (Q_c + Q_o)^2 \quad (4.21)$$

For $(P_r/P_o)_{\nu=\nu_o} = 0$, the cavity is considered to be 100% coupled and $Q_o = Q_c$.

Combining Equations (4.20) and (4.21) and eliminating Q_c , then

$$Q_o = \nu_o \left[(P_r/P_o) - r \right]^{1/2} / \left(\nu - \nu_o \right) (1+r)^{1/2} \quad (4.22)$$

Therefore, by measuring r and the frequency ν at some power level P_r/P_o , the quality factor Q_o can be determined.

Suppose now a lossy material is introduced into the cavity. Then the Q of the cavity changes and the new Q_T is related to the loss in the sample vis,

$$\frac{1}{Q_T} = \frac{1}{Q_L} + \frac{1}{Q_o} + \frac{1}{Q_c} \quad (4.23)$$

where $\frac{1}{Q_L}$ is determined by the dielectric loss ϵ'' of the material and the filling factor of the material in the cavity. Measurement of the Q of the cavity before and after the insertion of the sample then permits the determination of Q_L .

The solutions of Equation (4.14) and Equation (4.15) for the TM_{010} mode for the case of the empty right circular cylinder are,

$$E_z = J_0(K, r) ; E_r = E_\theta = 0 \quad (4.24)$$

$$H_\theta = \frac{i}{\mu\omega} \frac{\partial}{\partial r} J_0(K, r) ; H_r = H_z = 0$$

and the resonant frequency of the mode is given by,

$$\nu = (2.40483c) / (\pi D) \quad (4.25)$$

where c is the velocity of light in vacuum, D is the diameter of the cavity and μ_0 and ϵ_0 are assumed to be 1.

The theoretical quality factor Q_0 is given by,

$$Q_0 = (2.40483\lambda) / \pi (2 + D/L) \delta \quad (4.26)$$

where λ is the free-space wavelength, D/L is the ratio of the diameter of the cavity to its height, and δ is the skin depth at λ .

Expressions will now be given for the frequency shift and change in Q of the cavity due to the introduction of a sample tube of lossy dielectric material along the axis of the cavity. A simple straightforward perturbation calculation gives for the frequency shift,

$$\delta' \approx \left[\omega_0 / 2 J_1^2(x_0) \right] \left\{ \left[(\epsilon'_3 / \epsilon_0) - 1 \right] (r_1 / r_3)^2 + \left[(\epsilon'_2 / \epsilon_0) - 1 \right] (r_2^2 - r_1^2) / r_3^2 \right\} \quad (4.27)$$

where ϵ'_3 , ϵ'_2 and ϵ_0 are respectively the real part of the dielectric constant for the sample, the sample tube material, and air; r_1 , r_2 and r_3 are respectively the inner radius of the sample tube, the outer radius of the sample tube and the radius of the cavity; δ' is the frequency shift of the cavity from ω_0 ; and $J_1(x_0)$ is the value of the Bessel function $J_1(x)$ at the first zero of

$J_0(x)$. The first term is the frequency shift due to the sample material and the second term is the frequency shift due to the introduction of the empty sample tube, which is a constant.

If the frequency shift is measured from the resonant frequency of the cavity with the empty sample tube inserted ω'_0 , rather from that for an empty cavity, and taking $\epsilon_0 = 1$, then the shift δ is given by,

$$\delta \approx \left[\omega'_0 / 2 J_1^2(x_0) \right] (\epsilon'_3 - 1) (r_1/r_3)^2 \quad (4.28)$$

Similarly, for the case where the sample tube material has negligible dielectric loss, one obtains

$$1/2 Q_L = \left[1/2 J_1^2(x_0) \right] \left[\epsilon''_3 (r_1/r_3)^2 \right] \quad (4.29)$$

The ratio $\epsilon''/(\epsilon' - 1)$ then is given by,

$$\epsilon''_3 / (\epsilon'_3 - 1) = (1/2 Q_L) (\omega'_0 / \delta) \quad (4.30)$$

a quantity which is independent of sample size.

A more exact calculation was performed to the next higher order by computer for conditions typical of the present experiment, i. e., $\epsilon'_3 \approx 80$, $\epsilon''_3 \approx 40$, $r_3 = 4.31$ cm, $r_1 = 0.0122$ cm, $r_2 = 0.0254$ cm, and the results showed that Equations (4.28) and (4.29) are correct to about 0.1% accuracy, and are therefore more than adequate in the present application.

If the sample tube does not terminate at the end walls of the cavity but extends beyond, then an additional correction takes place for Equations (4.28) and (4.29) due to electric field perturbations at the end walls. It can, however, be shown that the error introduced in the measurements of ϵ' and ϵ'' due to this end wall effect is approximately (Estin and Bussey, 1960),

$$\delta (\epsilon'_3 - 1) / (\epsilon'_3 - 1) \approx \delta \epsilon''_3 / \epsilon''_3 \approx - (1/2 x_0) (a/h) \quad (4.31)$$

where a is the diameter of the sample, h is the height of the cavity and $x_0 = 2.405$, the first zero of the Bessel function $J_0(x)$.

For the present experiment, $h = 5.08$ cm and the maximum value for a used was 0.0254 cm. Therefore, $\frac{\delta(\epsilon' - 1)}{\epsilon' - 1}$ for all cases was kept below 0.1% . As it is much more convenient from the point of view of experimental procedure to let the sample tube protrude beyond the cavity walls, the experimental apparatus was accordingly so designed and Equation (4.31) was used to correct for the effect of end wall perturbations. Since the correction is almost negligible to begin with, no loss in accuracy in the measurements is expected due to this effect. The perturbation on $\delta\epsilon''/\epsilon''$ due to this effect is expected to be even smaller and hence is neglected in this work.

Cavity Design and Sample Tube Selection. An assembly drawing of the final cavity configuration is shown in Figure 4.10. The main body of the cavity was constructed of copper, and coupling was achieved via the coupling hole at one side of the cylinder. As present theory of coupling is not precise enough to predict the coupling hole size for a given coupling coefficient, r , the exact size was obtained by trial and error. The hole was slowly drilled out until a coupling of around 85% was obtained. When a typical sample was introduced in a 0.0152 cm diameter sample holder, this coupling value decreased to about 50% , which is roughly the value for maximum sensitivity in loss measurements. The sample tube is introduced into the cavity through the carefully aligned copper plugs. Sample tubes with O. D. ranging from 0.00762 cm to 0.0254 cm were used in the experiment and for each size tube, a pair of custom fitted plugs were employed to ensure proper axial alignment of the tube. The clearance between the O. D. of the tube and the I. D. of the plugs was kept to within 0.0025 cm. The main body of the cavity was fabricated from oxygen-free copper and the inside surfaces were honed to a fine finish. The I. D. of the cavity was measured with a precision caliper and found to be 8.646 cm \pm 0.005 cm. When the value of the measured frequency is substituted into Equation (4.25) the calculated value for D is 8.6481 cm, indicating excellent agreement. The entire cavity assembly was placed in a constant temperature enclosure which was controlled with a circulating bath. The constancy of the resonant frequency of the cavity over long period of time indicated that the temperature of the cavity was maintained to an accuracy of better than 0.01°C . No effect due to mechanical vibration was observed nor was there any noticeable degradation of the cavity Q with time.

The sample tubes used were made of quartz with an O. D. of approximately 0.051 cm and an I. D. ranging from 0.007 cm to 0.0254 cm. Quartz was chosen since it has negligible dielectric loss at microwave frequencies. The dimensions were uniform to about $\pm 5\%$. Because of the axial symmetry present in the cavity, it can be seen from Equation (4.28) and Equation (4.29) that uniformity of the sample tube size is not rigidly required except insofar

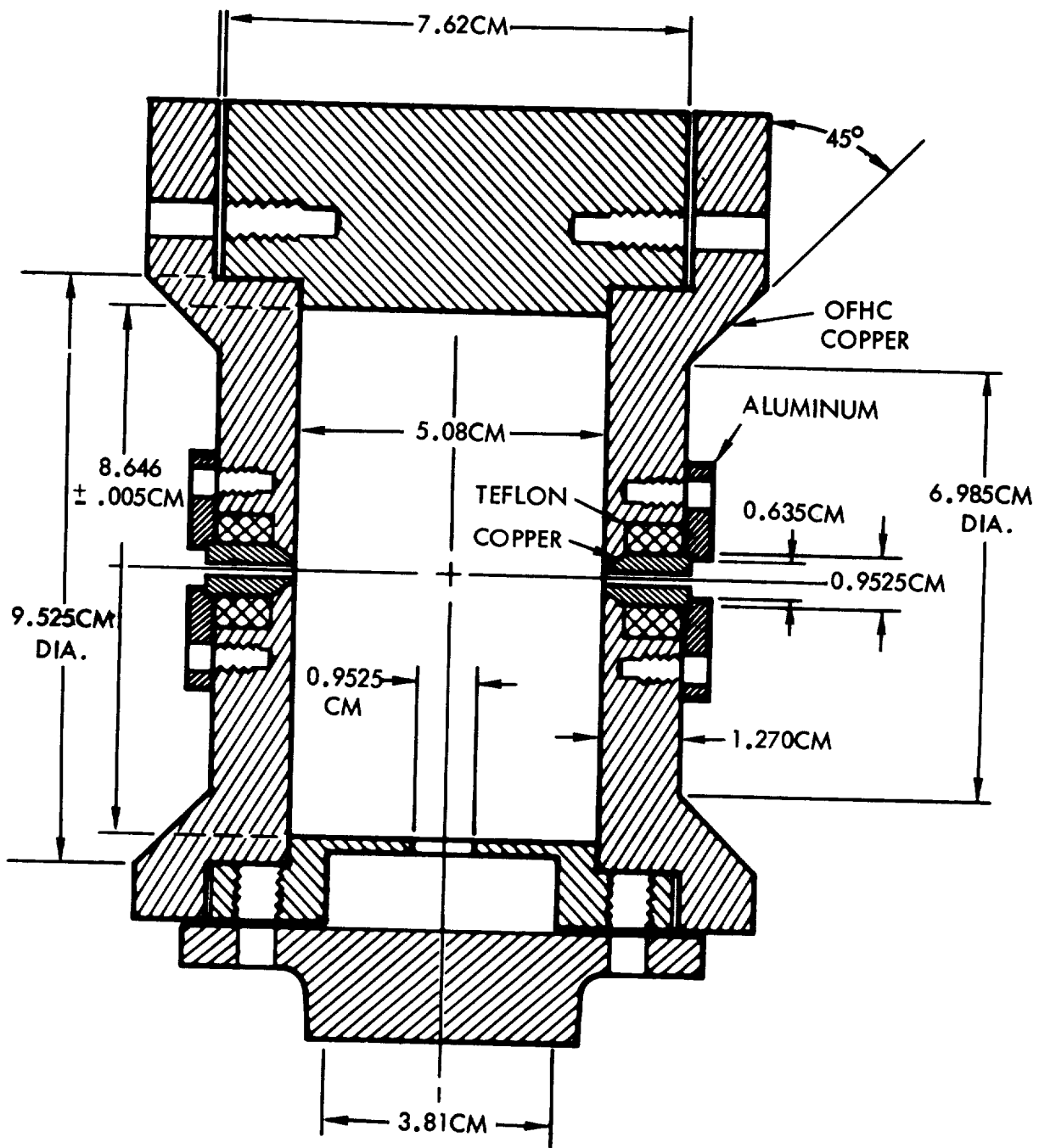


Figure 4.10. Cross-Sectional Diagram of 2.653 GHz Cavity

as it may introduce perturbations of the electric field at the walls of the cavity. Calculations were carried out which showed that the change in the electric field at the walls of the cavity is negligible when the sample is introduced into the cavity. On this basis, the perturbation effect due to a 5% change in sample diameter is expected to be even less significant. The only important parameter under consideration is, therefore, the volume ratio of the sample tube to that of the cavity or, more specifically, the ratio of the average diameter of the sample to that for the cavity. The procedure for the measurement of the average diameter of the sample tube is discussed in the section under results.

The choice of sample size represents a compromise between several competing effects. It must be small enough so that the previously derived expressions for the cavity characteristics are rigorously applicable and large enough such that the observed effects on the resonant frequency shift as well as the changes in Q of the cavity are easily measurable. In addition, we require that the Q of the cavity with the sample in the system be sufficiently large that the resonance is still well defined. With these criteria in mind different sample sizes were used for the different samples to maximize sensitivity in the measurement. The sizes were chosen to give an approximate frequency shift of about 1.5 MHz and a decrease in the Q of the cavity from Q_0 of about a factor of 3 to 4. This required that the sample tube sizes be from 0.010 cm to 0.018 cm in diameter. Measurements were, however, also carried out in sample tubes with 0.0076 cm I. D. and 0.0254 cm I. D. to check for possible systematic errors such as sample contamination from the walls of the quartz tube as well as to demonstrate that the perturbation expressions given by Equations (4.28) - (4.30) are rigorously applicable.

Microwave Circuits and Electronics. A block diagram of the microwave circuit used to measure the frequency shift and the change in Q of the cavity is shown in Figure 4.11. Microwave power is generated with a Rohde-Schwartz XUC secondary frequency standard which is locked to an oven-controlled quartz crystal. The 880 MHz output, which is stable to better than 1 part in 10^8 and has an absolute accuracy of better than 1 part in 10^7 , is then tripled with a harmonic mixer. Other harmonics generated are filtered out with a series of band pass filters and the resulting signal is then amplified to a suitable level with a travelling wave tube microwave amplifier. The output power to the system is kept constant as a function of oscillator frequency and time by a power levelling feedback circuit. The power is monitored with a 6 db directional coupler. The D.C. signal at the crystal detector is then compared to a reference D.C. signal provided by a mercury battery and the difference signal is amplified with a D.C. to 100 KHz bandwidth stable amplifier. The amplified difference voltage is then fed back to the microwave amplifier to control the gain of the

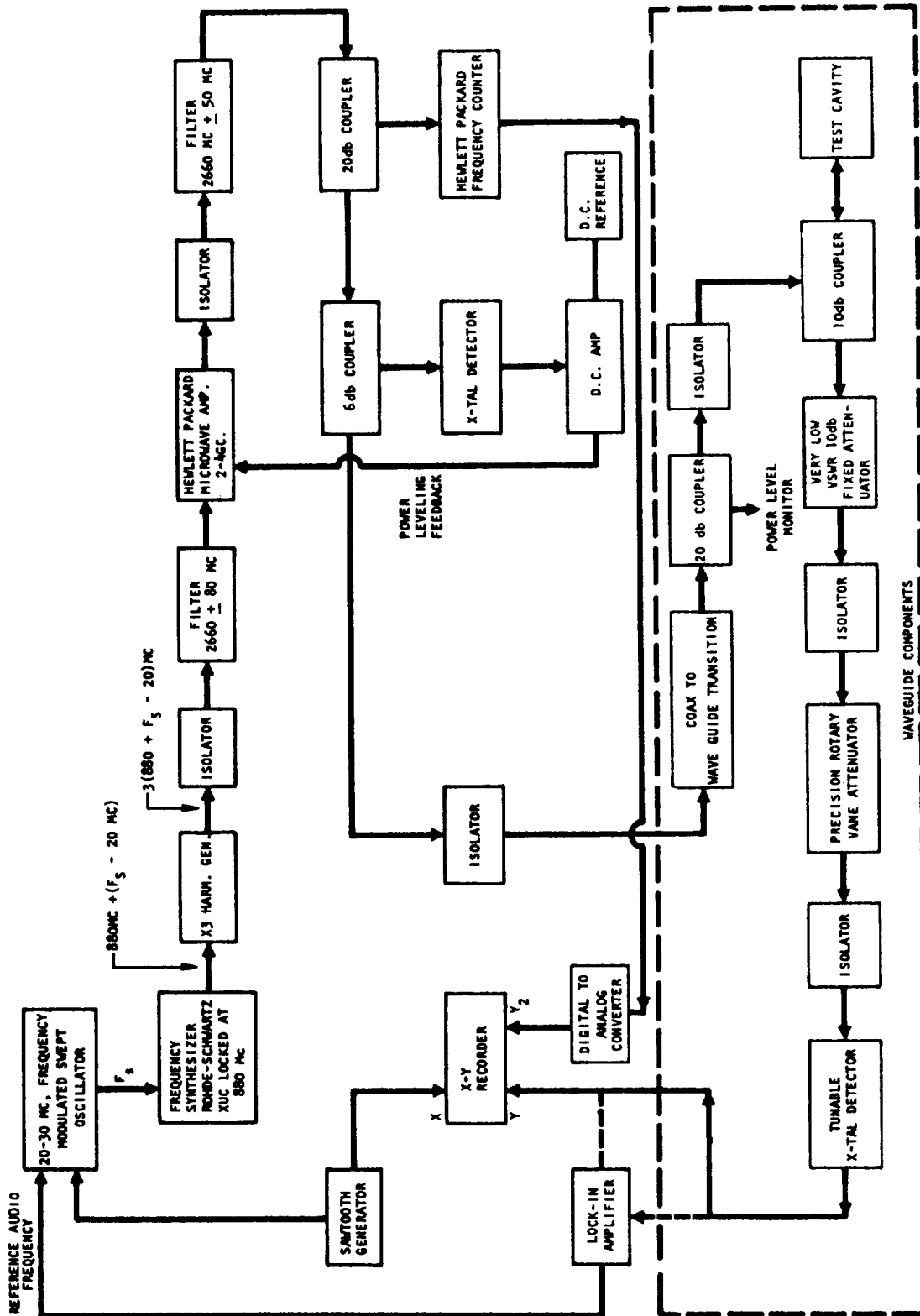


Figure 4.11 Block Diagram of Microwave and Electronic Components Used to Measure the Cavity Characteristics in the Experiment

system. In this manner the residual amplitude modulation on the microwave power output was kept to below 0.05%, while long term drift with time was found to be less than 0.02%. When the sampling crystal characteristic was carefully matched to that of the final tunable crystal detector, it was found that power transmission variation with frequency for the entire system could be kept below 0.05% over a frequency bandwidth of around 1 MHz, which is adequate in sweeping out the cavity response with no distortion.

Measurements of the cavity response were done in the waveguide component section indicated in the figure. The standing wave in the main line was kept to an extremely low level with a 1.01 VSWR, 10 db fixed attenuator. Ferrite isolators are placed at appropriate locations to ensure low VSWR as well as adequate isolation between the various components. The frequency of the system was swept with a 20-30 MHz interpolation oscillator whose frequency output is controlled by the voltage of a sawtooth generator. The response of the cavity is displayed on an x-y recorder whose x axis is driven by the same sawtooth generator and whose y axis is driven by the D. C. signal from the output of the tunable crystal detector. Power levels are measured with a precision calibrated rotary-vane attenuator and the frequency is measured by markers generated with a digital-to analog converter which is in turn driven by the output of a frequency counter. Typical cavity responses with and without the sample in the cavity are shown in Figure 4.12, where the frequency interval is compressed to show the relative shift in the resonance. The frequency widths measured in this manner, are accurate to ± 1 kHz, whereas the power levels are measured to an accuracy of ± 0.05 db.

To further improve the accuracy of the measurement of frequency shift of the cavity, the interpolation oscillator is FM modulated with the reference audio frequency of a Princeton Applied Research Lock-in Amplifier, Model HR8. When the output of the crystal is phase-sensitive detected with the lock-in amplifier, the response of the cavity is essentially differentiated and the resulting signal is illustrated in Figure 4.13. The resonant frequency of the cavity then corresponds to that frequency for which the output of the lock-in amplifier is zero. For these measurements, the interpolation oscillator is manually tuned for zero output at the lock-in amplifier and the frequency is directly measured with the frequency counter. It was found that the system is stable and accurate enough to make frequency measurements to ± 0.2 kHz.

4.4.2 Experimental Results

Sample Preparation. Sodium chloride solutions from 0.3 N to 0.7 N were prepared with distilled water and analyzed with an accuracy of better

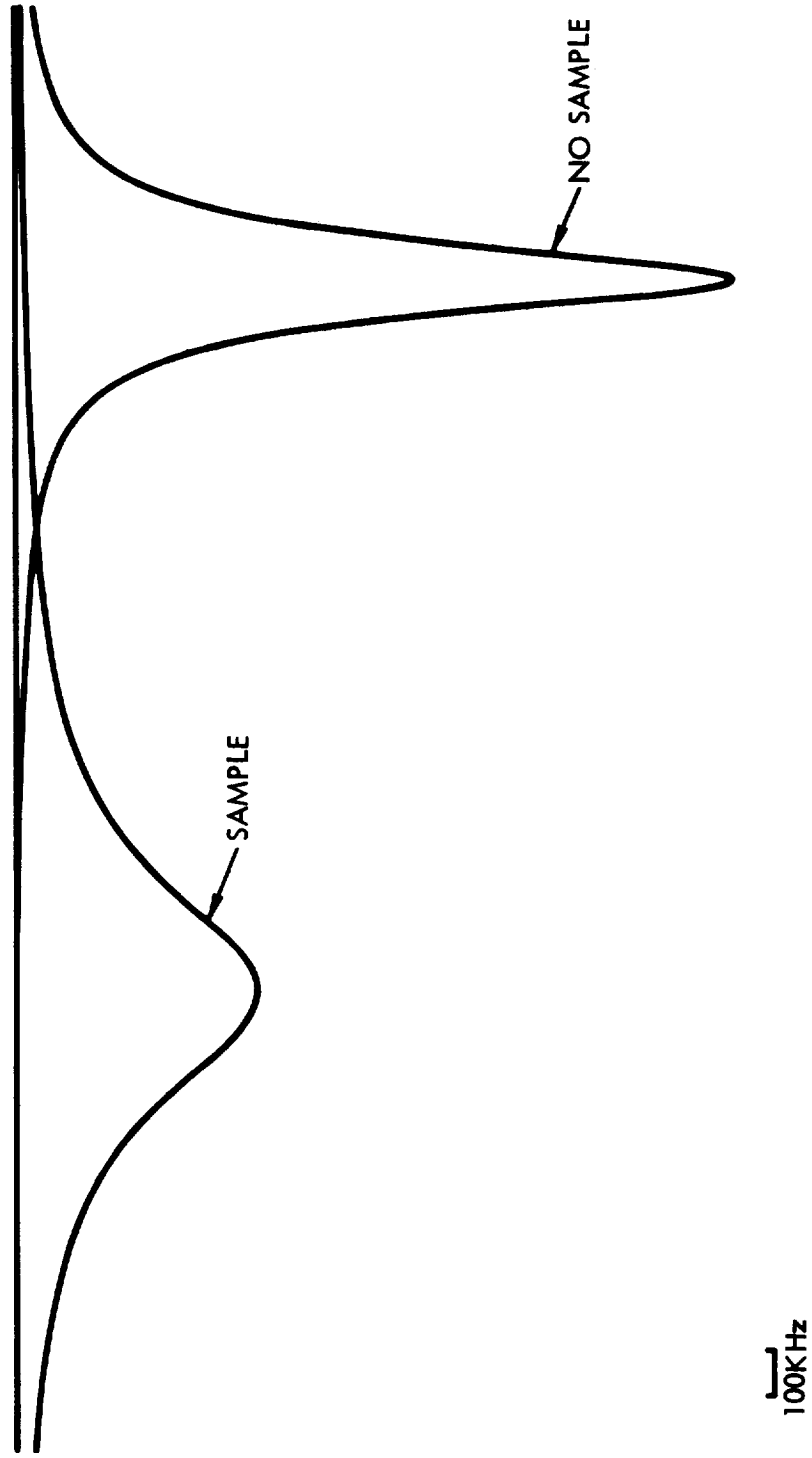


Figure 4. 12 Cavity Response as Measured by X-Y Recorder with and without Sample in the Cavity

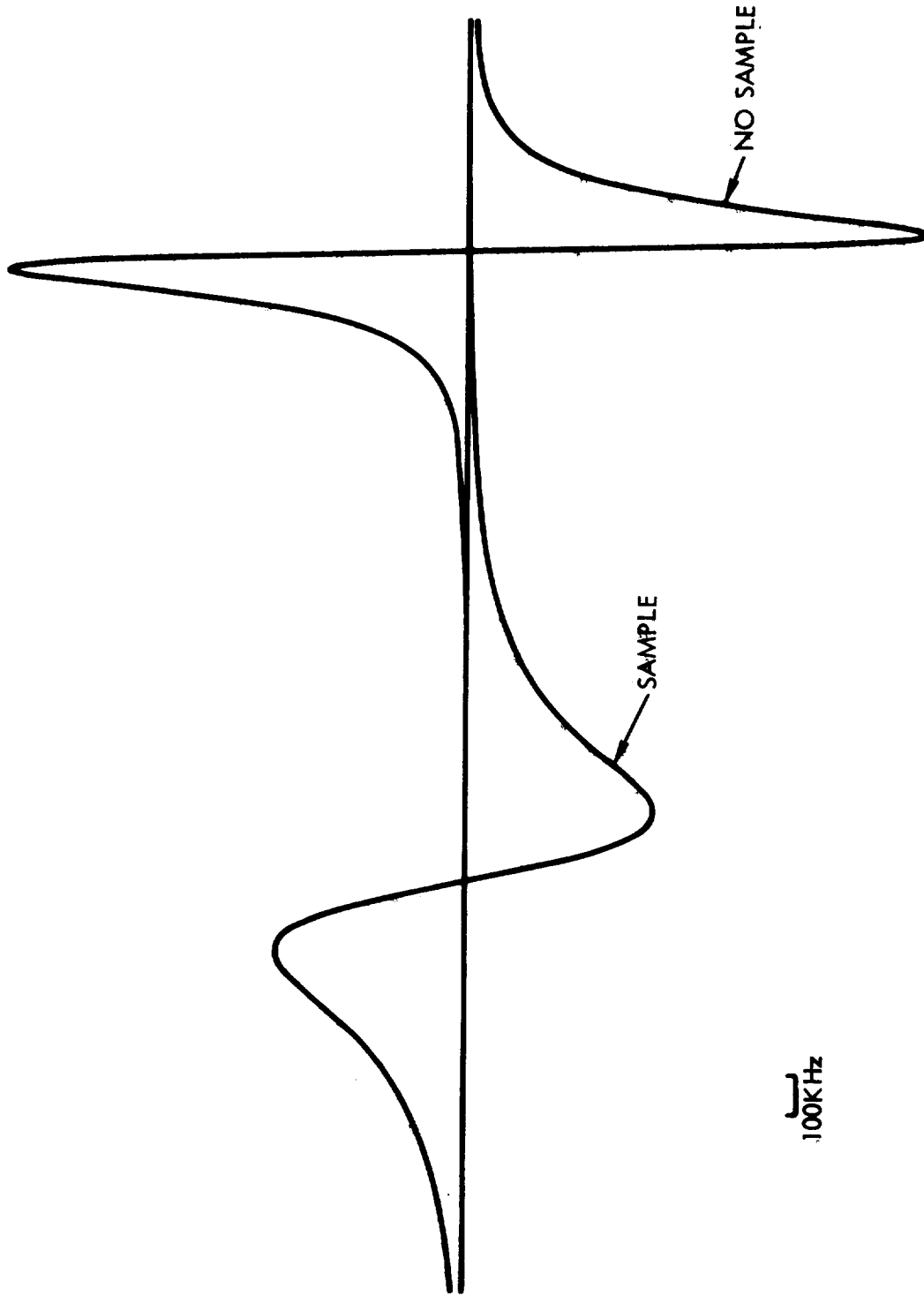


Figure 4.13 Differentiated Cavity Response as Measured by X-Y Recorder and Phase Sensitive Detection

than 0.5% with a silver nitrate titration method. Sea water samples from various localities were collected and kept in sealed bottles and analyzed for chloride concentration with the same technique. Occasional re-analysis was carried out to ensure that the chloride concentration did not change with time due to evaporation or sample deterioration. Except for those samples so indicated, all samples were collected at the surface. No noticeable suspended matter was present in any of the samples and no filtering of the water samples was done. The samples were kept in amber-colored bottles to ensure that no additional organic matter occurred due to algae growth. The ϵ' and ϵ'' for several samples were repeatedly measured over a period of several months with no noticeable change in the results.

Measurement Procedure. Measurements were made on distilled water and NaCl solutions of concentration 0.3N, 0.4N, 0.5N, 0.6N and 0.7N, and various samples of sea water. The measurements were done in a wide variety of sample tube sizes ranging from 0.007 cm I. D. to 0.0254 cm I. D. at 5.0°C, 15.0°C, 24.5°C and 30.0°C.

No systematic errors were detected between the measurements made on the same sample with different sample tube sizes, and in all cases, data taken with varying sample handling procedures agreed well within the experimental accuracy. For temperatures below room temperature, the cavity was kept in a dry nitrogen atmosphere to ensure that condensation of water vapor did not take place. Repeated insertion and withdrawal of the sample tube from the cavity produced no measurable change in the results, and possible changes in salinity of the sample due to evaporation from the end of the capillary tube were found to be negligible.

Measurement of ϵ' . The real part of the dielectric constant, ϵ' , was measured for all the samples by measuring the frequency shift due to the sample in a given sample tube size and then compared to the shift produced by distilled water in the same tube. As can be seen from Equation (4.28), the ratio of the frequency shifts gives directly the ratio of $(\epsilon'_{\text{distilled}})^{-1} / (\epsilon'_{\text{sample}})^{-1}$. This type of relative measurement is expected to be very accurate as all possible systematic errors tend to cancel, and absolute measurement need only be made once, namely that for distilled water, by measuring the sample tube size. The results for these relative measurements are shown in Figures 4.14, 4.15, and 4.16. As can be seen from the results for NaCl solutions the data can be fitted very accurately with a straight line and, except for the case of 5°C, there is no measurable difference among the various temperatures. The result for sea water, when plotted against the chloride concentration, is shifted from that for NaCl solutions and is undoubtedly due to the presence of other ions. It is noted, however, that the straight line fit to the sea water data does not go through the origin, as does the NaCl solution data, which suggests that there

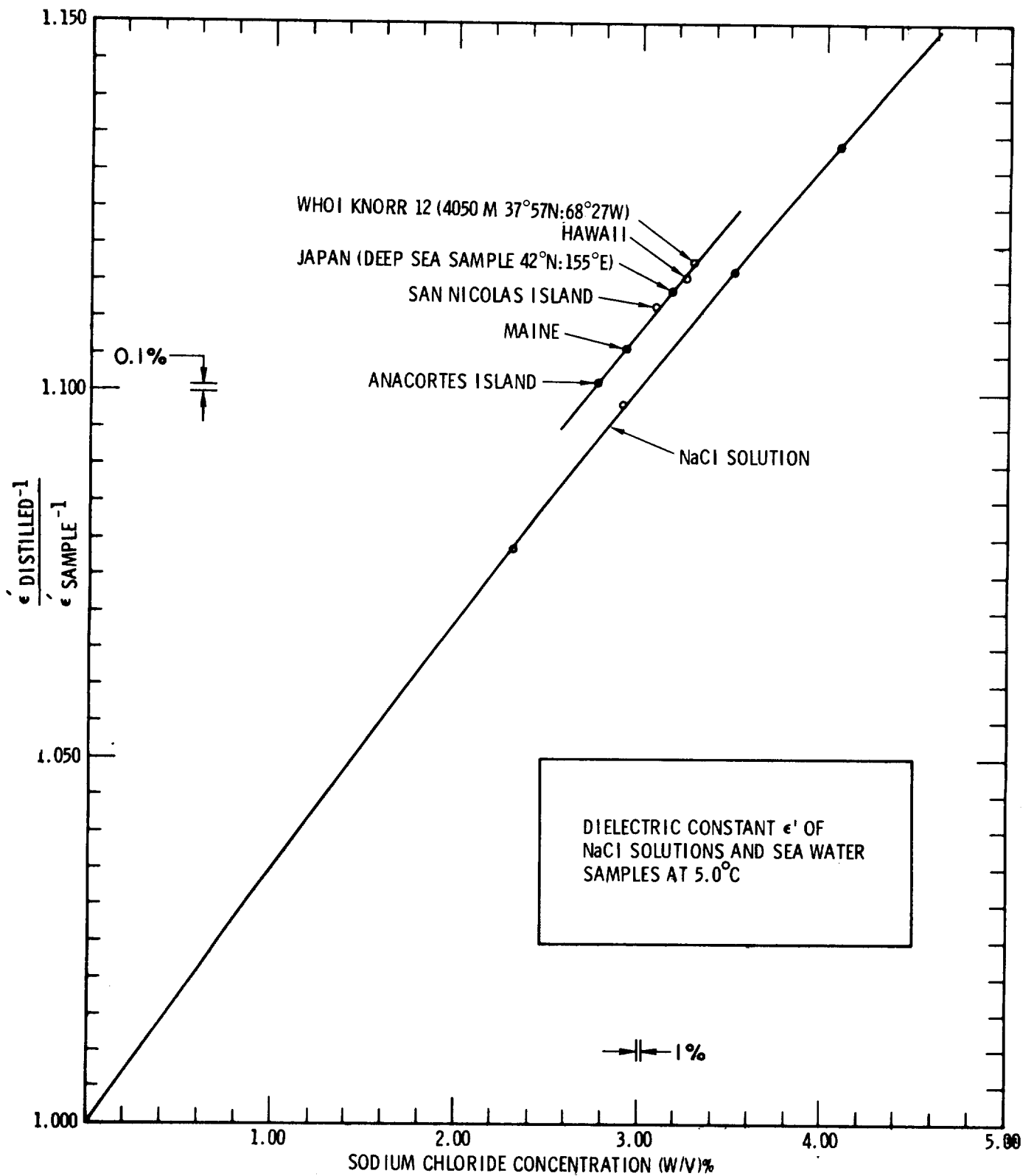


Figure 4.14 Values of $\epsilon' - 1$ Relative to that for Distilled Water as a Function of Salinity at 5°C for NaCl Solutions and Sea Water Samples at 2.653 GHz

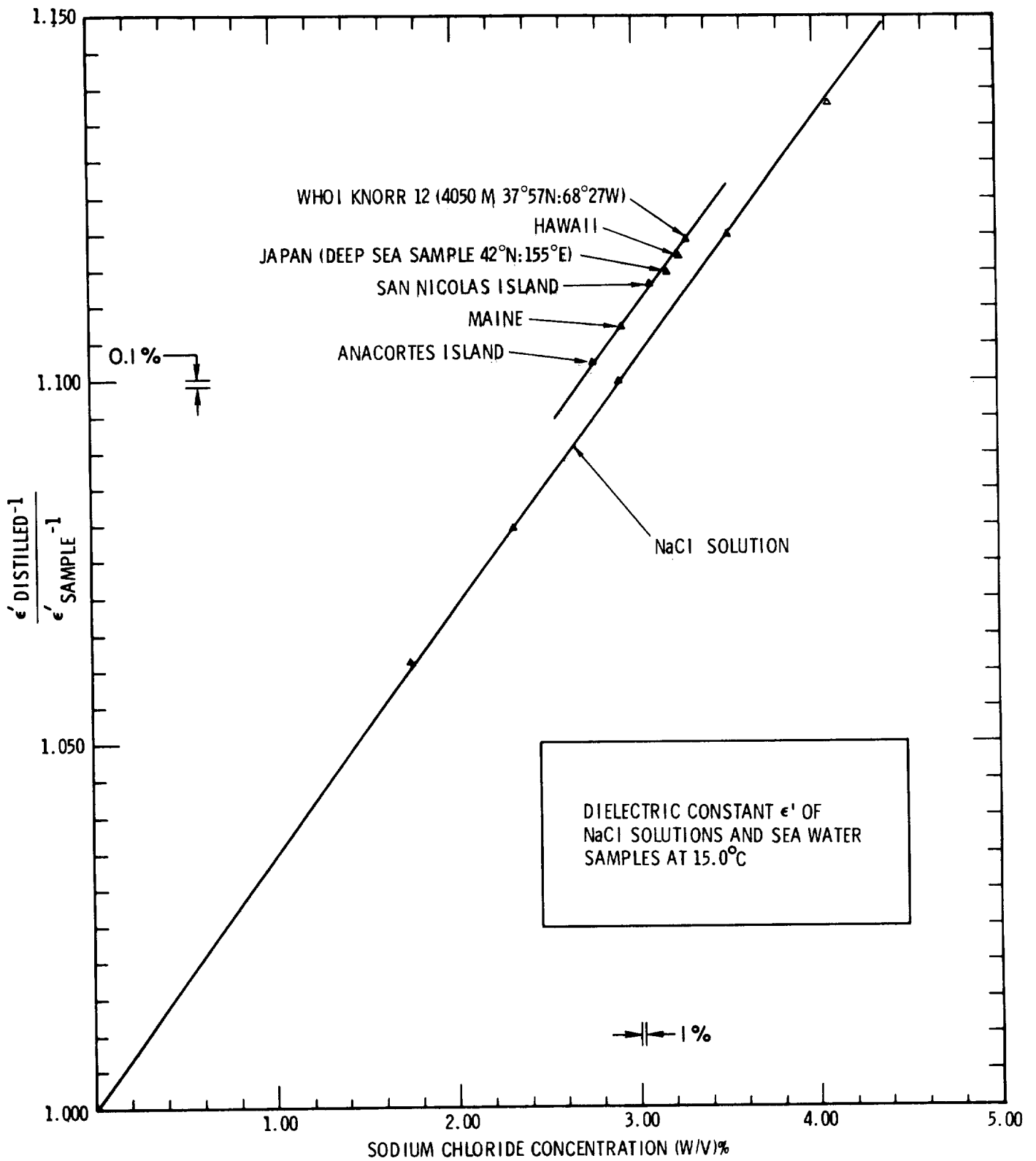


Figure 4.15 Values of $\epsilon' - 1$ Relative to that for Distilled Water as a Function of Salinity at 15°C for NaCl Solutions and Sea Water Samples at 2.653 GHz

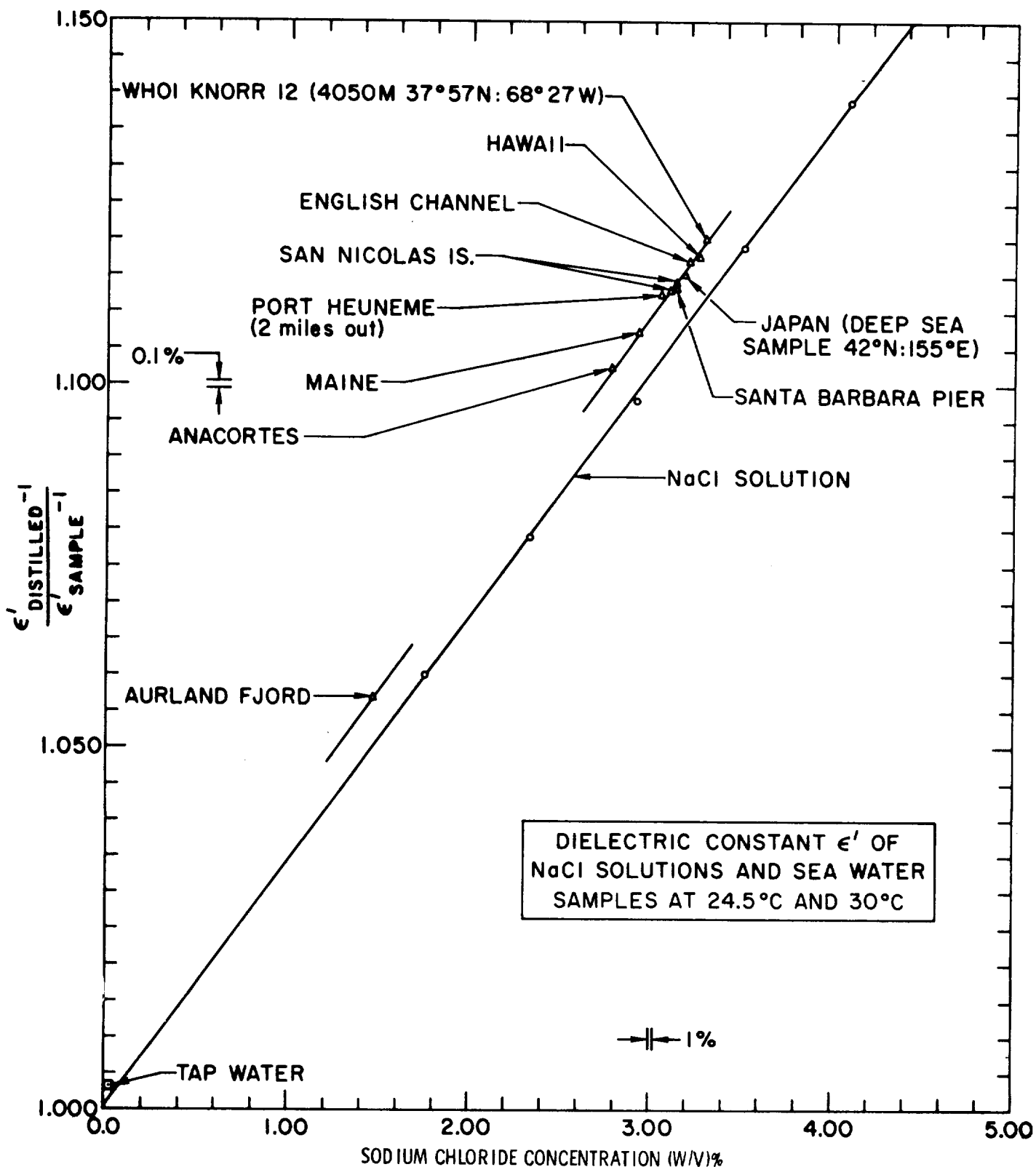


Figure 4.16 Values of $\epsilon' - 1$ Relative to that for Distilled Water as a Function of Salinity at 24.5°C and 30°C for NaCl Solutions and Sea Water Samples at 2.653 GHz

is a component in sea water which does not scale as its chloride concentration and which contributes to its dielectric properties. The remarkably good straight line fit to the sea water data, however, indicates that the dielectric property of the world's sea water can be uniquely determined from its salinity alone. The measurements are expected to be accurate to $\pm 0.1\%$.

Measurement of ϵ'' . The dielectric losses were measured by observing the changes in Q of the cavity from that of the empty cavity. Q_0 , the unloaded Q of the empty cavity was measured with a lossless quartz rod inserted into the cavity of a diameter such that the resonant frequency of the cavity was nearly that for the case with the sample in the system. In this case, any change in the wall loss of the cavity with frequency is compensated for. Typical traces from the x-y recorder for the cavity responses are shown in Figures 4.17, 4.18, and 4.19. The power levels were obtained by shifting the cavity response far away in frequency by the insertion of a large perturber (a 0.050 cm I. D. tube filled with water) and sweeping the frequency over the same range as before with the precision rotary-vane attenuator set at the various attenuation levels. In this manner, any residual variation of transmitted power in the system with frequency due to VSWR and non-linearity in the crystal and directional coupler characteristics is automatically taken into account. At each of the power levels, the width of the response curve was measured and the Q was calculated from Equation (4.22). For each curve, the Q's calculated from each of the power levels were compared with each other and agreement was obtained to better than 0.5%, which indicated that to this accuracy, the measured response curve agreed with the theoretically predicted response given by Equation (4.20). No distortion of the response curve is evident, and the frequency markers indicated that the sweep is extremely linear in frequency. The measured Q_L then was used in conjunction with the observed frequency shift obtained for each sample in the same sample tube to calculate $\epsilon''/(\epsilon' - 1)$ from Equation (4.30). The results for each temperature are shown in Figures 4.20, 4.21, 4.22, and 4.23.

Again, extremely good linear fits were obtained for all cases, with the sea water samples showing slightly larger dielectric loss compared to NaCl solutions for a given chloride concentration. This is to be expected, since the presence of other ions in sea water also contributes to the conductivity and, therefore, to the dielectric loss of the sample. These measurements are thought to be accurate to $\pm 0.3\%$.

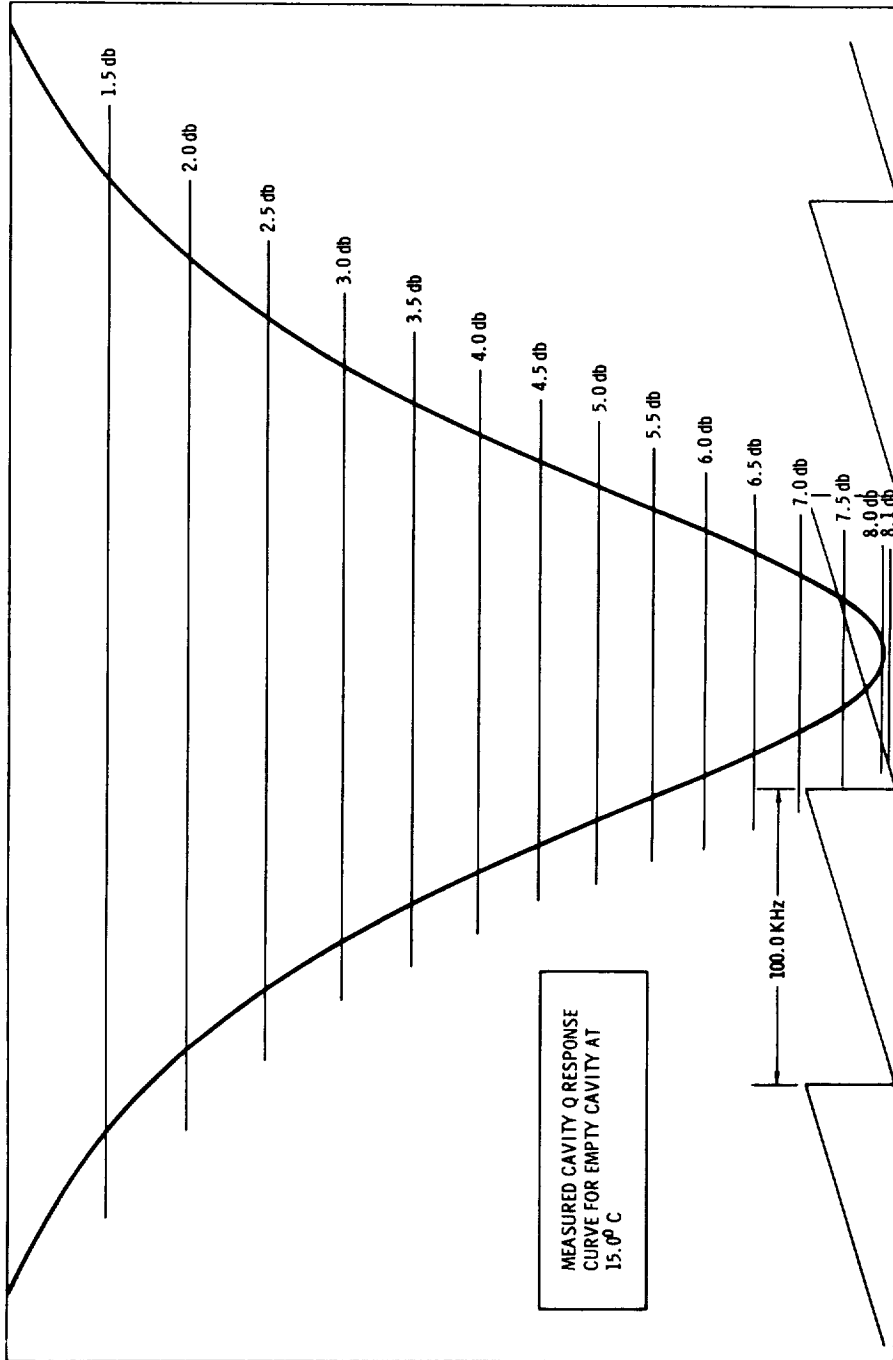


Figure 4. 17 Cavity Response for the Empty Sample Holder at 15° C

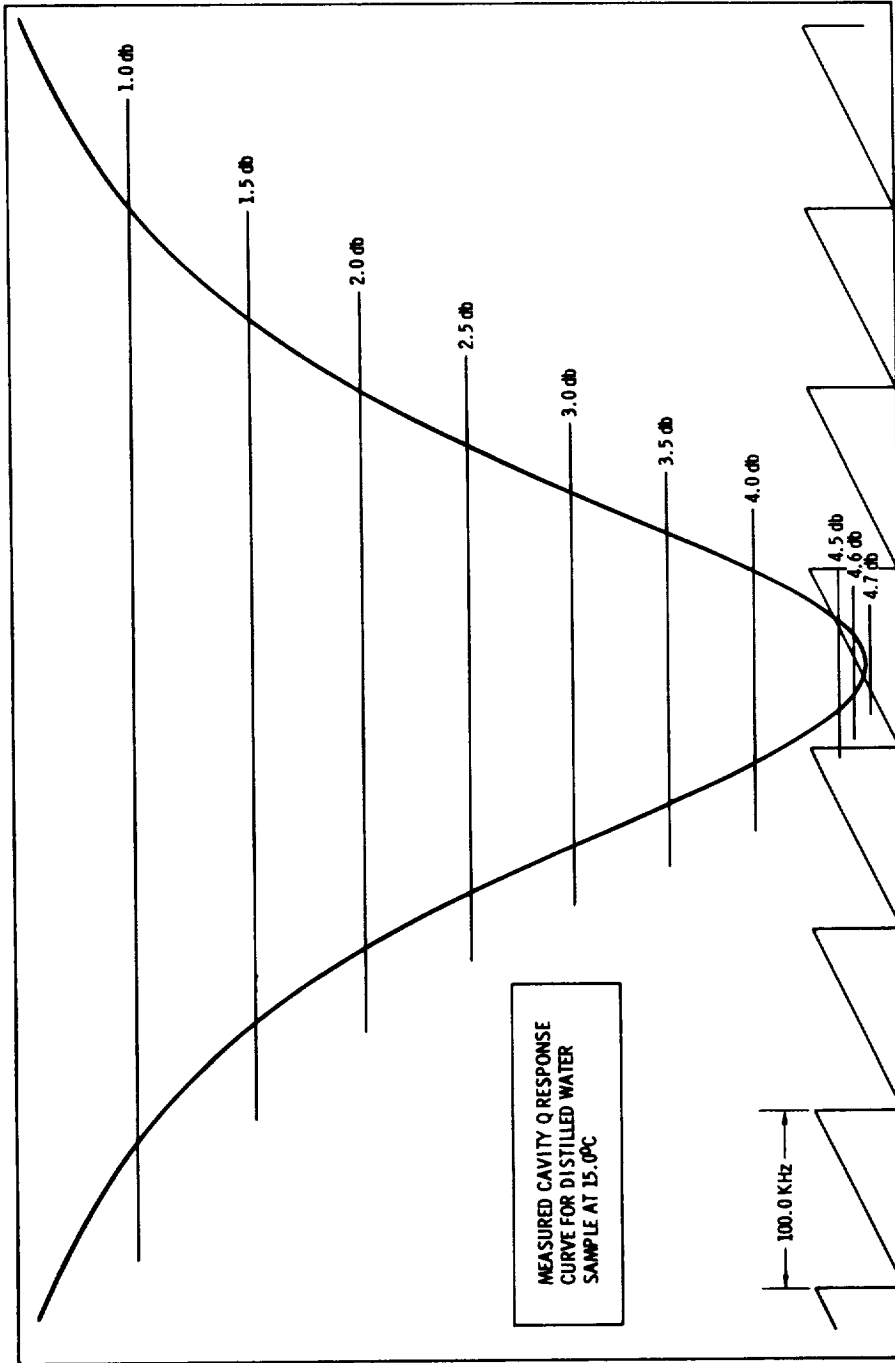


Figure 4.18 Cavity Response for Distilled Water in Sample Holder at 15°C

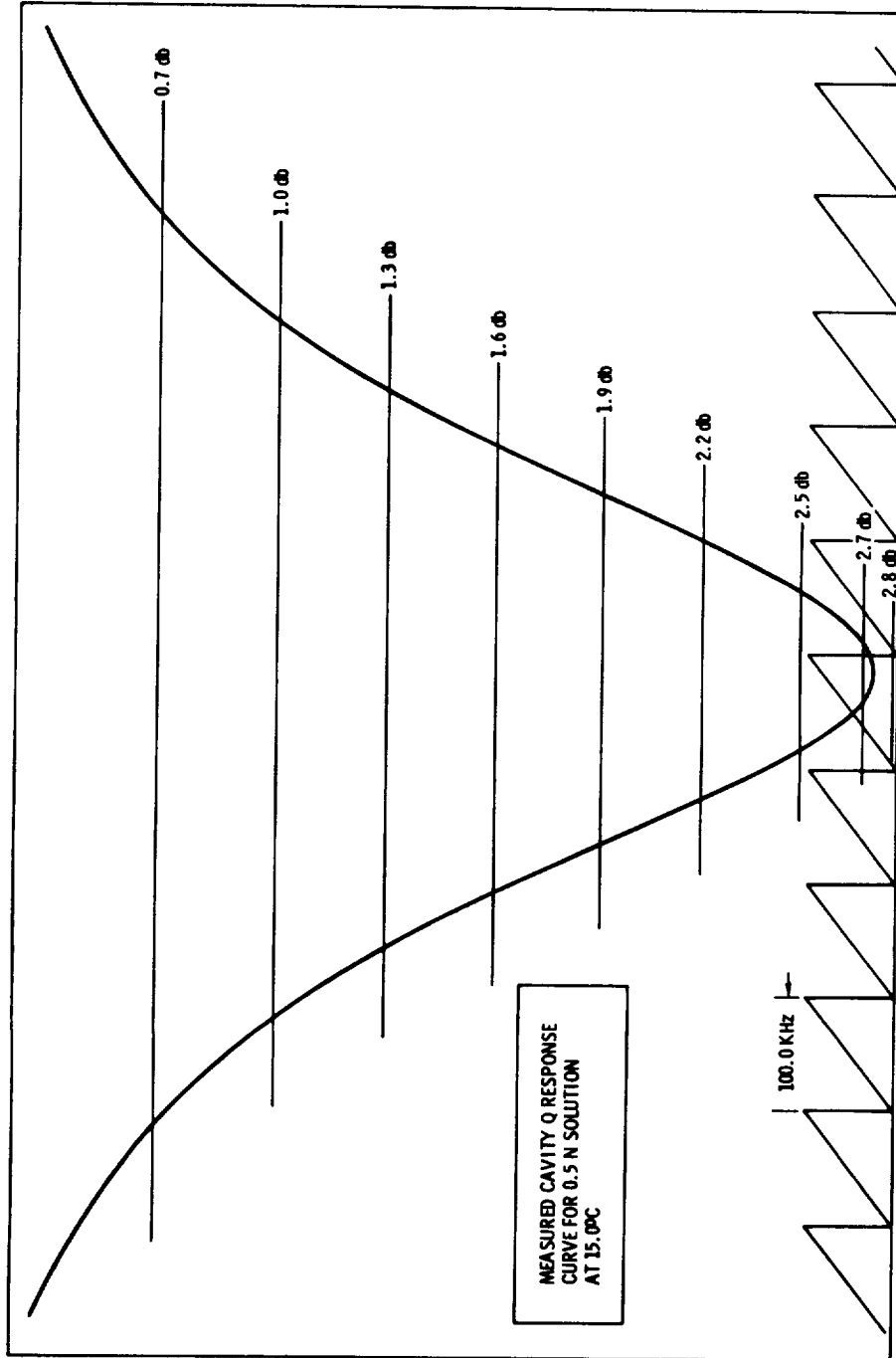


Figure 4. 19 Cavity Response for 0. 5N NaCl Solution in Sample Holder at 15°C

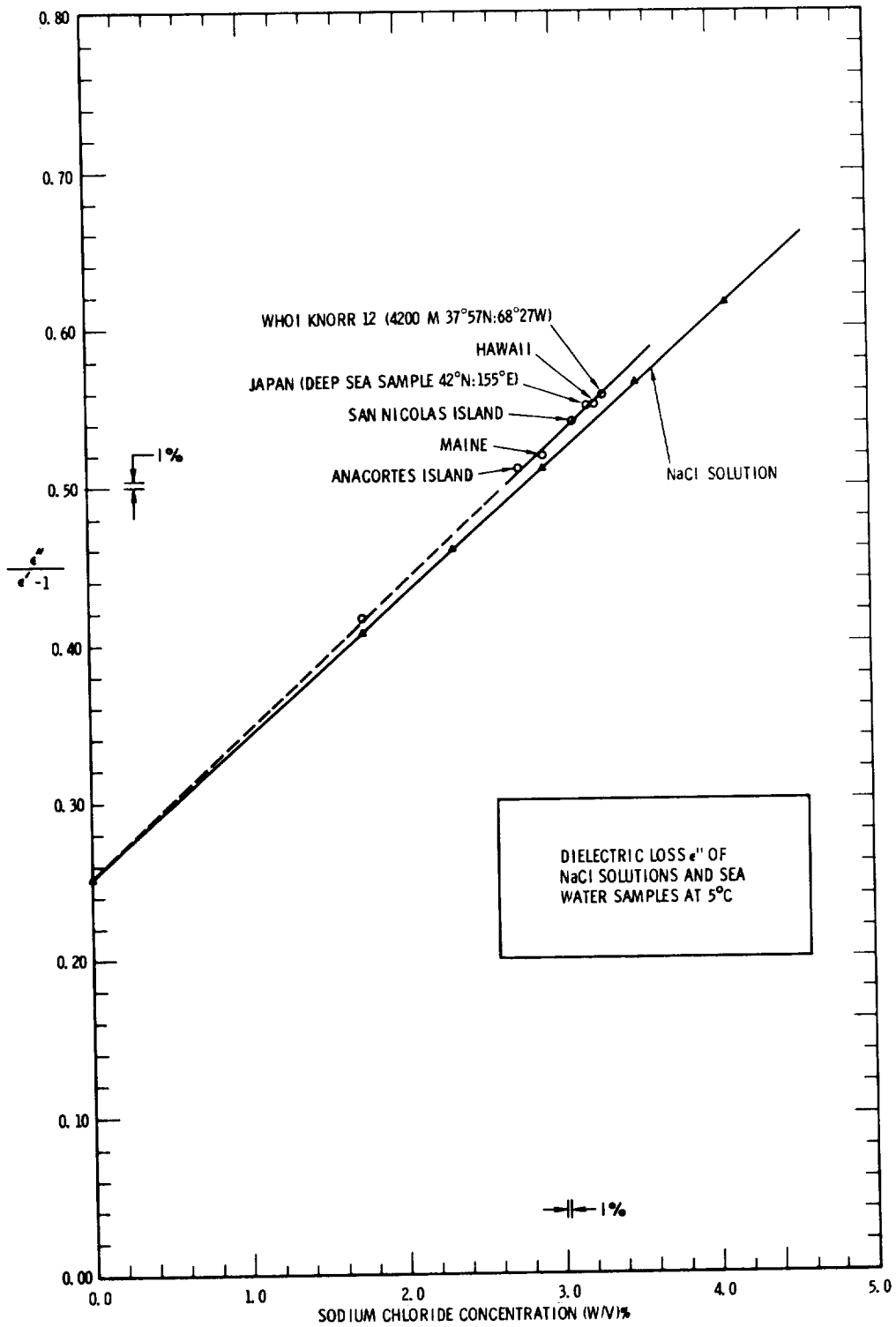


Figure 4.20 $\epsilon''/(\epsilon'-1)$ for NaCl Solutions and Sea Water Samples at 5°C and 2.653 GHz

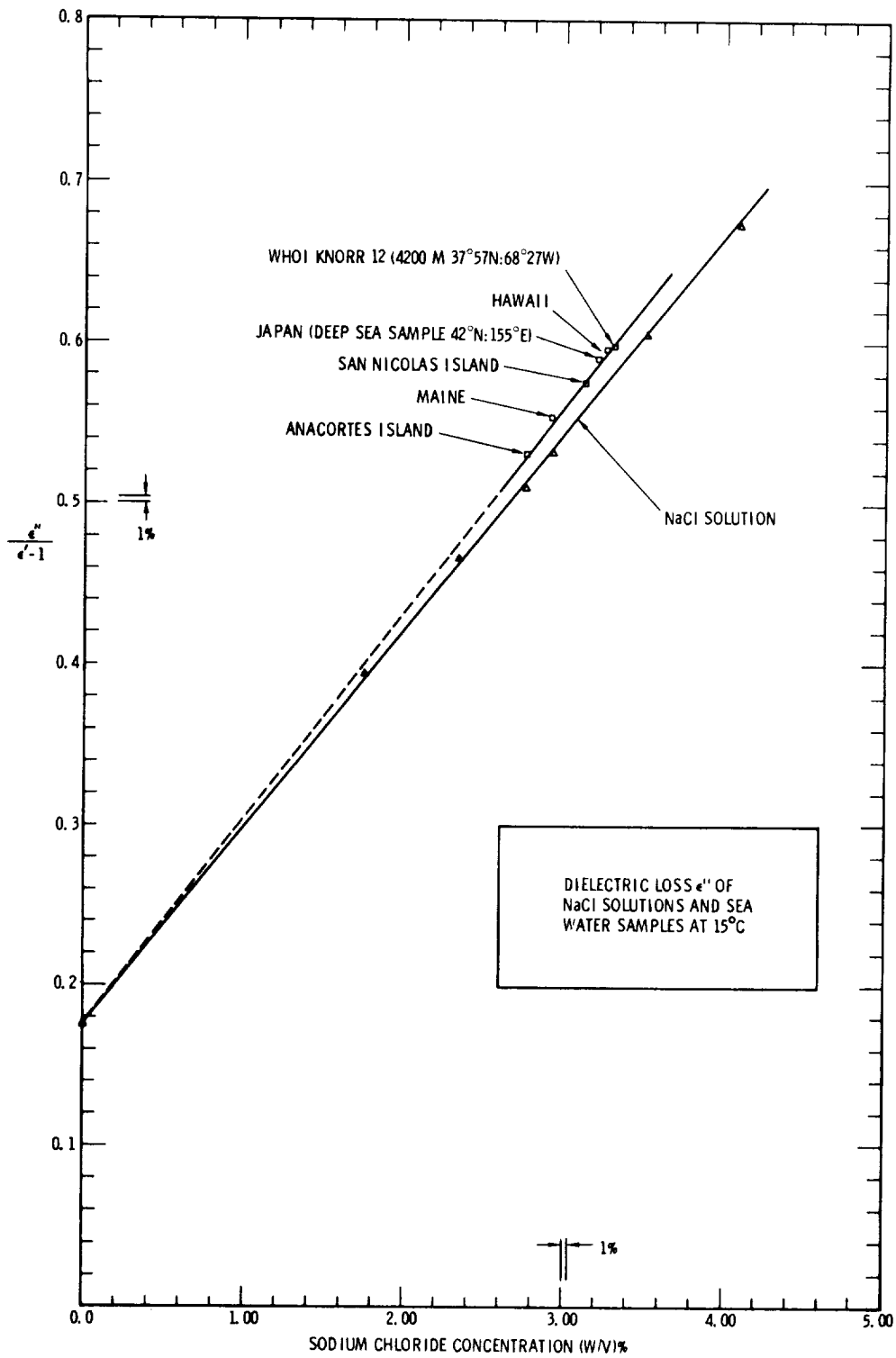


Figure 4.21 $\epsilon''/(\epsilon'-1)$ for NaCl Solutions and Sea Water Samples at 15°C and 2.653 GHz

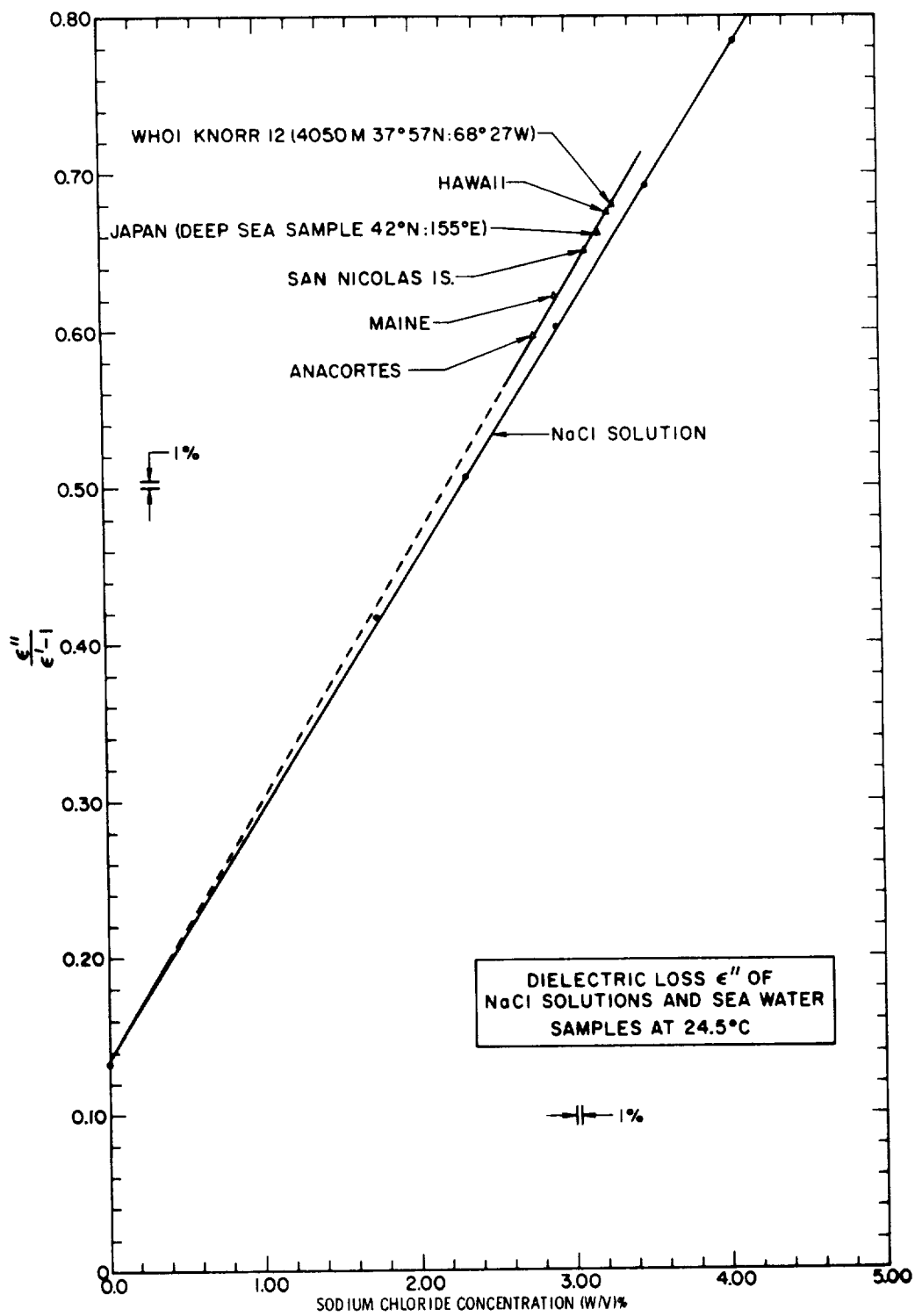


Figure 4.22 $\epsilon''/(\epsilon'-1)$ for NaCl Solutions and Sea Water Samples at 24.5°C and 2.653 GHz

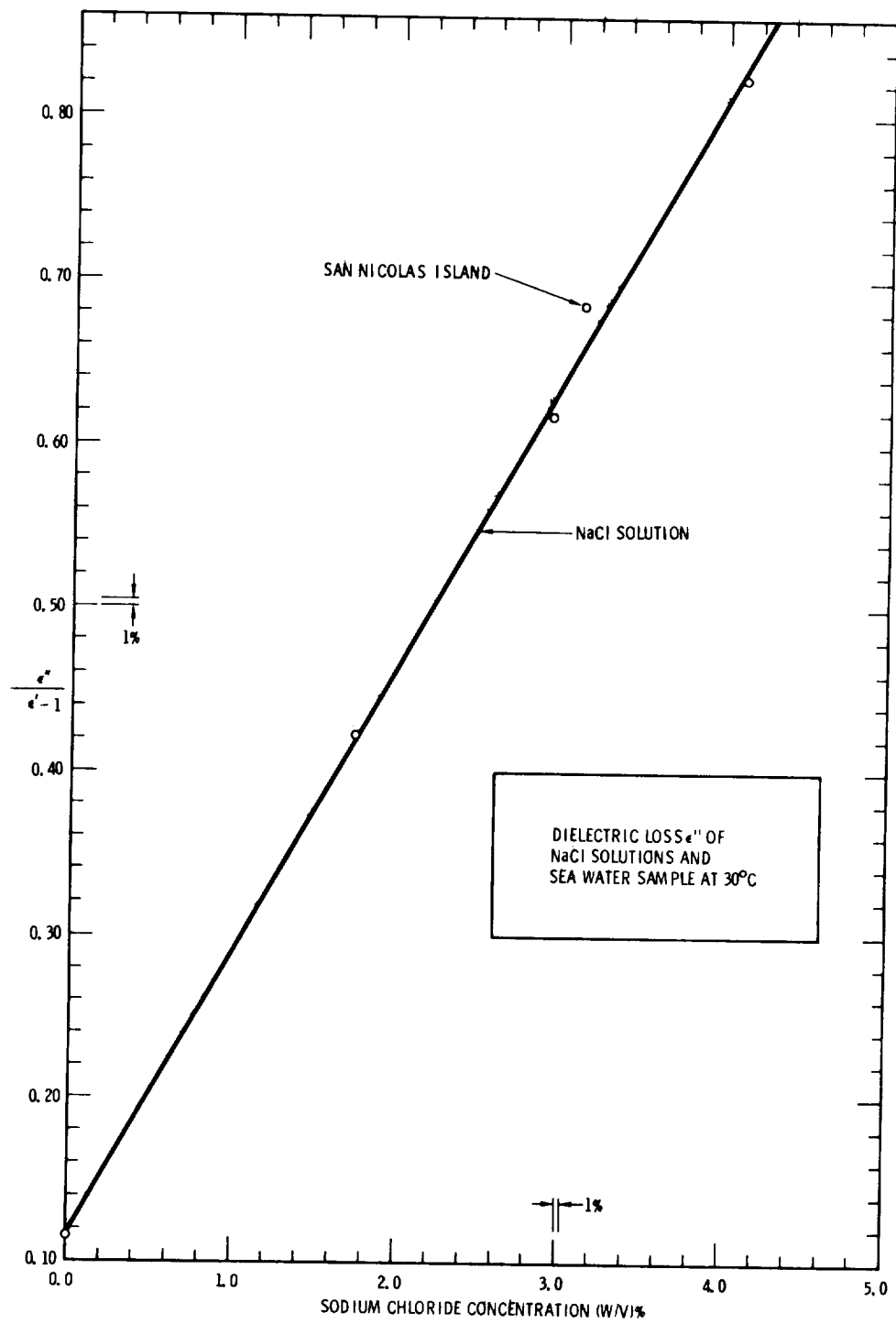


Figure 4.23 $\epsilon''/(\epsilon'-1)$ for NaCl Solutions and Sea Water Samples at 30°C and 2.653 GHz

Absolute measurements of ϵ' and ϵ'' for Distilled Water. We need only measure the absolute value of ϵ' and ϵ'' for distilled water at each of the temperatures to be able to convert the previously given results for NaCl and sea water solutions to absolute results. It is noted that these measurements need not necessarily be performed in the same sample tubes as those used previously, and that the absolute accuracy that can be achieved is dependent mainly on the accuracy with which the sample tube sizes are measured.

The frequency shift and change in Q of the cavity were measured for distilled water at each temperature, using different size sample tubes. The tube diameters were then measured destructively by potting them in epoxy and sectioning them. Each tube was cut into approximately 10 sections and the I. D. of the tube then measured with a microscope. For convenience, the tubes were photographed, and a Baush and Lomb certified scale, accurate to 0.05 micron, was used to compute the magnification factor of the microscope. The photographic plates of the ends of the sectioned tubes were then measured with a travelling microscope. Variation in the tube diameter with length was found to be less than 1% for selected sample tubes and the estimated uncertainty in the average I. D. determination is expected to be less than 0.25%. The absolute value of ϵ' and ϵ'' for distilled water at room temperature was measured in several different sample tubes and in all cases, the difference in the values obtained was found to be less than 0.2%.

The results for ϵ' and ϵ'' are tabulated in Table 4.2.

Table 4.2. ϵ' and ϵ'' for Distilled Water as a Function of Temperature

T (°C)	ϵ'	ϵ''
5.0	80.52	20.03
15.0	79.57	13.75
24.5	77.44	10.18
30.0	75.88	8.61

These values are plotted in Figures 4.1 and 4.2, and it can be seen that ϵ' agrees within about 0.25% of the previously published values of other workers and ϵ'' agrees to within about 2%. It is estimated that the data for ϵ' are accurate to 0.25% and for ϵ'' accurate to 0.5%.

Limited measurements were also made at 3.851 GHz. Although the data obtained were not nearly as accurate as those for 2.653 GHz due to the presence of standing waves in the microwave system as a result of operating at the edge of the specified band for the various components, they are consistent with the values obtained by extrapolating the lower frequency results with the Debye theory and Saxton and Lane's (1952) value for the relaxation time. The measured values for ϵ' and ϵ'' were accurate to about $\pm 2\%$ and the calculated values agreed well within this limit.

4.5 SUMMARY AND CONCLUSIONS

The data shown for sea water samples obtained from the world ocean indicated that the dielectric properties of sea water can be uniquely determined from sea-truth measurements of the salinity alone. Although there is currently no adequate theory to calculate the dielectric constant of sea water from its constituent concentrations, the curves shown in Figures 4.14 to 4.16 and 4.20 to 4.23, can be used empirically to compute the emissivity for sea water once the chloride concentration is known. It is also evident from the data that the behavior of the dielectric properties of sea water cannot be predicted from that for an equivalent salinity NaCl solution and that to do so may lead to serious errors.

The measurements of ϵ' and ϵ'' reported here are accurate to 0.25% and 0.5% respectively, corresponding to an accuracy of $\pm 0.2^\circ\text{K}$ in the measurement of the molecular temperature of the sea surface. In order to maintain this accuracy in actual use of the radiometer, it is required that the salinity of the world oceans be known to an accuracy of at least $\pm 0.5\%$.

REFERENCES

- Borgnas, F.E., and C.H. Papas, 1958, Hand. der Physik, 16, 406-422
- Bussey, H.E., 1967, Private Communications, NBS -251.03, N.B.S., Boulder, Colo.
- Christensen, J.H., A.J. Smith, R.B. Reed and K.L. Elmore, 1966, J. Chem. and Eng. Data, 11 (1), 60-63
- Collie, C.H., J.B. Hasted and D.M. Ritson, 1948, Proc. Phys. Soc., 60, 145-160
- Cooper, R., 1946, J. Instn. Elect. Engrs., Part III, 93, 69
- Defant, A., 1961, "Physical Oceanography," Vol. I, Pergamon Press, N. Y., Chap. IV
- Estin, A.J., and H.E. Bussey, 1960, I.R.E. Transactions on Microwave Theory and Techniques, MTT-8, 605-653
- Hasted, J.B., and G.W. Roderick, 1958, J. Chem. Phys., 29, 17-26
- Montgomery, C.G., 1947, Technique of Microwave Measurements, Rad. Lab. Ser. VII, p 286-293
- Muromtsev, A.M., 1963, "The Principal Hydrological Features of the Pacific Ocean (Trans. of Osnovnye cherty gidroogii Tikhogo Okeana, Gidrometer - ologicheskoe Iz datel'stoo, Leningrad, 1958) Israel Program for Sci. Trans., Jerusalem.
- Neumann, G., and W.S. Pierson, Jr., 1966, "Principles of Physical Oceanography," Prentice-Hall, Inc., Englewood Cliffs, N. J. p. 445-446
- Saxton, J.A., and J.A. Lane, 1952, Wireless Engineer, Oct. 269-275
- Von Hippel, A., 1961, Dielectric Materials and Applications, M.I.T. Press, Cambridge, Mass., p. 261

5.0 ATMOSPHERIC EFFECTS AND SKY EMISSION

Quantitative measurement of the thermal emission from the Earth's surface by remote sensors requires that correction be made for the radiative properties of the intervening atmosphere. At wavelengths of a few centimeters, there are four principal categories of interferences that are classed as atmospheric effects. They are:

1. Galactic background and cosmic background radiation
2. Radiation from discrete stellar radio sources¹
3. Attenuation from oxygen and water vapor in a cloudless atmosphere
4. Attenuation resulting from non-precipitating and precipitating rainclouds.

It has long been known that the Earth's atmosphere is approximately transparent to transmission of electromagnetic radiation at frequencies of about 3 GHz. Extensive work over the years on microwave signal propagation through the atmosphere at centimeter wavelength has indicated that the influence of clouds should be small at these frequencies except under severe storm conditions. An added factor for consideration is that the background noise of galactic radiation tends to decrease substantially as frequencies increase beyond about 1GHz, as drawn in Figure 5.1. Therefore, the frequency regime around 3 GHz is a well suited choice for minimizing the combination of the effects of sky background radiation and atmospheric interference.

5.1 COSMIC BACKGROUND RADIATION

Despite the advantages of choice of frequency near 3 GHz for minimal atmospheric effects, accurate surface temperature measurement by airborne or orbiting radiometers in this microwave region requires detailed knowledge of these effects for correcting the instrument observations. Even for operational frequencies near 3 GHz the correction to the measured apparent temperature of the ocean surface can still be of the order of a few degrees Kelvin and, therefore, must be taken into account.

¹The radiation at 3 GHz from the sun is excluded, but is considered in Section 6.

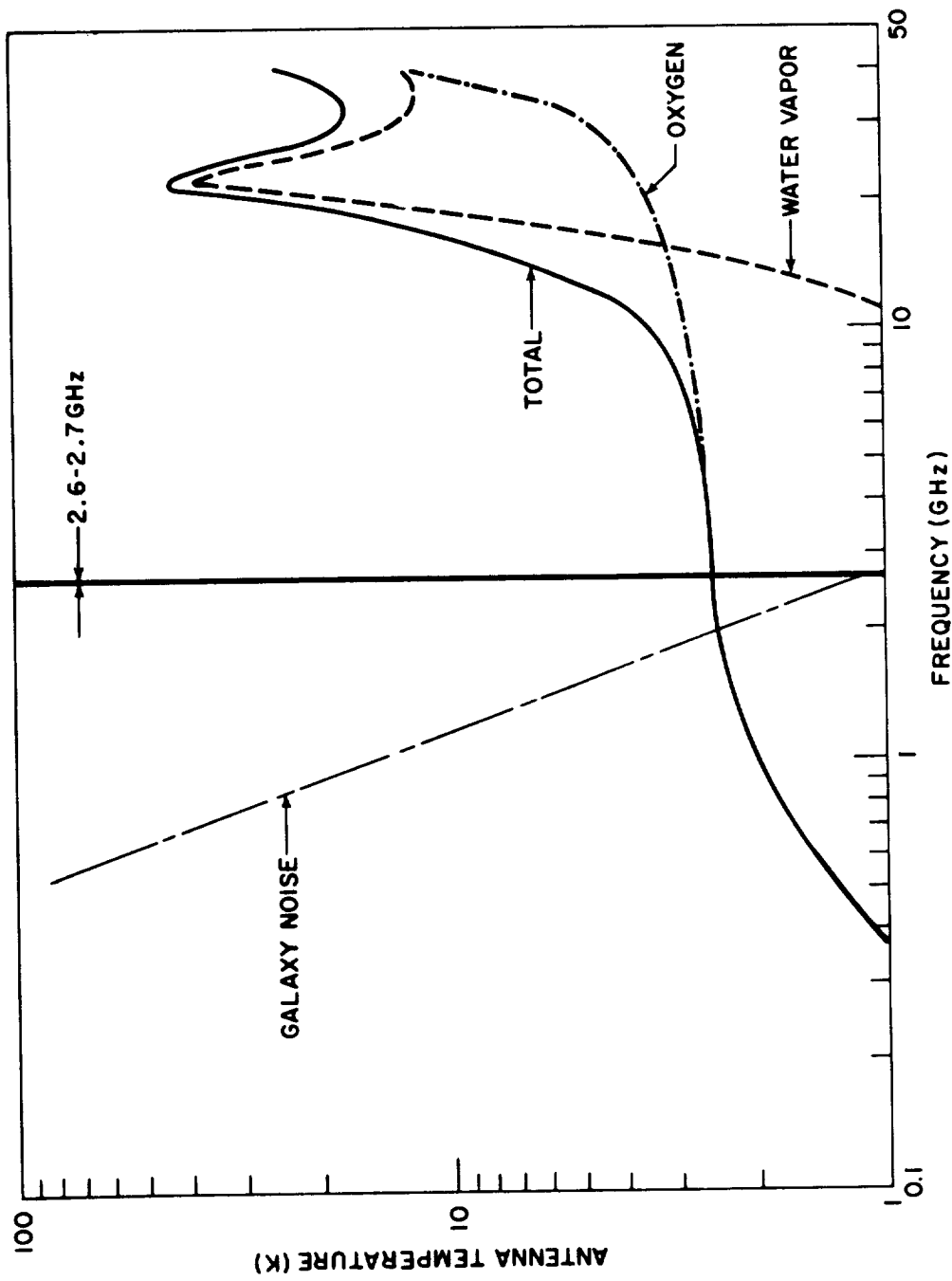


Figure 5.1 Comparison Between Antenna Temperature Contributions From Absorption by Oxygen and Water Vapor With Galactic Background

Until recently, the existing data for both direct observation and pertinent laboratory measurements, have not been accurate enough to allow a detailed treatment of the atmospheric attenuation problem. For instance, the values of the brightness temperature of the sky emission between 0.5 and 3.0 GHz obtained by various investigators differ by as much as a factor of two; it was only recently that the cosmic background radio noise was found to have a thermal spectrum corresponding to a brightness temperature of about 2.7°K.

In an effort to obtain more accurate corrections for these effects, we have undertaken to re-examine the calculations of the atmospheric attenuation and sky brightness temperature. These estimates are made in the light of the recent, more accurate observational results and take into account some new laboratory data we have obtained on microwave absorption in air, which are pertinent for this application.

By using the parameters obtained in the laboratory measurements, we were able to calculate the expected sky zenith brightness temperature as a function of frequency for standard models of atmospheric profiles. With a combination of ground based observations of the sky emission, and recent aircraft flights over water to 11 km altitude, it is possible to make a choice between the two sets of values quoted in the literature for the sky emission. On the basis of available theoretical arguments and evidence from experiments, we assign the sky background temperature to the lower of the two choices. This conclusion then has enabled us, in turn, to estimate the corrections to the radiometer measurements of the apparent ocean surface temperature accurate to better than one-half degree Kelvin. The corrections have been calculated for the frequencies of 2.65 GHz, 2.69 GHz, 3.85 GHz, and 4.20 GHz. A summary of the calculations and related experiments is presented below.

5.2 MICROWAVE ABSORPTION IN THE CLEAR ATMOSPHERE

Water vapor and molecular oxygen are the major known sources of opacity in the clear terrestrial atmosphere in the microwave region. Depending on the particular frequency under consideration, either one or the other molecule dominates the absorption process. For instance, at 22 GHz the attenuation at sea level due to 7.5 gm meter⁻³ of H₂O is about 0.1 db km⁻¹ whereas the absorption due to molecular oxygen is only about 0.01 db km⁻¹. As the frequency decreases, however, the attenuation due to water vapor decreases more rapidly than that for oxygen and the two become comparable at about 15 GHz. At frequencies below 5 GHz, the absorption due to the low frequency wing of the water vapor line located at 22 GHz becomes small compared with oxygen, and the atmospheric

absorption around 3 GHz would be, for our purposes, insensitive to diurnal changes. The differences in oxygen and water vapor at microwave frequencies are illustrated in Figure 5. 1.

5. 2. 1 Absorption by Oxygen Gas

The oxygen molecule, though electrically nonpolar, has a permanent magnetic dipole moment arising from the presence of two unpaired electron spins in its electronic ground state. The interaction between the magnetic moments of the two unpaired electrons, together with the coupling between the electronic spin angular momentum and the rotational (end-over-end) angular momentum of the molecule, causes a splitting of each state with rotational angular momentum K into three levels, with total angular momentum $J = K+1, K, \text{ and } K-1$. The selection rules for magnetic dipoles allow transitions for which $J = 0, \pm 1$; the transitions between levels of different K , however, all occur in the submillimeter and far infrared regions, so that the microwave absorption is due to transitions between the fine structure levels of each rotational state. Transitions for which $\Delta J = \pm 1$ are those from $J = K + 1$ to $J = K$, and give absorption lines in the vicinity of 60 GHz. The transitions for which $\Delta J = 0$ correspond to collision-caused realignments of the magnetic moment of the molecule in the states of $J = K \pm 1$, where the magnetic moment has a component in the direction of the rotational angular momentum. Since there is no change in total angular momentum, these transitions in the absence of a magnetic field are at zero frequency; the absorption process is analogous to the nonresonant absorption described by Debye. At frequencies below 10 GHz, these transitions are by far the most important process.

Many theories of microwave pressure-broadened line shape applicable to these transitions have been developed in the past, the more popular being the Van Vleck-Weisskopf (1947 a) theory, and more recently, R. G. Gordon's (1967) semiclassical lineshape theory. The expressions describing the dielectric loss due to oxygen in air at frequency ν are respectively, for the Van-Vleck-Weisskopf theory,

$$\epsilon'' = 3.926 \times 10^{-5}$$

$$\times \frac{p_A}{T} \left\{ \frac{\nu \Delta \nu}{(\nu_0 - \nu)^2 + \Delta \nu^2} + \frac{\nu \Delta \nu}{(\nu_0 + \nu)^2 + \Delta \nu^2} + \frac{\nu \Delta \nu}{\nu^2 + \Delta \nu^2} \right\}, \quad (5.1)$$

and for the Gordon theory,

$$\epsilon'' = 3.926 \times 10^{-5}$$

$$\times \frac{\rho_A}{T} \left\{ \frac{\nu \Delta \nu \nu_o^2 \left[\nu_o^2 + 3\nu^2 + \frac{27}{4} \Delta \nu^2 \right]}{\Delta \nu^2 \left[\nu_o^2 - 3\nu^2 \right]^2 + \nu^2 \left[\nu_o^2 - \nu^2 + \frac{9}{4} \Delta \nu^2 \right]^2} \right\} \quad (5.2)$$

where $\nu_o = 60$ GHz, T is the temperature, $\Delta \nu = \Delta \nu_o \rho_A$ where $\Delta \nu_o$ is the line-width at the density of one amagat, and ρ_A the density in amagats. Each expression has only one variable parameter, $\Delta \nu_o$, the linewidth at one amagat, which determines both the shape of the absorption vs. frequency curve and the absolute value of the absorption. The absorption coefficient α , in cm^{-1} , is then simply given by,

$$\alpha = \frac{2\pi}{\lambda} \epsilon'' \quad (5.3)$$

In order to determine the appropriate linewidth parameter for each theory, the microwave absorption in air was measured recently in the laboratory over a wide range of pressure and temperature. The details of the measurements are described elsewhere and we summarize here the result obtained for the linewidth parameter $\Delta \nu_o$ for air for each of the theories of lineshape. The fit of our laboratory data gave, for the Van Vleck theory.

$$\Delta \nu_o = 693 \pm 46 (T/300)^{0.47 \pm 0.39} \text{ MHz/amagat}, \quad (5.4)$$

and for the Gordon theory,

$$\Delta \nu_o = 587 \pm 28 (T/300)^{0.11 \pm 0.27} \text{ MHz/amagat}. \quad (5.5)$$

As can be seen, these results are accurate to about 5 percent and, therefore, the subsequent accuracy in the computation of the absorption coefficient is accurate to this precision.

5.2.2 Absorption by Water Vapor

The water molecule in its gaseous form absorbs in the microwave region of the spectrum because of its permanent electric dipole. Van Vleck (1947b) determined the absorptive characteristics from quantum theory in a manner similar to that used to determine the absorption coefficient of oxygen. In the case of water vapor, there is a single absorption line peaked at 22.235 GHz. Since water vapor is electrically polar, strong absorption also occurs at infrared frequencies. Broadening of the infrared absorption lines is believed to result in some additional absorption in the microwave region, often called "residual absorption." Many years ago, Becker and Autles (1946) showed that the contribution to the absorption coefficient of water vapor resulting from the residual absorption was about five times larger than estimated by Van Vleck. The quantum mechanical expression for the absorption coefficient as developed by Van Vleck can be simplified and corrected for the observed residual absorption. Such an expression has been reported by Staelin (1966). Defining the absorption coefficient for water vapor as α_w , Staelin's model gives

$$\alpha_w (\text{db km}^{-1}) = 140.71 \exp(-644T) \nu^2 p \rho_w T^{-3.125} (1 - 0.0147 \rho_w T/p) \quad (5.6)$$

$$\times \left\{ 1 / \left[(\nu - 22.234)^2 + (\Delta\nu)^2 \right] + 1 / \left[(\nu + 22.234)^2 + (\Delta\nu)^2 \right] \right\}$$

$$+ 0.01107 \rho_w^2 \Delta\nu T^{-1.5}.$$

where ν is frequency in GHz, p is total pressure in mb, and ρ_w is the density of water vapor in gm m^{-3} .

$$\Delta\nu (\text{cm}^{-1}) = 2.58 \times 10^{-3} p (1 + 0.0147 \rho_w T/p) (T/318)^{-0.625} \quad (5.7)$$

At 3 GHz, the calculated value of α_w is 7.83×10^{-5} (db/km per gm m^{-3}) for a pressure of 1013.25 mb and a temperature of 293°K.

In the atmosphere, the total atmospheric content of water vapor over a given location varies somewhat in time and in space. However, an upper limit can be set for a saturated, isothermal atmosphere at 20°, which could contain 17 gm m^{-3} of water vapor. In model atmospheres for the Earth, it

is often assumed that the average water vapor content is about 7.5 gm m^{-3} at sea level. For these cases,

$$\alpha_w \text{ (isothermal, } 20^\circ\text{C)} \approx 1.3 \times 10^{-3} \text{ db km}^{-1}$$

$$\alpha_w \text{ (model)} \approx 5.9 \times 10^{-4} \text{ db km}^{-1}.$$

At 1 atm and 20°C , the Van Vleck model predicts the oxygen absorption to be about $6.6 \times 10^{-3} \text{ db km}^{-1}$ at 3 GHz. Thus in the extreme, water vapor can be only about 20 percent of the total absorption in the clear atmosphere. However, it normally will be less than 10 percent of the total and can be corrected for to first order.

5.3 ATTENUATION BY RAIN CLOUDS

Correction for the influence of the atmosphere on the apparent temperature of the sea at microwave frequencies is greatly complicated by the presence of liquid water and ice in the air. Hydrometeors in the atmosphere can absorb, scatter or emit microwave radiation. The magnitude of these effects varies considerably with frequency, thermodynamic phase of the water, temperature, hydrometeor size distribution, and condensed water concentration. Considerable information from radar research has been accumulated over the years about scattering of radiation at microwave frequencies. However, comparatively little information is available on the combined scattering and absorptive properties of rain clouds and their relationship to interpretation of radiometric observations. Recently, Lhermitte (1968) has reviewed the subject with reference to the application of microwave radiometry to the measurement of liquid water content in clouds. Paris (1969) has considered this problem briefly in relation to interpretation of radiometer observations of thermal emission from the sea at 19 GHz and higher frequencies. The hydrometeor size and spatial concentration distribution in clouds is generally not known; it is therefore difficult to estimate in any detail their total contribution to the apparent temperature sensed by a radiometer.

Some appreciation for the current state of knowledge may be obtained by comparing some exploratory data with calculated effects at frequencies higher than 3 GHz. Calculations for the parallel polarized sky temperature as a function of frequency for a clear atmosphere are readily available, and estimates of the influence of non-precipitating clouds and rain also have been made. Extrapolations of Weber's (1960) calculations are shown in Figure 5.2 as an example. Also plotted in this diagram are some observations of the sky temperature at the zenith made by Wulfsberg (1964) and Cummings and Hall (1966).

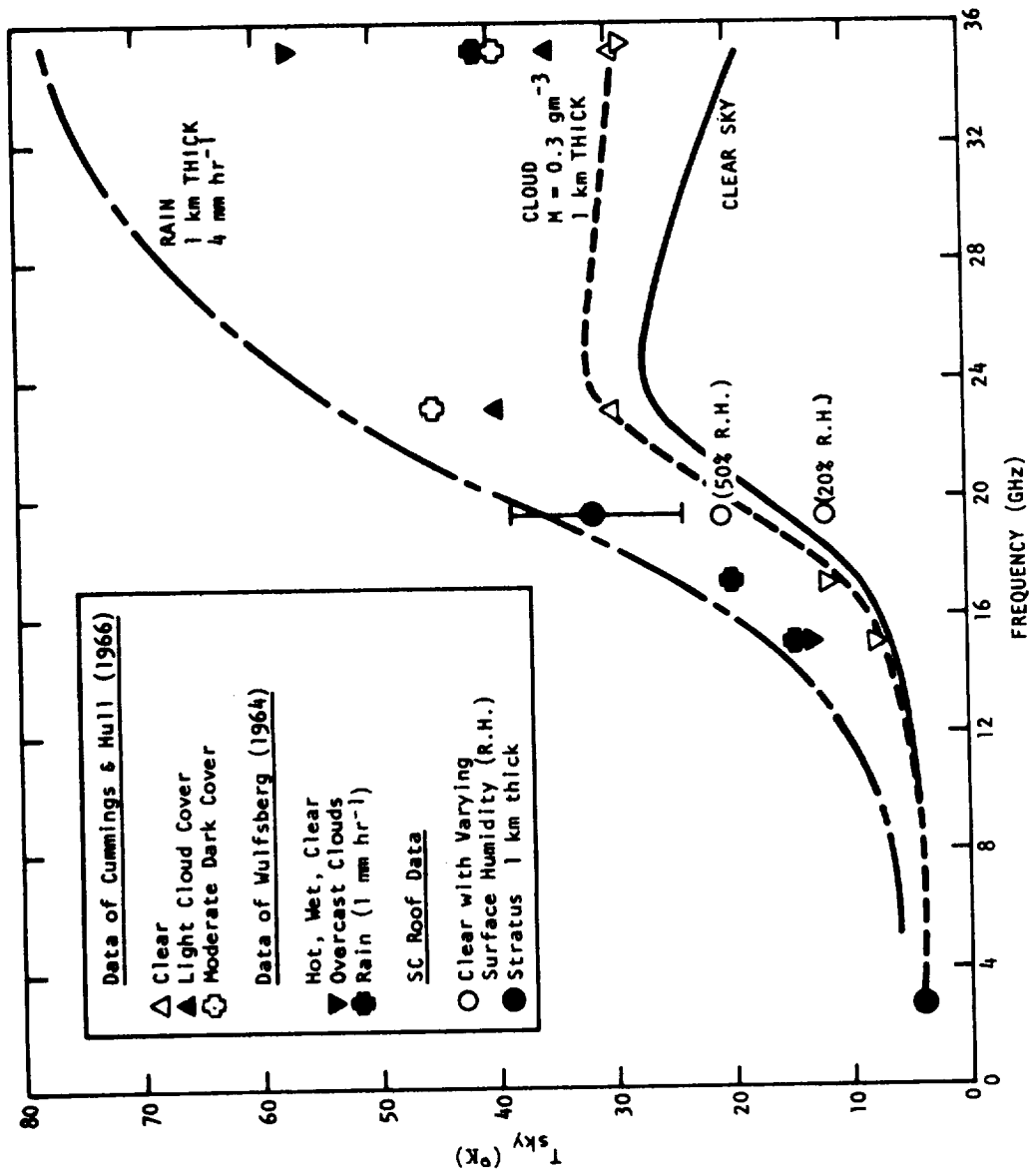


Figure 5.2 Parallel Polarized Sky Temperature as a Function of Frequency for Clear and Cloudy Skies

The radiometer data roughly agree with calculations for a clear atmosphere, but the results for cloudy air are scattered. They appear to be somewhat higher than expected from consideration of Rayleigh's absorption equation.

More recent results for the relation between sky temperature and clouds at frequencies from 19 GHz to 33 GHz have been reported by Toong and Staelin (1970). These workers indicate that multifrequency experimental radiometer results can yield values of liquid water content and cloud thickness consistent with other observations. Some Soviet results have been reported Shifrin (1969).

Since useable data for cloud effects are virtually non-existent at frequencies lower than 19 GHz, it is difficult even to check the validity of the crudest available approximate theories. We feel at the present time only these first order models warrant consideration as candidate models for estimating the upper limit of interferences expected from hydrometeors.

5.3.1 Attenuation by Non-Precipitating Clouds

For wavelengths much larger than the average drop size in a cloud, Gunn and East (1954) determined that the scattered component of incident radiation should be negligible, and the attenuation should be well approximated by Rayleigh's theory. The Rayleigh model then should be applicable to clouds whose droplets range typically from a few hundred of microns to a few microns. This is the range of droplet size commonly observed in terrestrial clouds. Accordingly, the absorption coefficient in one direction is (db km⁻¹)

$$\alpha_c = 0.434 \frac{6\pi M}{\lambda \rho_c} \epsilon'' \quad (5.8)$$

where λ is the wavelength at which the absorption is evaluated; M is the liquid water content in gm m⁻³, ρ_c is the condensed water density in gm cm⁻³, and (ϵ'') is the imaginary part of the complex dielectric constant of condensed water.

For water clouds at about 10°C, in the 3 GHz frequency range, the absorption coefficient is given by the approximate expression (Goldstein, 1951):

$$\alpha_c \cong \frac{10^{-1} M}{\lambda^2} \cdot (\text{db km}^{-1}) \quad (5.9)$$

Gunn and East (1954) calculated the values of a_c for different temperatures corresponding to assumed spheres of liquid water or ice, and they are listed in Table 5.1.

Table 5.1. Attenuation by Non-Precipitating Cloud (One-Way) in db km^{-1} (From Gunn and East, 1954)

	T(°C)	$\lambda = 10 \text{ cm}$	$\lambda = 5.7 \text{ cm}$
Water Cloud (M in gm m^{-3})	20	$3.9 \times 10^{-3} \text{ M}$	$1.36 \times 10^{-2} \text{ M}$
	10	$5.6 \times 10^{-3} \text{ M}$	$1.96 \times 10^{-2} \text{ M}$
	0	$9.0 \times 10^{-3} \text{ M}$	$2.72 \times 10^{-2} \text{ M}$
	-8	-	$3.4 \times 10^{-2} \text{ M}$ (Extrapolated)
Ice Cloud (M in gm m^{-3})	0	$7.87 \times 10^{-4} \text{ M}$	$13.8 \times 10^{-4} \text{ M}$
	-10	$2.62 \times 10^{-4} \text{ M}$	$4.60 \times 10^{-4} \text{ M}$
	-20	$1.80 \times 10^{-4} \text{ M}$	$3.16 \times 10^{-4} \text{ M}$

From Equation (5.8) it is readily seen that the equivalent absorption of radiation by non-precipitating clouds is independent of the size distribution of hydrometeors in the first approximation, and is linearly proportional to the liquid water content in the path of the radiometer. Furthermore, the absorption is inversely proportional to the square of the wavelength of incident radiation (Eq. 5.9).

The calculations of Gunn and East (1954) indicate the absorption by ice is roughly an order of magnitude or more lower than that for liquid water. This effect, of course, is associated with the hindrance of rotational motion of water molecules in ice, causing the microwave absorption of this material to be quite low compared with liquid water.

The relative significance of clouds at different temperatures is illustrated further in Figure 5.3. Here, the total absorption in db is given by

$$\Gamma_t = \int_0^{\infty} a_c(z) dz.$$

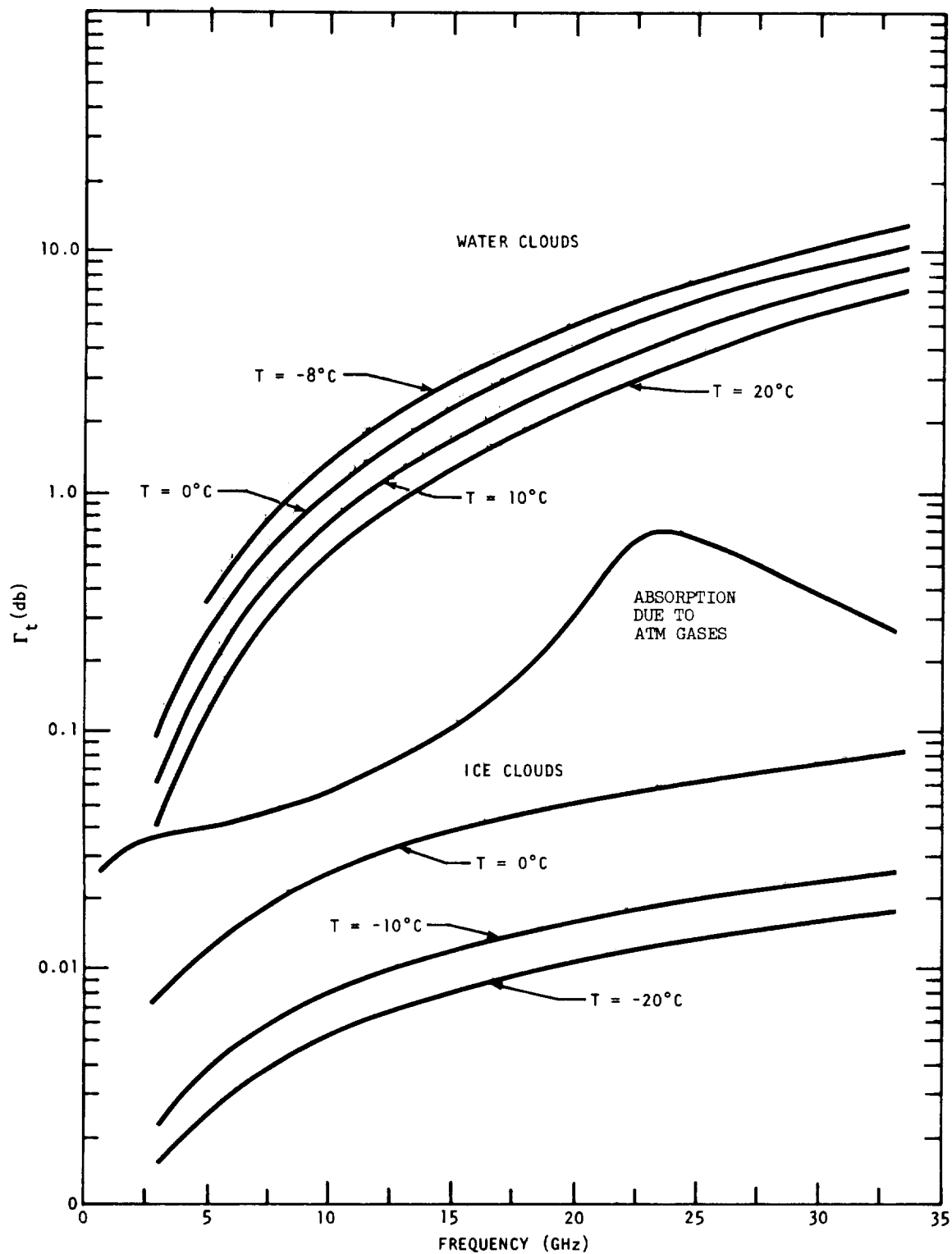


Figure 5.3 Relationship Between Integrated Absorption in db and Radiometer Frequency for Liquid and Ice Clouds With 10 gm m^{-3} (From Lhermitte, 1968)

Curves for Γ_t have been drawn based on results of Gunn and East for an integrated liquid water content of $10\text{gm m}^{-3}\text{ km}$. This is equivalent to 1cm of precipitable water, a reasonably severe shower (Lhermitte, 1968). For such a case, the influence of water clouds exceeds the influence of oxygen and water vapor, but as expected, the latter is greater than the estimated influence of ice clouds with the same condensed water content. Once the attenuation coefficient a_c is estimated, the excess temperature ΔT_{cl} , seen by the radiometer due to the presence of clouds, in turn, can be calculated.

5.3.2 Attenuation By Precipitating Hydrometeors

The estimation of the influence of precipitation elements on attenuation of microwave radiation is more difficult than for cloud particles because the hydrometeors are large enough to approach the wavelength of the incident radiation. Under such circumstances, the scattering of radiation is appreciable and must be considered with absorption. The theory commonly cited uses the Mie model for single spheres to approximate the scattering from a cloud of hydrometeors. No account is taken of multiple scattering. In the absence of any exploratory data to indicate otherwise, it is assumed that the first approximation for scattering is adequate to estimate the attenuation from precipitation.

The radiation attenuation from rain and snow have been evaluated by Gunn and East (1954) for precipitation rates of 0.1mm hr^{-1} to 100mm hr^{-1} liquid water. These calculations applied Mie's solution for single dielectric spheres and used Laws and Parson's (1948) model drop size distribution. The results of Gunn and East's calculations are listed in Table 5.2. These relations suggest that the attenuation from hydrometeors should be roughly linearly proportional to the precipitation rate. Snow fall effects are at least two orders of magnitude smaller than liquid water, so that ice in clouds should have a minimal attenuation. This is contrasted to graupel or hail, which may have a coating of super cooled liquid water. Their large scattering cross-section combined with a skin of liquid water will create appreciable scattering and attenuation in the microwave regime. Indeed, this conjecture is justified from current knowledge of intense radar returns from hail storms.

5.4 CALCULATION OF THE BRIGHTNESS TEMPERATURE OF THE EARTH'S CLOUDLESS ATMOSPHERE

The zenith brightness temperature of the terrestrial sky has been measured by many investigators and was first calculated by Hogg (1959) from the Van Vleck-Weisskopf equation for oxygen absorption.

Table 5.2. Attenuation Resulting from Precipitating Clouds in db km⁻¹ (From Gunn and East, 1954)

	T(°C)	λ = 10 cm	λ = 5.7 cm
Rain (R in mm hr ⁻¹)	18	3 × 10 ⁻⁴ R ^{1.00}	2.2 × 10 ⁻³ R ^{1.17}
Snow* (R in mm hr ⁻¹ of melted water)	0	3.5 × 10 ⁻⁷ R ^{1.6} +22.0 × 10 ⁻⁵ R	3.3 × 10 ⁻⁶ R ^{1.6} +38.5 × 10 ⁻⁵ R
	-10	3.5 × 10 ⁻⁷ R ^{1.6} +7.3 × 10 ⁻⁵ R	3.3 × 10 ⁻⁶ R ^{1.6} +12.9 × 10 ⁻⁵ R
	-20	3.5 × 10 ⁻⁷ R ^{1.6} +5.0 × 10 ⁻⁵ R	3.3 × 10 ⁻⁶ R ^{1.6} +8.8 × 10 ⁻⁵ R
*Based on Rayleigh approximations, which are not valid for wavelengths less than ~ 1.5 cm. A value of R = 10 mm hr ⁻¹ is considered the upper limit for snowfall rates.			

This calculation was repeated with our laboratory data, evaluating the contribution of O₂ to the atmospheric zenith opacity in the frequency interval of 0.1 GHz to 10 GHz for both the Gordon and Van Vleck pressure broadening theories. The computation was done for both the 1962 U.S. Standard Atmosphere and a typical high latitude winter atmosphere model which assumes a ground temperature of 245°K and a constant lapse rate of 2.5°K km⁻¹ to an isothermal stratosphere at T = 220°K (for the tropopause at 10 km). The zenith brightness temperature, T_B, is given by the usual solution to the equation for radiative transfer in the absence of scattering,

$$T_B = \int_0^\infty \left[T(z) \alpha(z) \exp \int_0^z \alpha(z') dz' \right] dz, \quad (5.10)$$

where z is the altitude, $\alpha(z) = (2\pi/\lambda) \epsilon''$ and ϵ'' is given by Equation (5.1) for the Van Vleck theory, and Equation (5.2) for the Gordon theory. The linewidths are given in Equations (5.4) and (5.5), respectively.

The integral of Equation (5.10) was evaluated numerically, with the results shown in Figure 5.4 for the two pressure-broadening theories and the standard atmosphere. The calculations for the winter atmosphere give results which are only about 0.2°K higher in the 2-10 GHz region. This result indicates that, as a first approximation, even the diurnal changes in the atmospheric profile can reasonably be neglected in the determination of the sky brightness temperature and consequently a mean value can be used in the calculations which should be adequate for all atmospheric conditions. The zenith brightness temperature predicted by Gordon's semi-classical theory falls slightly below the Van Vleck-Weisskopf prediction in each case in the region where the microwave background measurements have been made. At around 2 GHz where the discrepancy is largest between the two theories, Gordon's theory gives a zenith brightness temperature which is 0.3°K less than the Van Vleck-Weisskopf theory. It can be concluded, therefore, that with the experimentally determined linewidth parameters, there is a small, but significant difference between the two theories in deducing the sky brightness temperature or the atmospheric attenuation below 10 GHz.

The measurements of zenith sky brightness temperatures as reported by Howell and Shakeshaft (1967), and Medd and Fort (1966) are shown in Figure 5.4. At decimeter wavelengths many of the measured temperatures appear to be abnormally high. These measurements cannot be understood on the basis of any of the current theories of pressure broadening, nor are they consistent with the results of the present investigation. As it is unlikely that an unknown source of absorption exists in the atmosphere near 1 GHz, and in view of the surprisingly good agreement between the calculated value and the rest of the direct observational data, it is concluded that the measurements that give 4°K are probably in error, and the value of 2.3°K ± 0.5°K for the zenith brightness temperature of the terrestrial sky at 3 GHz is tentatively adopted.

5.5 CORRECTION TO THE RADIOMETER MEASUREMENTS

The apparent temperature, T_R , ideally measured by the radiometer at an altitude h above the surface of the ocean whose temperature is at T_S , may be calculated from the solution of the equation of radiative transfer. The accounting for the absorbed radiation is shown schematically in Figure 5.5. Using the Rayleigh-Jeans approximation to express the radiation intensity as a temperature, we find,

$$T_R = r \left[T_c e^{-\int_0^\infty a(z) dz} + \int_0^\infty T(z) e^{-\int_0^z a(z) dz} a(z) dz \right] e^{-\int_0^h a(z) dz} + (1-r) T_S e^{-\int_0^h a(z) dz} + \int_0^h T(z) e^{-\int_0^z a(z) dz} a(z) dz, \quad (5.11)$$

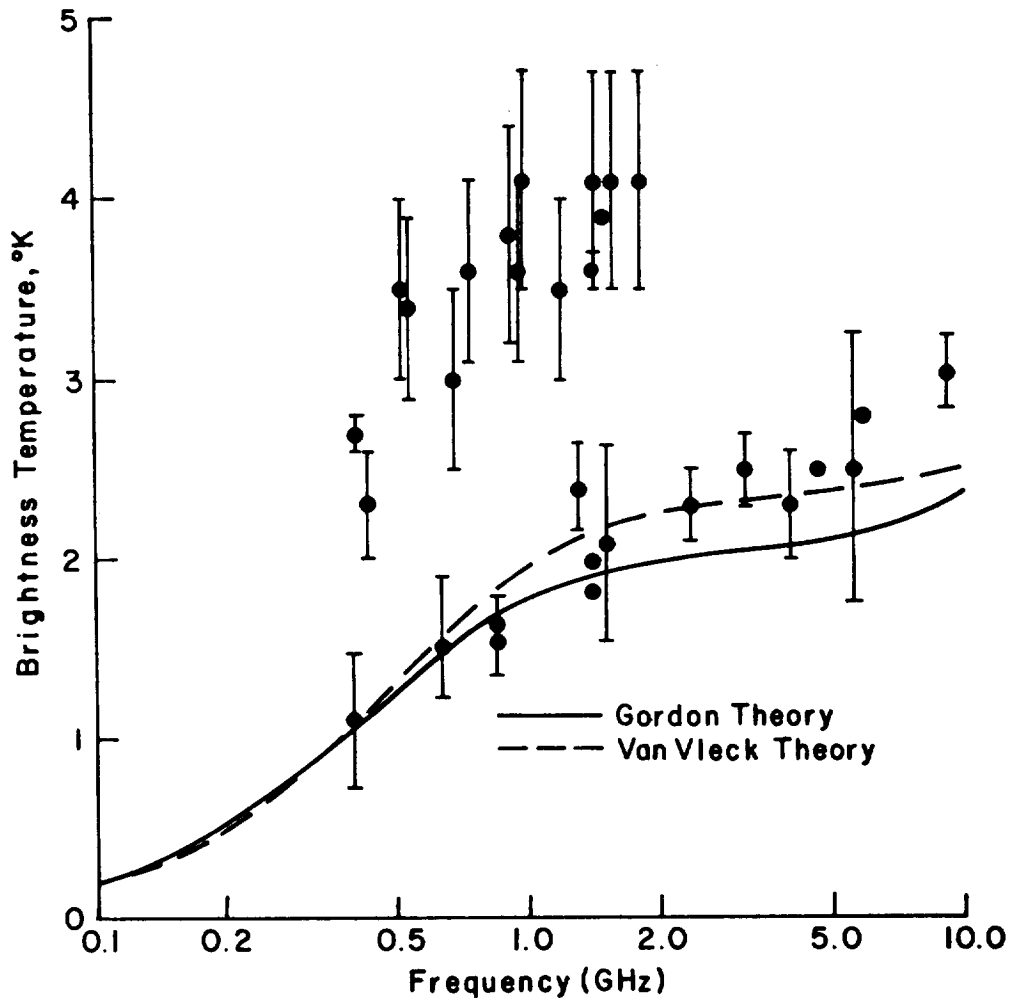


Figure 5.4. Zenith Brightness Temperature of the Earth's Atmosphere Due to Oxygen Absorption as a Function of Frequency (from Ho, 1969)

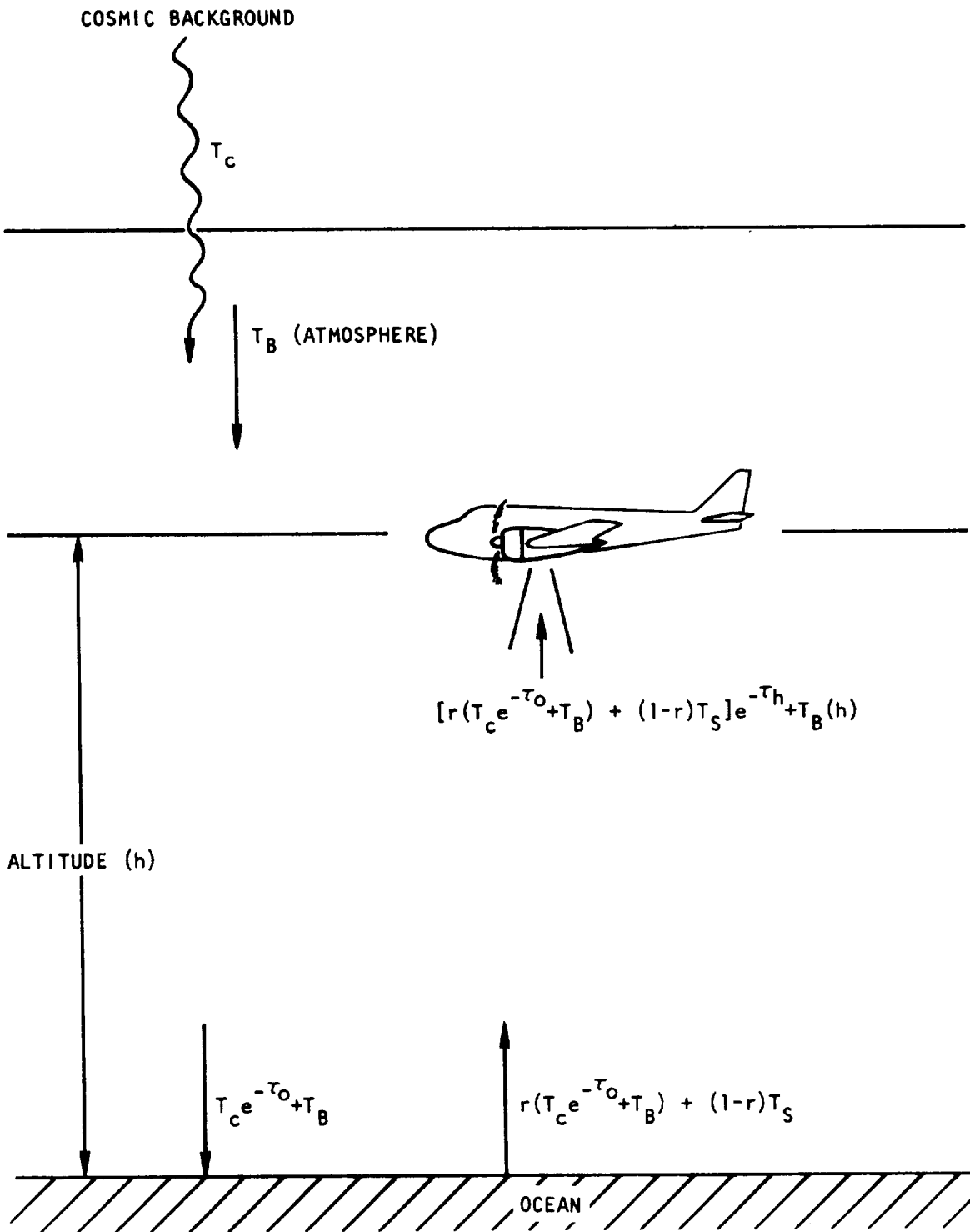


Figure 5.5 Sketch of Terms in Radiometer Equation

where T_c is the temperature of the cosmic background, r is the reflectivity of the ocean surface, and $T(z)$ and $\alpha(z)$ are respectively the variation of the atmospheric temperature and absorption coefficient with altitude z .

This expression may be generalized to all viewing angles θ , but for simplicity, we shall illustrate the results only for the case of normal incidence.

The first term is the downward radiation of the radio noise background and sky emission reflected by the ocean surface into the radiometer which is in turn attenuated by the intervening atmospheric path-length from the ocean surface up to the radiometer. The second term is the emission from the ocean surface and the third term is the upward emission of the atmosphere between the ocean surface and the radiometer.

The radio noise background consists of ionospheric radio emission, galactic noise and emission from strong radio sources, and the thermal component of the cosmic background. For frequencies in the 3 GHz region, the ionospheric emission is less than 0.01°K and, therefore, quite negligible. The average radio noise in the galactic plane is only about 0.3°K , as indicated by the Reference Data for Radio Engineers (1968). Therefore, if we avoid the cases where the galactic center and strong radio sources come into view of the radiometer, we can use an average background value of 0.3°K .

The thermal component of the cosmic noise (believed to have been emitted by the primeval fireball) is, to a very good approximation, isotropic and has a value of 2.7°K . These observations have been summarized in detail by Shakeshaft and Webster (1968) and Boynton et al. (1968). Therefore, T_c can be taken to be approximately $3.0 \pm 0.5^\circ\text{K}$. In this approach, we have excluded the influence of reflected radiation from the sun (sun glitter). In the case of a smooth surface, the sun will be viewed by a satellite radiometer only at the angle of specular reflection from the surface. For a radiometer looking straight down, this effect, though significant, can occur only at very limited, regular times that are readily accountable during the passage of the satellite. Thus, for the smooth ocean, the interference from reflected solar radiation can easily be corrected for. For a rough sea, however, the sun glitter problem can be more serious, as discussed in Section 6.

Based on the Van Vleck model, the atmospheric opacity has been calculated for the 1962 U.S. Standard Atmosphere and is indicated over the range 2.65-4.2 GHz in Figure 5.6. Over this frequency range, the opacity of the dry atmosphere is approximately the same, with slightly higher values at the higher frequencies. Because the bulk of the mass of oxygen in the atmosphere is contained below 10 km, the greatest contribution to the attenuation of microwave radiation lies below this altitude.

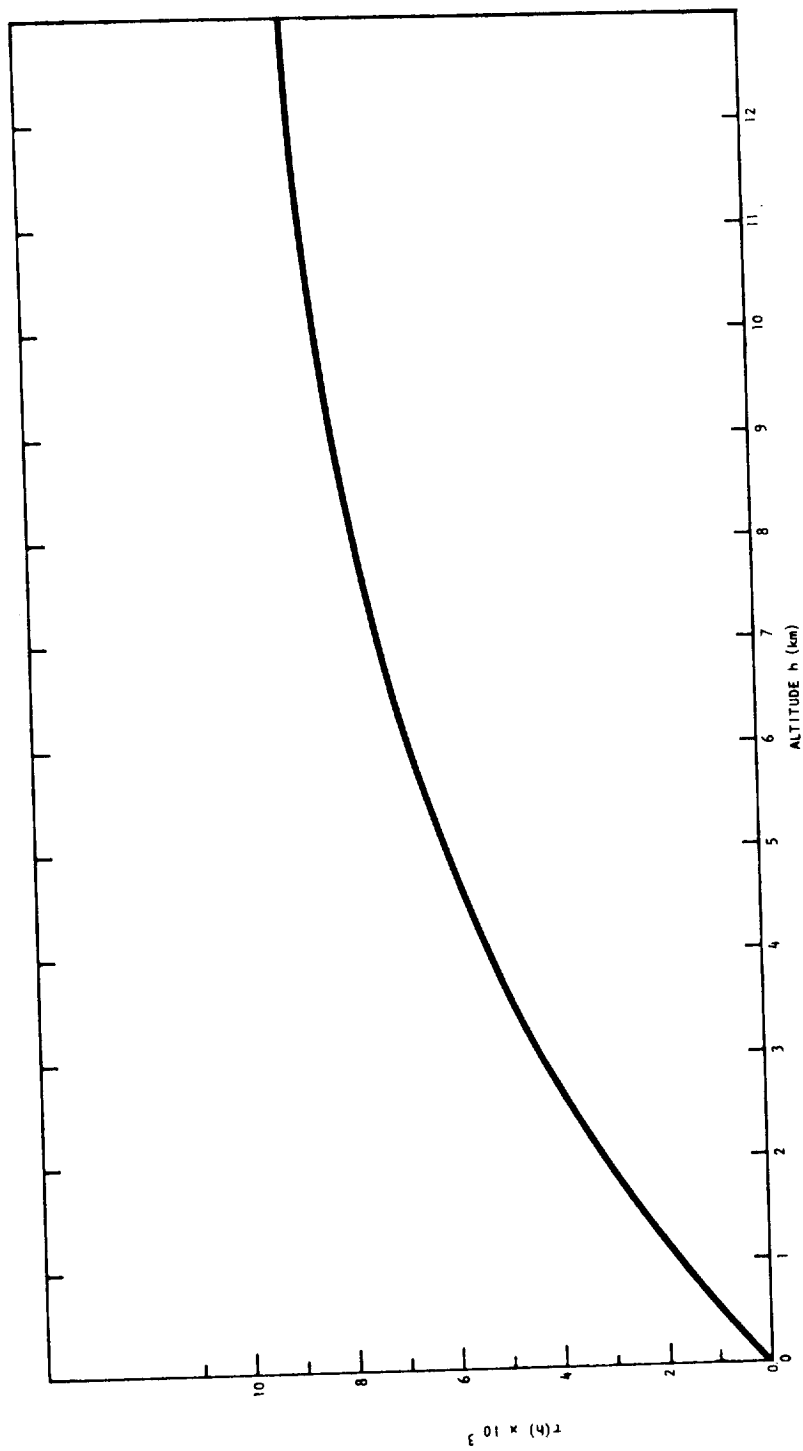


Figure 5.6. Downward Atmospheric Opacity as a Function of Altitude for the Frequency of 2.65 GHz.

The brightness temperature, T_R , "seen" by an ideal airborne radiometer may be calculated using the opacities in Figure 5.6. Such a calculation is illustrated in Figure 5.7 for a reflectivity of 0.65 and a sea surface temperature of 280°K. Over the frequency range 2.65-4.2 GHz there is little difference in the expected atmospheric effect without clouds.

To apply the calculated opacities in Figure 5.6 as a correction to the apparent temperature ideally measured by an airborne radiometer, Equation (5.11) may be approximated by,

$$T_R \cong T_B(h) + r \left[T_c(1-\tau_o) + T_B \right] (1-\tau_h) + (1-r)T_s(1-\tau_h) \quad (5.12)$$

where τ_o is the total one-way opacity of the atmosphere, τ_h is the opacity from ground to an altitude h , T_B is the total downward atmospheric emission, and $T_B(h)$ is the atmospheric emission for altitude from ground to height h .

$$T_R \cong \Delta T_R(h) + (1-r)T_s, \quad (5.13)$$

where the correction factor $\Delta T_B = T_R(h) + r [T_c(1-\tau_o) + T_B] (1-\tau_h) - \tau_h(1-r)T_s$. Assuming that $(1-r) \cong 0.35$, and $T_x = 280^\circ\text{K}$, ΔT_R has been evaluated from the opacity data. Values of ΔT_R are plotted as a function of altitude at four frequencies in Figure 5.8. For the case of an observation from a satellite, $h \rightarrow \infty$ and the apparent temperature is simply given by,

$$T_R = r \left[T_c e^{-\tau_o} + T_B \right] e^{-\tau_o} + (1-r)T_s e^{-\tau_o} + T_B, \quad (5.14)$$

where $\tau_o = \int_0^\infty \alpha(z)dz$, the total one-way opacity through the atmosphere. T_B is that given by equation (5.10). For $h \rightarrow \infty$, T_B is calculated to be 2.41°K for 2.60 GHz, based on the 1959 standard atmosphere.

In the other extreme case of an observation from a low flying aircraft, where the altitude h is of the order of a kilometer,

$$T_R = r \left[T_c(1-\tau_o) + T_B \right] (1-\tau_1) + (1-r)T_s(1-\tau_1) + \bar{T}(\tau_1), \quad (5.15)$$

where $\tau_1 = \int_0^h \alpha(z)dz$, and the last integral is approximated by assuming that $T(z)$ is a slowly-varying function of z and hence can be replaced by an average value \bar{T} and be treated as a constant in the integration.

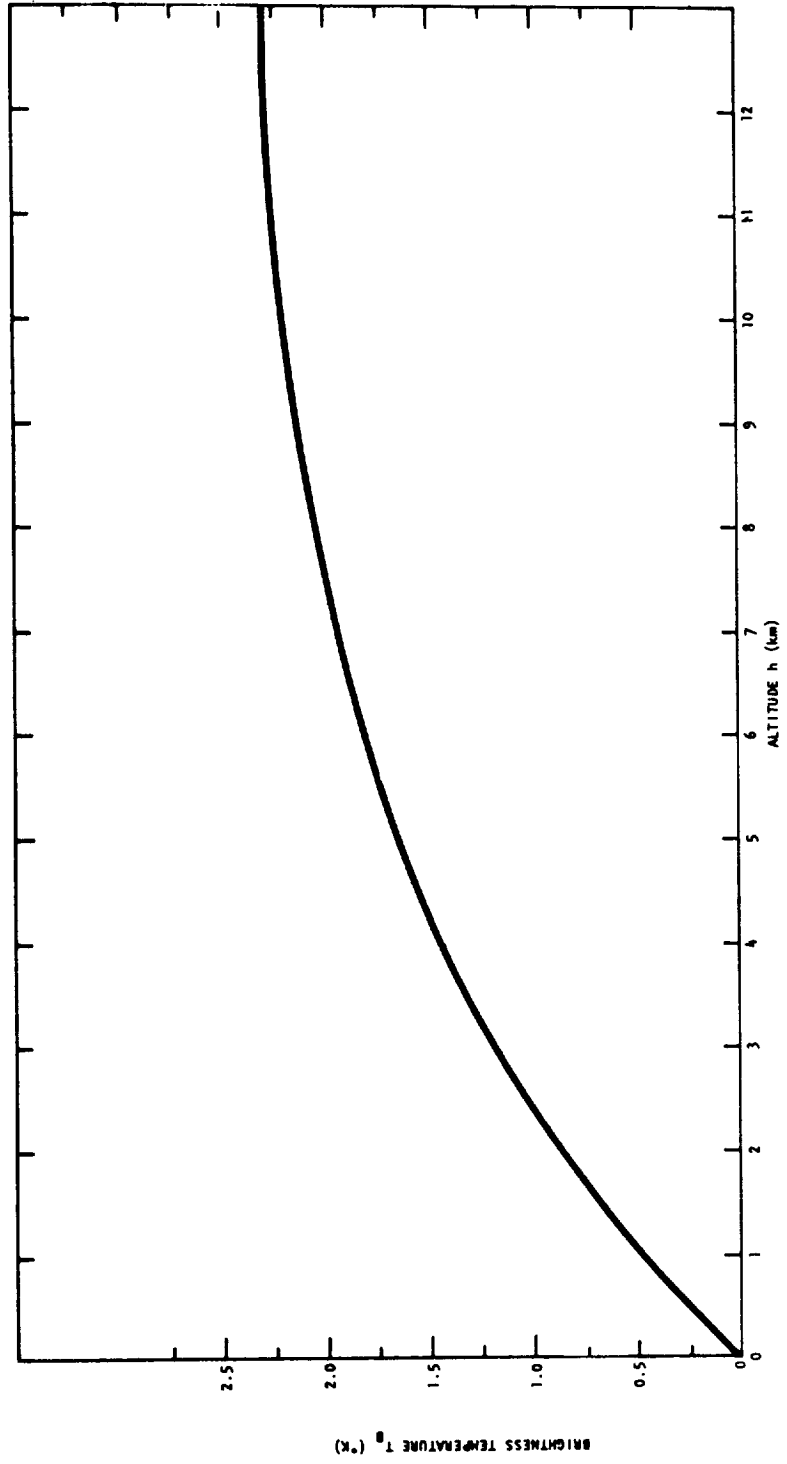


Figure 5.7. Emission of a Layer of Air Between the Ground and Altitude h at the Frequency of 2.65 GHz

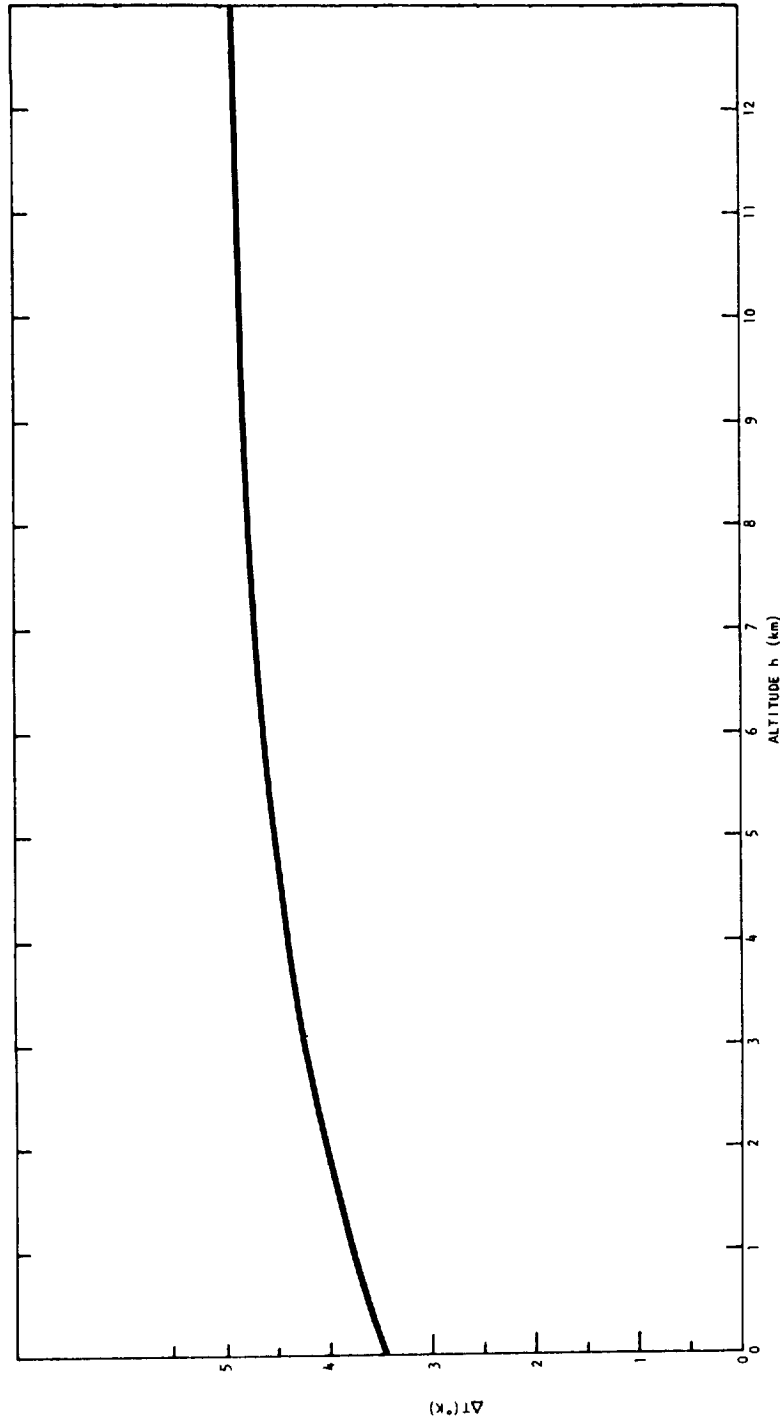


Figure 5.8. Correction in Apparent Temperature Seen by an Airborne Radiometer as Calculated for $r = 0.65$, $T_s = 280^{\circ}\text{K}$, $T_c = 3.0^{\circ}\text{K}$ at the Frequency of 2.65 GHz

For τ_1 very small ($\approx 2 \times 10^{-3}$), corresponding to a height about 1 km, the expression can be further approximated by, assuming $rT_s \approx \bar{T}$,

$$T_R = r \left[T_c (1 - \tau_o) + T_B \right] + (1-r)T_S + rT_S \tau_1, \quad (5.16)$$

where the first two terms are just the radiometric temperature at the surface of the ocean ($h=0$) and the last correction term is small, of the order of 0.2°K . Therefore,

$$T_R \cong 5.4r + (1-r)T_S, \quad h \rightarrow 0, \quad \text{at } 2.69 \text{ GHz} \quad (5.17)$$

based on the Van Vleck Model.

When cloud layers are present in the atmosphere, a further correction has to be made for the attenuation by hydrometeors. Knowing a_c , such an estimate of the contribution of clouds to the brightness temperature can be made using the information in Section 5.3.

An approximate expression for the added temperature increment in radiometer temperature for a vertically downward looking radiometer is:

$$\Delta T_{cl} \approx \bar{T}(1+r)(a_c L) - (1-r)T_s(a_c L), \quad (5.18)$$

where \bar{T} is the average temperature between the bottom and top of the cloud, and L is the thickness of the cloud.

5.6 EXPERIMENTAL VERIFICATION OF THE THEORY

Even though the atmospheric effects are estimated to be small, they must be known quantitatively to interpret radiometer observations of the oceans. This part of the NASA sponsored program was to use available opportunities to experimentally test the theoretical conclusions concerning the magnitude of the correction due to sky emission expected from both a clear and a cloudy atmosphere.

5.6.1 Measurements in a Cloudless Atmosphere

Two different classes of experiments were attempted to measure the attenuation of 10 cm wavelength radiation in a cloudless atmosphere. These were: (1) ground based observations of the variation in apparent sky temperature as a function of viewing angle measured from the zenith, and

(2) airborne measurements of the apparent temperature of the sea as a function of altitude. These two programs were sponsored primarily by NR independent research and development (IR&D) funds, but their results bear on this study contract and will be described briefly here.

Ground Based Observations of Sky Temperature. The overall attenuation of extraterrestrial radiation and reflected radiation from the Earth's surface can be measured by measuring the relative change in sky brightness temperature as a function of zenith angle with a precision radiometer. The sky brightness temperature should increase with approximate proportionality to the secant of the zenith angle. By fitting the experimentally determined variation in sky temperature with zenith angle to a family of theoretical curves for an assumed sky temperature taking into consideration the horn pattern of the radiometer, it should be possible to deduce the most likely value of the atmospheric absorption.

Equipment and Observations. Observations were made in the early mornings and late at night during the Spring of 1970 on the roof of the NR Science Center. The time of the day during which the data was taken and the location of the experimental equipment were chosen to minimize spurious effects introduced through the side lobes of the antenna pattern. Strong microwave sources such as the sun and the galactic center were either not in view or low enough in the horizon so that the contribution to the apparent temperature of the sky was expected to be small. The southwest corner of the laboratory roof was chosen to minimize the influence of hilly terrain to the north and east of the building. The distant hills on the west side of the Science Center were less than 5° above the horizon.

Two antennas were used with the radiometer. The Potter horn, with half power point beam width (HPBW) of 16° was the rotatable antenna. A diagonal horn with HPBW of 18° was used as a reference load. The diagonal horn was pointed at an angle of about 25° from the zenith to minimize any coupling between the two antennas. It was connected to the reference arm of the radiometer (see Figure 5.9). Thus, the rotatable Potter horn was on one side of the circulator and the fixed diagonal horn was on the other. The Prototype I radiometer has been described in detail by Hidy et al. (1969). It consists of a ferrite circulator switching between the two horns, followed by a tunnel diode amplifier, an 80 MHz filter centered at 2.66 GHz, a square law detector and an audio amplifier with an automatic gain control system. Calibration of the radiometer was carried out before and after each set of observations using cryogenically cooled coaxial terminations (See Hidy, et al., 1969). All of the microwave components were interconnected with precision, rigid, 14 mm coaxial transmission lines. The radiometer was in turn coupled to the antennas through coaxial-to-waveguide transition sections.

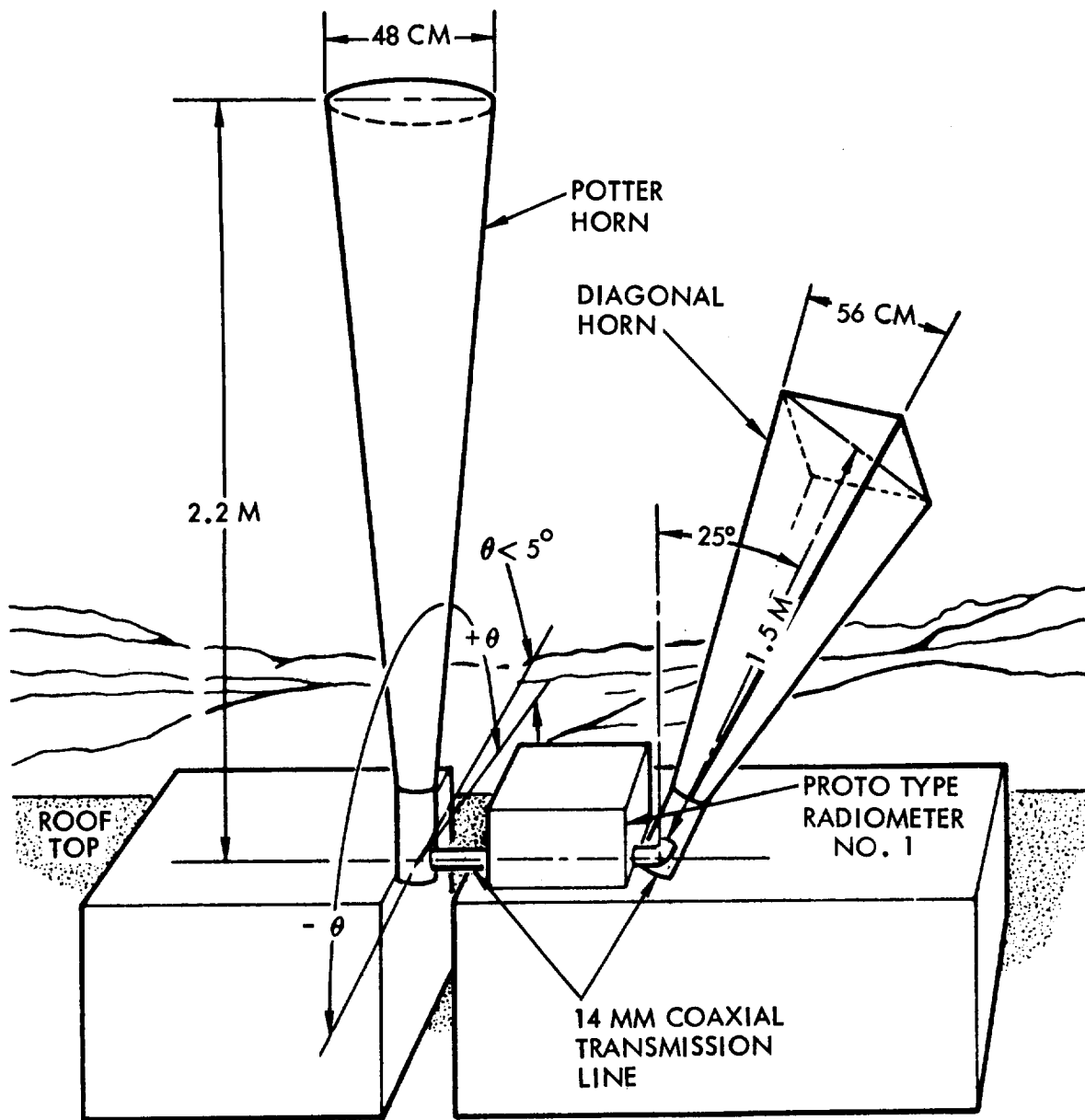


Figure 5.9 Sketch of the Science Center Rooftop Experiment to Observe The Sky Temperature as a Function of Viewing Angle, θ .

These precision coaxial lines required exacting tolerances and were the main source of the experimental problems. Two coaxial lines were butt jointed together by the pressure exerted through the action of the coupling nut on the gear ring. Therefore, the coaxial transmission lines had to be very well aligned or the outer conductors of the rigid lines would not touch at all points around the circumference, resulting in higher losses.

In the course of the experiment, the coaxial connector from the Potter horn to the input arm of the radiometer suffered much abuse from constant stress and usage. When the Potter horn changed position, or a calibration was performed the connector was disconnected and reconnected again. Whenever the antenna was moved, a slight misalignment was introduced requiring more pressure to be exerted on the coupling nut in order to force the mating of the outer conductors. The transmission characteristics and the reliability of the connectors were degraded as a result. Consequently, during a set of observations, readings for each angular position were repeated to ensure consistency. In general, the data were reproducible over several rotations of the Potter horn in an east-west arc to $\pm 0.5^\circ \text{K}$.

Interpretation of the Data. The observations of sky temperature obtained with the Potter horn are plotted in Figure 5.10. For comparison, two theoretical curves taking into account the finite beam width of the antenna are also given. The lower (dashed) curve was obtained using a Gaussian approximation to the pattern, while the upper (solid) curve was obtained by numerical integration on the measured horn pattern, shown in Figure 5.11.

The measured sky temperature represents an average over the horn pattern of the actual temperature $T_B(\theta)$, which for a horizontally stratified atmosphere is given to a high degree of accuracy by

$$T_B(\theta) = \int_0^\infty \frac{dz \alpha(z) T(z)}{\cos \theta'(z)} \exp \left[- \int_0^z \frac{dz' \alpha(z')}{\cos \theta'(z')} \right] + T_c \exp \left[- \int_0^\infty \frac{dz \alpha(z)}{\cos \theta'(z)} \right] \quad (5.19)$$

where θ is the zenith angle, α is the atmospheric absorption coefficient at altitude z , T is the temperature at z , T_c is the equivalent temperature of

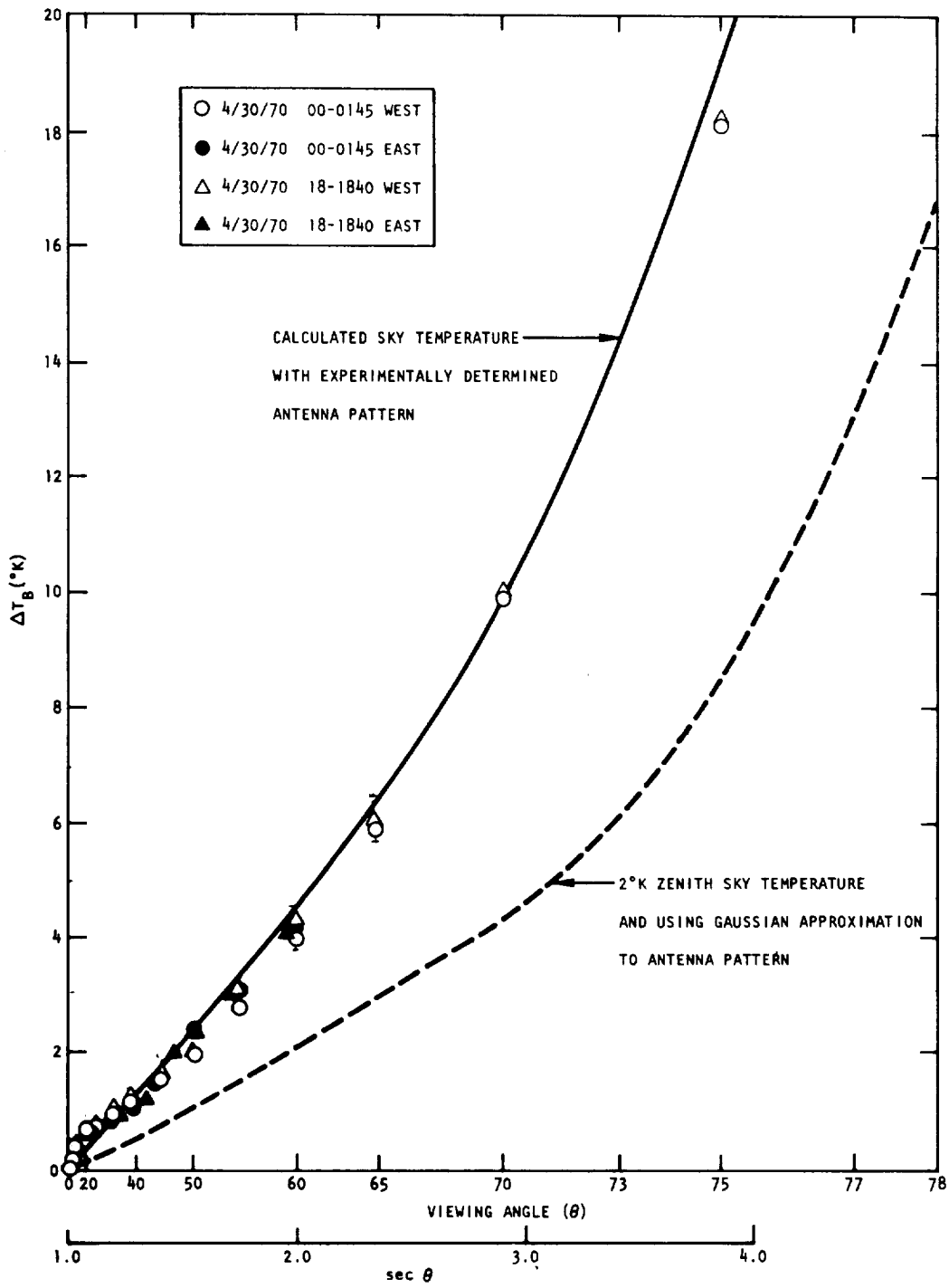


Figure 5.10 Sky Temperature as a Function of Viewing Angle

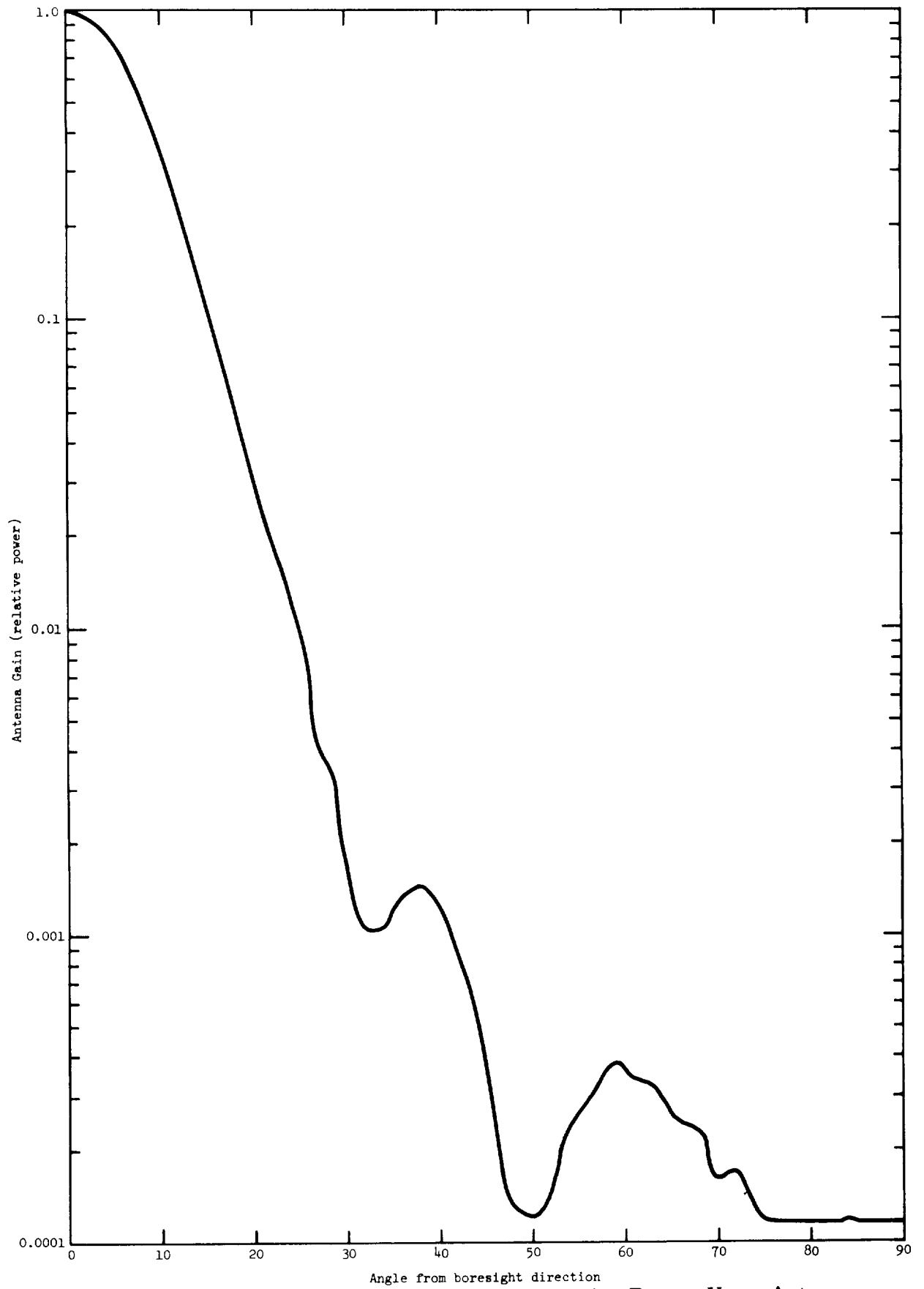


Figure 5.11 Experimentally Measured Pattern for Potter Horn Antenna

the average cosmic and galactic microwave radiation incident on the atmosphere, and $\cos \theta'(z)$ is given by

$$\cos \theta'(z) = \left\{ 1 - \frac{\sin^2 \theta}{\left(1 + \frac{z}{R}\right)^2} \right\}^{1/2} \quad (5.20)$$

where R is the radius of the Earth.

Assuming azimuthal symmetry for the horn pattern, the observed sky temperature can be written as

$$T_H(\theta) = \int_0^{2\pi} d\phi \int_0^\pi d\theta' T_B(\theta') G(\cos \gamma(\theta, \theta', \phi)) \quad , \quad (5.21)$$

where G is the normalized antenna gain and γ is the angle between the horn axis and the direction specified by θ' and ϕ :

$$\cos \gamma = \cos \theta \cos \theta' + \cos \phi \sin \theta \sin \theta' \quad . \quad (5.22)$$

For directions (θ', ϕ) intersecting the ground, T_B is taken to be in the Earth temperature, 300°K , since the ground emissivity at S-band is very close to unity.

The upper theoretical curve of Figure 5.10 was generated using the U.S. 1962 Standard Atmosphere for the atmospheric profile and the parameters of the Van Vleck-Weisskopf line shape theory deduced from laboratory measurement, given by equation (5.4). The lower curve was generated using a much cruder model for $T_B(\theta)$, where it was assumed that $T_B(\theta) = 2 \sec \theta$ in degrees Kelvin for $\theta \leq \frac{\pi}{2} - 0.02$. It is likely that the large difference between this curve and the upper one is due to the contribution of antenna sidelobes. The Gaussian approximation is clearly inadequate for this application.

Conclusions. As can be seen from Figure 5.10, there is very good agreement between the measured brightness temperature and the upper theoretical curve. This indicates that the lower measured value for the zenith sky temperature presented in Figure 5.4, which is implicit in the theoretical calculation, is the correct value for the sky contribution.

5.6.2 Aircraft Measurements

During the Winter of 1971 an experimental program utilizing the Convair 990 of the NASA Airborne Science Office at Ames Research Center, the NR Prototype II Radiometer was flown. Details of this program, the new instrument, and the observational results are described elsewhere and are not repeated here. In summary, however, it should be mentioned that the instrument flown was a prototype of the instrument described in Section 8. It was operated at 2690 ± 10 MHz. The instrument as mounted in the Convair 990 was capable of measuring the antenna temperature to a precision of $\pm 0.1^\circ\text{K}$; the achieved absolute accuracy of the observations based on the twenty-four stability of the radiometer was approximately $\pm 0.5^\circ\text{K}$.

On two occasions, flights were made over the Pacific Ocean such that the apparent temperature of the sea was measured over the same area of water from a few hundred meters altitude to more than 11 km altitude. From such data, the atmospheric attenuation at 2.69 GHz could be deduced and compared with the theoretical predictions. The relative temperature differences from the surface to approximately eleven kilometers obtained from the aircraft data are shown in Figure 5.12. These results are considered preliminary in nature at this time because the complete tape recordings are not yet available from the flight program. However, the observations agree within the experimental errors, with the theoretical variation as a function of altitude calculated for the Van Vleck model oxygen line shape, and the 1962 U.S. Standard Atmosphere. It is assumed in this calculation that the surface temperature was 280°K , and the reflectivity was 0.650.

Close to the water surface, below ~ 0.5 km, the reflection of energy from the aircraft was detectable in the 2.69 GHz radiometers, as well as the other radiometers on board the aircraft. This can be seen readily as a sharp increase in ΔT near the sea surface.

The error bands shown in Figure 5.12 include the inherent instrument error plus the uncertainty of readings over a weakly roughened sea. The error bands were estimated directly from the instrument recordings. The reason why one set of errors is larger than the other is related to the fact that more radar interference was experienced in Run No. 5.

There is a possible positive deviation in the data of about 0.2°K at the high altitude, based on the "best fit" indicated in Figure 5.12. However, these points at high altitude were taken in the presence of scattered clouds, so that a small positive correction may be required from this interference.

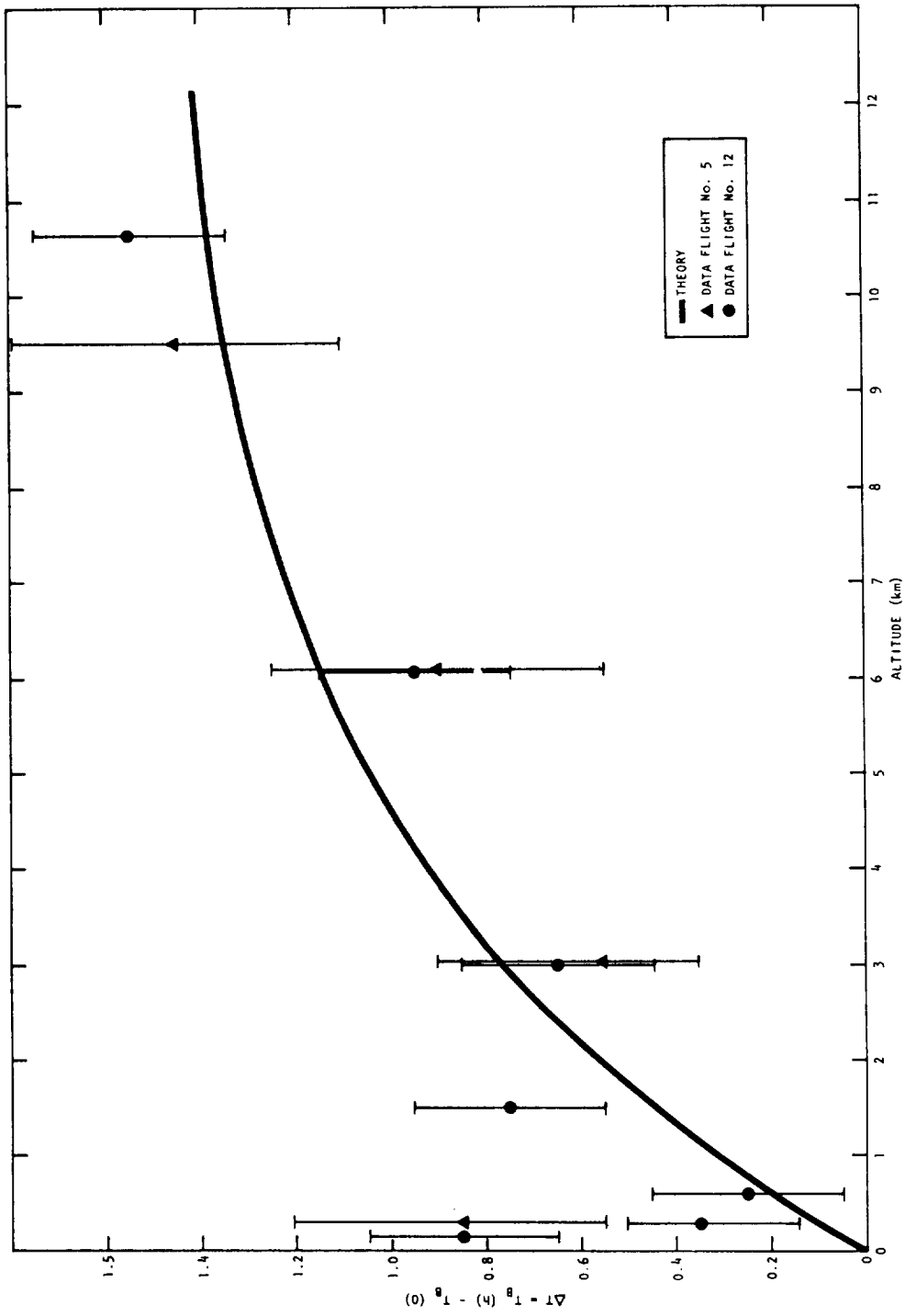


Figure 5.12 Comparison Between Van Vleck Model and Changes in Brightness Temperature of the Sea From the 1971 Convair 990 Flights

5.6.3 Observations of Attenuation by Clouds

During the course of the NR atmospheric observation program, it was hoped that opportunities would arise to detect the attenuation of microwave radiation by clouds under a variety of conditions. Unfortunately neither the ground based operations nor the aircraft flights provided more than limited results on this question.

The early flights using the NR Prototype I radiometer in the late fall of 1969 showed only a weak attenuation associated with thin stratoform clouds. The maximum effect based on these observations was $\leq 1^\circ\text{K}$ for clouds with rain ≤ 1 km thick.

During the tests on the NR Science Center roof, very few opportunities were afforded to detect the effect of clouds because of the nature of the Southern California weather. However, a few observations of stratoform cloud layers were obtained with the 2.65 GHz radiometer, and a prototype 19.35 GHz radiometer described by McLeod (1969). The results of these data are indicated in Figure 5.2. As expected the higher frequency instrument displayed a stronger influence of thin clouds than the S-Band system.

Although many cloud conditions were overflowed during the Convair 990 flights, the data in its present form are difficult to interpret as unique indications of cloud effects since the nature of the surface under the cloud layers was generally poorly known, and the average cloud temperature and thickness are uncertain.

Data from the flights have been examined and an attempt was made to estimate the maximum attenuation of clouds of varying thickness from samples of the observations. The cloud thickness is estimated from infrared cloud top temperature data and an assumed cloud base of ~ 1 km. The mean cloud temperature is taken as the average expected from the U.S. Standard Atmosphere for the mid-point in cloud thickness. These data are listed for the various observational conditions in Table 5.3 and are considered to be the maximum absorption expected. Unfortunately, these results must remain somewhat ambiguous because no information was available on the nature of the condensed phase, or the liquid water content in these clouds.

A very crude preliminary comparison of the cloud data from the DC-3 and Convair 990 flight programs can be made with the aid of Equation (5.18). The data are plotted as

$$\frac{(\Delta T_{cl})_{\text{meas}}}{K} = \frac{(\Delta T_{cl})_{\text{meas}}}{T_{\text{estimated}} - \left[(1-r)T_s \right]_{\text{meas}}} \text{ vs. } L,$$

and are shown in Figure 5.13. Shown with the data is a line with a slope

$$\alpha_c = 10^{-3} \text{ db km}^{-1},$$

corresponding to the absorption coefficient expected for a cloud of uniform liquid water content, 1 gm m^{-3} . Roughly speaking, the effect of the clouds appears to be consistent with this value of α_c , except for precipitating systems. These latter cases give higher values of α_c , as expected. The best cloud observations available to us were those over weathership PAPA in the C/V 990 flight 12. Here the maximum attenuation associated with the double cloud layer $\sim 6 \text{ km}$ thick is $\sim 2^\circ\text{K}$, if roughness contributed $\sim 1^\circ\text{K}$. This is approximately equal to the theoretical model for $M = 1 \text{ gm m}^{-3}$ and is consistent with other data recorded in Table 5.3.

It is surprising in view of the assumptions made in Figure 5.13 and in interpretation of the aircraft observations that any correlation at all could be derived.

In view of the fact that climatologically at least 50 percent of the globe is covered with clouds, and many areas over the oceans are frequently under nearly permanent cloud cover, it is important to assess in detail the effect of this potential interference to the application of microwave radiometer considered here. This conclusion was made sometime ago and is reinforced by the exploratory observations derived from the current study. In future efforts it will be vital to carry out a more extensive quantitative investigation of the attenuation of 10 cm electromagnetic radiation through rain clouds. To test the applicability of available theory, clouds of a variety of thicknesses must be examined, and these clouds will have to be characterized by direct aircraft sampling of their liquid water content as a function of space, as well as their thickness in the direction of the radiometer beam.

A study of the influence of clouds on radiometry is a difficult and expensive area to undertake because of the need for aircraft support and the requirement of special kinds of weather. It is likely that such a program should be coordinated with meteorological and cloud physics studies. One interesting "side" application of the S-Band radiometer, for example, should be explored further—the remote measurement of liquid water content in clouds. Such studies have been suggested by Lhermitte (1968) and have been reported for 10.7 GHz system by Decker and Dutton (1970).

Table 5.3 Preliminary Evaluation of Attenuation at 2.7 GHz From Clouds Observed on the 1971 NASA Convair 990 Flights, Ground Data, and 1969 DC-3 Flights

Flight No.	Date	$\Delta T_{\text{meas}} (^{\circ}\text{K})$	L (km)	T	$(1-r)T_s (^{\circ}\text{K})$	$\frac{\Delta T_{\text{LO}}^3}{[T(1+r) - (1-r)T_g]}$	Remarks
C/V 12	3/17/71	0.7	1.0	276	104	1.99	Over WeatherShip PAPA; two layers of clouds-alto and strato cu. Assume PAPA T _S - stratus and alto cum layers. Rain cell or roughness - over storm front. Broken stratus.
		2.0	6.1	253	103	6.36	
		2.4	6.9	250	103	7.75	
		3.3	6.8	250	107	10.8	
		1.0	1.0	278	106	2.83	
C/V 8	3/11/71	0.1	0.3	278	108	0.29	Roughness, light broken stratus. Thick stratus layer, roughness (?). Scattered cu. Rough sea, altitude profile thru broken stratus. Stratus - cumulus.
		2.0	6.0	261	107	6.18	
		1.0	1.7	270	111	2.99	
		1.0	1.0	270	110	2.98	
		1.7	5.0	260	109	5.31	
DC-3	10/29/69	1.5	0.6	278	107	4.26	Rain (?) - stratus. Stratus.
	11/5/69	0.1	0.3	280	106	0.28	
Grounds (SC Roof)	Spring 1970	0.1	0.6	280	7	-	Looking upwards, strato cumulus.

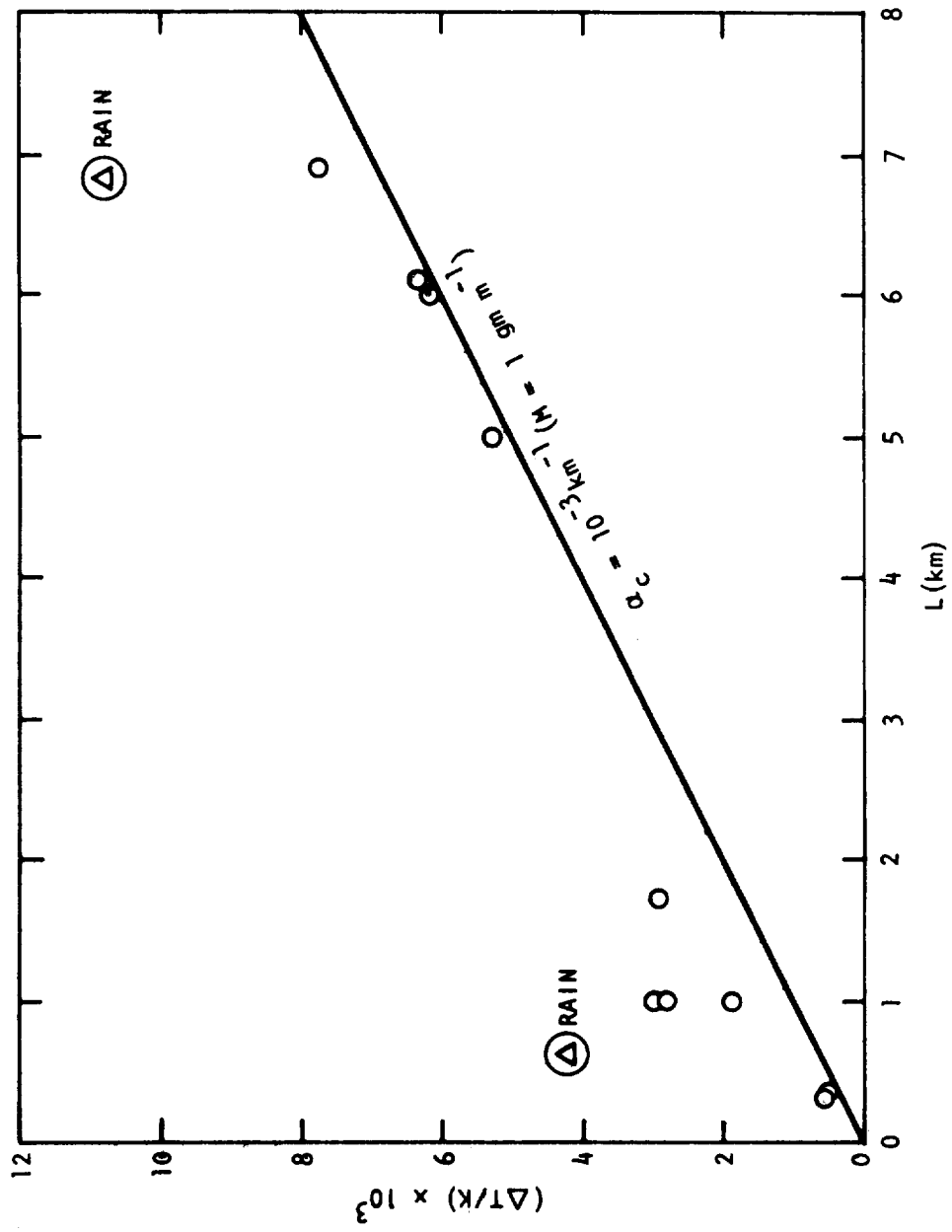


Figure 5.13. Effect of Clouds on the Apparent Temperature of the Sea

5.7 SUMMARY OF ATMOSPHERIC EFFECTS AND THE SATELLITE INSTRUMENT

Review of the results obtained on the influence of the sky background and atmospheric attenuation reveal that the state of knowledge in this area is not entirely satisfactory for achieving the desired absolute accuracies of sea temperature measurement by a satellite borne microwave radiometer. The various phenomena and their problem areas are summarized in Table 5.4.

Table 5.4. Summary of Effects on Radiometric Observation of Sea Temperature Associated With Sky Background and Atmospheric Attenuation at 2.69 GHz

Phenomenon	Correction	Comment
1. Cosmic Radiation Background (average galactic noise + isotropic residual)	$3.0 \pm 0.3^{\circ}\text{K}$	Does not include strong radio sources near the galactic center
2. Atmospheric contribution to Sky Temperature by Oxygen	$2.4^{\circ}\text{K} \pm 0.3^{\circ}\text{K}$	Taken as consistent with Van-Vleck model and the U.S. Standard Atmosphere
3. Atmospheric Contribution to Sky Temperature by water vapor	$\leq 0.2^{\circ}\text{K}$	Depends on water vapor present in viewing path but is correctible to first order.
4. Non Precipitating Clouds	$\leq 1^{\circ}\text{K}$ up to 2 km thickness	Varies substantially with liquid water content, and is uncertain at present.
5. Precipitation	Highly Variable	Ice and snow much smaller effect than liquid water

For a clear atmosphere, the total sky temperature contribution is considered to be known at present. Experimental evidence indicates that the atmospheric contribution to the sky temperature is predictable to $\pm 0.5^{\circ}\text{K}$ with knowledge of the cosmic background and oxygen absorption in the atmosphere based on the Van Vleck model.

From our survey, it is felt that the influences of the cosmic background and oxygen absorption are well enough specified and understood to be predictable for the current radiometer application.

In any case, the cosmic background will in time be measured and accounted for to an accuracy beyond requirements for our oceanographic applications. The attenuation due to the clear atmosphere will be essentially a constant because of its dominance by oxygen. It can be calculated to sufficient accuracy to be satisfactory from current model atmospheres.

Perhaps the most uncertain effect of the atmosphere for the projected oceanographic application of the microwave radiometer is that of rain clouds. Currently it is difficult to account quantitatively for this interference. No simple way appears to be under development to estimate a correction factor for clouds with accuracies comparable to corrections expected for other effects. Ultimately it may be necessary to include imaging capability in a satellite instrument system. At least a multifrequency microwave radiometer may be required. Systems operating at 3 to 19 GHz may offer the optimum prospects for supplying enough simultaneous data to resolve the ambiguities associated with clouds and a rough surface (see also the next section). In any case, considerable emphasis should now be placed on more quantitative study of cloud attenuation of radiation at S-Band frequencies.

REFERENCES

Becker, G. E. and S. H. Autles, 1946, Water Vapor Absorption of Electromagnetic Radiation in the Centimeter Wavelength Range. *Phys. Rev.*, 70, 300-307.

Boynton, P. E., R. A. Stokes, and D. T. Wilkinson, 1968, "Primeval Fireball at $\lambda = 3.3$ mm," *Phys. Rev. Letters* 21, 462.

Cummings, C. A. and J. W. Hull, 1966, Microwave Radiometric Meteor Observations, Proc. 4th Symposium on Remote Sensing of Environ., Ann Arbor, Mich., 263-271.

Decker, M. T. and E. J. Dutton, 1970, "Radiometric Observations of Liquid Water in Thunderstorm Cells," *J. Atmos. Sci.* 27, 785-790.

Goldstein, H., Propagation of Short Radio Waves (ed. by D. E. Kerr), McGraw-Hill Book Company, Inc., N. Y., N. Y.

Gordon, R. G., 1967, "On the Pressure Broadening of Molecular Multiplet Spectra," *J. Chem. Phys.* 46, 448-455 (1967).

Gunn, K. L. and T. W. R. East, 1954, "Microwave Properties of Precipitating Particles," *Quart. T. Roy. Meteor. Society* 80, 522-545.

Hidy, G. M., K. W. Gray, W. N. Hardy, W. F. Hall, W. W. Ho, A. W. Love, and E. J. Thompson, Dec. 1969, "S-Band Radiometer for Measurement of Sea Temperature," North American Rockwell Science Center Report SCTR-69-31, 60 p.

Ho, W. W., 1969, "Brightness Temperature of the Earth's Atmosphere due to Microwave Absorption by Molecular Oxygen," North American Rockwell Science Center Report SCTR 69-12.

Hogg, D. C., 1959, "Effective Antenna Temperatures Due to Oxygen and Water Vapor in the Atmosphere," *J. Appl. Phys.* 30, 1417-1419.

Howell, T. F. and J. R. Shakeshaft, 1967, "Attenuation of Radio Waves by the Troposphere over the Frequency Range 0.4-10 GHz," *Atmos. and Terr. Phys.* 29, 1559.

- Laws, J.O. and D.A. Parsons, 1948, "The Relation of Raindrop Size to Intensity," Trans. of Amer. Geophys. Union 24, 452.
- Lhermitte, R.M., 1968, "Indirect Probing of Cloud and Precipitation by Microwave Radiometer," ISA Transactions 7, 138-142.
- Medd, W.J. and D.N. Fort, 1966, "Total Atmospheric Attenuation at 3.2 Gigahertz," J. Geophys. Res. 71, 4749-4753.
- McLeod, A., 1969, "19.35 GHz Radiometer," Autonetics Div. Report C9-1615/401, North American Rockwell Corp., Anaheim, Calif.
- Nautical Almanac Office, 1969, The Nautical Almanac (1970) U.S. Naval Observatory, U.S. Govt. Printing Office, Washington, D. C.
- Paris, J.F., 1969, "Microwave Radiometry and Its Appl. to Marine Meteor. and Oceanography," Report on Project NR 083-036, Texas A&M University, Dept. of Oceanography, College Station, Texas.
- Reference Data for Radio Engineers, 1968, Howard W. Sams and Co., Inc., N. Y.
- Shakeshaft, J.R. and A.S. Webster, 1968, "Microwave Background in Steady State Universe," Nature 217, 339.
- Shifrin, K.S. (ed.), 1969, Transfer of Microwave Radiation in the Atmosphere. (trans.) NASA Tech. Note TTF-590, National Aero. and Space Admin., Washington, D. C.
- Staelin, D.H., 1966, Measurements and Interpretation of the Microwave Spectrum of the Terrestrial Atmosphere Near 1-centimeter Wavelength., J. Geophys. Res. 71, 2875-2881.
- Toong, H.D. and D.H. Staelin, 1970, "Passive Microwave Spectrum Microwave Spectrum Measurement of Atmosphere Water Vapor and Clouds," J. Atmos. Sci. 27, 781-784.
- U.S. Committee on Extension to the Standard Atmosphere, 1962, U.S. Standard Atmosphere, U.S. Government Printing Office, Washington, D. C.
- Van Vleck, J.H., 1947a, "The Absorption of Microwaves by Oxygen," Phys. Rev. 71, 413-424 (1947a).

Van Vleck, J.H. 1947b, The Absorption of Microwaves by Uncondensed Water Vapor, Phys. Rev. 71, 425-433.

Weger, E., 1960, Apparent Sky Temperatures in the Microwave Region, J. Meteor. 17, 159-165.

Wulfsberg, K.N., 1964, Apparent Sky Temperature at Millimeter Wave Frequencies, Phys. Sci. Ref. Papers, No. 38, Air Force Cambr. Res. Labs., USAF, Hanscom Field.

|

6.0 EMISSION FROM A ROUGH SEA

A necessary condition for determining the sea surface temperature from the observed brightness temperature is that the effect of surface waves on the microwave emissivity be accurately known over the range of conditions expected in the world ocean. Yet at this writing no experimental work has been reported which is of sufficient depth to allow direct prediction of this effect, or even to permit an accurate comparison with current theory. At the same time, only first-order theoretical calculations of unknown accuracy have been carried out.

Under the present contract, calculations based on the currently accepted theoretical models were extended and an approach was developed which could yield the emissivity to arbitrary accuracy. The results of these efforts are reported in the following sections. In addition, measurements in the rooftop pool of the effect of standing water waves on the brightness temperature are included which show increases of 2° to 6°K, an order of magnitude larger than that predicted in simple model calculations.

6.1 INTRODUCTION

The principle of detailed balance, which follows from the requirement of thermodynamic equilibrium, relates the emissivity e_a of a half-space¹ at constant temperature to the power reflection coefficient r_{ab} for radiation incident on the half-space in the form

$$e_a(\hat{q}) = 1 - \int d\Omega_k \sum_b r_{ab}(\hat{q}, \hat{k}), \quad (6.1)$$

where \hat{q} is a unit vector in the direction of emission, $r_{ab}(\hat{q}, \hat{k})$ is the fraction of the power incident along \hat{k} with polarization b which would be reflected into \hat{q} with polarization a, and the integral $d\Omega_k$ is over all directions intersecting the surface of the half-space (Peake, 1959). The emissivity $e_a(\hat{q})$ is the ratio between the power actually emitted (in the direction of \hat{q} , with polarization a) to the power a blackbody at the same temperature would emit. A more general approach, which allows for variation of the temperature from point to point in the half-space, is to calculate the contribution of each

¹ A dielectric body infinite in extent along two orthogonal directions and semi-infinite along the third.

radiating volume element to the emitted power. This approach, however, still requires that one properly treat the scattering at the irregular interface. Possibly for this reason, no such calculation has yet been reported. Rather, theoretical work has been concentrated on the electromagnetic boundary value problem which must be solved to obtain the power reflection coefficient r_{ab} . Since the sea temperature is essentially constant over the electromagnetic skin depth for microwave radiation, this approach, in principle, should yield acceptable estimates for the emitted power.

Reflection from a rough surface has been the subject of theoretical investigations since Lord Rayleigh (1929) published his perturbation calculations for the scattering of sound waves by a slightly rough surface at the turn of the century. S. O. Rice in 1951, using Rayleigh's technique obtained the analogous results for the scattering of electromagnetic waves, and in the last few years G. R. Valenzuela (1967, 1968) has applied Rice's results to obtain radar differential scattering cross-sections. A similar perturbation method has been used by J. W. Wright (1966) to obtain radar backscattering cross-sections for the sea surface. Parallel developments in the theory of rough-surface scattering have taken place in Russia. (Bass, et al, 1968).

While sea surface backscatter appears to be adequately treated by these perturbation techniques, there is a divergence in the theory, first pointed out by Rice, which leads to infinite total reflected power for a perfect conductor. When the perturbation theory is carried out to second order in the surface height to obtain the emissivity, one finds that this divergence shows up in the form of a "correction" term to smooth surface emissivity which is proportional to the square root of the dielectric constant ϵ for large ϵ , a form which cannot be correct in the limit $\epsilon \rightarrow \infty$. Since at microwave frequencies the relative dielectric constant of the sea is large ($|\epsilon/\epsilon_0| \approx 80$), this method ought not to be used for calculating the emissivity of a rough sea surface.

The generally accepted alternative to the Rayleigh perturbation method is to employ the tangent plane (or Kirchoff) approximation to obtain the electromagnetic field on the scattering surface, which then determines the field everywhere through Maxwell's equations. Since this approach has been pursued to the point of yielding rough surface emissivity, it is worthwhile to examine its structure in some depth.

Basic to this approach is the exact integral equation for the scattered electric field \vec{E} at any point \vec{r} in terms of its values on the scattering surface $z = h(x, y)$ (cf., Stratton, 1941).

$$\vec{E}(\vec{r}) = \lim_{\sigma \rightarrow 0^+} \frac{i}{(2\pi)^3} \int \frac{d^3\vec{q}}{q^2 - k^2 - i\delta} e^{i\vec{q} \cdot \vec{r}} \int ds \{ \vec{q} \times (\hat{n} \times \vec{E}) + i \vec{q} \times (\vec{q} \times (\hat{n} \times (\vec{\nabla} \times \vec{E})) \} e^{-i\vec{q} \cdot \vec{r}'} \quad (6.2)$$

Here \hat{n} is the unit upward normal to the surface element dS , k is the magnitude of the wave vector of the incident field (the wave number) and $\hat{q} = \vec{q}/k$.

In the tangent plane approximation one treats each element dS of the surface as an infinite plane onto which the incident wave \vec{E}^0 falls, so that the Fresnel reflection coefficients may be used to determine the scattered field \vec{E}^s on dS . This approximation inherently ignores multiple reflections, which undoubtedly occur on the ocean surface, along with diffraction effects associated with the curvature of the scattering surface; shadowing may be incorporated by taking \vec{E}^0 to vanish on the unilluminated parts of the surface.

Putting $\vec{E}^s = R(\hat{k}, \hat{n})\vec{E}^0$, where R is the Fresnel reflection matrix, one can write the a-polarized electric field resulting from an incident b-polarized wave of unit amplitude ($\vec{E}^0 = \hat{u}_b e^{i\vec{k} \cdot \vec{r}}$) as

$$E_{ab}(\vec{r}) = \lim_{\delta \rightarrow 0^+} \frac{ik}{(2\pi)^3} \int \frac{d^3q}{q^2 - k^2 - i\delta} e^{i\vec{q} \cdot \vec{r}} \int dx' dy' \hat{u}_a \cdot K(\hat{q}, \hat{k}; z - \vec{\nabla}h) R(\hat{k}, \hat{n}) \hat{u}_b e^{i(\hat{k} - \hat{q}) \cdot \vec{r}}, \quad (6.3)$$

where $K(\hat{q}, \hat{k}; \vec{\nabla}h) = \hat{q} \times (\vec{\nabla}h \times \hat{k}) - \hat{q} \times (\hat{q} \times (\vec{\nabla}h \times \hat{k}))$, \hat{u}_a and \hat{u}_b are unit vectors in their respective directions of polarization, and the substitutions $dS = dx' dy'$, $|1 + (\vec{\nabla}h)^2|^{1/2}$, $\hat{n} = (\hat{z} - \vec{\nabla}h) |1 + (\vec{\nabla}h)^2|^{-1/2}$ have been made. The reflection coefficient r_{ab} for a particular surface $h(x, y)$ can be computed directly from the Fourier transform of (6.3). However, in general, one knows only the statistics of the surface height rather than its actual value, so that r_{ab} can only be determined in a statistical sense. Assuming that $h(x, y)$ is a stationary, ergodic random process, one can write r_{ab} in the form

$$r_{ab}(\hat{q}, \hat{k}) = \frac{k^2}{(4\pi)^2 \hat{q} \cdot \hat{z}} \int d^2\vec{\lambda} e^{-i(\vec{k} - \vec{q}) \cdot \vec{\lambda}} \langle [\hat{u}_a \cdot K R \hat{u}_b]_2^* [\hat{u}_a \cdot K R \hat{u}_b]_1 \rangle_x e^{i(\vec{k} - \vec{q}) \cdot \hat{z} (h_1 - h_2)} \quad (6.4)$$

where the subscripts 1 and 2 indicate that the functions of h are to be evaluated at the points $\vec{\rho} = (x, y)$ and $\vec{\rho} + \vec{\lambda} = (x + \lambda_1, y + \lambda_2)$, respectively, and the angular brackets $\langle \rangle$ denote an ensemble average over the surface height.

The direct numerical evaluation of r_{ab} from (6.4) using a reasonable model for the surface height statistics is not presently feasible, as it would require carrying out six integrals of an oscillatory integrand over an infinite range. Rather, asymptotic methods have been used in the small wavelength limit to derive an approximate expression for r_{ab} in terms of the maximum value of the integrand. Stogryn (1967a) has used the classical method of steepest descents combined with Gaussian statistics for the

surface height to evaluate r_{ab} solely in terms of the contribution from those parts of the surface whose normal \hat{n} is so directed that radiation is reflected specularly from \hat{k} into \hat{q} (i. e., $\hat{n} = (\hat{q}-\hat{k})/|\hat{q}-\hat{k}|$). Other investigators have introduced a modification to the method of steepest descents in the hope of generating an expression for r_{ab} which would be approximately correct over a wide range of wavelengths. By displacing the point at which the integrand is evaluated a small distance from the specular point, they obtain a formula for r_{ab} in which this displacement enters essentially as a free parameter. The resulting model for the emissivity is sufficiently good that a large body of experimental data has been fitted qualitatively by appropriate choice of the free parameter.

The central objective which must be raised to the latter procedure, is that it is a postulate for the form of the reflection coefficient, rather than a prediction of its value. Until a rationale is found for calculating the free parameter from the surface properties of the sea, one cannot estimate the effect of roughness on the emissivity by this technique.

Using the specular approximation to r_{ab} , Stogryn (1967b) has evaluated the apparent temperature of fresh water for microwave frequencies of 19.4 and 35 GHz, including the effects of atmospheric absorption and emission. These calculations show increases in brightness temperatures due to roughness of a few degrees at large nadir angles, largely as a result of reflections from the hotter parts of the sky (at 19 and 35 GHz the zenith sky temperature is 25°K). Hollinger (1970) has made radiometric observations of the sea at Argus island which generally agree with Stogryn's model. One should note, however, that Stogryn's reported values are inconsistent at nadir, due probably to numerical difficulties in evaluating the integrals where $\hat{q} \times \hat{z} = 0$.

6.2 THE GEOMETRICAL OPTICS MODEL

A reasonable alternative to the procedure adopted by Stogryn, which ultimately takes into account only the specular contributions to r_{ab} , is to treat the sea surface as a collection of randomly oriented facets whose sizes are large compared to the electromagnetic wavelength, and to compute the (specular) scattering from each facet using the Fresnel reflection coefficients. Facet models for radar reflections from the sea surface were developed in the late 1950's by Katzin (1959) and by Spetner and Katz (1960), but no emissivity calculation based on these models has been reported.

If multiple reflections are ignored, a single facet of area A with unit normal \hat{n} will scatter into the direction \hat{q} with polarization a that part p_{ab} of the power per unit area incident along the specular direction $\hat{k} = \hat{q} - 2(\hat{q} \cdot \hat{n})\hat{n}$ with polarization b given by

$$p_{ab}(\hat{q}, \hat{n}) = A(\hat{q} \cdot \hat{n}) |\hat{u}_a \cdot R(\hat{q}, \hat{n})\hat{u}_b|^2. \quad (6.5)$$

Consequently, a patch of the scattering surface made up of N facets of area A , bathed in black body radiation at the surface temperature T_s from all directions, will scatter a total power

$$I_a(\hat{q}) = A \sum_b \sum_{i=1}^N p_{ab}(\hat{q}, \hat{n}_i) P^{BB}(T_s) \quad (6.6)$$

into \hat{q} with polarization a , where p^{BB} is the blackbody power per unit area, and the inner sum is over all the facets in the patch. The horizontal area covered by this patch is given by

$$A_h = A \sum_{i=1}^N (\hat{n}_i \cdot \hat{z}), \quad (6.7)$$

so that the power per unit area perpendicular to \hat{q} that this patch reflects into \hat{q} with polarization a is

$$P_a(\hat{q}) = \frac{I_a(\hat{q})}{(\hat{q} \cdot \hat{z}) A_h} \quad (6.8)$$

As the number of facets N tends to infinity, the sum over facets in the numerator and denominator of (6.8) tend toward N times an average over the direction of the facet normal. Thus, dividing numerator and denominator by N and denoting this average by angular brackets $\langle \rangle$, one may rewrite (6.8) as

$$P_a(\hat{q}) = \frac{\langle (\hat{q} \cdot \hat{n}) |\hat{u}_a \cdot R\hat{u}_b|^2 \rangle}{(\hat{q} \cdot \hat{z}) \langle \hat{n} \cdot \hat{z} \rangle} p^{BB} \quad (6.9)$$

By the principle of detailed balance, the total power per unit area travelling in the direction q with polarization a , reflected plus emitted, must equal the black body power per unit area at the surface temperature T_s :

(6.10)

$$P^{BB}(T_s) = P_a(\hat{q}) + e_a(\hat{q}) P^{BB}(T_s), \quad (6.10)$$

so the emissivity $e_a(\hat{q})$ of the surface in the direction \hat{q} with polarization a is given in this approximation by the formula

$$e_a(\hat{q}) = 1 - \frac{\sum (\hat{q} \cdot \hat{n}) |u_a \cdot Ru_b|^2}{(\hat{q} \cdot \hat{z})(\hat{n} \cdot \hat{z})} \quad (6.11)$$

This formula, which must be equivalent to the tangent plane result in the short wavelength limit, has the advantage of simplicity in derivation and in evaluation. Also, it is readily generalized to include the effects of multiple reflection. Numerical agreement with Stogryn's (1967b) calculation of the apparent temperature of fresh water has been obtained for nadir angles from 5° to 40° .

There are two ways in which multiple reflections can modify (6.11): First, the power per unit area incident on a given facet from the specular direction \hat{k} need not come directly from the sky; a certain fraction of the rays parallel to \hat{k} arriving at the facet, when traced backwards, will intercept other facets. Second, a fraction of the rays parallel to \hat{q} leaving the facet will strike other facets and be deviated out of the direction \hat{q} .

To account for these effects exactly would require a specification of the location and orientation of every facet on the surface. However, a first approximation can be obtained by considering a second facet of area identical to the first, arbitrarily oriented, which may intercept rays leaving the first, and to ignore the possibility of further reflections. The fraction $F(\hat{q}, \hat{n})$ of the rays leaving the first facet in the direction \hat{q} which escape reflection by the second facet can then be approximated by

$$F(\hat{q}, \hat{n}) = \Theta(\hat{q} \cdot \hat{z}) \left(1 + \frac{\hat{q} \cdot \hat{n}'}{\hat{q} \cdot \hat{n}} \right) \Theta \left(1 + \frac{\hat{q} \cdot \hat{n}'}{\hat{q} \cdot \hat{n}} \right) \Theta(-\hat{q} \cdot \hat{n}') \\ + \Theta(\hat{q} \cdot \hat{n}') \Theta(\hat{q} \cdot \hat{n}), \quad (6.12)$$

where $\Theta(x)$ is the step function, zero for $x < 0$ and unity for $x > 0$, and the average is over the direction \hat{n}' of the second facet. The factor $\left(1 + \frac{\hat{q} \cdot \hat{n}'}{\hat{q} \cdot \hat{n}} \right)$ represents the fraction of the area of the first facet not covered by the projection of the second facet parallel to $-\hat{q}$.

The power per unit area incident along \hat{k} in this approximation either comes directly from the sky, or indirectly after reflection by a single facet with normal \hat{n}' . For those rays which have suffered a single reflection, the power per unit area reflected into \hat{k} with polarization b is

$$Q_b(\hat{k}, \hat{n}') = \sum_c |\hat{u}_b \cdot R(\hat{k}, \hat{n}') \hat{u}_c|^2 P^{BB}. \quad (6.13)$$

This expression must be averaged over the direction \hat{n}' of the normal to the scattering facet to obtain its expected contribution to the intensity incident along \hat{k} with polarization b . Recalling that $F(-\hat{k}, \hat{n})$ is the fraction of rays traced backward along \hat{k} which escape directly to the sky, while $1-F(-\hat{k}, \hat{n})$ is the fraction of rays which encounter another facet, one has that the average total power per unit area incident along \hat{k} with polarization b is

$$N_b(\hat{k}, \hat{n}) P^{BB} = F(-\hat{k}, \hat{n}) P^{BB} + [1-F(-\hat{k}, \hat{n})] \frac{\sum_c |\hat{u}_b \cdot R \hat{u}_c|^2 \langle \Theta(\hat{k} \cdot \hat{n}') \rangle}{\langle \Theta(\hat{k} \cdot \hat{n}') \rangle} P^{BB} \quad (6.14)$$

The role of the step function $\Theta(\hat{k} \cdot \hat{n})$ in (6.14) is to restrict the average to those facets which can scatter radiation into the direction \hat{k} .

By the same line of argument used in obtaining (6.9), one can now show that the power per unit area reflected into \hat{q} with polarization a can be written as

$$P_a(\hat{q}) = \frac{\sum_b |\hat{u}_a \cdot R(\hat{q}, \hat{n}) \hat{u}_b|^2 N_b(\hat{k}, \hat{n}) F(\hat{q}, \hat{n})}{(\hat{q} \cdot \hat{z})(\hat{n} \cdot \hat{z})} P^{BB}, \quad (6.15)$$

and the corresponding emissivity now becomes

$$e_a(\hat{q}) = 1 - \frac{\sum_b |\hat{u}_a \cdot R \hat{u}_b|^2 N_b(\hat{k}, \hat{n}) F(\hat{q}, \hat{n})}{(\hat{q} \cdot \hat{z})(\hat{n} \cdot \hat{z})}. \quad (6.16)$$

This expression, together with equation (6.11), has been evaluated numerically for Gaussian slope statistics; the results are summarized in Figure 6.1, which presents the brightness temperature of the faceted surface, averaged over the two polarizations, as a function of viewing angle for rms slopes of zero (flat surface), 0.09, and 0.25. According to the data of Cox and Munk (1954), an rms slope of 0.09 corresponds roughly to a wind velocity of 8 knots, a frequent occurrence over the world ocean. The rms slope of 0.25, by extrapolation on the same data, would correspond to a wind velocity of over 60 knots; it is included to indicate the minimal effect of surface roughness on the brightness temperature.

There are several points to note with regard to these calculations: a) At rms slopes of less than 0.1 the brightness temperatures calculated from (6.11) and from (6.16) are identical to five significant figures; that is, the effect of multiple reflections is negligible; b) the total effect of roughness on the polarization-averaged brightness temperature for rms slopes less

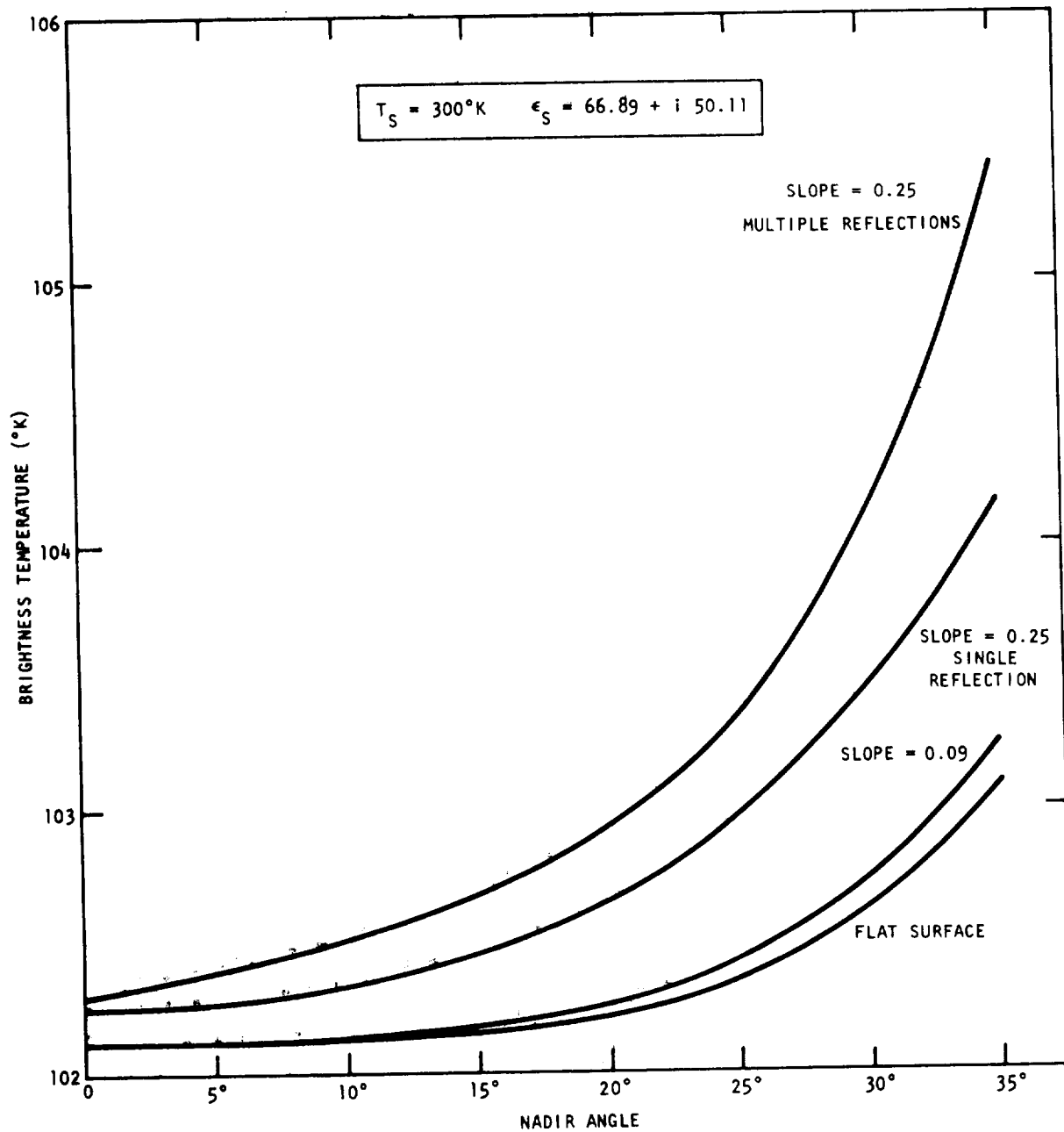


Figure 6.1 Polarization Averaged Brightness Temperature of the Rough Sea in the Geometrical Optics Model

than 0.1 is less than 0.2°K for viewing angles up to 35° from nadir; c) even for hurricane winds the total effect of roughness at nadir is about 0.2°K, with only 0.05°K due to multiple reflections.

On the basis of these results one is tempted to dismiss surface roughness as a source of error for S-band radiometric measurements at nadir. There are, however, three additional effects of the presence of waves on the surface which must be accounted for. First, there is reflection from the hotter parts of the sky. This is the dominant contributor at 19 and 35 GHz, where the atmospheric contribution to the sky temperature ranges from 25° at zenith to 50° at an angle of 60° from the zenith. Approximately 80% of the 1.75°K increase in apparent temperature calculated by Stogryn (1967b) for horizontal polarization at 20° from nadir for 35 GHz and a wind speed of 7 meters per second comes from sky reflection. The sky at S-band, however, is cooler by a factor of ten, the atmospheric contribution at zenith amounting to about 2°K. The corresponding increase in apparent temperature is also reduced by a factor of ten, so that sky reflections represent a negligible source of error at S-band.

Next, there is sun glitter. Due to the high apparent temperature of the sun in the microwave region (about 50,000°K at S-band, as compared with 6,000°K in the optical and infrared (cf., Kraus, 1966)), it can contribute appreciably, under rough sea conditions, to the observed brightness temperature at large angular separation from the specular direction. For an rms slope of 0.09, the sun at 25° from zenith contributes 1°K to the apparent temperature at nadir. Certainly, it will be necessary to apply a first-order correction for this effect, either by measuring the brightness temperature of the sun's image (which decreases directly as the surface roughness) or by estimating the surface roughness from other observations.

Finally, there is the diffraction effect associated with surface waves of amplitude and wavelength comparable to and smaller than the electromagnetic wavelength (about 10 cm), which are thought to be prevalent on the ocean surface. No calculation of the change in emissivity due to this effect is feasible within currently accepted theoretical models; as was mentioned earlier, the tangent plane approximation encounters severe computational difficulties, while the perturbation treatments give results which diverge with $\sqrt{\epsilon}$. It is partially to overcome this difficulty that the development of a new theoretical approach to the problem of rough surface scattering was undertaken as part of the present program. While this development is still incomplete, it is likely that a perturbation treatment of the equations summarized in the next two sections will yield a numerically tractable formula for the effect of short waves on the sea surface emissivity.

6.3 AN INTEGRAL EQUATION SOLUTION FOR THE SCATTERING PROBLEM

The currently employed calculations of rough surface scattering all share one common defect: They start from an expression for the scattered field which is in error by an unknown amount. The tangent plane approximation, for instance, assumes a value for the field on the scattering surface based on the Fresnel reflection coefficients and calculates all quantities of interest from that assumption. Even if the subsequent calculations were carried out to arbitrary accuracy, there would still remain the error incurred by the original assumption. Moreover, there is no way to estimate the magnitude of that error for a surface containing any significant degree of structure. As a consequence, the small departures from smooth-surface emissivity that one seeks to calculate for the surface of the sea may well be magnified or cancelled by the errors inherent in the theory.

To overcome this difficulty, we have derived an exact integral equation for the scattered field which can be solved by successive approximation. In principle, one can obtain the scattered field to arbitrary accuracy from this equation, but of greater significance is the fact that the error committed by breaking off the sequence of approximations at any stage can be determined by comparing the scattered field at that stage with its value in the previous stage. Ultimately, then the magnitude of the error made in calculating rough surface emissivity from this field can be bounded, and hence, by extending the sequence, it can be reduced to an acceptable level.

At the present time, only the derivation of the equation itself is complete. Its application to the calculation of rough surface emissivity and its connections with the perturbation approach of Rice (1951) and with the tangent plane approximation remain to be established.

The exact problem which has been treated is the following: Consider an electromagnetic wave of time dependence $e^{-i\omega t}$ incident from above on a surface $z = h(x, y)$ which is the static interface between two homogeneous media with differing dielectric constants E and conductivities σ . Define the effective dielectric constant \bar{E} by the relation $\epsilon = E + i\sigma/\omega$ and denote its value above $z = h$ by E_v , and its value below $z = h$ by E_w . Denote the electric and magnetic fields of the incident wave by \vec{E}_0 and \vec{H}_0 , respectively, both taken to vanish for $z < h$, and write the total electric field \vec{E} as the sum $\vec{E}_0 + \vec{E}_1$. Then for $z > h$, \vec{E}_1 satisfies the following Fredholm integral equation of the second kind:

$$\vec{E}_1(\vec{r}) = J(\vec{r}) + \int_{-\infty}^{\infty} dx' \int_{-\infty}^{\infty} dy' \int_{-\infty}^{h(x', y')} dz' K_v(\vec{r} - \vec{r}') \int_{-\infty}^{\infty} dx'' \int_{-\infty}^{\infty} dy'' \int_{h(x'', y'')}^{\infty} dz'' K_w(\vec{r}' - \vec{r}'') \vec{E}_1(\vec{r}'') \quad (6.17)$$

Here the kernels K_v and K_w are dyadics given by

$$K_{\frac{v}{w}}(\vec{r}) = \omega^2 \mu_0 \left(\epsilon_{\frac{w}{v}} - \epsilon_{\frac{v}{w}} \right) + \frac{1}{\epsilon_{\frac{v}{w}}} \left(\epsilon_{\frac{w}{v}} - \epsilon_{\frac{v}{w}} \right) \vec{\nabla}(\vec{\nabla} \phi_{\frac{v}{w}}(\vec{r})) \quad (6.18)$$

where μ_0 is the magnetic permeability of both media and $\phi_{\frac{v}{w}}$ is the Green's function for the scalar Helmholtz equation:

$$\phi_{\frac{v}{w}}(\vec{r}) = e^{i\omega \sqrt{\mu_0 \epsilon_{\frac{v}{w}}} r} / 4\pi r. \quad (6.19)$$

The source term \vec{J} in (6.17) is given by

$$\begin{aligned} \vec{J}(\vec{r}) = & \iint dS' \{ [\hat{n} \times \vec{H}_0(\vec{r}')]] i\omega \mu_0 \phi_{\frac{v}{w}}(\vec{r}-\vec{r}') + \\ & + [\hat{n} \times \vec{E}_0(\vec{r}')]] x \vec{\nabla}' \phi_{\frac{v}{w}}(\vec{r}-\vec{r}') + [\hat{n} \cdot \vec{E}_0(\vec{r}')]] \vec{\nabla}' \phi_{\frac{v}{w}}(\vec{r}-\vec{r}') \} + \\ & - \int_{-\infty}^{\infty} dx' \int_{-\infty}^{\infty} dy' \int_{-\infty}^{h(x',y')} dz' K_{\frac{v}{w}}(\vec{r}-\vec{r}') \iint dS'' \{ [\hat{n} \times \vec{H}_0(\vec{r}'')]] i\omega \mu_0 \phi_{\frac{v}{w}}(\vec{r}'-\vec{r}'') + \\ & + [\hat{n} \times \vec{E}_0(\vec{r}'')]] x \vec{\nabla}'' \phi_{\frac{v}{w}}(\vec{r}'-\vec{r}'') + \left(\frac{\epsilon_{\frac{v}{w}}}{\epsilon_{\frac{w}{v}}} \right) [\hat{n} \cdot \vec{E}_0(\vec{r}'')]] \vec{\nabla}'' \phi_{\frac{v}{w}}(\vec{r}'-\vec{r}'') \}, \end{aligned} \quad (6.20)$$

where dS is an element of area on the scattering surface and \hat{n} is the corresponding upward unit normal to the surface. The primes on the gradients indicate with respect to which argument the Green's function is to be differentiated.

The procedure of successive approximations for solving (6.17) consists of inserting a first guess for \vec{E}_1 , such as the tangent plane approximation, into the integral on the right-hand side of (6.17), evaluating the integral, and adding the source term \vec{J} to obtain the next approximation to \vec{E}_1 . If the integral operator in (6.17) is denoted T , and if the first guess is denoted \vec{A} , then after N successive substitutions the resulting approximate expression for \vec{E}_1 becomes

$$\vec{E}_1^{(N+1)} = \vec{J} + \sum_{n=1}^{N-1} T^n \vec{J} + T^N \vec{A} \quad (6.21)$$

This sequence will converge to the true field provided only that the remainder term $T^N \vec{A}$ tends to zero as $N \rightarrow \infty$. The resulting infinite series is known as the Neumann series solution, and the total squared error made in breaking off the sequence at N terms is given by

$$\int d^3\vec{r} |\vec{E}_1^{(N+1)}(\vec{r}) - \vec{E}_1(\vec{r})|^2 \leq \|T\|^{N-1} \int d^3\vec{r} |\vec{J} + T\vec{A} - \vec{A}|^2, \quad (6.22)$$

whenever the norm of the operator T, defined as

$$(\text{norm } T)^2 \equiv \|T\|^2 = \text{least upper bound over all square-integrable } g \text{ of } \frac{\int d^3\vec{r} |Tg|^2}{\int d^3\vec{r} |g|^2}, \quad (6.23)$$

is less than unity.

While evaluating the norm of T for an arbitrary surface $h(x, y)$ represents a task of some difficulty, the special case of a constant $h \neq 0$ can be readily treated. For horizontal polarization of the incident electric field, one finds that (6.17) reduces for constant h to the algebraic equation

$$\vec{E}_1 = \frac{R \hat{u}_h}{1-R^2} e^{-2ivh} e^{i\vec{\kappa} \cdot \vec{r}} e^{ivz} - \frac{R^2}{1-R^2} \vec{E}_1 \quad (6.24)$$

where $R = \frac{v-w}{v+w}$ is the Fresnel reflection coefficient for $h = 0$, v and w are the vertical components of the propagation constant $k = \omega\sqrt{\mu_0\epsilon}$ above and below $z=h$, respectively, $\vec{\kappa}$ is the horizontal component of k , and \hat{u}_h is a unit vector in the direction of polarization of the incident electric field. In this case T operating on E_1 simply multiplies it by the constant $-R^2/(1-R^2)$. Therefore, the condition that $\|T\|$ be less than unity reduces to

$$|R^2/(1-R^2)| < 1, \text{ or } \text{Re } R^2 < \frac{1}{2}. \quad (6.25)$$

The important conclusion to be drawn from this result is the following; for $\text{Re } R^2 > 1/2$, the successive approximation scheme will not converge to a solution of the original integral equation. Conversely, one should expect that a detailed analysis of the operator T for arbitrary $h(x, y)$ will show that successive approximation will converge rapidly for $\text{Re } R^2$ sufficiently small. Therefore, the integral equation (6.17) represents a promising approach to the problem of scattering from a dielectric half-space.

From the point of view of treating the problem of the emissivity at S-band from a rough sea surface, the successive approximation approach to the integral equation (6.17) is a failure, for $\text{Re } R^2$ in this case is greater than $1/2$. However, by Fourier transformation of (6.17) it has proved possible to separate the divergent part which comes from scattering by a flat surface, and to write a new integral equation in the transform variables for which the iterative approach can converge for $|R^2| < 1$.

The tasks which remain to be performed before the integral equation approach will yield rough-surface emissivities may be summarized as follows: First, the rate of convergence of the iterative solution must be established, and the number of terms to be retained for specified accuracy in the electric field must be determined. Next, the statistical description of the rough surface must be introduced through an ensemble average of the resulting expression for the reflection coefficient, as was done by Stogryn (1967a) for the tangent plane approximation. Finally, the various terms contributing to the integral over the reflection coefficient which defines the emissivity must be evaluated, and a bound on the error in calculating the emissivity must be derived.

6.4 AN EXPERIMENT ON THE EFFECT OF SURFACE ROUGHNESS

To obtain some measure of the magnitude of the brightness temperature increase one would expect at S-band for a rough sea surface it was decided to conduct an exploratory experiment using radiometric observations on the rooftop pool described in Section 7. A simple mechanical arrangement in which a variable-speed motor drove a long plank against the water at one side of the pool was set up in the positions illustrated in Figure 6.2. The plank, which was about 40 cm shorter than the pool width, was hinged below the water line so that it rotated about its lower edge. The height of the resulting water waves was measured with a capacitance bridge that could be moved about in the pool.

The results of the measurements are summarized in Figures 6.3 and 6.4. Standing waves of wavelengths varying from 15 to 30 cm were observed at viewing angles of 15° and 26° from the nadir with both circular and horizontal polarizations, and with the plane containing the horn axis and the vertical both parallel and perpendicular to the wave crests. The data collected had a large scatter (about $\pm 2^\circ\text{K}$) due largely to the fact that the amplitude of the waves could not be independently controlled; also, the coupling of mechanical energy into the pool from the driver was dependent on the details of the geometry, including water level, and was poorly reproducible.

The most significant conclusion which emerges from these experiments is that brightness temperature increases of order 2° to 6°K are obtainable. These experiments were all performed after sunset, and several checks were made to rule out the possibility that reflections of hotter objects, either on the horizon or on the roof around the pool, were contributing to the observed increase. Figure 6.3 shows the observed brightness temperature increase for circular polarization plotted against wave slope, H is the wave height from the mean water level and λ is the wavelength of the standing water waves. Arrows are used to indicate the direction of motion of the waves relative to

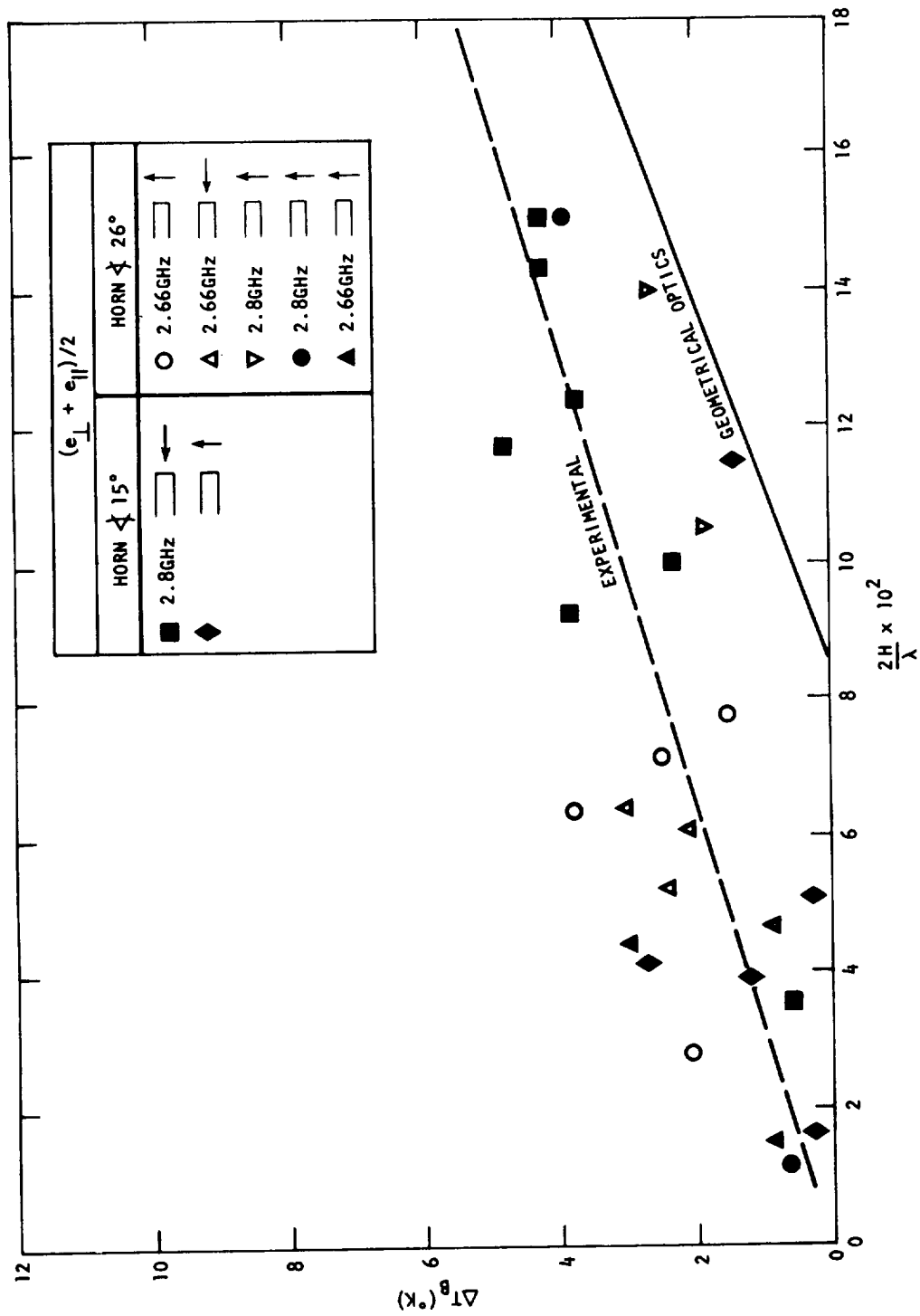


Figure 6.3 Antenna Temperature vs Equivalent Slope

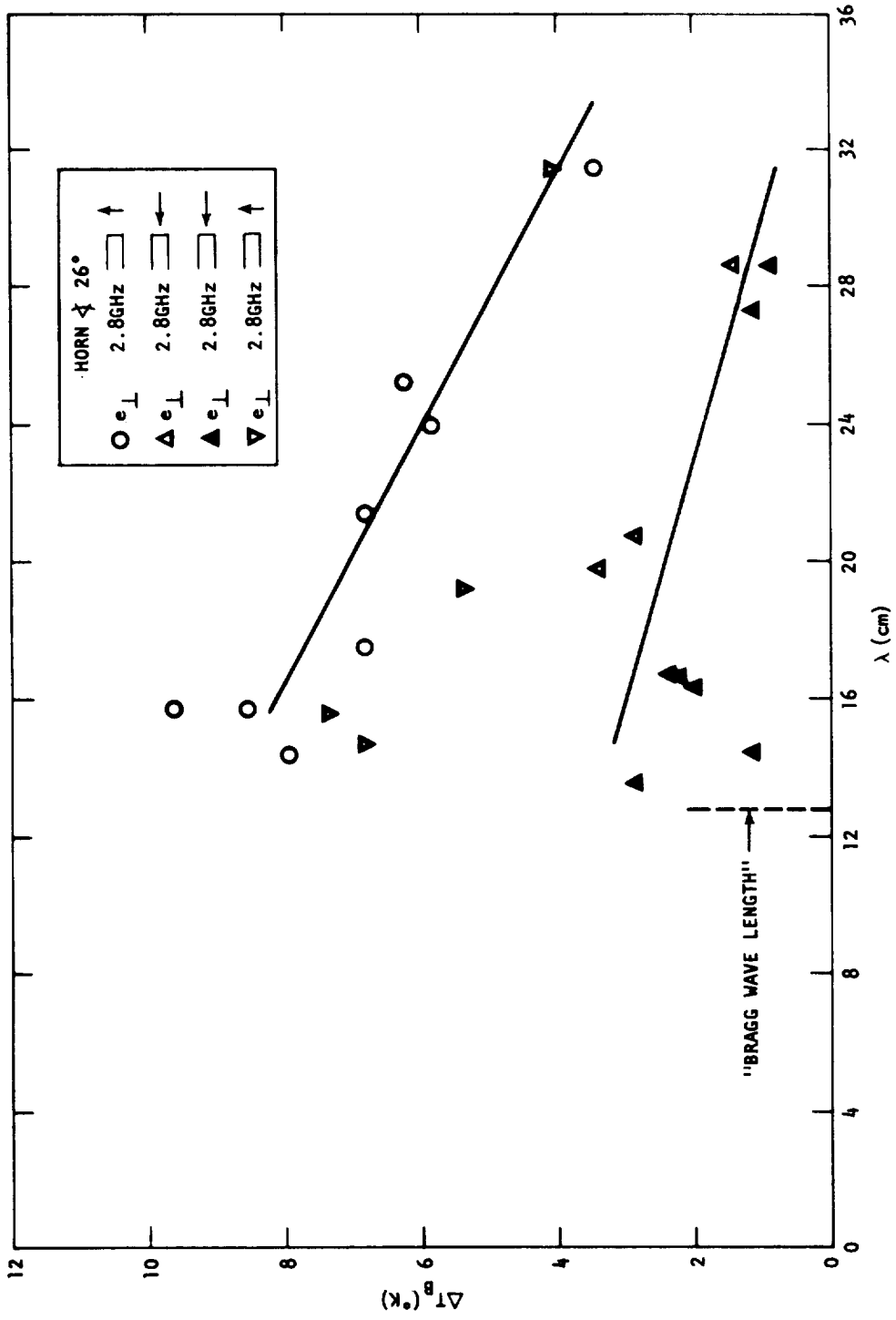


Figure 6.4 Antenna Temperature vs Wave Length

the horn. The predictions of the geometrical optics model, also indicated in the figure, fall well below the trend of the measured points.

Figure 6.4 shows the effect of direction of the water waves on the increase in brightness temperature for horizontal polarization plotted against the surface wavelength. Waves with crests parallel to the plane containing the horn axis and the vertical appear to have double the effect of waves with crests perpendicular thereto. The increase in the magnitude of this effect with decreasing wavelength must be interpreted with caution, since the wave amplitude also changed with wavelength. The broken vertical line labelled "Bragg wavelength" is the wavelength for maximum radar backscatter into the horn; it is possible but not likely on the basis of current theory that surface disturbances of this wavelength will prove to have a maximum effect on the emissivity.

The magnitude of the effects observed in this series of experiments clearly indicates the need for careful experimental investigation of this phenomenon under conditions allowing all the significant parameters such as wave amplitude and frequency, to be independently varied.

REFERENCES

- Bass, F. G., I. M. Fuks, A. I. Kalmykov, I. E. Ostrousky, and A. D. Rosenberg, 1968, "VHF Radiowave Scattering by a Disturbed Sea Surface", IEEE Trans. AP-16.
- Cox, C., and W. Munk, 1954, "Measurements of the Roughness of the Sea Surface from Photographs of the Sun's Glitter", J. O. S. A. 44, 838.
- Hollinger, J. P., 1970, "Passive Microwave Measurements of the Sea Surface", J. Geophys. Res. 75, 5209.
- Katzin, M., 1959, "On the Mechanism of Sea Clutter", Proc. I. R. E. 45, 44.
- Kraus, J. D., 1966, "Radio Astronomy", McGraw-Hill (New York).
- Peake, W. H., 1959, "Interaction of Electromagnetic Waves With Some Natural Surfaces", I. R. E. Trans. on Antennas and Propagation (Special Suppl.) AP-7, 5324.
- Lord Rayleigh, 1929, "Theory of Sound", Vol. II, pp. 89-96, Macmillan (London)
- Rice, S. O., 1951, "Reflection of Electromagnetic Waves From Slightly Rough Surfaces", Comm. Pure and Applied Math. 4, 351.
- Spetner, L. M., and I. Katz, 1960, "Two Statistical Models for Radar Terrain Return", Trans. I. R. E. AP-8, 242.
- Stogryn, A., 1967, "Electromagnetic Scattering from Rough, Finitely Conducting Surfaces", Radio Science 2, 415.
- _____, 1967, "The Apparent Temperature of the Sea at Microwave Frequencies", IEEE Trans. AP-15, 278.
- Stratton, J. A., 1941, "Electromagnetic Theory", First Edition pp. 464-470, McGraw-Hill (New York).

Valenzuela, G. R. , 1967, "Depolarization of Electromagnetic Waves by Slightly Rough Surfaces", IEEE Trans. on Antennas and Propagation AP-15, 522.

_____, 1968, "Scattering of Electromagnetic Waves from a Tilted Slightly Rough Surface", Radio Science 3, 1057.

Wright, J. W. , 1966, "Backscattering from Capillary Waves with Application to Sea Clutter", IEEE AP-14, 749.

_____, 1968, "A New Model for Sea Clutter," IEEE AP-14, 217.

7.0 MICROSCALE SURFACE DISTURBANCES

7.1 TYPES OF SURFACE DISTURBANCE

The thermal emission from the sea which reaches an earth orbiting radiometer is affected not only by the intervening atmosphere and by surface waves, but also by processes which interpose additional material between the actual sea surface and the atmosphere. Three general categories of surface contamination must be considered: (1) oil slicks, whether natural or man made; (2) ocean spray; and (3) foam. These last two disturbances are strongly dependent on wind speed on the open ocean. Figure 7.1, taken from the recent work of Monahan (1968), shows that both the area coverage of foam and the droplet density of ocean spray rise sharply above wind speeds of 6 meters per second (12 knots); foam coverage essentially vanishes below the threshold and saturates at 6-7 foam patches per 10^4 square meters above the threshold, while droplet density appears to rise indefinitely. Monahan studied the droplet size distribution of ocean spray within 20 cm of the sea surface for a wide range of wind speeds, and it can be concluded from his data that the volume fraction of sea spray in this region does not exceed 10^{-5} .

Natural variations in the total area covered by foam on the ocean surface are summarized in Figure 7.2 (Blanchard, 1963). In the middle latitudes, climatologically, one expects about 2% of foam coverage, but as much as 8% of the visible surface may be foam-covered in the higher latitudes. Recently, Nordberg *et al* (1971) have reported significant contributions of foam to the brightness temperature of the sea at cm wavelengths, beyond $\approx 1\%$ surface coverage. Thus, this phenomenon represents a potentially crucial and uncertain factor in degradation of the received signal at S-Band for application to sea temperature measurement.

7.2 THEORETICAL MODELS AND THEIR PREDICTIONS

The direct effect of interposing a surface covering between the atmosphere and the ocean surface is to increase the thermal emission entering the atmosphere by providing a medium with index of refraction intermediate between that of water (about 7) and that of air. If a portion of the sea surface is covered by a film of area large compared to the square

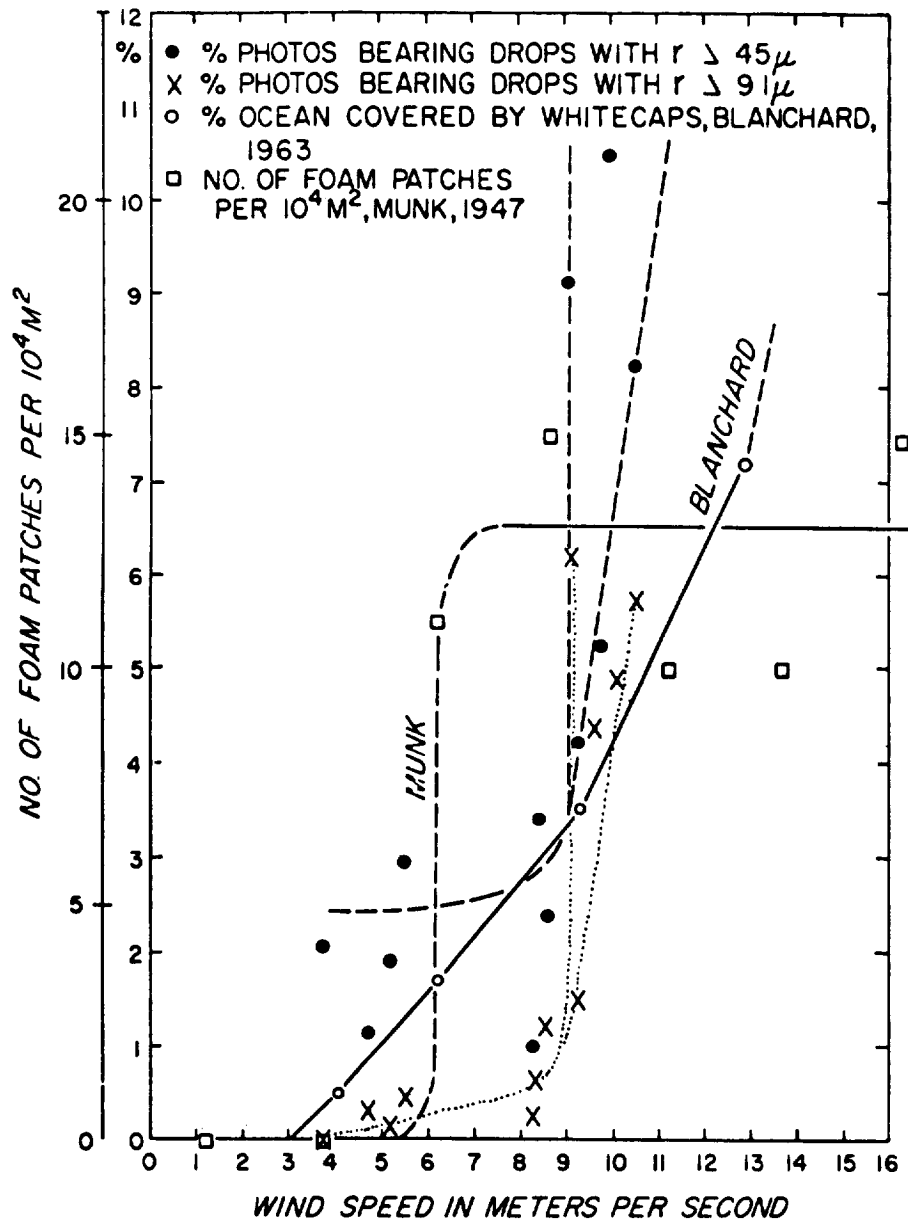
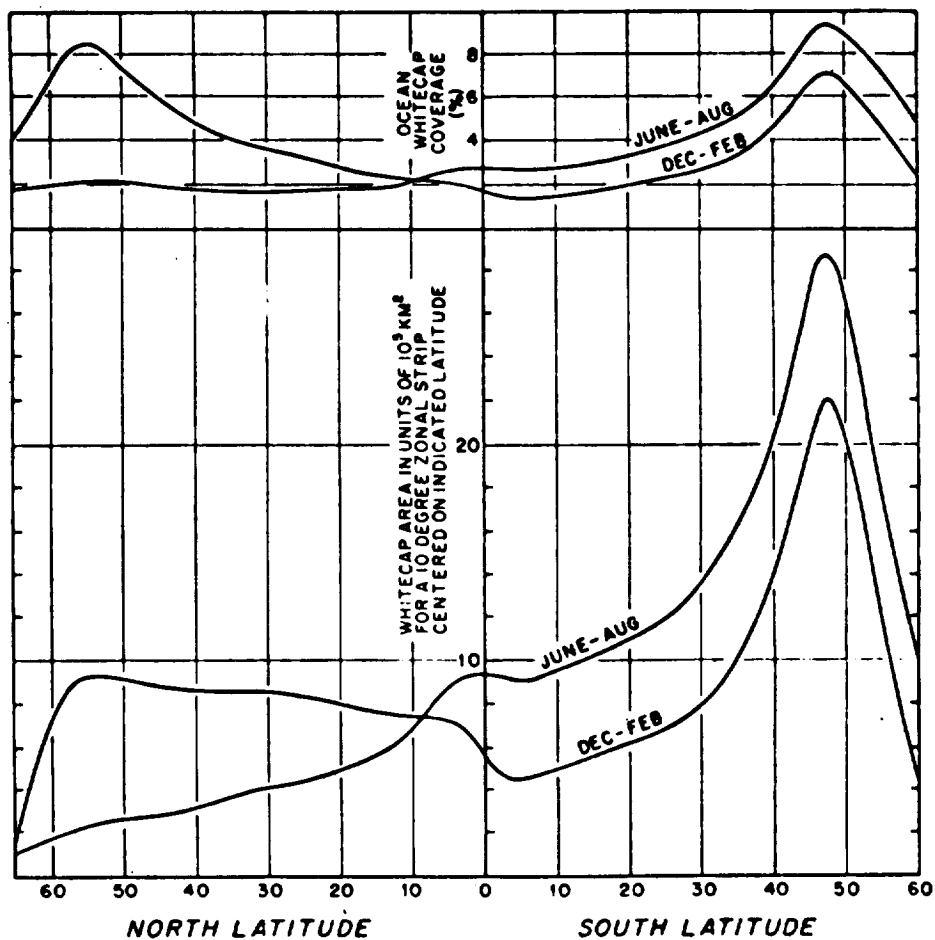


Figure 7.1. Wind Dependence of Whitecap Coverage and Spray Concentration (Monahan, 1968)



The latitudinal variation of the world ocean whitecap distribution. The upper set of curves give the percentage coverage during the winter and summer seasons. The lower set gives the area of the sea surface that is covered with whitecaps. The bump in the June-August curves near the equator reflects the monsoons in the Indian Ocean.

Figure 7.2. Latitudinal Variations of the World Ocean Whitecap Distribution (Blanchard, 1963)

of the electromagnetic wavelength, one can calculate the emissivity of this patch directly in terms of the dielectric constant ϵ_f and the thickness d of the film:

$$e_h(\hat{k}) = 1 - \left| \frac{(v+f)(f-w)e^{ifd} + (v-f)(f+w)e^{-ifd}}{(v-f)(f-w)e^{ifd} + (v+f)(f+w)e^{-ifd}} \right|^2$$

$$e_v(\hat{k}) = 1 - \left| \frac{(\epsilon_v v + \epsilon_f f)(\epsilon_f f - \epsilon_w w)e^{ifd} + (\epsilon_v v - \epsilon_f f)(\epsilon_f f + \epsilon_w w)e^{-ifd}}{(\epsilon_v v - \epsilon_f f)(\epsilon_f f - \epsilon_w w)e^{ifd} + (\epsilon_v v + \epsilon_f f)(\epsilon_f f + \epsilon_w w)e^{-ifd}} \right|^2$$

(7.1)

Here the subscripts h and v on e denote horizontal and vertical polarizations, and the quantities v , f , and w are the vertical component of the electromagnetic wave vectors in vacuum, the surface film, and water, respectively.

When the film is sufficiently thin that the product $fd \ll 1$, one can write the emissivity normal to the surface approximately as

$$e(z) \approx e^0 - 4vd(1-e^0)\text{Im} \left(\frac{\epsilon_f f - \epsilon_v v}{\epsilon_w - \epsilon_v} \right), \quad (7.2)$$

where e^0 is the emissivity when $d = 0$. For oil ($\epsilon_f/\epsilon_v \approx 2$) on sea water ($\epsilon_w/\epsilon_v \approx 70 + i50$ at S-band) this gives an increase in brightness temperature of 0.5°K per millimeter of oil at a sea surface temperature of 300°K . Direct calculation on Equations (7.1) shows that the higher order terms neglected in obtaining (7.2) begin to become important at thicknesses of a few tenths of a millimeter, so that the actual contribution of a layer of oil one millimeter thick is 1°K in this model. At viewing angles up to 30° from nadir the magnitude of this effect for circular polarization does not change by more than 10 percent from its nadir value. Under the same conditions a one millimeter-thick layer of oil on fresh water ($\epsilon_w/\epsilon_v \approx 77 + i12$) increases the brightness temperature by 0.6°K . Since naturally occurring slicks are only microns thick, their contribution to the brightness temperature should be undetectably small.

Foam and spray represent mixtures of air and water in volume fractions γ_w ranging from 10^{-7} to unity at the ocean surface. Droppleman(1970) has reported extensive calculations of the effect of a foam layer on the emissivity, based on Equation (7.1). Figure 7.3 shows how the emissivity at nadir depends upon the volume fraction of water in the layer for a foam layer 10 cm. (about one wavelength) thick over sea water. For volume

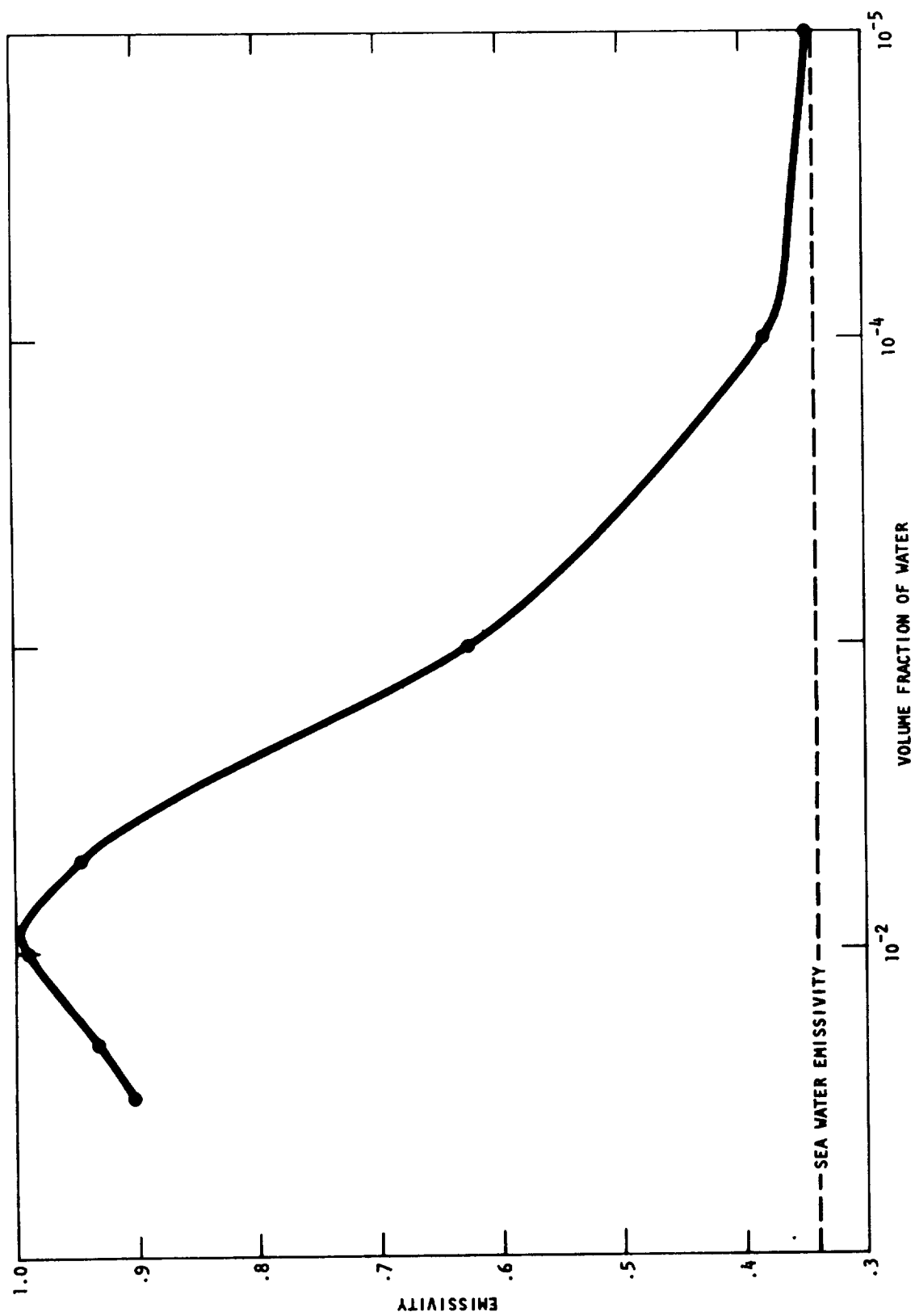


Figure 7.3 Variation of Emissivity With Composition for a 10 cm Thick Foam Layer on Sea Water

fractions near 10^{-2} , the emitted brightness temperature reaches the physical temperature of the sea surface; the magnitude of this effect falls off rapidly as the volume fraction decreases, corresponding to an emissivity change equivalent to 1.2°K at a volume fraction of 10^{-5} . For volume fractions still smaller, the effect decreases as $(\gamma_w)^2$, due to the fact that the first-order term in Equation (7.2) vanishes identically.

The thickness dependence of the brightness temperature at fixed composition for the covering layer is equally strong. As the phase $\text{Re}(fd)$ of the electromagnetic wave inside the layer passes through odd multiples of $\pi/2$ the emissivity oscillates to a maximum which can reach unity if $\sqrt{\epsilon_w} = \epsilon_f$, provided both dielectric constants are real. For a dissipative medium ($\text{Im}(\epsilon) \neq 0$), the emissivity at thickness large compared to the skin depth in the layer will approach the emissivity e^f of the layer material alone:

$$e^f = 1 - \left| \frac{1 - \sqrt{\epsilon_f}}{1 + \sqrt{\epsilon_f}} \right|^2 \quad (7.3)$$

The significance of these results is that the effect of foam on the brightness temperature varies from fractions of a degree to 200°K , depending on the thickness and composition of the foam layer. Even allowing for the fact that the fraction of a square kilometer of sea surface covered by foam rarely exceeds 10 percent, this uncertainty in its contribution to the brightness temperature is intolerably large. To adequately correct for the effects of foam it will be necessary to determine the variations in thickness and composition to be found on the world ocean and to determine how these parameters depend upon the meteorological variables such as wind speed and fetch.

7.3 EXPERIMENTAL STUDY

7.3.1 Set-Up and Operation

The experimental set-up employed to measure surface effects is shown in Figures 7.4, 7.5, and 7.6. It consisted of a square pool some 4.5 meters on a side and 15 cm deep, with the Prototype I radiometer and Potter horn antenna described in Hidy, et al (1969) looking down at an angle of 26° to the vertical from a height of 3.6 meters. The pool is in the far field and intercepts more than 97 percent of the power in the antenna pattern; it was located on the roof of the North American Rockwell Science Center in Thousand Oaks, where the view of the sky was unobstructed for angles greater than 5° from the horizon.

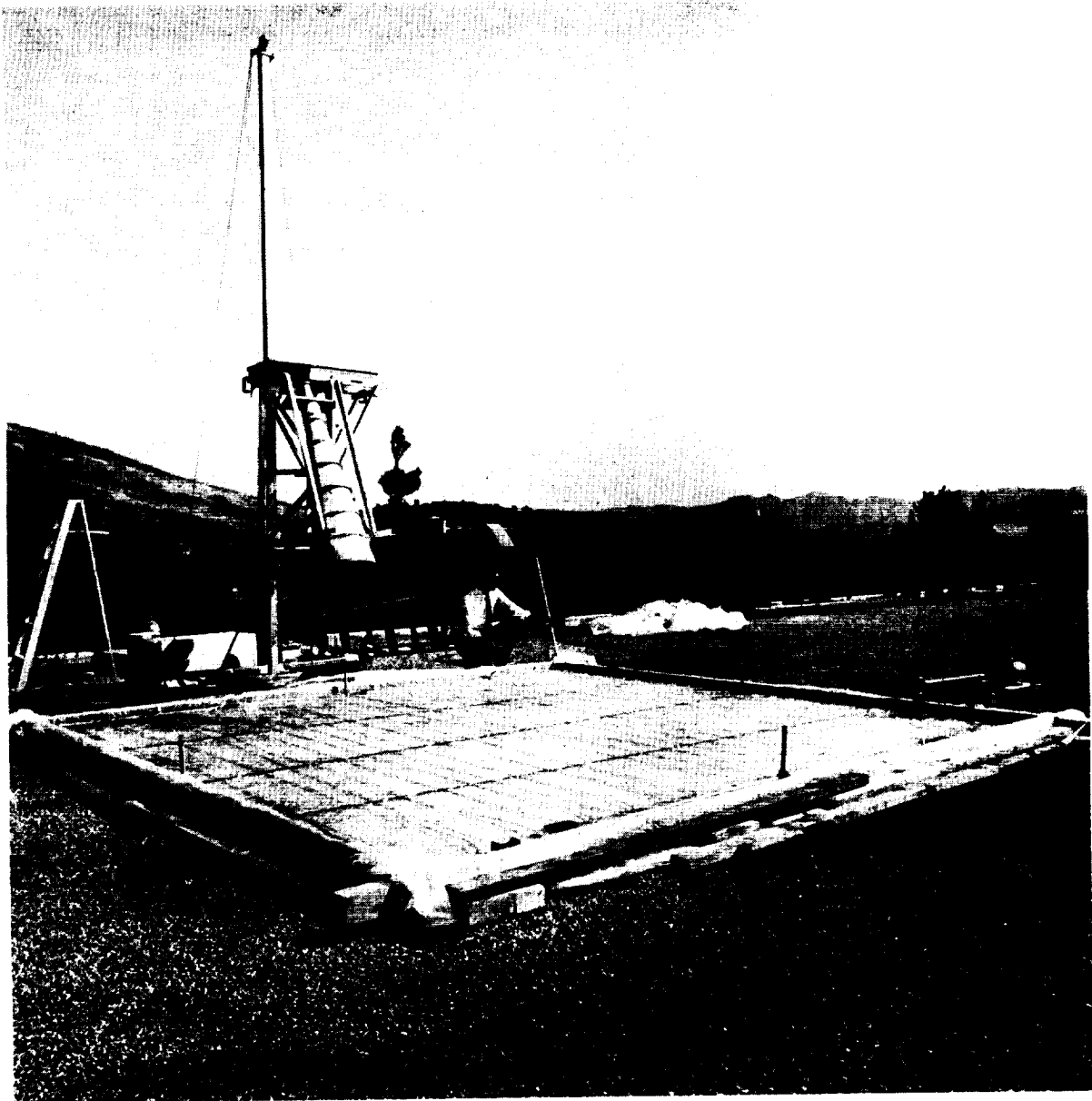


Figure 7.4 Front View of Rooftop Pool, Horn Lowered for Calibration



Figure 7.5 Side View of Rooftop Pool, Horn in Operating Position

With rare exceptions, measurements were made after sunset, when the prevailing winds were too weak to noticeably agitate the water surface. The radiometer, whose reference cold load was cooled to the temperature of boiling liquid nitrogen, was calibrated at the beginning and end of each evening's run by measuring the voltage corresponding to the difference in temperature between another liquid nitrogen load and an ambient temperature termination replacing the input from the antenna. The cold loads were refilled during the run when necessary to compensate for evaporation.

The whole radiometer was mounted on a rigid metal platform reinforced with I-beams to minimize the relative motion of the reference load, the radiometer electronics, and the antenna. Despite these precautions, flexure of this structure caused by the attached guy wires was found to affect the connection between the reference cold load and the radiometer electronics to the extent that the effective temperature of the load could be made to vary by more than 1°K . Consequently, great care had to be exercised to avoid stressing this platform once it was elevated.

Most of the measurements were made in circular polarization with a bandpass filter 40 MHz wide whose lower edge was at 2.660 GHz. A few measurements at 2.80 GHz were made on the effect of surface waves, but radar interference was encountered frequently in this band. The theoretical resolution of the radiometer operating with a one second integration time was better than 0.3°K , and the reproducibility of the measurements in general bore this out. Our absolute accuracy was probably no better than 1°K , owing to the connector troubles discussed above.

The water temperature in the pool frequently varied by 0.5°K from the SE corner to the NW, presumably due to air conditioning ducts beneath the roof. The brightness temperature observed by the horn consisted of three contributions: (1) emission from the water surface, (2) emission from the surroundings into the antenna sidelobes; and (3) reflection of the sky temperature into the horn by the water surface. The magnitude of these last two effects, calculated from observations on smooth, fresh water, totaled $5.7^{\circ}\text{K} \pm 0.2^{\circ}\text{K}$, on the average. The sky alone should contribute 3.5°K , so $\sim 1.0^{\circ}\text{K}$ came from the antenna side lobes.

A comparison of the brightness temperature observed for salt water of various salinities with that calculated from the dielectric constants measured by cavity perturbation is presented in Table 7-1. The calculated values are the sum of the smooth surface emission at 26° from nadir and the sky and roof contributions deduced above. The observed brightness temperatures have been obtained from the measured antenna temperature

Table 7.1. Smooth Water Observations on the Rooftop Pool

Salinity (%)	Water Temp. T_W (°C)	Rad. Temp. T_B (°K) (observed)	Dielectric Constant ϵ'	Imag. Part ϵ''	Emissivity $\bar{\epsilon}$	Corrected T_B (observ.) for horn losses (°K)	ΔT	T_B °K Calculated
.02	17.75	115	79.07	12.6	0.3617	110.6	5.70	
.02	18	115.5	79.05	12.5	0.3617	111.2	5.64	
.02	19	115.6	78.85	12.15	.3622	111.2	5.56	
.02	19.75	116.5	78.67	11.8	.3627	112.1	5.88	
.02	20.2	116.6	78.55	11.65	.3629	112.4	5.44	
.02	21	116.8	78.4	11.35	.3633	112.6	5.87	
.02	21.5	117.2	78.3	11.2	.3636	113.0	5.45	
2.22	17.25	113.9	73.6	33.6	0.3543	109.3		108.6
2.59	16.1	113.0	72.7	38.0	.3505	108.5		107.0
3.14	16.1	112.7	71.6	40.3	.3492	108.3		106.7
3.57	18.0	111.7	70.6	44.5	.3450	107.0		106.2
3.57	15.5	110.6	70.9	43.3	.3462	106.3		105.7
3.57	15.5	111.2	70.9	43.3	.3462	106.8		105.7
4.47	16.25	107.9	68.8	50.15	.3393	103.5		103.9
4.7	14.75	106.9	68.8	50.8	.3384	102.5		103.3
4.78	17.0	108	68.4	53.3	.3353	103.5		103.8
4.78	17.75	107.9	68.25	53.75	0.3348	102.5		103.3

by correction for the horn loss. The calculated brightness temperatures average 0.5°K less than the observed values, with a maximum disagreement of 1.6°K . Time variations in salt concentration of order 0.2 weight percent were observed during these runs, which are probably sufficient to explain the scatter in these data.

Sea Spray Simulation. Halfway along each edge of the pool a vertical section of pipe was extended 10 cm above the water surface and terminated in a spray head whose droplet fan was roughly horizontal and directed toward the pool center. The angular span covered by the fan was about 160° . These sections of pipe were connected along the bottom of the pool to a pump capable of forcing up to 19 liters of water per minute through the spray heads. In normal operation the pump drew from the pool itself, to avoid dilution problems when the pool was filled with salt water. The volume fraction of water averaged over the first ten centimeters above the pool was of order 10^{-5} at the highest flow rate; the exact value is uncertain because the average vertical velocity of the water droplets at the spray head is unknown. The most dense spray visibly obscured the surface of the pool, which is a condition rarely encountered on the open ocean.

Surface Films. Slicks of thickness 0.88 mm and 1.76 mm were obtained on the pool surface by pouring 5 gallons and 10 gallons of oil, respectively, onto the pool. Three different grades of oil were used: Velocite, a light machine oil; Lubrite, an SAE 10-weight motor oil; and crude oil from the Wilmington oil field in Long Beach. All three grades are expected to have dielectric constant ϵ_f about twice that of vacuum. Cavity perturbation measurements on Velocite and Lubrite gave values for ϵ_f/ϵ_v of 2.1 to 2.2.

Foam Simulation. Plastic tubing was laid along the bottom of the pool in parallel strands separated by about 20 cm, as illustrated in Figure 7.6. Air was forced through this network of hose and was allowed to escape through tiny holes in the hose as bubbles to the surface. The holes were spaced roughly 15 cm apart along the hose. The type of surface disturbance produced in this fashion is illustrated in Figure 7.7, which shows the pool surface at near maximum airflow rate where it takes on the appearance of a seething cauldron, and in Figure 7.8, which shows a side view of the bubbles rising from the hose toward the surface. This bubbling of the surface is a poor model for sea foam, since the size and spacing of the bubbles is much too large. However, this surface disturbance has the advantage that the size and distribution of the bubbles is directly measurable from photographs such as Figures 7.9 - 7.12 and therefore permits an accurate comparison with theory.

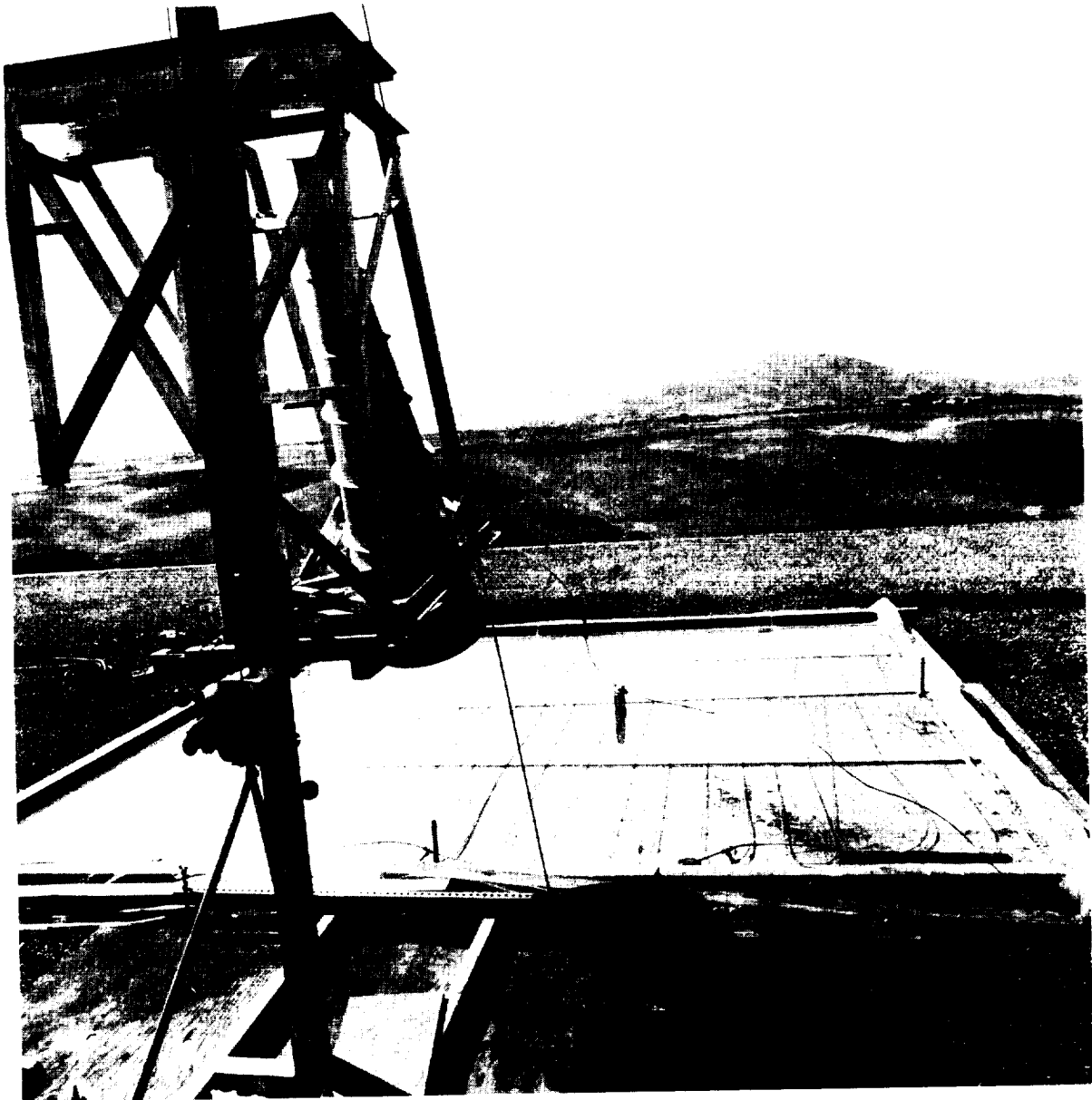


Figure 7.6 Back View of Rooftop Pool Showing Air Hose Used in Foam Simulation

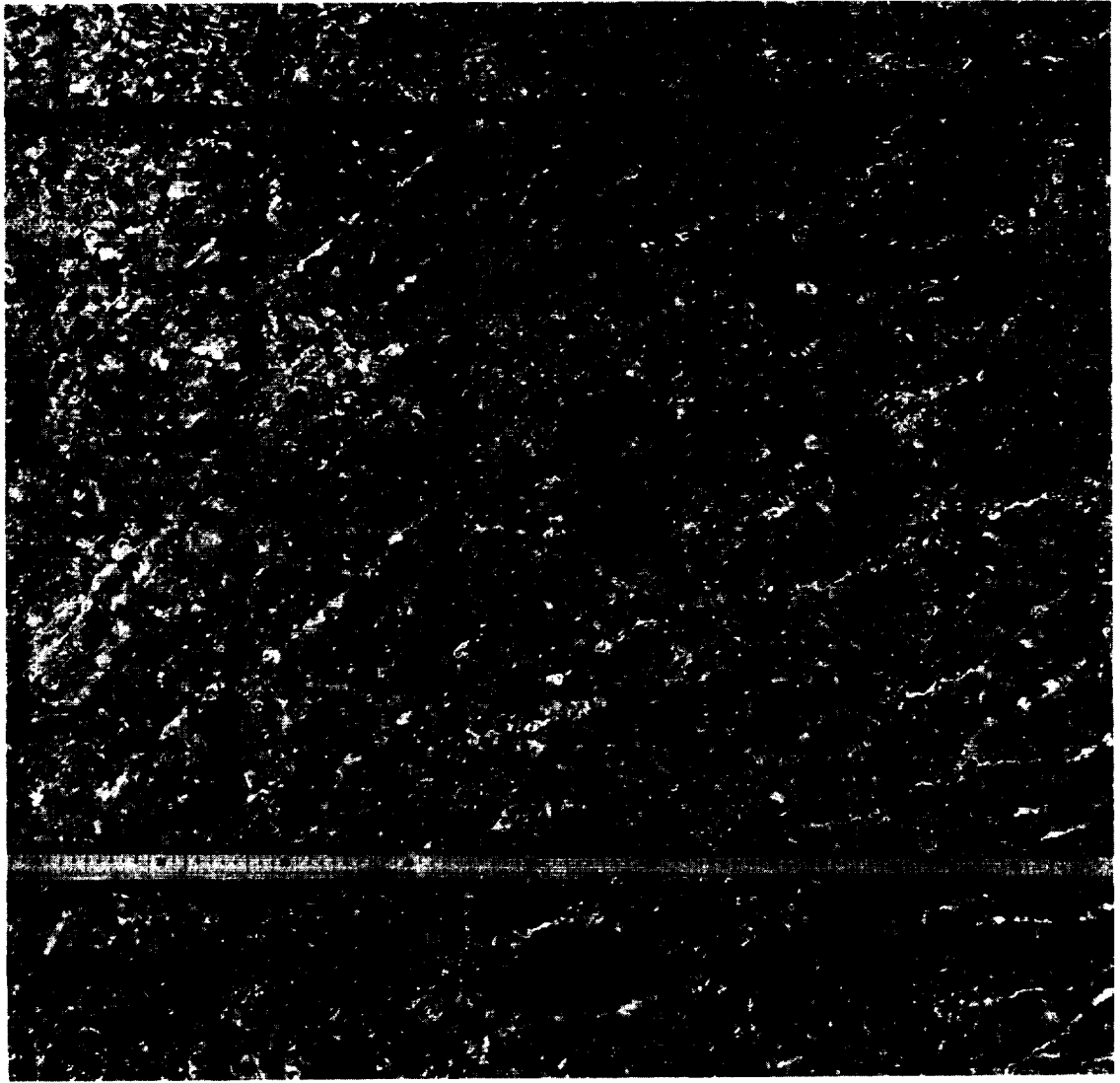


Figure 7.7 Surface of Pool at Maximum Air Flow Rate (Foam Simulation)

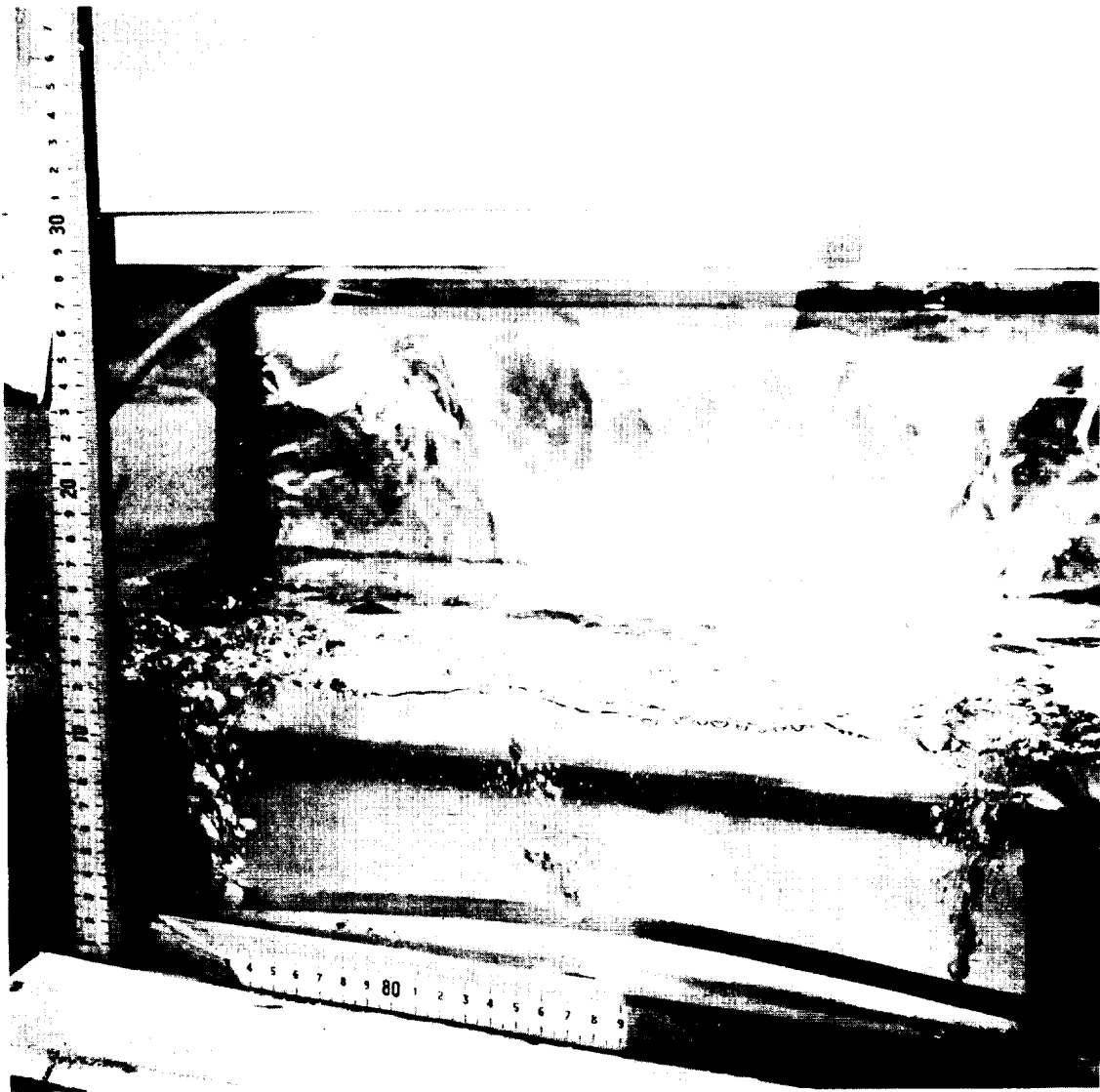


Figure 7.8 View of Bubbles Rising From Air Hose to Water Surface



Figure 7.9 Surface of Pool at Air Flow Rate of 0.94 Liters Per Second
or 3% Coverage



Figure 7.10 Surface of Pool at Air Flow Rate of 1.88 Liters per Second
or 6% Coverage



Figure 7.11 Surface of Pool at Air Flow Rate of 2.83 Liters Per Second or 12.3% Coverage

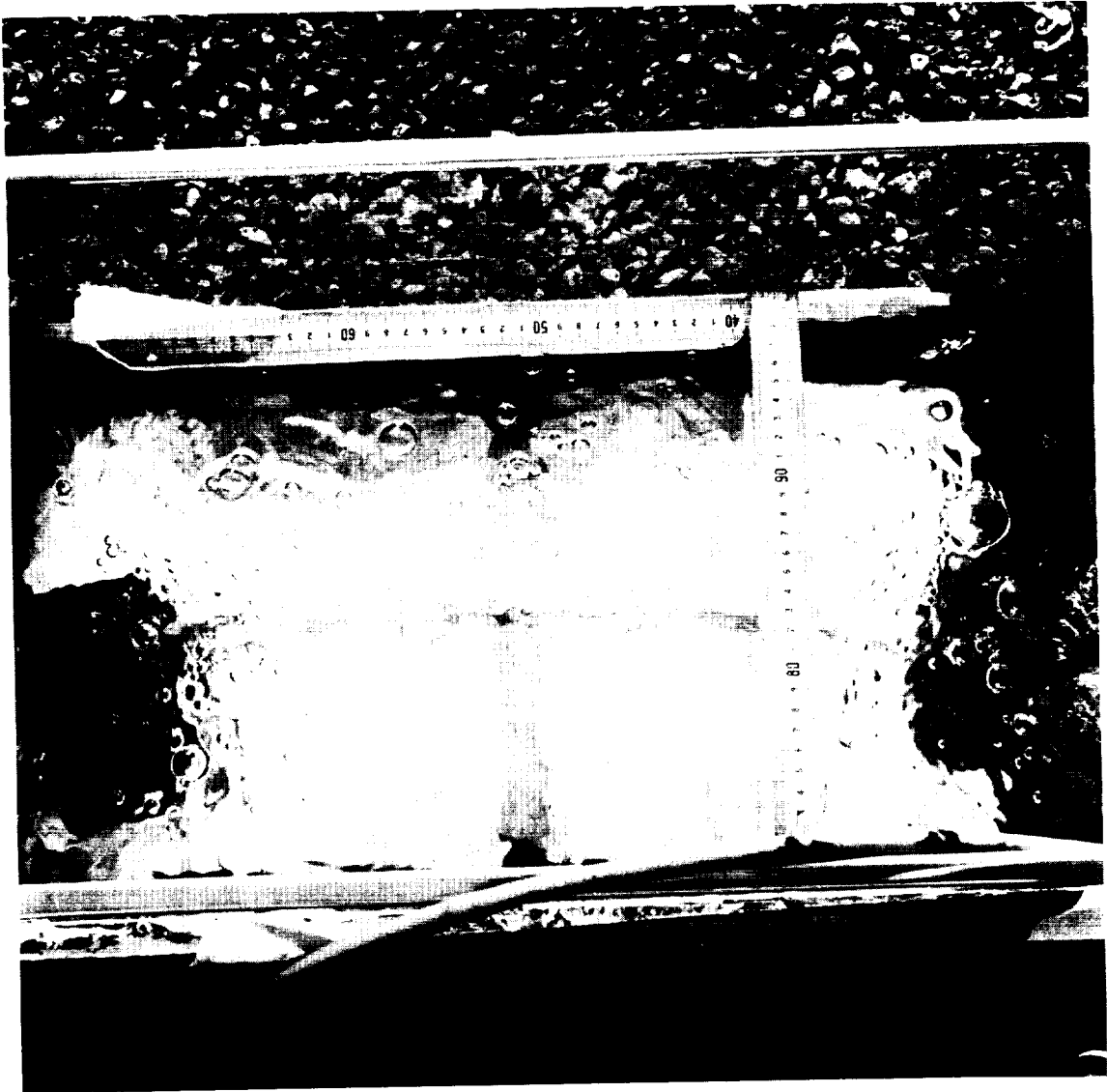


Figure 7.12 Surface of Pool at Air Flow Rate of 3.77 Liters Per Second
or 20% Coverage

7.3.2 Results of Experiments

Spray. No effect on the brightness temperature was observed except at the highest flow rate of 19 liters per minute, which gave an increase of roughly 0.4°K for both fresh and saltwater. The dielectric-layer model gives an effect of this magnitude for a volume fraction of 0.5×10^{-5} water in the first 10 cm above the pool surface, which is consistent with the estimated droplet density.

Oil Slicks. The most striking feature of the observations on oil films was a large, transient rise in the brightness temperature which occurred immediately upon addition of the oil, or when the oil was stirred sufficiently to expose the water surface. This rise decayed from an initial value near 10°K to the vicinity of the value expected on the dielectric-layer model with a time constant of 1-2 minutes as shown in Figure 7.13. A plausible explanation of this large effect is that water droplets become temporarily trapped in the oil during mixing, raising the average dielectric constant and therefore the brightness temperature. A peak volume fraction of 15 percent water in the oil is sufficient to give the observed effect. In support of this interpretation, it was found that patches apparently containing numerous small water bubbles appeared on the surface of the oil during mixing and were observed to disappear with about the same time constant as the brightness temperature effect. Any direct thermal contribution from hot oil could be ruled out, since the oil temperature before addition averaged 2° cooler than the water. Possibly this mixing effect can account for the anomalously large microwave radiometric temperatures which have been reported over the Santa Barbara oil seepage of 1969 and over recent controlled oil spills. (Microwaves, 1970, and Chandler, 1970)

Considerable difficulty was experienced in determining the steady-state value of the brightness increase caused by the oil film, as is evident from the large scatter in the data presented in Tables 7.2 and 7.3. The primary contributor to this scatter was oscillation about the steady-state value of the sort illustrated in Figures 7.14 and 7.15. Apparently, the tendency of the oil to puddle on the pool surface, which was most pronounced for the crude oil, was combined with a slow drift of the puddles in and out of the center of the horn pattern to produce this oscillation. Despite these problems, the results agree qualitatively with the 1°K per mm predicted by the dielectric-layer model. Naturally occurring slicks, which are seldom more than microns thick, are therefore expected to have a negligible effect on the brightness temperature.

Bubbling. The brightness temperature increase caused by bubbles on the water surface is plotted versus the fractional area covered by the bubbles in Figure 7.16, for both fresh and salt water. The measured effect is roughly linear, with a slope of 0.3°K per percent of area covered. Analysis of this

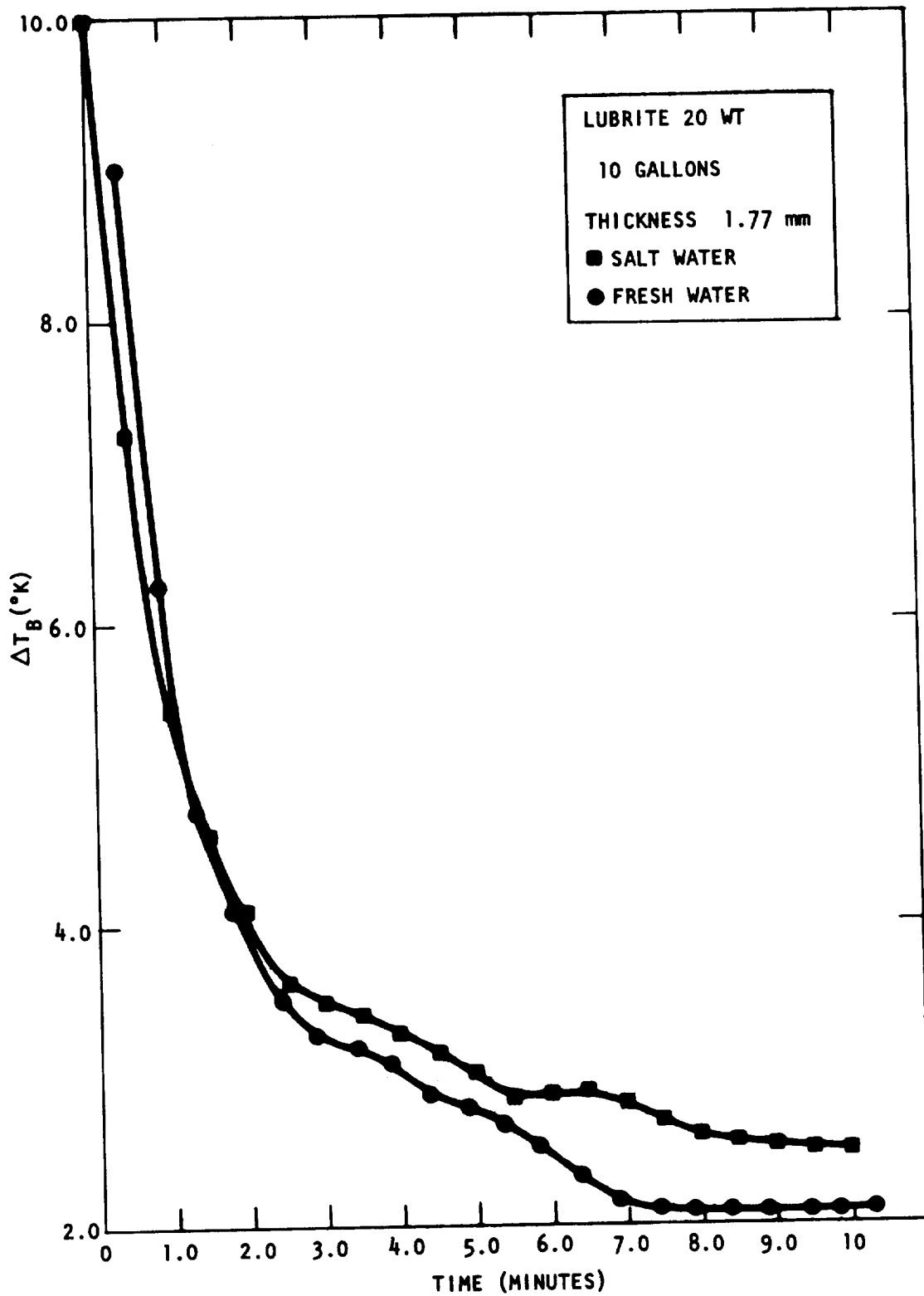


Figure 7.13 Transient Response of Oil on Water Surface (10 minute period)

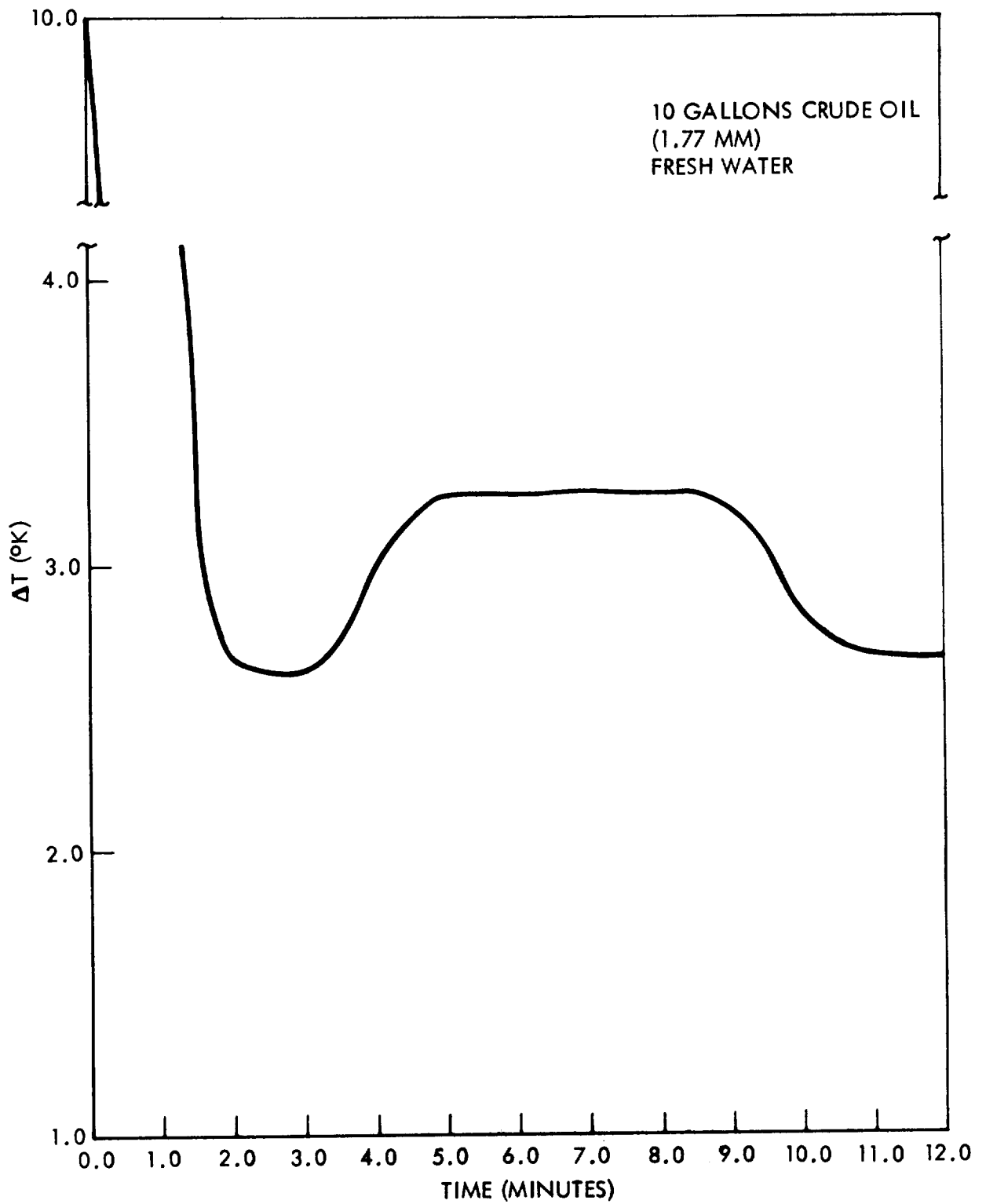


Figure 7.14. Transient Response of Crude Oil Poured on Fresh Water Over 12 Minutes

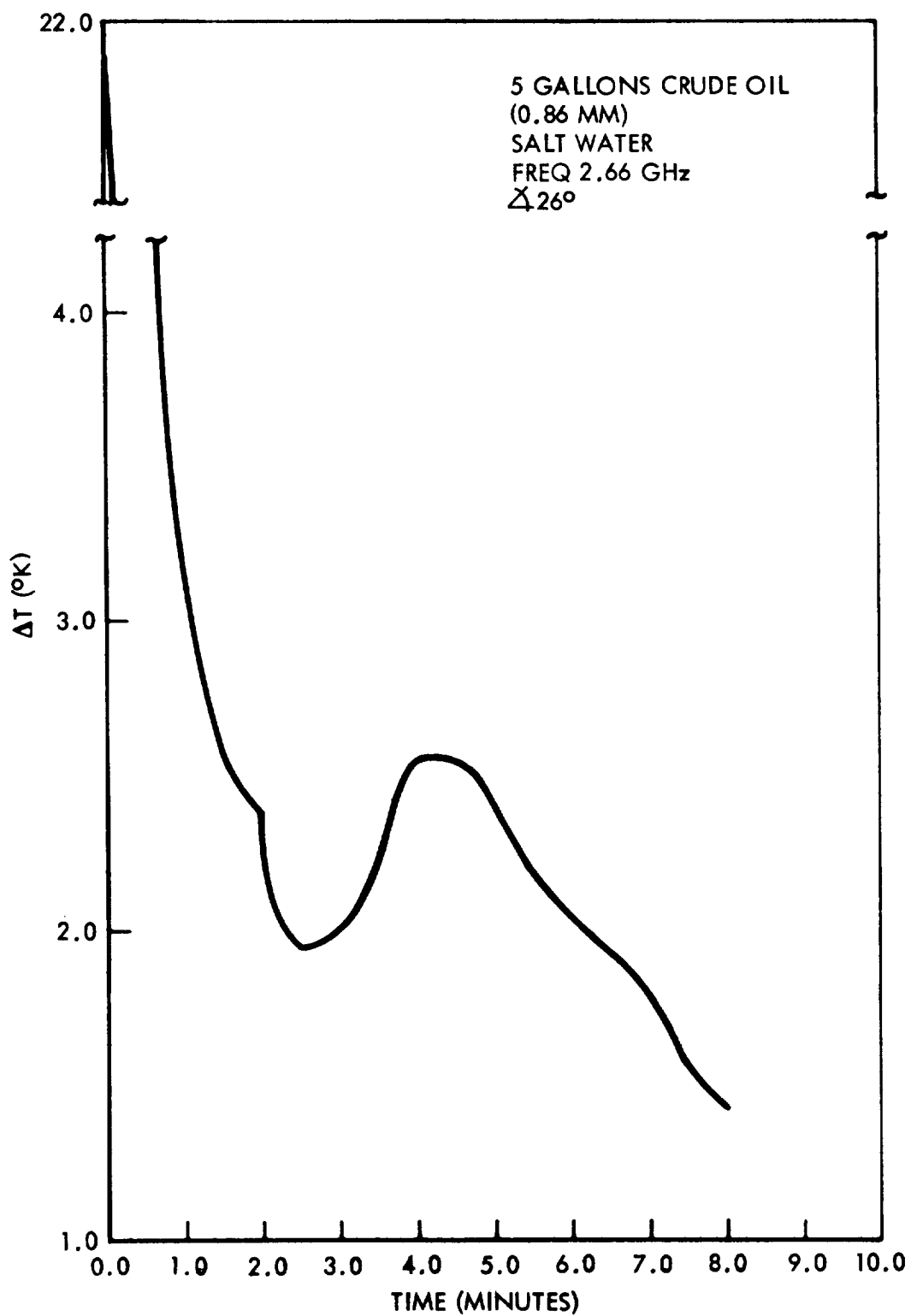


Figure 7. 15. Transient Response of Crude Oil on Salt Water

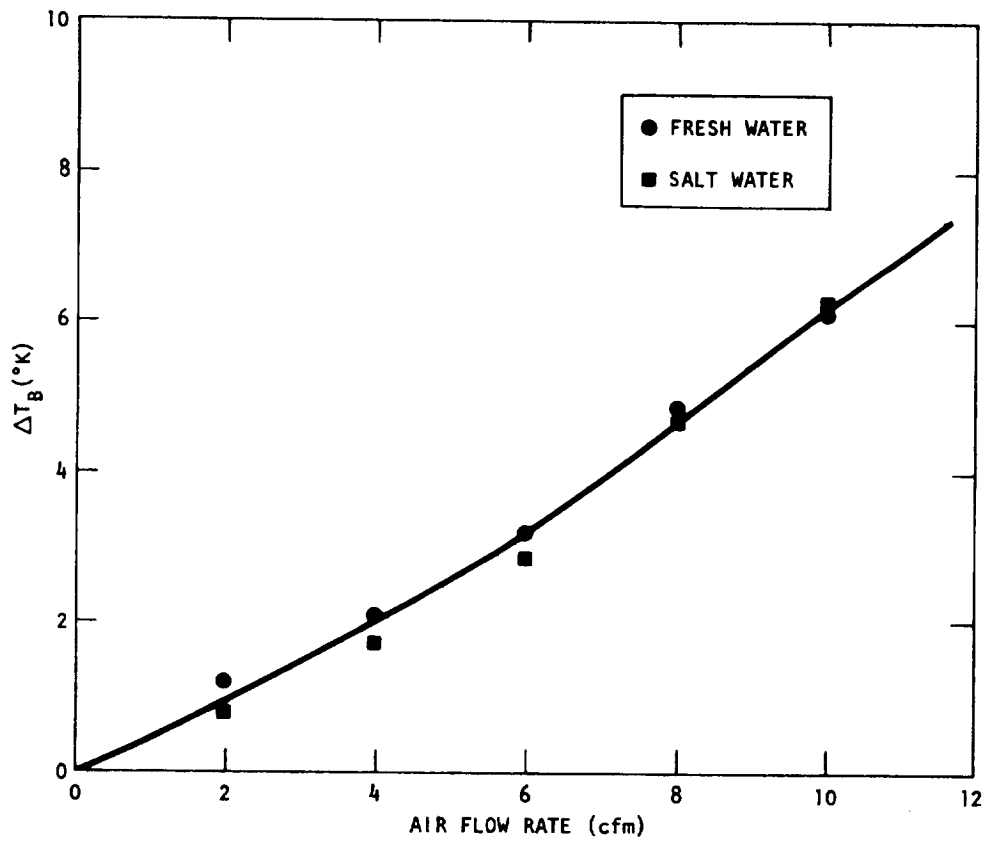


Figure 7.16 Effect of Bubble Formation on Antenna Temperature

effect in terms of the dielectric-layer model is complicated by the following factors: a) bubble wall thickness is uncertain to within a factor of ten; b) contributions from bubbles just beneath the water surface are difficult to estimate; and c) the effect of wave disturbances caused by bursting bubbles is unknown. However, one can match the observed increase within the model by assuming that the thickness of the bubble walls was on the order of 100 microns, and that the effective layer thickness was the average bubble height. Further experimental and theoretical work are needed to determine the exact nature of the observed effect.

7.4 SUMMARY AND CONCLUSIONS

From these exploratory experiments on microscale disturbances on water surfaces, it is concluded that:

- (1) Sea spray and naturally occurring surface films will not constitute a significant spurious factor in the brightness temperature measured by an S-Band radiometer in an aircraft or in a satellite.
- (2) Sea foam is expected to be a potentially large factor in the apparent brightness temperature of the sea surface. The extent of increase in brightness temperature associated with foam will depend on the thickness and composition of the foam layer. Further, experiments and field observations are necessary to seek simple correlations between brightness temperature and such measurable parameters as foam coverage.

Table 7.2. Oil Film Effect on Brightness
Temperature of Salt Water

Oil Type	Thickness (mm)	ΔT (Temp. Increase $^{\circ}K$)	
		Time Delay	
		5 min.	10 min.
Velocite	0.88	0.8	0.53
	1.77	0.96	0.84
Lubrite	0.88	2.0	
	1.77	3.25	2.38
Crude Oil	0.88	2.43	1.7
	1.77	4.25	2.31

Table 7.3. Oil Film Effect on Brightness
Temperature of Fresh Water

Oil Type	Thickness (mm)	ΔT (Increase $^{\circ}K$)	
		Time Delay	
		5 min.	10 min.
Velocite	0.88	1.1	0.37
	1.76	2.7	2.1
Lubrite	0.88	1.25	1.25
	1.76	2.8	2.1
Crude Oil	0.88	1.26	
	1.76	3.2	3.0

REFERENCES

- Blanchard, D. , 1963, "Electrification of the Atmosphere," Progress in Oceanography, Vol. I, M. Sears (Ed.) Pergamon Press, N. Y. p. 151.
- Chandler, P. B. , 1970, "Remote Sensing of Oil Polluted Water," Space Division Report SD 70-377, North American Rockwell Corp.
- Droppleman, J. D. , 1970, "Apparent Microwave Emissivity of Sea Foam," Journal Geophys Res. 75, 696
- Hidy, G. M. , K. W. Gray, W. N. Hardy, W. F. Hall, W. W. Ho, A. W. Love and E. J. Thompson, Dec. 1969, "S-Band Radiometer for Measurement of Sea Temperature," North American Rockwell Science Center Report SCTR-69-31, 60 p.
- Monahan, E. C. , 1968, "Sea Spray as a Function of Low Elevation Wind Speed, Journal Geophys Res. 73, 1127
- Microwaves, 1970, "Microwave Radiometry to Spot Oil Spills," 9, 20.
- Munk, W. H. , 1947, "A Critical Wind Speed for Air-Sea Boundary Processes," J. Marine Res. 6, 203
- Nordberg, W. , J. Conaway, D. B. Ross and T. Wilheit, 1971, "Measurements of Microwave Emission from a Foam-covered, Wind-driven Sea," J. Atmos Sci., 28, 429-435.

8.0 INTERPRETATION OF 1969 EXPERIMENTAL FLIGHTS

8.1 INTRODUCTION

Even before undertaking this study program for NASA, NR conducted a preliminary development effort to demonstrate the feasibility of making precision radiometer observations at S-Band in aircraft. This project was described by Hidy, et al (1969) and is reviewed here as a prelude to considering the data obtained during the early DC-3 flight program.

8.2 TEST PROGRAMS

The initial program for field testing the performance of the NR Prototype I S-Band radiometer was carried out in 1969 and consisted of two phases. The first phase comprised ground-based observations with the radiometer mounted on a scaffolding to look at fresh water in Morris Dam Lake, Azusa, California. In the second phase, limited flight tests were conducted with the radiometer mounted in the University of California, San Diego, Scripps Institute of Oceanography DC-3 aircraft.

8.2.1 Morris Dam Experiments

The first performance tests of the NR instrument were conducted during the summer of 1969 at Morris Dam. At this time the radiometer was used within a frequency range of 2.800 ± 0.042 GHz, corresponding to the originally chosen design configuration. The Morris Dam site was selected because it was quiet with respect to radar interference. Unfortunately, it suffered from two disadvantages in that surface roughness conditions were severely limited and the lake is surrounded by very steep hills, rising several hundred feet above the water. The topographical situation which shielded the area from radar interference, also may have contributed to an error in measurement of apparent water temperature because of the reflection of thermal radiation off the water from the "hot" mountains and the surface of the dam into the antenna beam.

Generally, sequences of preliminary tests were made at Morris Dam to examine the stability of the termination loads and electronics, as well as the reproducibility of the coaxial line connectors. In addition, observations of the water surface were made to compare the measured apparent temperature with that calculated from the molecular temperature.

The instrument was located on a scaffolding on which was a cart that could be rolled out over the water but still provide access to the device during calibration. The antenna was fixed at an angle of incidence of approximately 20° .

During the tests, the radiometer was repeatedly calibrated using termination loads containing liquid nitrogen, liquid argon, and liquid natural gas. Using these three points and numerous microwave measurements taken in the laboratory, a calibration curve could be deduced to estimate the antenna temperature within a precision (reproducibility) of $\pm 1^\circ\text{K}$ or less. The resolution of the measurements approached 0.3°K with a 1 sec. integration time.

The water temperature was measured directly either in bulk with a mercury-in-glass thermometer, or by a thermocouple array designed to measure the vertical temperature distribution near the water surface. The "bucket" temperature varied during the summer program from 17°C to 27°C . It was found that the temperature difference between the cooler surface water and the water 0.5 cm below the surface did not exceed 0.4°C . Therefore, for most cases, the water temperature was taken as the bucket temperature.

The surface roughness was estimated either qualitatively by eye or by a semi-quantitative method evaluating glitter photographs. In general, the wind-generated ripples on the lake were very weak, corresponding to small waves of length 3-20 cm and amplitudes of 0.1-2 cm. During one series of tests, however, an effort was made to generate more severe disturbances of the surface by running a motorboat near the area observed by the radiometer. The boat produced large gravity waves in its wake with wavelengths up to about 2-3 meters, with amplitudes of 20-30 cm. The waves appeared to be symmetrical in shape.

Despite the problems encountered in this initial usage of the radiometer, it was possible to obtain some limited results on the apparent temperature of fresh water. Typical data for the antenna temperature taken during the Morris Dam program agreed to within $\pm 1^\circ\text{K}$ of the expected value. The corrections applied to the measured antenna temperature involved the calculated antenna and connector losses and the reflected sky temperature. Based on the estimated antenna loss, the transmission coefficient was 0.982 for the Potter horn antenna and its transmission line.

The effect of roughness equivalent to small wind waves amounted to approximately 1°K in apparent temperature. If the surface temperature of the water is taken to be $\sim 1^{\circ}\text{K}$ cooler than the bucket temperature, due to evaporation, the radiometer may be recording a temperature too warm by $\sim 1^{\circ}\text{K}$. There should have been a tendency for the radiometer to give an antenna temperature systematically too warm as a result of (1) the influence of the reflected emission from the mountains surrounding the lake, (2) the fact that the antenna does not receive quite a circularly polarized signal, and (3) oil films on the surface, which were observed under calm water conditions.

It was felt that the performance of the prototype radiometer was satisfactory enough to warrant the extension of the field tests to aircraft observations over the ocean, where more severe surface roughness conditions could be expected.

8.3 AIRCRAFT FLIGHT TEST PROGRAM

After further improvements, the Prototype I instrument, including the addition of an automatic gain control, was flown on the University of California Scripps Institute of Oceanography (UCSD-SIO) DC-3 over the Pacific Ocean in late October and early November, 1969. This aircraft was chosen so that the instrument could be flown with the infrared radiometers described by McAlister (1964). In this way, the microwave device could be compared with an instrument known to measure sea surface temperatures to an accuracy of $\pm 0.1^{\circ}\text{K}$ under favorable observational conditions.

The set up of the radiometer in the aircraft is sketched in Figure 8.1. The instrument was arranged in such a way that the Potter horn antenna pointed aft at an angle of 26° to the floor of the aircraft. Since the DC-3 cruises tail down at 4° below the horizontal plane, the actual horn angle to the zenith is 22° during "level" flight. The horn is rigged so that it protrudes 30 cm at the forward edge and 8 cm at the rear edge from the bottom of the aircraft. A streamlining section was added in front of the antenna to provide a more aerodynamically compatible unit and to help minimize vibrations associated with the aircraft slipstream.

Inside the DC-3, the radiometer was mounted so that calibrations could be made with two cryogenic loads, or the antenna could be connected to one side of the Dicke Switch. The two removable sections of the antenna, one with a circular polarizer and one linear, could be interchanged in flight.

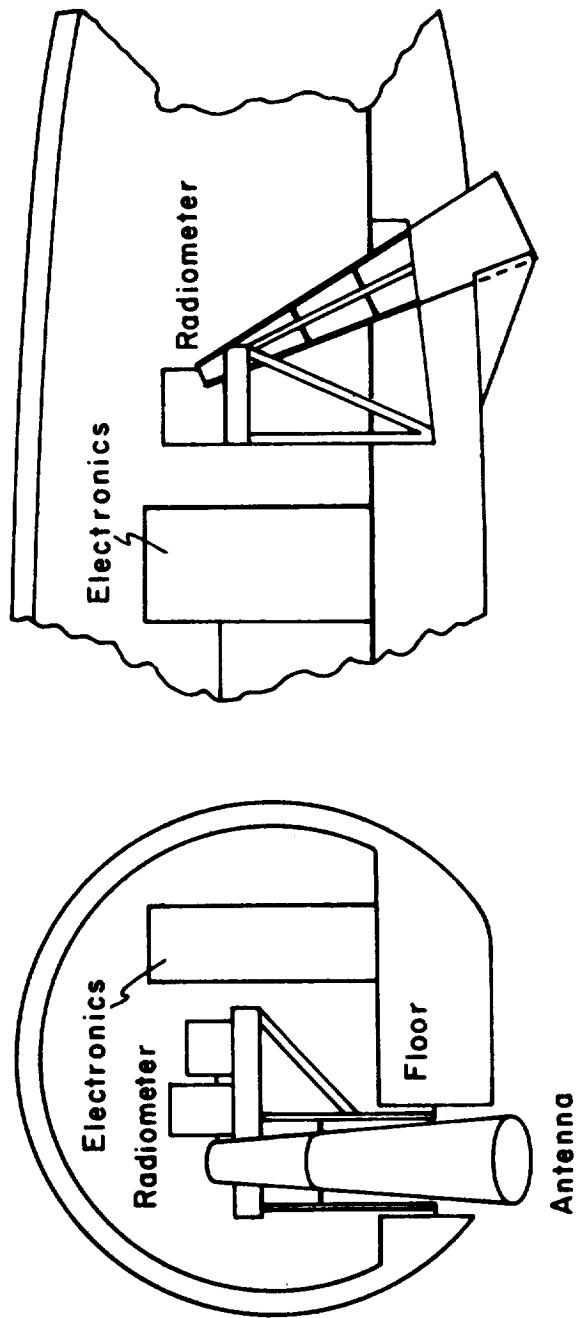


Figure 8. 1. Radiometer Arrangement in SIO DC-3

Installation and operational tests of the radiometer on board the aircraft indicated that the instrument exhibited minimal susceptibility to noise in the aircraft electrical system. Inside the aircraft, the peak to peak noise level with both cryogen loads on the radiometer was $\pm 0.2^\circ\text{K}$, with a one second time constant.

Two flights were made in directions south and west of San Diego, the first on October 29, 1969, and the second on November 5, 1969. The weather conditions and sea state for these two days are listed in Table 8.1. The courses for the two flights are drawn in Figure 8.2. On both days a relatively light sea was overflown, but the cloud conditions were quite different. On the first day, clouds were stratocumulus in nature and scattered and broken. The second day was completely overcast with thicker stratus containing some light rain. In the latter case, the cloudiness was a forerunner of a weak frontal system passing through the region.

The main purpose of the two flights was to check the performance of the radiometer under aircraft conditions. Of primary importance were measurements of relative temperature changes and absolute molecular temperatures as compared with the two frequency infrared radiometer systems of Scripps Institution of Oceanography (See also McAlister, 1964). In addition a number of exploratory experiments were conducted including: (1) variation of antenna temperature with altitude from 45m to 1200m, (2) variation of antenna temperature looking through clouds, (3) change in antenna temperature with angle of incidence, and (4) variation in antenna temperature with rotation of the antenna into the sun.

It should be noted at this point that the microwave radiometer operated continuously throughout both flights except for radar interference. Relative temperature changes and nearly constant antenna temperatures were observed through a variety of (fair, mildly stormy) weather conditions, as will be seen below. However, the infrared radiometer system of SIO, in contrast, was unable to operate effectively near mid-day in sunny conditions because of interference from sea glitter and was not operable in or above clouds.¹

¹ It has been found that the SIO system can achieve its very high accuracy and precision only under special conditions where the sun is near the horizon and at altitudes only up to a few thousand feet because of sun glitter and atmospheric attenuation.

Table 8.1

Weather and Sea Conditions During San Diego Flights

Date	Estimated Winds	Sea State	Weather	Remarks
10-29-69 1230-1530 PST	Approximately 4 knot winds from 280° mag. reading. (Pilot-observer estimate)	1 meter swell with light sea, no white caps, 1 meter waves traveling from 160-170° magnetic reading.	Scattered and broken stratocumulus deck with base 480m; later, mostly clear with haze to 480m clouds 300m thick	Winds light and variable. Cloud deck was associated with fog breaking up over coastal region.
11-5-69 1530-1910 PST	1530-1630 winds at 5 knots from 180° 1630 - winds increased to 12-13 knots (pilot observation and check at San Clemente weather station)	1-1.5 meter swell with light sea. 1530-1630 no white caps. After 1630 white caps covering 1% of surface.	Almost completely overcast with base 0.7 km and 0.7 km thick. Light rain on occasion	Clouds and gusty winds associated with passage of a weak storm front along Southern California coast.

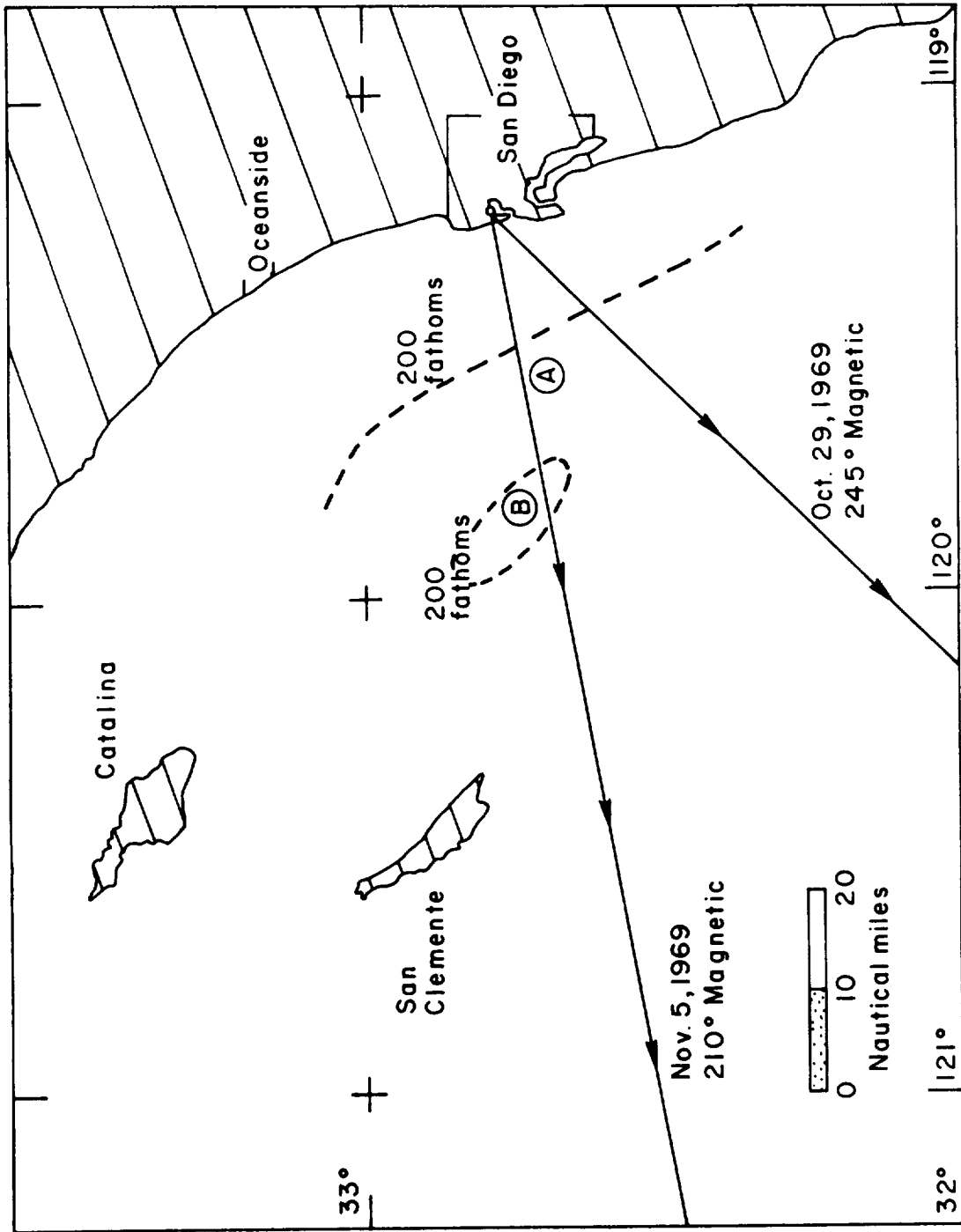


Figure 8.2. Flight Trajectories over Pacific Ocean

8.3.1 Measurements of the Apparent Sea Temperature

Some typical results for measured antenna temperatures during the DC-3 flights are listed in Table 8.2. The aircraft parameters such as heading and altitude are included with estimated sea temperature either from the infrared radiometer or from independent surface observations. The data indicated that the observations from the microwave instrument were consistent from flight to flight. Furthermore, the microwave radiometer detected relative molecular temperature variations which were consistent with the infrared detector. The antenna temperatures were corrected to give values of brightness temperature by taking into account sky reflection and the estimated antenna loss (0.081 db). Using an unpolarized emissivity⁽¹⁾ for sea water of $\bar{\epsilon} = 0.341$ (24.5°C), the brightness temperature of the sea measured by the radiometer was found to be 6-7°K greater than that calculated from the molecular temperature (Hidy et al., 1969). The value of $\bar{\epsilon}$ used in this calculation was based on the only experimental measurements of dielectric properties of sea water available at that time. It was later thought to be too small (Hidy et al., 1970), and new calculations were made based on $\bar{\epsilon}$ of 0.351. The increased smooth water emissivity reduced the deviation between the corrected measurements and the calculated brightness temperature to 3-4°K. The remaining difference was assigned to uncertainties in salt water emissivity, instrument losses, and inadequate accounting of surface roughness. The smooth water dielectric properties of sea water had to be measured accurately.

The Potter horn was designed for operation at a narrow frequency band centered at 2.80 GHz. Because it was found during the first DC-3 flight that radar interference prevented the use of the radiometer at this frequency, a change was made to a more "quiet" region at 2.66-2.67 GHz.

It was possible that the sun also contributed to the deviation in observed temperature in the DC-3 flights. During the second flight, the aircraft flew over a region of a single break in the clouds about 2-3 mi. in radius where the sun was shining through. The microwave radiometer recorded a 0.3°K increase in antenna temperature over the sunny area as compared with the surrounding overcast covered regions. This increase is likely to be a measure of the reflected solar radiation at microwave frequencies (see also Section 6).

Though no dependence on zenith angle of the horn could be isolated, an asymmetry in antenna temperature was detected when the aircraft was flown slowly in a circle. The aircraft was set at a bank of 5° or less during the circular flight path, and a pattern of antenna temperature was observed as indicated in Figure 8.3 with angles shown as aircraft headings.

$$^1 \epsilon = (\epsilon_{\perp} + \epsilon_{\parallel}) / 2$$

Table 8.2 Typical Data From DC-3 Flights

Time ⁵ PST	Distance From San Diego	Altitude (km)	Measured Antenna Temp (°K)	Molecular Sea Temp. (°K)	Estimated ² Brightness Temp (°K)	Measured Brightness Temp (°K)	Remarks
1408	150nm/210°mag	0.6	111.9	291.4 ¹	100.8	104 ± 1	(Circular polarizer) (scattered clouds)
1421	140nm/50°mag	0.6	111.5			103 ± 1	
1534	30nm/245°mag	0.3	112.7	292 ³	101	105 ± 1	Under clouds
1548	58nm/245°mag	0.6	113.2	292 ³		105 ± 1	At cloud base
1554	73nm/245°mag	1.2	114.5	292 ³		106 ± 1	Above clouds diff between 2-3 identified at ocean temp
1559	78nm/245°mag	0.21	113.9	292 ³		106 ± 1	Below clouds
1635	150nm/245°mag	0.3	113.1	292 ³		105 ± 1	Under clouds
1638	145nm/245°mag	0.9	113.8	292 ³		105 ± 1	Above clouds
1641	145nm/245°mag	0.3	113.3	292 ³		105 ± 1	Under clouds, light rain
1700	130nm/065°mag	0.13	113.4	291.40 ⁴	100.8	105 ± 1	SIO IR Rad. operating over 1 mile avg.
1703		0.3	112.4	290.07	100.4	104 ± 1	SIO IR Rad. operating over 1 mile avg.
1706		0.21	112.9	290.17	100.4	105 ± 1	SIO IR Rad. operating over 1 mile avg.
1750	15nm/065°mag	0.3	111.8			104 ± 1	Crossed over a thermal front equivalent to 3.5°K
1753	5nm/065°mag	0.3	112.6			104 ± 1	(13-14) molecular temp. Return and reproduced thermal gradient

¹ Only one measurement was made on October 29 because of IR interference from sun glitter. Series of SIO flights on October 30th indicated essentially the same temperature over the same area.
² Based on a smooth sea water emissivity (19°C), salinity 32.2%, e = 0.346.
³ Average sea temperature from San Clemente Station also confirmed by the U.S. Navy Fleet Numerical Weather Facility estimates.
⁴ Infrared radiometer observations.
⁵ The first two results are for Oct. 29, 1969. The remainder of the results were taken on Nov. 5, 1969.

There is a definite distortion in signal on this day with the elongation oriented in direction of the sun. The distortion amounted to $\sim 1^\circ\text{K}$ in antenna temperature. Similar circular flight patterns were carried out on under completely overcast conditions during the second flight. No asymmetry in antenna temperature was observed in this case. This flight was made later in the day, and the sun was nearer the horizon than the first run.

The experience of the DC-3 flight program pointed to several areas of uncertainty in interpreting the radiometer observations uniquely in terms of sea temperature. Indeed, one of the principal aims of the current study program was to study the "interfering" factor further to evaluate the flight data better.

8.3.2 Instrument Tests

To improve our interpretation of the DC-3 flight observations, further studies of the performance of the NR Prototype I radiometer, described by Hidy, *et al* (1969) first had to be conducted. Several studies of the VSWR and ohmic losses of the Potter horn antenna and General Radio (GR) coaxial coupling lines were made. It was found that the VSWR of the antenna varied considerably from nearly unity to more than 1.10 over the frequency range used during the DC-3 flights. Attempts to adjust the VSWR of the antenna to be less than 1.05 over a $\pm 20\text{ MHz}$ range about 2.67 GHz were not too fruitful. The effect of the uncertainty in VSWR at the center frequency of 2.67 GHz used during the flights, combined with the possible changes in antenna performance associated with surface corrosion are difficult to assess, and are expected to reduce the accuracy of the observation to $\sim \pm 1^\circ\text{K}$ from the anticipated earlier estimates of $\leq \pm 0.5^\circ\text{K}$.

Recently, during the NASA Convair 990 flight program, conducted under NR IR&D funds, a new external calibration load was developed. This device makes it possible to calibrate directly the ohmic and mismatch loss of the antenna-connector hardware up to the Dicke switch in an aircraft mounted radiometer. The new load has been used to determine the ohmic loss of the Potter horn antenna-GR connector combination used on the NR Prototype I radiometer. The procedure is described below.

8.3.3 External Load Design and Application

The external load was constructed with a porous, high loss microwave absorber, covered by a layer of non-porous styrofoam and contained in an insulated metal box, (see Figure 8.4). The lossy absorber has many

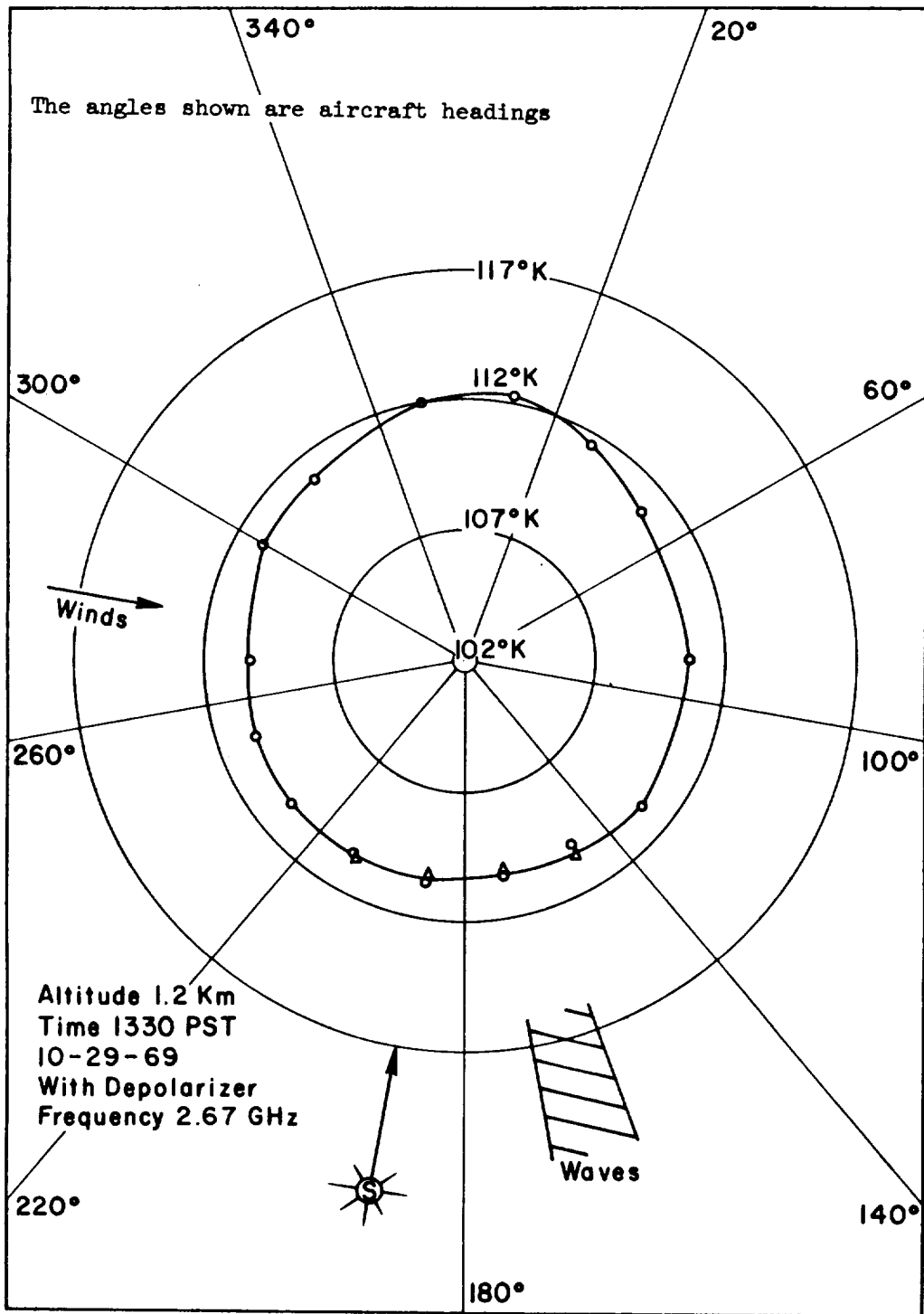


Figure 8.3 Antenna Temperature During a Circular Flight Path

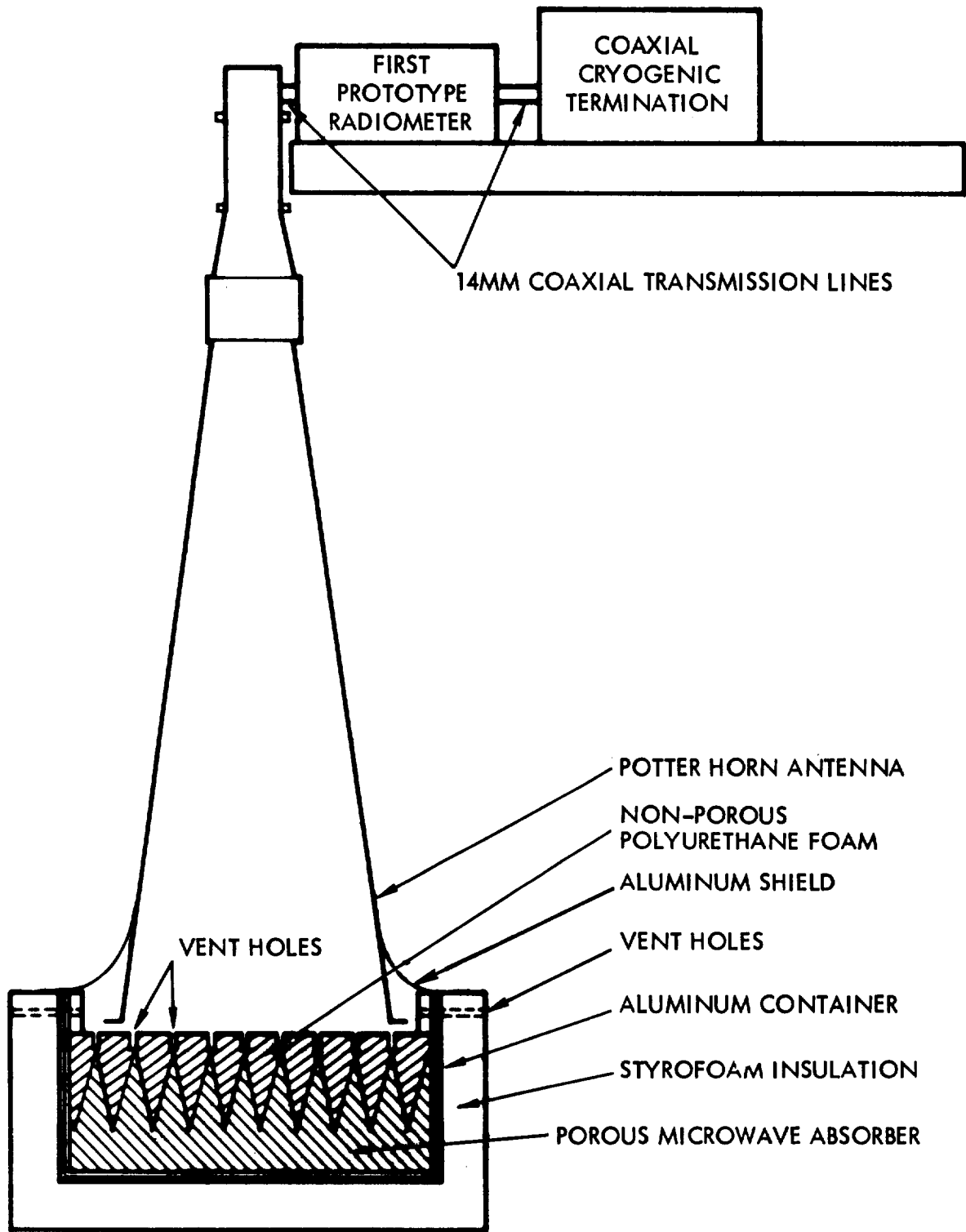


Figure 8.4. Schematic Diagram of Cryogenic Load for Aircraft Calibration

pyramidally shaped cones to reduce reflections. Its porosity allows penetration of the cryogen and therefore insures the maintenance of the absorber at the boiling point of the cryogen. The cryogen used was liquid nitrogen and to force the liquid to take the shape of the absorber, thereby avoiding additional reflections, a layer of low loss non-porous styrofoam was used to fill the spaces between the cones of the absorber. Small holes were drilled through the styrofoam at the point of each cone to permit the venting of the vaporized nitrogen. This combination of absorber and foam was then placed in an aluminum box. The aluminum serves two purposes. First, it electrically insulates the inside from external microwave interferences. Second, it serves as a physical structure upon which is bonded a two inch thick layer of insulating styrofoam. Physical strength is needed to support the styrofoam because styrofoam contracts drastically and cracks at liquid nitrogen temperatures. Finally, the antenna is placed close to the absorber with a sheet of aluminum foil enclosing the load and the antenna aperture to further reduce interference from fluorescent lamps in the laboratory. The measurements of ohmic antenna loss may be calculated by the following considerations. A measurement of the apparent temperature (T_2) of boiling liquid nitrogen in the external load as viewed by the Potter horn antenna is made. The antenna is replaced by a Maury Microwave Corporation calibration load containing boiling liquid nitrogen, and a new apparent temperature observation (T_1) is made. But

$$T_2 = tT_{N_2} + (1-t) T_h$$

$$T_1 = T_{N_2}$$

where t is the transmission coefficient for the antenna and its transmission line, T_{N_2} is the corrected liquid nitrogen temperature in the Maury load (77.1°K), and T_h is the antenna skin temperature (23.7°C). Thus

$$(1-t) = \text{horn loss} = \frac{T_2 - T_1}{T_h - T_{N_2}} \quad (8.1)$$

For the Potter horn antenna, the observed value of ($T_2 - T_1$) was 5.3°K, from which $(1-t) = 0.024$. This value is somewhat larger than the estimated value of 0.0178 (Hidy, et al, 1969). Of course, it is difficult to know if this value of the horn loss is representative of the antenna as it was flown in 1969 because of uncertainty due to corrosion of the skin. However, this number has to be used as the best value for the losses in any new interpretation of the aircraft observations.

An important implication must be noted in connection with the interpretation of the influence of surface roughness on the apparent temperature of the sea. It is difficult to assess how the sea conditions varied between the two days of the flights. During both days, there were light seas; however, on November 5th, a few whitecaps were sighted, and the ocean surface appeared slightly rougher at times than on October 29th. Despite this, the effect of surface roughness appears to be essentially constant to the $\pm 1^\circ\text{K}$ accuracy of the observations. If verified in further studies, this finding will be highly significant in developing a practical method of correcting for the influence of roughness.

The "constant" nature of the surface roughness effects may be associated with the known tendency for the short wavelength components of the ocean wave spectrum to achieve an equilibrium state of energy. This equilibrium condition is well illustrated in ocean wave amplitude spectra as compared with laboratory results. The correlation of Hess *et al.* (1970) shown in Figure 8.5 shows the relationship of the equilibrium amplitude spectrum for the high frequency (short water wavelength) components. Here the water wave frequency is given by n . If the spectral density ϕ of the amplitude spectrum achieves such an equilibrium configuration, then the slope spectrum will achieve a similar equilibrium level. With the emissivity roughly proportional to the r.m.s. slope of the small wavelength components, one would expect to see a nearly constant "correction" factor for the influence of surface roughness. Confirmation of such a speculation must await further aircraft flight programs. Hopefully, the NR Science Center data recently taken on the NASA Convair 990 experimental program can be used as a further test of the equilibrium surface roughness hypothesis.

8.4 SUMMARY AND CONCLUSIONS

Re-evaluation of the 1969 flights with the NR Prototype I S-Band radiometer on the SIO DC-3 indicates that there is a positive deviation of $\sim 4^\circ\text{K}$ from the expected brightness temperature of the sea. This deviation is now attributed mainly to the effect of surface roughness on the emissivity of the surface, with a possible influence of sun glitter. This effect is substantially greater than calculated from geometrical optics theory, but is supported by other tests on the roof of the NR Science Center. The fact that the 4°K deviation appears to be essentially constant for light seas with $< 1\%$ foam coverage suggests that a calibration factor may be established for roughness. The constancy of the factor may depend on the ability of the small wavelength components of the sea surface to quickly achieve an equilibrium condition of energy content. In any case, surface roughness and sun glitter on a rough surface are significant uncertainties in interpretation of the radiometer observations of sea temperature. Their effects have to be assessed to a better accuracy, comparable to that achieved for the influence of salinity.

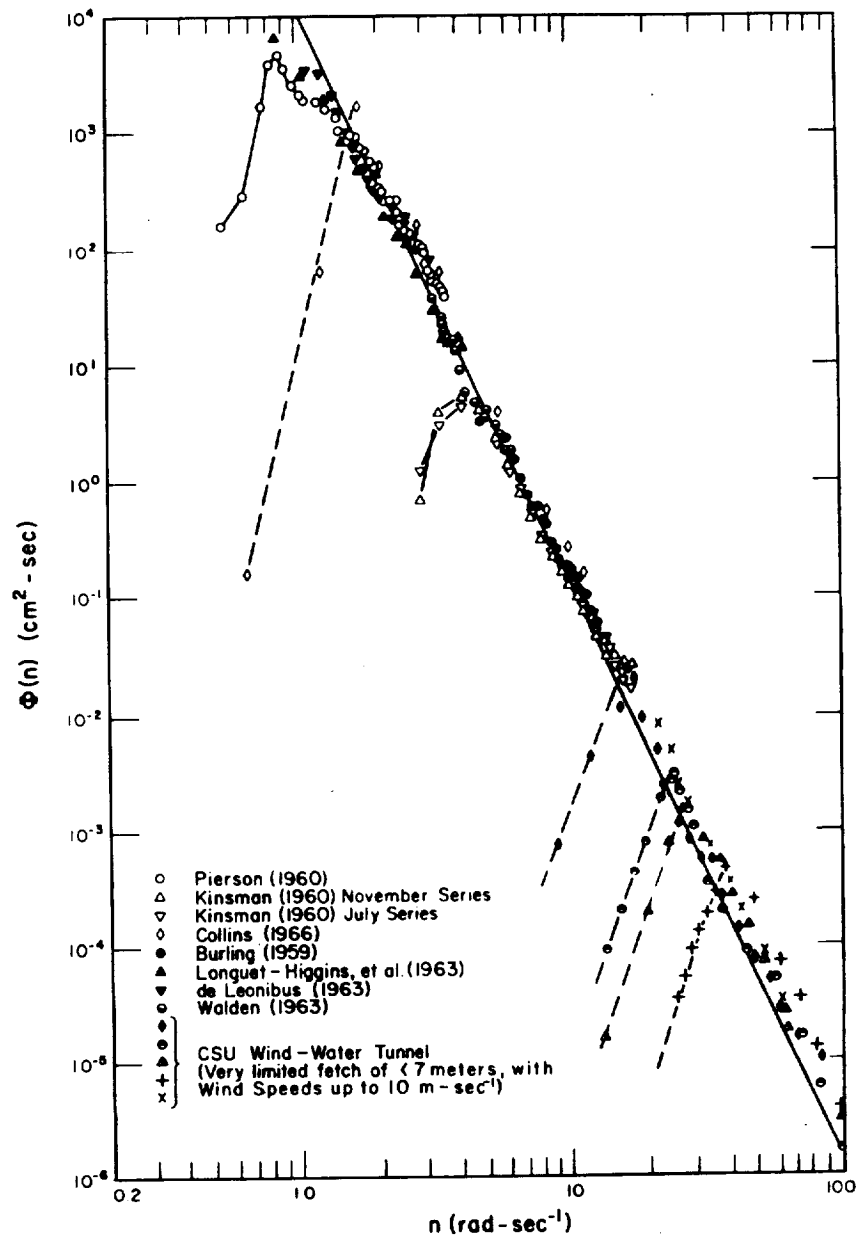


Figure 8.5. Equilibrium Amplitude Spectra for Gravity-Capillary Waves on the Sea and in the Laboratory (From Hess et al., 1970)

REFERENCES

- Hess, G.D., G.M. Hidy and E.J. Plate, 1969, "Comparison between Wind Waves at Sea and in the Laboratory," *Journal of Marine Research*, 27, 216-225.
- Hidy, G.M., K.W. Gray, W.N. Hardy, W.F. Hall, W.W. Ho, A.W. Love, and E.J. Thompson, Dec. 1969, "S-Band Radiometer for Measurement of Sea Surface Temperature," North American Rockwell Science Center Report SCTR-69-31, 60 p.
- Hidy, G.M., K.W. Gray, W.F. Hall, W.N. Hardy, W.W. Ho, A.C. Jones, A.W. Love, E.J. Thompson, and H.H. Wang, 1970, "Measurement of Sea Surface Temperature by Microwave Radiometry," in Proc. of 6th Marine Technology Soc. Conf., Vol. 2, Washington, D.C., p. 1003-1013.
- McAlister, E.D., 1964, "Infrared Optical Techniques Applied to Oceanography, 1, Measurement of Total Heat Flow From the Sea Surface," *Appl. Optics* 3, 609-612.
- Nautical Almanac Office, 1968, Nautical Almanac (1969), U.S. Naval Observatory, U.S. Government Printing Office, Washington, D.C.

9.0 CONCEPTUAL DESIGN FOR SATELLITE PROTOTYPE INSTRUMENT

9.1 INTRODUCTION

Two crucial design parameters for the satellite radiometer are the temperature resolution and the absolute accuracy of the measured antenna temperature. The design goal that has been chosen for both the resolution and the absolute accuracy of the proposed radiometer antenna temperature is $\pm 0.1^\circ\text{K}$. Antenna temperature resolutions of 0.1°K are routinely achieved in microwave radiometers provided adequate predetection bandwidth is used. On the other hand, the requirement of long term absolute accuracy of $\pm 0.1^\circ\text{K}$ is not easily satisfied and necessitates extreme care in the system design. Care in the design of the electronic circuitry, in the choice of microwave components, etc., is taken for granted. In addition, the high precision brings in practical difficulties of a more fundamental nature, such as the stability of reflective and dissipative transmission losses in the antenna and the input to the radiometer, and the absolute accuracy of the reference terminations.

It is important to keep in mind that, although in the following discussion 0.1°K is used as the nominal tolerable uncertainty from each effect, clearly an overall accuracy of 0.1°K requires even less uncertainty from separate uncorrelated sources.

Consider first the ohmic transmission losses. (In a Dicke radiometer these would include antenna losses, and all transmission losses up to the radiometer switch, and including at least the asymmetric part of the switch losses.) Such losses will modify the apparent source temperature in accordance with the usual relation

$$T_a = (1 - \ell) T_A + \ell T_o \quad (9.1)$$

where T_a is the apparent temperature of the source whose brightness temperature is T_A , T_o is the physical temperature at which the losses are sustained, and ℓ represents the fractional power loss. For a source temperature of 100°K , a transmission loss of 0.001 db ($\ell = 0.00023$) sustained at 300°K , increases the source temperature by 0.046°K . Therefore, in order to achieve the target accuracy, losses in the microwave transmission

path that directly affect the measured antenna temperature must either remain constant to ~ 0.001 db over the lifetime of the satellite (~ 1 yr.) or be monitored in a calibration cycle.

In the absence of reliable experimental data on the long term constancy of microwave component losses to the level of 0.001 db, the design approach has been to insist that all critical components have the lowest practical loss in order that a reasonable fractional change in loss can be tolerated. Typically, the undesired attenuation is due to conductor losses and therefore depends on the surface condition of a very thin layer of the metal (the skin depth for copper at 2.7 GHz is $\sim 10^{-4}$ cm) which, for example, is susceptible to chemical change in many types of environments. The attenuation in copper waveguide is about 0.023 db/meter at S-Band, whereas the best silver-layered 14 mm coaxial line has a loss of 0.13 db/meter and microstrip a loss of approximately 1 to 2 db/meter. Waveguide is bulky and heavy at S-Band and the severe restriction on the amount that may be used due to the constraints of satellite use has a profound effect on the suitability of the various possible radiometer configurations. It seems impractical to consider designing a satellite instrument using only waveguide RF components. If intrinsic loss were the only consideration, coaxial transmission line RF circuitry could be tolerated. However, the necessity for using connectors between the various components introduces additional losses of an unstable nature, so that use of purely coaxial RF circuitry is ruled out. In spite of the high loss per unit length of microstrip, the fact that connectors are eliminated and path lengths become extremely short makes microstrip the preferred choice for the less critical parts of the microwave circuitry.

Next let us consider the effect of a reflective discontinuity in the input section of the radiometer. In this case the apparent source temperature is given by

$$T_a = (1-\rho) T_A + \rho T_r \quad (9.2)$$

where ρ is the fractional power reflected and T_r is the effective microwave temperature seen looking into the radiometer. Again it is the stability of such disturbances that is of greatest concern since in principle a correction can be applied for a constant effect.

As a matter of experience the stability and repeatability of even the very best coaxial connectors is not down to the level of 0.001 db except under carefully controlled laboratory conditions where near perfect alignment of the connectors can be made, no further stresses have to be applied and where the ambient temperature is nearly constant. The best coaxial line from the point of view of loss, the General Radio, GR-900 type, uses butt

joints in the connectors that require very close tolerances, are very sensitive to misalignment, and under many practical conditions did not repeat to within 0.005 db. This is not to dispute the specifications given by General Radio which at 3 GHz are 0.051 db loss with 0.002 db reproducibility and VSWR 1.004, but it is considered that the connectors are impractical for this application. Furthermore, 0.002 db stability is insufficient even if achieved. It should also be noted that the inner conductor of high quality coaxial line is supported by materials such as teflon or polystyrene which have thermal expansion coefficients much larger than metals and it is suspected that thermal cycling could significantly change the alignment in the connectors.

Finally, let us consider in a preliminary way the problem of achieving 0.1°K accuracy for the reference terminations, keeping in mind that at this level of precision there is no way to calibrate them. They are primary standards and must be designed and fabricated with enough care that the output temperature can be calculated to the required precision from the physical and electrical parameters. The problems fall under 3 categories:

- (1) Determination of the temperature of the load material (or its effective temperature if gradients exist).
- (2) The loss and temperature distribution of the nominally lossless components such as the transmission line,
- (3) The loss, reflections, and stability of the connectors.

By applying equations 9.1 and 9.2 to the load proper as a source, it is seen that the importance of conductor losses depends on the temperature of the load with respect to ambient, whereas the effect of reflections depends on the effective temperature seen by the load. Explicitly, for small ℓ and ρ ,

$$T_{\text{apparent}} = (1 - \ell - \rho) T_s + \ell T_o + \rho T_r \quad (9.3)$$

where T_s is now the physical temperature of the load material and the term ℓT_o represents the integral $\int \ell(x) T(x) dx$ where $\ell(x)$ and $T(x)$ are the loss per unit length and temperature at position x on the transmission line respectively. As an example, consider a liquid N₂ cooled coaxial load with a 10 cm length of GR-900 coaxial line (loss \approx 0.013 db or $\ell = 0.003$), and a VSWR of 1.05 ($\rho = 0.0006$). Taking $T_r = 300^\circ\text{K}$, $T_s = 77^\circ\text{K}$, and approximating ℓT_o by $\ell(T_s + T_r)/2$, one gets

$$\begin{aligned} \Delta T = T_a - T_s &= \ell (T_o - T_s) + \rho (T_r - T_s) \\ &= 0.33^\circ\text{K} + 0.13^\circ\text{K} \end{aligned} \quad (9.4)$$

The value of l used is rather lower and the value ρ higher than what would normally be encountered, so that it is usually the transmission losses that are of primary concern. An accurate correction requires the knowledge of the loss and temperature at each point of the transmission line. Only the total loss of a coaxial or waveguide component can be measured by normal methods, and uniform loss must then be assumed. Furthermore the uncertainty of such measurements contributes a significant error to the correction factor. The temperature distribution of a section of waveguide is easily measured with a series of temperature sensors on the outside wall. On the other hand, the lack of firm thermal anchoring of the center conductor of coaxial line makes its temperature profile difficult to control. Its measurement, although possible in principle, is extremely awkward and complicated. Coaxial loads have the further disadvantage of heat flux down the center conductor which tends to produce temperature gradients in the load resistor. This has proved to be a very serious difficulty even in the most carefully designed cold loads.

Table 9.1 shows the correction factors and the errors therein for four cooled terminations, taken to be representative of the best available for use near 3 GHz. The large error in the correction factor for the coaxial loads is due to heating of the load resistor. It was determined a priori by comparing two loads of similar construction, one using stainless steel for the center conductor of the isolation section, and the other using gold plated pyrex having lower thermal conductivity. The corrections were estimated a priori to be reliable to within 0.2°K.

Table 9.1. Correction Factors and Errors for Cooled Terminations

Type of Load	Ref	Cryogen Temperature	Correction	Error (peak)
Waveguide, 4.2 GHz	Penzias (1965)	4.2°K	0.98°K	0.21°K
Waveguide, 2.295 GHz	Stelzreid (1968)	77.4°K	0.73°K	0.12°K
GR-900 Coax, 2.8 GHz Stainless Steel isolation section	Maury Microwave/No. Am. Rockwell	77.4°K	1.11°K	≥ 0.6°K
GR-900 Coax, 2.8 GHz Gold plated pyrex isolation section	do.	77.4°K	0.77°K	≥ 0.2°K

The remarks made concerning cold loads are equally valid for hot loads. Clearly, the highest accuracy is achieved when T_O and T_R are close to T_S . In the limit when all are equal, the correction is zero and one need only measure the temperature sufficiently accurately.

9.2 CANDIDATE RADIOMETERS

Over the past 25 years a wide variety of microwave radiometer configurations have been proposed of varying complexity and sensitivity.¹ Although it is common practice in the literature to state the theoretical and experimental temperature resolution of a radiometer, there is almost a complete lack of information on the absolute accuracy achieved. For the present application, where it is important to have as high an absolute accuracy as possible, the resolution is of secondary importance and can be compromised somewhat for an advantage in accuracy. In this section the basic radiometer types will be reviewed with emphasis on their potential for absolute accuracy.

The output voltage of the unmodulated radiometer shown in Figure 9.1A (assuming a square law detector) is given by

$$V = G(T_A + T_n) \quad (9.5)$$

where T_A is the source temperature to be measured, T_n the system noise temperature referred to the antenna aperture, and G is the gain factor of the system (also referred to the antenna aperture). Even for modest radiometric requirements, it is usually quite impractical to maintain adequate stability for G and T_n . There are two basic approaches to eliminating the effects of changes in T_n ; (1) the cross-correlation technique (Fujimoto, 1964), and (2) the signal modulation technique (Dicke, 1946).

Cross correlation radiometers without signal modulation can be eliminated from our list of candidate radiometers because of their poor gain stability. For the present application, stabilization of their gain by signal modulation destroys their advantage over simple signal modulated radiometers, and the considerable added complexity of two receivers with stringent phase tracking and stability requirements is more than enough to rule them out.

The output of the simple signal modulated or Dicke radiometer shown in Figure 9.1B is given by

$$V = G[T_A(1 - l_s) - T_{Ref}(1 - l_r) + (l_s - l_r)T_O] \quad (9.6)$$

¹Dicke, 1946; Drake and Ewen, 1958; Graham, 1958; Orhaug and Waltman, 1962; McGillem and Seling, 1964; Fujimoto, 1964; Tiuri, 1964; Haroules and Brown, 1967; Coggins, 1967; Hach, 1968.

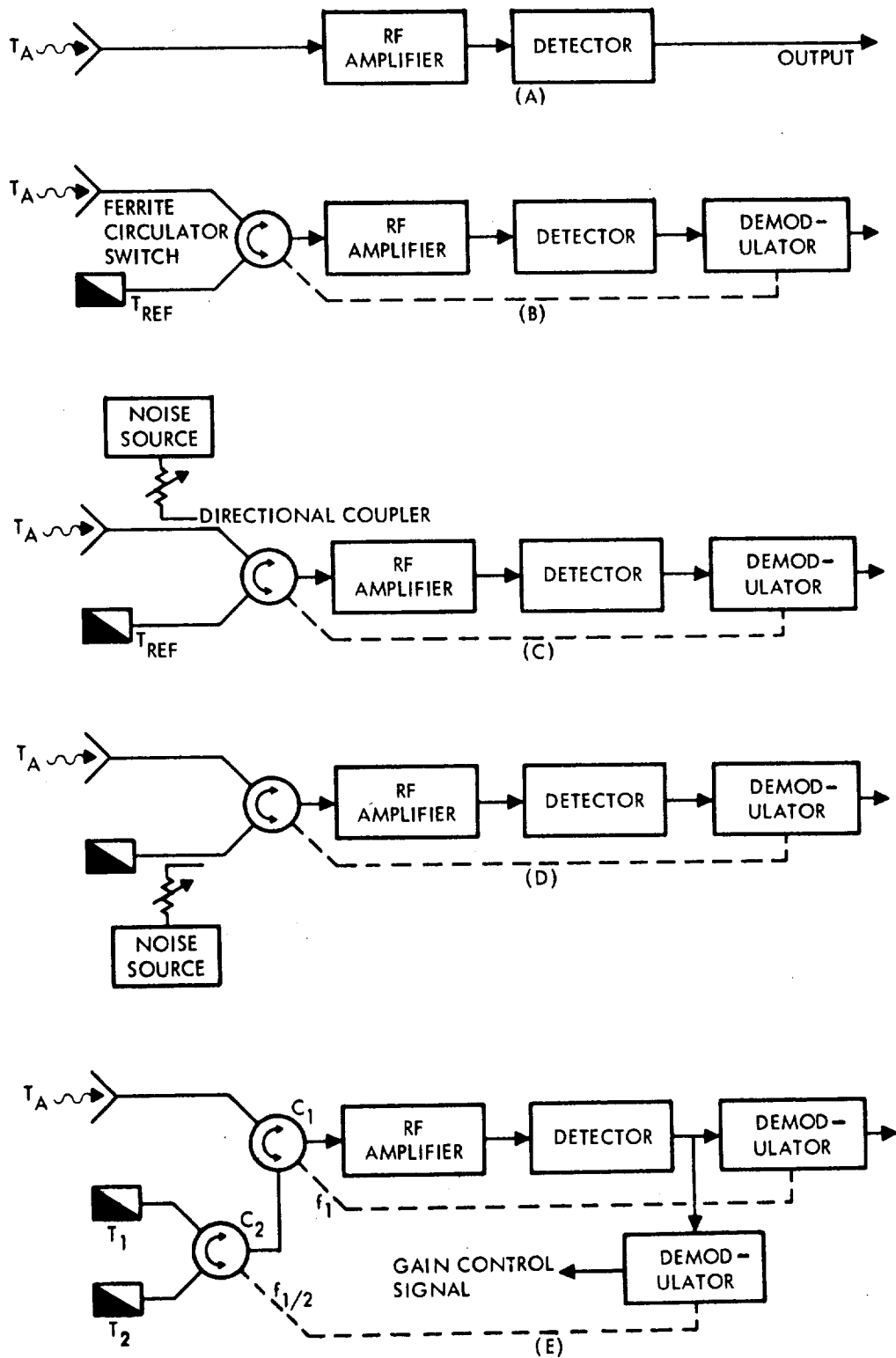


Figure 9.1 Candidate Radiometer Configurations

where l_s and l_r are the fractional ohmic losses in the signal and reference arms respectively and T_o is the physical temperature of the radiometer components. (For simplicity reflective losses are being ignored). Clearly the effect of the rf amplifier contributions to T_n has been eliminated but not the contributions to T_n from front end losses.

The next step in the evolution of the signal modulated radiometer is to eliminate the effects of changes in G . Again there are two basic approaches. One is to add noise to either the signal or reference arm until the output ac signal reaches a null; such arrangements are shown schematically in Figure 9.1C and 9.1D. For rapidly varying values of T_A some sort of automatic adjustment of the attenuator in series with the noise source must be devised. The other approach of Hach (1968), and shown in Figure 9.1E, is to use two reference terminations at different temperatures from which the gain can be inferred and appropriate compensation can be applied. A second circulator switch is used to switch between the two loads at $1/2$ the primary modulation frequency. A hybrid of the two approaches is obtained if the switching frequency of the second circulator is made equal to twice the primary modulation frequency in the arrangement shown in Figure 9.1E. The dwell time on the load at temperature T_1 is adjusted until an ac null is achieved at the output for the primary modulation frequency.

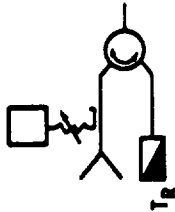
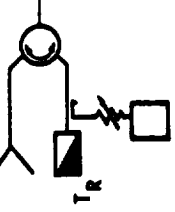
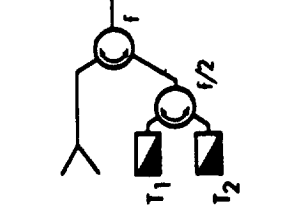
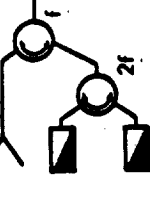
There are, of course, other variations on these two basic types and the details of the execution of a particular design can vary considerably. At this point, however, further analysis is restricted to four radiometers of Figure 9.1 C, D, E and the variant of E just described.

In Table 9.2 a comparison of the characteristics of the selected radiometer types is given. First several explanatory comments are made, then some general conclusions are drawn about the suitability of each for satellite use. For the purpose of calculating resolution it is assumed that radiometers I, II, and IV are manually adjusted to be operating at or near null; later it will be seen that for a properly designed feedback system the result is still valid when the loop is closed. Radiometer III, however, does not operate at null in general. The gain is derived from the difference $T_2 - T_1$ and details of the feedback system must be considered from the outset.

List of Symbols Used in Table 9.2

T_{rms}	=	rms fluctuation of the radiometer output expressed in degrees Kelvin, or equivalently the rms error made in a measurement of T_A , the source temperature. The modulation and demodulation is assumed to be square wave.
B	=	Predetection bandwidth in Hz
τ	=	Interval over which output is averaged.
τ_{agc}	=	Time constant of gain control feedback loop.
T_n	{	= Noise temperature of rf amplification system (including the effects of losses from the horn aperture to the rf amplifier, and also second stage noise) = $(F-1) \times 290^\circ\text{K}$ where F is the system noise figure (IEEE definition)
T_o	=	Ambient temperature, assumed to be temperature of circulators.
T_A	=	Microwave temperature seen by antenna
ΔG	=	rms value of the predetection fluctuations in the power gain G at the modulation frequency f .
α_a	=	Asymmetric part of transmission loss in the ferrite circulator switch (expressed as fractional power loss)
α	=	Total transmission loss of second circulator switch in the two load type radiometers.
f	=	Switching frequency of primary circulator.

Table 9.2. Characteristics of Selected Radiometers

RADIOMETER TYPE	RESOLUTION ΔT_{rms}	REFERENCE REQUIREMENTS	APPROXIMATE SENSITIVITY TO NON-IDEALITY OF CIRCULATORS
 <p>I</p>	$2(T_o + T_n) \left[\frac{1}{B_r} + \left(\frac{\Delta G}{G}\right)^2 \right]^{1/2}$	<p>ONE REFERENCE LOAD $T_R > T_A$ NOISE SOURCE</p>	$\alpha_o (T_o - T_R)$
 <p>II</p>	$2(T_A + T_n) \left[\frac{1}{B_r} + \left(\frac{\Delta G}{G}\right)^2 \right]^{1/2}$	<p>ONE REFERENCE LOAD $T_R < T_A$ NOISE SOURCE</p>	$\alpha_o (T_o - T_A)$
 <p>III</p>	$\left[2(T_A + T_n)^2 + (T_1 + T_n)^2 + (T_2 + T_n)^2 \right]^{1/2} \times \left[1 + \frac{1}{1 + \text{rogc}/r} \left(\frac{T_2 + T_1 - 2T_A}{T_2 - T_1} \right)^2 \right]^{1/2} \times \left[\frac{1}{B_r} + \left(\frac{\Delta G}{G}\right)^2 \right]^{1/2}$	<p>TWO LOADS OF ARBITRARY BUT DIFFERENT TEMPERATURES</p>	$\alpha_o \times \left[2(T_o - T_A)^2 + (T_o - T_1)^2 + (T_o - T_2)^2 \right]^{1/2} + \alpha \left(T_o - \frac{T_1 + T_2}{2} \right)$
 <p>IV</p>	$2(T_A + T_n) \left[\frac{1}{B_r} + \left(\frac{\Delta G}{G}\right)^2 \right]^{1/2}$	<p>TWO LOADS, ONE WITH $T > T_A$, ONE WITH $T < T_A$</p>	$\alpha_o (T_o - T_A) + \alpha (T_o - T_A)$

9.2.1 Resolution

The theoretical resolution (excluding gain fluctuations) of the unmodulated radiometer (Figure 9.1A) is given by (Tiuri, 1964);

$$\Delta T_{\text{rms}} = (T_A + T_n) \left[\frac{2 B_{\text{lf}}}{B_{\text{hf}}} \right]^{1/2} \quad (9.7)$$

where B_{hf} is the predetection bandwidth and B_{lf} is the output bandwidth. If the output is averaged over intervals τ then

$$B_{\text{lf}} = \frac{1}{2 \tau} \quad (9.8)$$

and Equation (9.7) becomes (putting $B = B_{\text{hf}}$)

$$\Delta T_{\text{rms}} = \frac{T_A + T_n}{(B \tau)^{1/2}} \quad (9.9)$$

If, instead, a single stage lowpass RC filter is used then τ should be replaced by $2 RC$. In the presence of gain fluctuations, Equation (9.9) is modified to

$$\Delta T_{\text{rms}} = (T_A + T_n) \left[\frac{1}{B \tau} + \left(\frac{\Delta G}{G} \right)^2 \right]^{1/2} \quad (9.10)$$

where ΔG is the rms value of the predetection power gain fluctuations and G the average gain. The detector and following circuitry may add noise and gain fluctuations of their own, but these are ignored here and treated separately later.

The formulae given in Table 9.2 are then simply derived from Equation (9.10) by taking account of the effects of modulation and demodulation, and where $\Delta G/G$ is now the rms fractional gain fluctuation at the modulation frequency f ; for radiometer III the expression for ΔT_{rms} was taken from Hach (1968). Since the spectral density of the gain fluctuations will not vary greatly over a small interval near f , $\Delta G/G$ will be proportional to $1/\sqrt{\tau}$ and hence the relative importance of gain fluctuations increases with $(B)^{1/2}$.

Strictly speaking, for square wave demodulation, fluctuations at the odd harmonics also enter (with decreasing importance at the higher harmonics), but the result still holds.

The resolutions of II and IV are seen to be the same and superior to that of I by the factor $(T_o + T_n)/(T_A + T_n)$. A typical value for the emissive temperature of the ocean is 110°K , T_o is of order 300°K and therefore the maximum value of this factor is about 3. For $T_n = 70^\circ\text{K}$, a value that can be achieved with good parametric amplifiers, the factor is 2.0.

The resolution of III is intermediate between I and II provided $T_A \lesssim T_1, T_2 \lesssim T_o$ and provided the second factor in the formula for the resolution is close to 1. This factor is a result of the fluctuations in gain due to the uncertainty in measuring $T_2 - T_1$. In order to avoid a substantial degradation in the resolution both $T_2 - T_1$ and τ_{agc}/τ must be kept fairly large. The second requirement imposes restrictions on the low frequency gain fluctuations.

9.2.2 Sensitivity to Non-Ideality of the Circulator Switches

Ohmic loss encountered by the signal in reaching the rf amplifier increases the noise temperature of the system according to the equation

$$T_n' = \frac{T_n}{1-\ell} + \frac{\ell}{1-\ell} T_o \quad (9.11a)$$

or

$$\Delta T_n = \frac{\ell}{1-\ell} (T_n + T_o) \quad (9.11b)$$

where ℓ is the fractional power loss, T_n is the noise temperature of the amplifier alone and T_o the physical temperature at which the loss is sustained. The transmission losses of the best available circulators at S-band are of order 0.3db ($\ell \approx 0.07$) so that for $T_o = 300^\circ\text{K}$ and $T_n = 70^\circ\text{K}$, $\Delta T_n \approx 28^\circ\text{K}$. This change in T_n has the greatest effect on radiometers with the highest resolution but clearly does not cause a serious loss in sensitivity when the source temperature is 100°K or greater.

A potentially much more serious effect is the change in radiometer calibration with a change in circulator loss, and in Table 9.2 an estimate is given of the sensitivity of each radiometer type to this form of instability. The result is expressed as a degree Kelvin contribution to the radiometer output. For the primary circulator, only the difference between the losses in the signal and reference paths is effective (designated by α_a), whereas

for the secondary circulator of radiometers III and IV both asymmetric and symmetric parts of the losses enter. The exact result is complicated and the average loss α is used as an approximation.

9.2.3 Suitability for Satellite Use

The usefulness of a satellite radiometer for measuring the ocean surface temperature depends so critically on the accuracy achieved that it is not meaningful to impose tight constraints on its size, weight and power consumption at the outset. Rather, the accuracy requirement is first imposed and then an optimum design developed. The general limitations of satellite use must be respected however, and the following guide has been used.

Power Consumption - Less than 5 watts would be ideal, 10 watts still feasible but 100 watts prohibitive.

Size and Weight - At S-Band the antenna would require an aperture diameter of .3 to .6 m and a length greater than .6 m. Therefore a volume of ~ .03 cu. m for the radiometer proper would not be unreasonable. The weight should not exceed ~ 50 lbs. and preferably would be much less.

Unattended Lifetime - The radiometer should maintain its accuracy for a period of one year.

The most important consequence of the restriction on power is that the use of cryogenic fluids for cooled reference loads is ruled out; a cryogenic refrigerator of useful capacity would certainly require much more than 100 watts. It is possible that a thermoelectric element working in tandem with a radiative cooler might achieve a temperature comparable to T_A , but whether or not a useful reference load using reasonable amounts of power could be realized with $T < T_A$ is an unanswered question, and in this report their use will not be considered. This immediately implies that radiometers II and IV must use sky horns as their cold reference loads. A fixed sky horn has the disadvantage that part of the time hot celestial objects (the galactic center, sun, etc.) would be in view. A moveable horn is probably out of the question for a satellite not specifically designed around this particular instrument and therefore radiometers II and IV are tentatively eliminated. However, much of the following analysis also applies to II and IV so their elimination at this stage is not irreversible.

In order to make a choice between I and III a more detailed look at the possible ways of executing the design must be made. Specifically, the question of waveguide vs coaxial line has to be decided for the circulators and the reference loads, and the performance of available noise sources

must be considered. Since radiometer I could be eliminated immediately if sufficiently stable noise sources were not available, this aspect is discussed first.

Stability of Noise Sources. Although plasma noise sources have long been established as microwave noise sources, their absolute accuracy and long term stability have left much to be desired. However, in a recent article, Denson and Halford (1968) show that most of the problems can be eliminated with good mount design and properly chosen operating current. The results of interest are given in Table 9.3. It is seen that in spite of the significant improvement over previous plasma sources, they cannot be used in the present application as reference loads without calibration. On the other hand, the ± 0.002 db stability achieved is close to the 0.001 db stability that would be required for the noise source of radiometer I. However, the power requirements seem excessive for spacecraft use, the mounts at S-Band are very large, and the problem of heating of other components would be very serious. It is concluded that their use in spacecraft is very undesirable.

The recently developed solid state avalanche noise diodes have shown promise as an alternative to the plasma noise source (see for example Haitz and Voltmer, 1968), although data on their long term performance is scarce. Some preliminary tests on certain commercial units showed only fair long term stability (~ 0.005 db in 100 hrs.) and very poor reproducibility (0.3 db) on turning off and refiring the diode (See Table 9.3). These results were at odds with the claims of another manufacturer and this prompted an investigation of such units at the NAR Science Center. The results were much more encouraging, yielding an upper limit on the variation in noise power of 0.002 db in 72 hrs. Furthermore, with a resolution of 0.001 db, there was no discernible change in output on turning off and refiring the diode.

The experimental arrangement used in the measurements is shown in Figure 9.2. By adjusting the variable attenuator for a null at the output the requirements on the gain stability of the radiometer are minimized. The gain stability achieved by regulating the total noise power during the reference half of the switching cycle was more than adequate. All critical components were kept within an enclosure made of insulating foam and temperature stabilized to better than $1/20^{\circ}\text{C}$ by clamping them to copper heat exchangers through which flowed water from a Haake temperature controlled bath.

Table 9.3 Performance of Noise Source

Noise Source (S-band)	Investigator	Excess Noise Ratio			VSWR	Temperature Coefficient	Power Require- ments
		Mean Value	Absolute Accuracy +	Stability			
				Continuous Operation	Discontinuous Operation		
Argon Plasma Tube	Denson and Halford (1968)	15.38db	0.11db*	<0.004db change in 1000 hrs.	same	~1.05(tube on) ~1.1(tube off)	25W @ 127V (plus heater power)
Avalanche Diode	Keen (1970)	31db	>1db	<0.05 db change in >100 hrs.	0.3db variation	~2.5(diode on) ~∞ (diode off)	~0.11W @ 22V
Avalanche Diode (MSC)	Hardy and Gray (1971)	35db	>1db	<0.002db change in 72 hrs.	<0.001db variation between switchings	~5(diode on) ~∞ (diode off)	~0.024W @ 12V

+ The absolute accuracy refers to the variation from unit to unit.

* The 3σ spread of ENR measured for a large number of tubes and mounts was 0.042 db. The rest of the error is due to uncertainties in the thermal comparison standard.

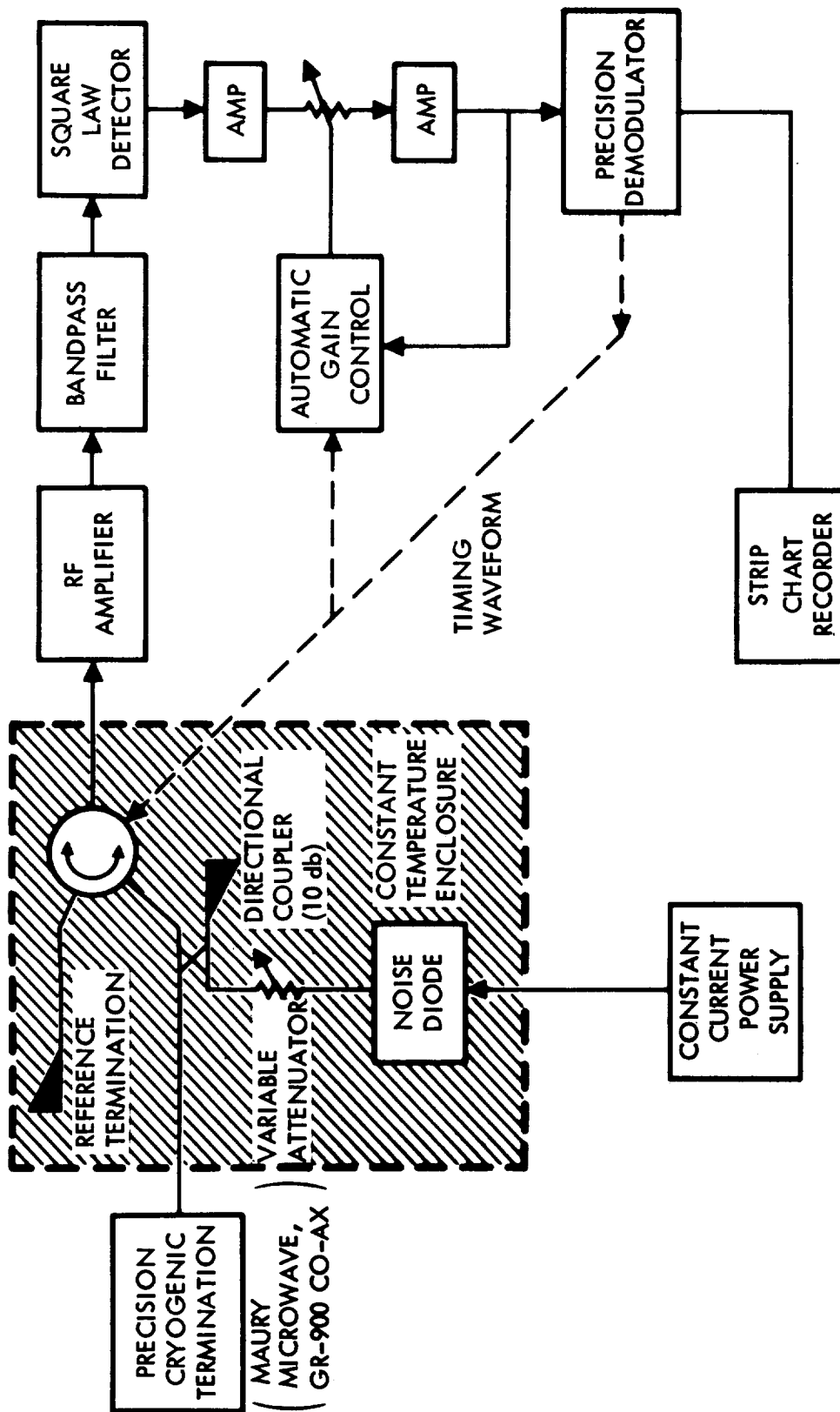


Figure 9.2 Schematic of Test Setup for Measuring Noise Diode Stability

9.2.4 Waveguide Versus Coaxial or Microstrip Transmission Line

In a comparison of waveguide and transmission line, the areas of concern are:

- (1) the circulator switches,
- (2) the reference terminations,
- (3) the connectors
- (4) the waveguide to coaxial line transition, if it occurs in a sensitive part of the input.

Table 9.4 lists partial performance specifications of waveguide, stripline and microstrip latching circulators that are representative of the best available. (Latching types use high coercivity ferrite material and require no holding power). Waveguide types are superior in all electrical specifications and, surprisingly, the advantage is most marked in switching times and switching energies. This is a result of the switching coil being essentially embedded in the ferrite in the case of the waveguide circulator, whereas the strip-line circulator requires an inefficient external magnetic circuit. The mechanical integrity of waveguide and microstrip circulators is very good, whereas the general awkwardness of stripline definitely puts it at a disadvantage especially with respect to interconnection with other components. The only disadvantage of waveguide is of course its size and weight; an S-band circulator would weigh 5 - 10 lbs even after excess metal was removed, and have dimensions of order 8" x 7" x 4".

Reference terminations have already been discussed (Section 9.1) and it is concluded that because of the center conductor coaxial loads of the required precision are extremely difficult to produce when the reference temperature is well away from ambient. Stripline would be even more problematic. A good thermal design in microstrip seems feasible, but the electrical specifications would be poor, necessitating a large correction to the output temperature. Waveguide loads are bulky and would require considerably more power for cooling than transmission line types.

The connector problem has already been discussed, with the result that anything but a waveguide joint is considered undesirable. If microstrip is used, connectors can be avoided, but the waveguide to microstrip transition then becomes a critical component. With great care such a transition of the required stability can be achieved; part of the problem has already been touched on in reference to coaxial connectors, namely the thermal incompatibility of the dielectrics and the conductors.

Table 9.4. Characteristics of High Quality Waveguide, Stripline and Microstrip Latching Circulators

Type	Frequency	Isolation	Insertion Loss	VSWR	Switching Time (10 - 90%)	Switching Energy
Waveguide	3.3 GHz	>25db	<0.3db	<1.15	1 μ sec	600 μ J
Stripline	3 GHz	>20db	<0.4db	<1.25	10 μ sec	3,000 μ J
Microstrip	3 GHz	>20db	<0.5db	<1.15	<50 μ sec	300 μ J

To summarize, from the electrical point of view, waveguide is heavily favored for all critical components and seems to present the only course that promises to achieve the 0.1°K absolute accuracy. It has considerable disadvantage in size and weight, and also in power consumption if thermoelectric cooling is employed for the reference terminations. Radiometer III, which would require 2 waveguide circulators and 2 waveguide loads, is thereby eliminated. However, taking a clue from the last column of Table 9.2 which shows that radiometer I is insensitive to circulator losses when $T_r = T_o$, a radiometer design was conceived that used a tolerable amount of waveguide components and could still achieve the desired accuracy. It is described in detail in the next section.

9.3 CONCEPTUAL DESIGN OF SATELLITE RADIOMETER

9.3.1 Introduction

The proposed radiometer is of Type I (See Table 9.2 and Figure 9.1) and is designed around three basic concepts:

1. The use of a constant temperature enclosure at the same temperature as the main reference termination which, in conjunction with a nulling mode of operation, avoids the effects of time dependent losses in the high loss components such as the circulator switch.
2. The use of low loss waveguide components in critical sections outside of the calibration loop.
3. The use of a pulsed noise source to provide variable noise injection. A constant pulse width is easy to achieve so that antenna temperature changes are accurately proportional to changes in pulse repetition rate.

The advantages of maintaining the input components at a common temperature can be most easily understood by reference to Figure 9.3. This shows the usual Dicke type radiometer to which is added a noise injection arm and a constant temperature enclosure which includes the reference termination. If the output is amplified, detected and then demodulated at the switching frequency, then the condition for zero ac signal is exactly that $T = T_o$, the temperature of the enclosure. This result is completely independent of losses or reflections in the circulator switch, imperfections in the reference termination, finite switching times, etc., provided only that the isolator "isolates" well enough and that a single electromagnetic mode propagates in the input and output transmission lines. To see this, one need only imagine the input arm

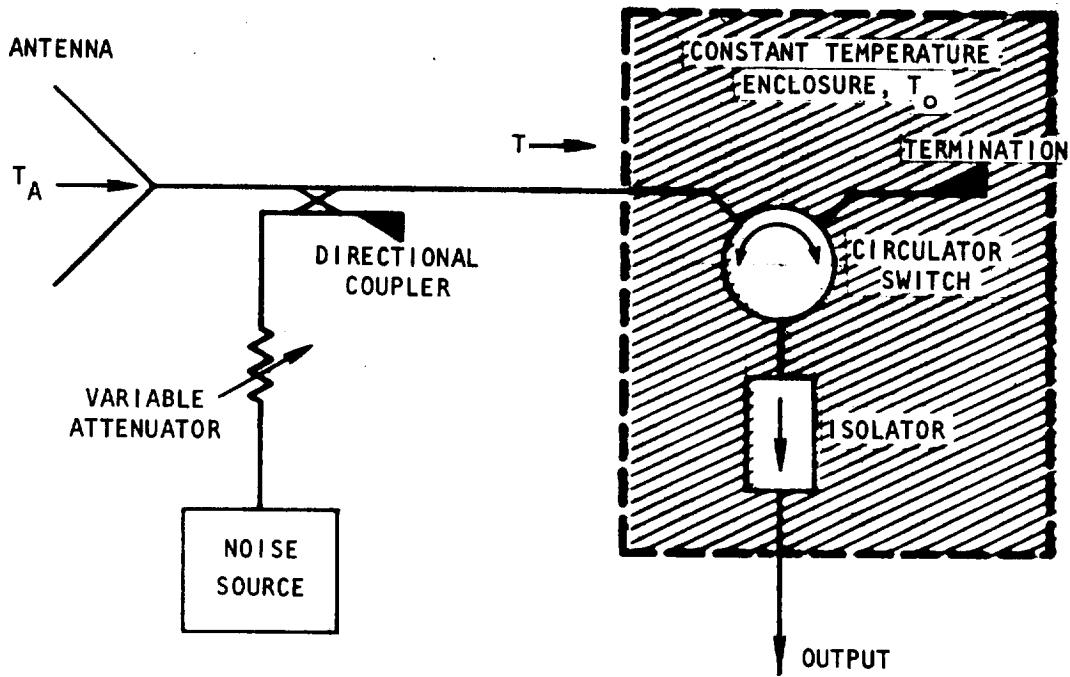


Figure 9.3 Simplified Block Diagram of Precision Comparator Concept

terminated with a load at the same temperature as the enclosure. Then since all of the components including the circulator are passive and at a common temperature T_0 , by Nyquist's theorem (Van der Ziel, 1954) the power emitted at the output into a single electromagnetic mode is given by (assuming for the moment that the isolator gives zero reflection)

$$P_o = kT_oB \quad (9.12)$$

which is strictly independent of time and which of course is totally independent of details of the components within the constant temperature enclosure. This obviously satisfies the condition for ac null. Provided the amount of input signal reaching the output varies in some way with the switching state, the condition $T \neq T_0$ results in an ac signal. The purpose of the isolator is to ensure that should there be a reflection looking into the output arm that it remain constant. (The reflection coefficient of the circulator switch for example is different in general for its two states.) How well the isolator need isolate depends on the effective temperature T_{eff} seen looking towards the rf amplifier. If $\Delta\rho$ is the change in power reflection coefficient of the

circulator, for example, and t the transmission coefficient of the isolator in the reverse direction, then the error in the radiometer output is given by

$$\Delta T = (T_{\text{eff}} - T_o) t \Delta \rho \quad (9.13)$$

For parametric or tunnel diode amplifiers which have circulator inputs, T_{eff} never deviates by more than a few degrees from ambient temperature. In an extreme case $\Delta \rho$ might be as large as 0.01 and therefore taking $T_{\text{eff}} - T_o \approx 10^\circ\text{K}$, $\Delta T = 0.1t^\circ\text{K} = 0.001^\circ\text{K}$, a completely negligible quantity, for a modest isolation of 20db ($t = 0.01$).

The radiometer operates in a feedback mode whereby the injected noise power level is adjusted to achieve a null at the output. At the point of noise injection one must have

$$T = T_o - (T_A)_{\text{eff}} \quad (9.14)$$

where T represents the injected noise. $(T_A)_{\text{eff}}$ is the antenna temperature as modified by loss in the antenna and components up to the point of noise injection,

$$(T_A)_{\text{eff}} = t T_A + (1-t) T_p \quad (9.15)$$

where t is the transmission coefficient and T_p the effective physical temperature of the antenna and lossy transmission line. In order to extract T_A , t must be known and stable, and T has to be known accurately. Concepts 2) and 3) constitute our solution to these requirements. A simplified block diagram of the complete radiometer is given in Figure 9.4. The use of a waveguide directional coupler satisfies 2) and by gating the noise with constant width pulses an extremely linear relationship between the pulse frequency f_p and the average injected noise is established. However the null condition for the radiometer has to be re-examined when the noise is injected intermittently in the form of pulses. Deferring this question to the next section, it is assumed that the null condition holds for the average input noise.

The operation of the radiometer is then easily followed by reference to Figure 9.4. The output of the noise diode is injected into the "comparator" input in the form of, for example, $20\mu\text{sec}$. pulses. An error signal at the output of the demodulator causes the frequency of the pulses to vary in such a way as to reduce the error signal. For feedback response times much longer than the characteristic time lag of the demodulator, the response is

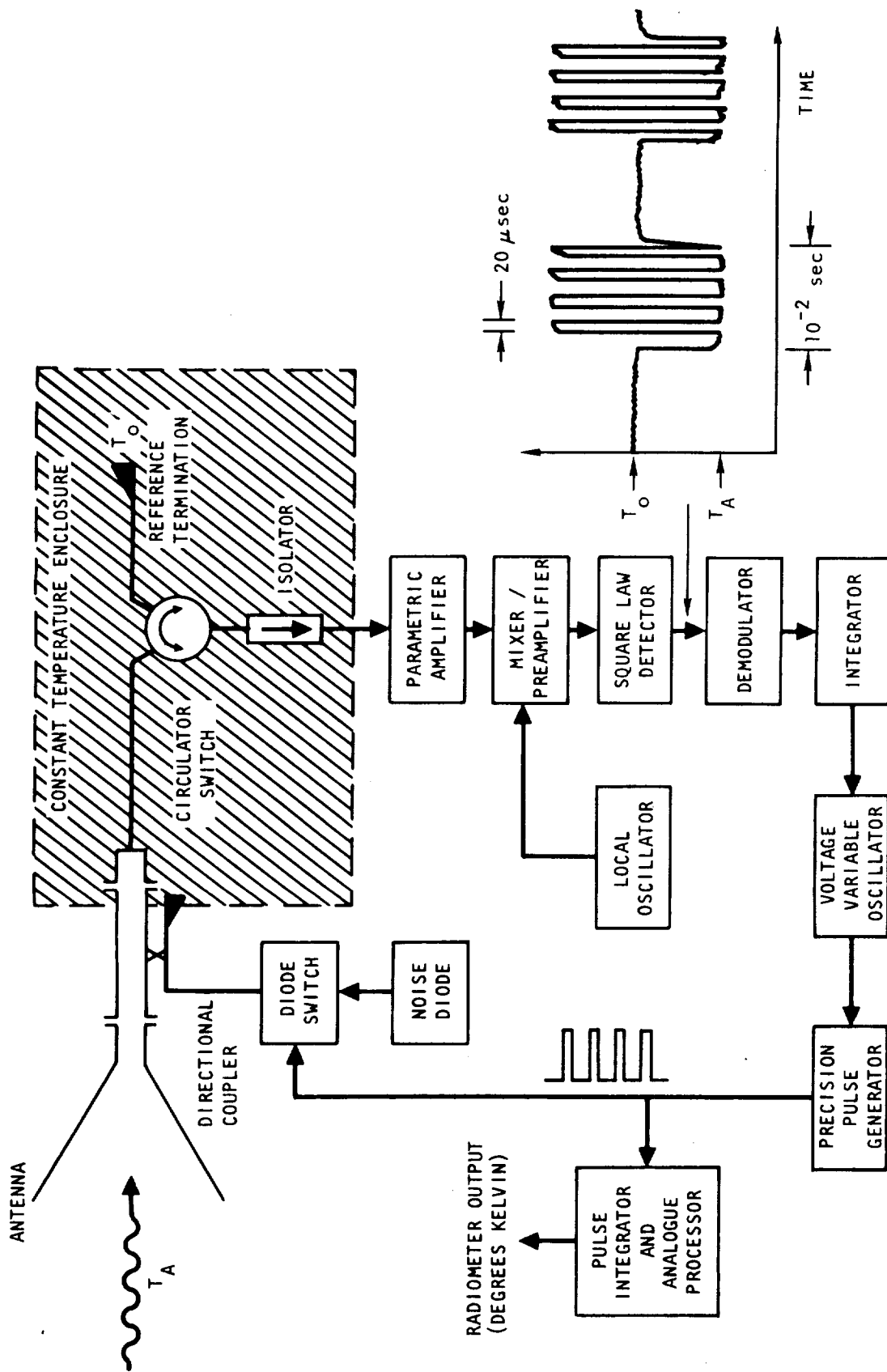


Figure 9.4 Simplified Block Diagram of Precision Nulling Radiometer

a simple exponential. If the noise is gated with constant width pulses, then at null the antenna temperature T_A is related to the pulse frequency f_p by

$$f_p = KT = K \left[T_o - (t T_A + (1-t) T_p) \right] \quad (9.16)$$

where K is a calibration constant for the noise injection system. There is an approximation made in Equation (9.16) that amounts to assuming that the VSWR in the auxilliary arm of the coupler does not change when the diode is pulsed and hence that t (which includes losses to the coupler) does not change.

The radiometer can be calibrated either by replacing the antenna with a cooled reference termination and correcting for antenna losses separately, or by pointing the antenna at a cold source whose temperature is accurately known. In the first case it is a very good approximation to take $T_p = T_o$ so that $f_p^{cal} = Kt'(T_o - T_{ref})$ and the constant Kt' is obtained immediately (t' is the transmission coefficient from the input flange to the point of noise injection). Two simple algebraical operations that can be done to high precision by analog circuits then suffice to give the effective antenna temperature at the flange:

$$T'_A = T_o - f_p / Kt' \quad (9.17)$$

T'_A then has to be corrected for losses between the antenna aperture and the flange.

For the second case, rewriting equation (9.16),

$$f_p^{cal} = Kt \left[T_o - T_{cal} - \frac{1-t}{t} (T_p - T_o) \right] \quad (9.18)$$

To the degree that $T_p - T_o$ is small, only a rough value of $1-t$ is needed in order to extract Kt . Performing the same operations electronically, one obtains

$$\begin{aligned} T_A &= T_o - \frac{1-t}{t} (T_p - T_o) - f_p / Kt \\ &= T'_o - f_p / Kt \end{aligned} \quad (9.19)$$

9.3.2 Need for Square Law Detection for Pulsed Mode

Consider the situation in Figure 9.5 where half of the time the effective input temperature to the precision comparator, T_{in} , is rT_o , and the other half of the time $(2-r)T_o$, so that $\langle T_{in} \rangle = T_o$. Since the system is linear and passive and since uncorrelated noise voltages add quadratically, one has

$$T_{out} = k_1 T_o + k_2 T_{in} \quad (9.20a)$$

$$= k_1 T_o + (1-k_1) T_{in} \quad (9.20b)$$

where k_1 and k_2 are constants depending on the components in the enclosure. It is important to note that (9.20a) includes all losses, both reflective and dissipative, and that k_1 and k_2 will change as the state of the circulator changes. That $k_2 = 1-k_1$ follows from the requirement that $T_{out} = T_o$ when $T_{in} = T_o$. (For simplicity it is assumed that a reflectionless isolator is in series with the output, but the results are valid within the errors given by Equation 9.13). The average value of T_{out} is therefore given by

$$\begin{aligned} \langle T_{out} \rangle &= 1/2 \left[k_1 T_o + (1-k_1) r T_o \right. \\ &\quad \left. + k_1 T_o + (1-k_1) (2-r) T_o \right] \\ &= T_o \end{aligned} \quad (9.21)$$

This result holds for all values of k_1 and for noise pulses of arbitrary spacing provided $\langle T_{in} \rangle = T_o$. It follows that if a square law detector precedes the demodulator ($V_{out} = K T_{out}$), the demodulator output is zero on the average provided there are no fixed phase relationships between the noise gating pulses and the demodulation waveform. However, when the number of pulses within 1/2 of a modulation cycle is low, the output can have fluctuations well above the level determined by the ultimate resolution of the radiometer. A detailed theory of this type of fluctuation has not yet been constructed but a rough estimate of the rms deviation ΔT yields

$$\frac{\Delta T}{T} = \frac{f_m}{f_p} (1-p) \left(1 - \frac{T_A}{T_o} \right) \frac{1}{(2\tau_i f_m)^{1/2}} \quad (9.22)$$

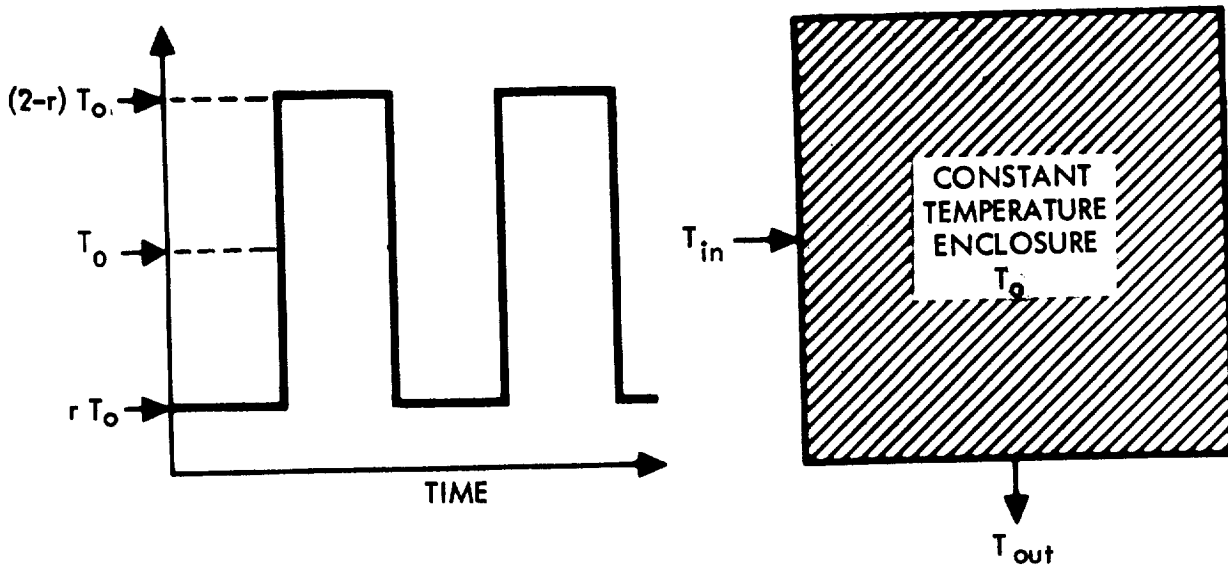


Figure 9.5 Input to Precision Comparator in Pulsed Mode

where f_m and f_p are the modulation and pulse frequency respectively, p is the duty factor of the pulses and τ_i the output integration time. This expression is approximately valid if the pulse phase is randomized between modulation cycles. However in practice, the phase is maintained for at least a few cycles and the factor $(2\tau_i f_m)^{1/2}$ should be replaced by $(2\tau_i/\tau_c)$ where τ_c is the correlation time for phase coherence.

9.3.3 Radiometer Sensitivity

The sensitivity of the nulling variable pulse rate radiometer is given by (ignoring for now the fluctuations due to the finite pulse frequency)

$$\Delta T_{\text{rms}} = 2 \frac{(T_o + T_n)}{1 - \ell} \left[\frac{1}{B\tau} + \left(\frac{\Delta G}{G}\right)^2 \right]^{1/2} \quad (9.23)$$

where T_n is now the noise temperature of the rf amplifier alone. This can be derived from the expression given in Table 9.2 by using Equation (9.11), or by simply noting that a temperature change at the horn aperture is reduced by the factor $1 - \ell$ at the amplifier input.

9.3.4 Radiometer Calibration

It is proposed that the radiometer be calibrated using one of the schemes shown in Figure 9.6. For highest reliability and accuracy the system 1 is preferred as the effect of waveguide losses up to the point of noise injection are minimal. However it necessitates that periodically the whole satellite or perhaps just the antenna be physically rotated so as to point nearly parallel to the galactic pole. It is realized that this arrangement may be impractical. The alternative to rotation is to have a fixed antenna pointing away from the earth that can be switched in using a low loss waveguide switch. Aside from the extra weight, the main disadvantage of this scheme is that the loss of the switch, although low, still adds substantially to the total input attenuation. Should these two configurations be unsuitable for the satellite in which the instrument is to be flown, then a radiatively and/or thermoelectrically cooled waveguide termination would have to be seriously considered.

9.4 PRACTICAL DESIGN

A practical design embodying the general principles just outlined is shown in Figure 9.7. The constant temperature enclosure now includes the noise injection system, the directional coupler and the RF amplifier, for obvious reasons of stability.

9.4.1 RF and IF Amplifiers

A degenerate parametric amplifier is a natural choice for the first stage of amplification of a high sensitivity radiometer. At 2.7 GHz double sideband noise temperatures of less than 50°K can be achieved, a factor of 2 better than non-degenerate types and a factor of 10 better than tunnel diode or transistor amplifiers. Gain stability is always of concern in a parametric amplifier, but the combined use of a quiet pump source, temperature stabilization of the amplifier and finally pump leveling via the varactor bias current results in quite acceptable performance.

A mixer with local oscillator at 2.7 GHz was chosen to follow the paramp mainly because of the simplicity of varying the output bandwidth; this may be especially useful during aircraft flights if radar interference is to be investigated. It is convenient then to use a crystal controlled fundamental oscillator at 2.7 GHz as both the local oscillator and the drive for a doubler which serves as the pump source. Crystal control is necessary both to avoid gain fluctuations due to frequency modulation, and to achieve the long term stability required by prospective satellite operation. Since the IF is effectively at zero frequency, it is important to discard the lower

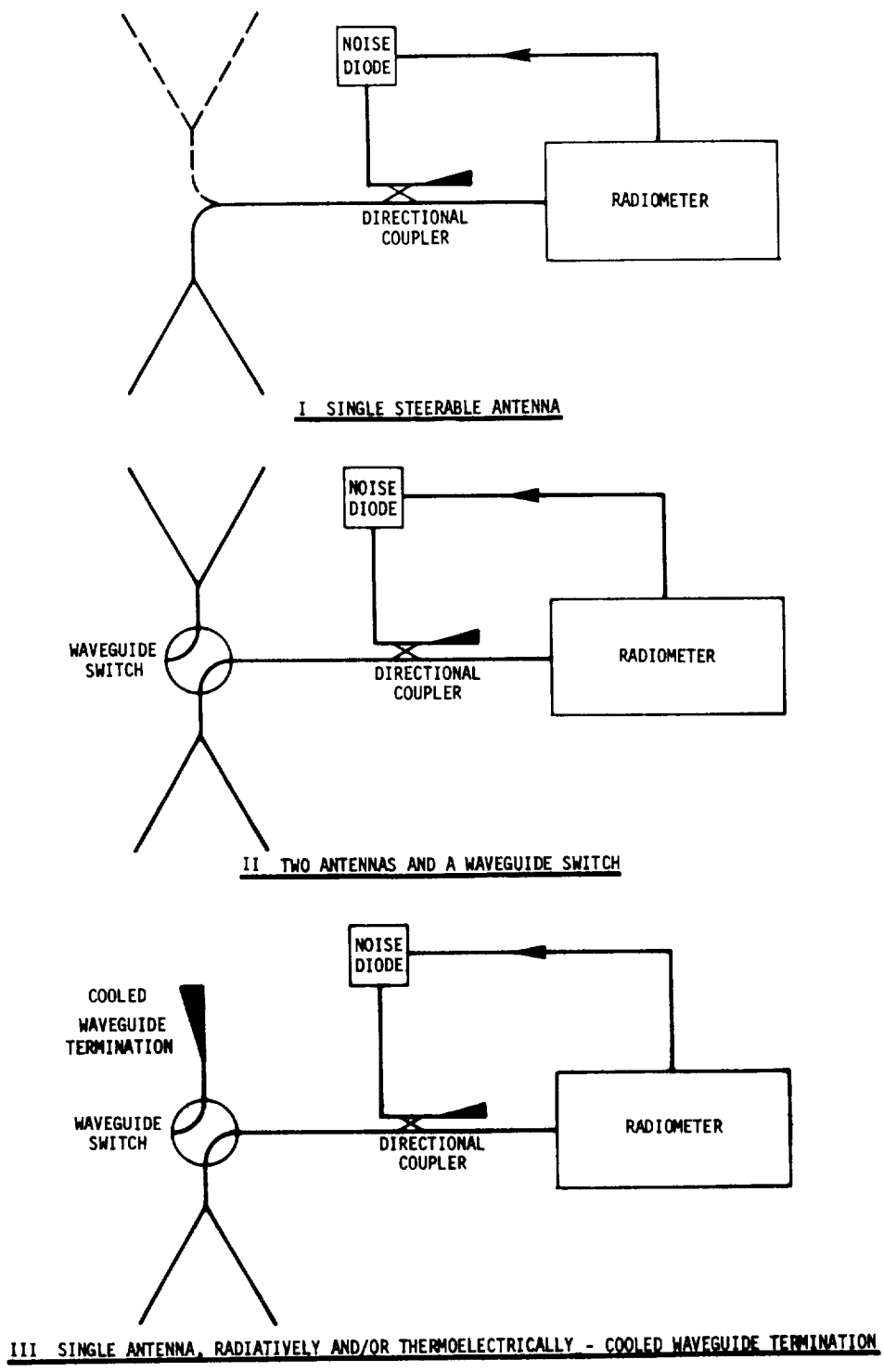


Figure 9.6 Three Different Calibration Techniques

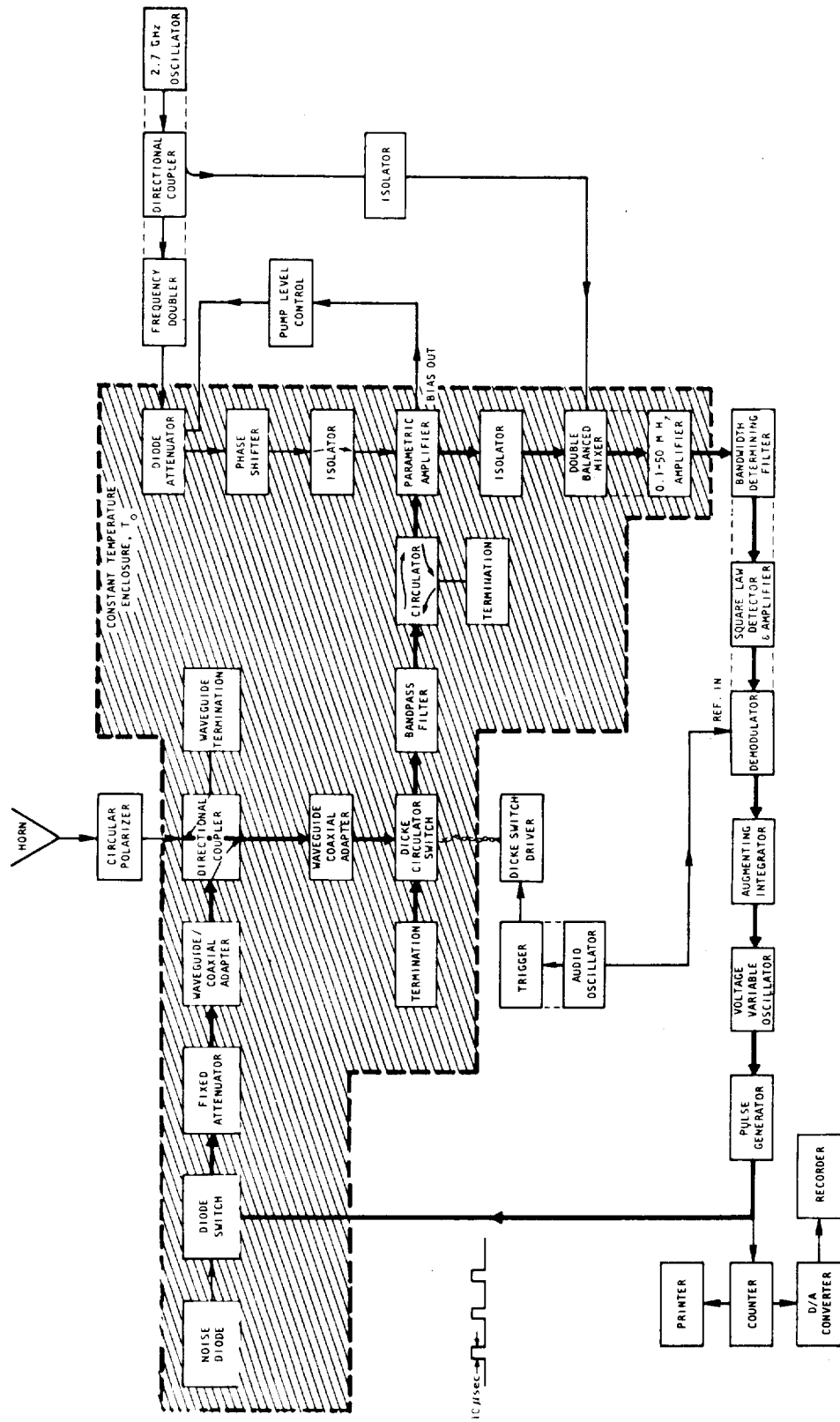


Figure 9.7 Detailed Block Diagram of Practical Design for Proposed Radiometer

100 kHz or so of the IF passband in order to avoid the carrier and its amplitude modulation sidebands. Gain fluctuations due to amplitude variations of the local oscillator are minimized by the balanced configuration.

The purpose of the bandpass filter following the circulator switch is to avoid overloading of the parametric amplifier by very strong out-of-band radar. The isolator on the output of the paramp serves to keep 2.7 GHz local oscillator power from reaching the input, and the other isolators are primarily to keep the VSWR down at the output of the pump. The mixer is double balanced to minimize noise from local oscillator fluctuations; this is especially important when a low modulation frequency is used.

9.4.2 Electronics Subsystem

The low frequency electronics are straightforward and except perhaps for the augmenting integrator, the functions of each of the blocks shown in Figure 9.7 are self-explanatory. The augmenting integrator provides both proportional and reset control for the pulse frequency; that is, an error signal at its input causes a proportional change in the output voltage at the same time that the integrating part of the circuit adjusts the average output voltage for zero error signal.

As a result of the feedback mode of the radiometer, most of the electronic units need not be designed for high stability or linearity. The exceptions are the demodulator which must have a very low offset, and the pulse generator that actuates the diode switch. Gain fluctuations at the modulation frequency must also be minimized in all units. If the radiometer output is obtained by measuring the pulse frequency then the requirements on the stability of the pulse width are very stringent, i. e. $\sim 0.01\%$. An alternative method that has been considered (and is in fact outlined in Figure 9.4) is to integrate the area under the pulses. In this case a pulse generator of very high amplitude stability is required.

9.4.3 Noise Injection Subsystem

The simplest way to achieve pulsed noise injection is to pulse the diode itself. However, available standard commercial units have large bypass capacitors across the current input and take several microseconds to switch. Furthermore, the relatively large temperature coefficient of the excess noise ($0.01 \text{ db}/^\circ\text{C}$) makes it likely that the peak noise output will vary with duty cycle. For these reasons a diode switch in series with the noise diode was chosen. A simple reflective type is adequate, but for highest stability it should only be used in the full on (diodes backbiased) and full off (diodes forward biased) positions. The attenuation in the off position can be expected to be quite temperature sensitive, but as long as the attenuation is high

enough this will not be important. The diodes themselves can add excess noise in the forward biased condition, but it is small for the type of switch envisioned (~ 0.2 db excess noise above its physical temperature) and the combined attenuation of the resistive pad following the switch and the (20db) directional coupler reduce its contribution to a negligible level.

The coupling coefficient of the directional coupler is chosen to be low enough that the sensitivity of the radiometer is not appreciably degraded by the thermal noise contribution of the noise injection arm, but large enough that resistive pads can be used on either side of the diode switch. Although not shown in Figure 9.7, it is important to include an attenuator between the noise diode and the diode switch, otherwise the large reflection coefficient of the noise diode (see Table 9.3) could seriously reduce the isolation of the switch which is reflective.

Alternatively one could either arrange the electrical path length between the two components to be an odd multiple of a quarter wavelength and possibly enhance the isolation, or use an isolator.

9.4.4 Quantitative Analysis of Square Law Detector

Any rectifying device will behave as a square law detector at low enough RF voltages. However, there is a limit to how far the RF signal can be lowered because of the noise, thermal or otherwise, generated by the device and the following amplifier. As a consequence, for any device there is a one-to-one correspondence between the signal/noise ratio of the detected signal and the deviation from square law response. This relationship may of course depend on the bias current and the frequency at which the noise is measured. In the present application, the combination of low demodulation frequency and the desired accuracy of square law response puts unusually stringent requirements on the square law detector. Due to its very low $1/f$ noise the Hot Carrier (Schottky barrier) diode has greater square law range than the point contact diode (even when optimum loading is used) and has been chosen for the present design. A quantitative analysis of its performance is given so that the errors sustained are known, and the operating conditions can be optimized. Much of the information to be presented concerning Hot Carrier diodes has been extracted from "Solid State Devices", Hewlett Packard, 1967.

Consider the diode to be connected as in Figure 9.8. For the purposes of this discussion one can assume the source impedance ρ to be zero. The capacitor is chosen to be effectively a short at the rf frequency but to have an impedance much greater than the diode impedance at the demodulating frequency. The low level characteristic of a Schottky barrier diode is given quite accurately by (Sorenson, 1965).

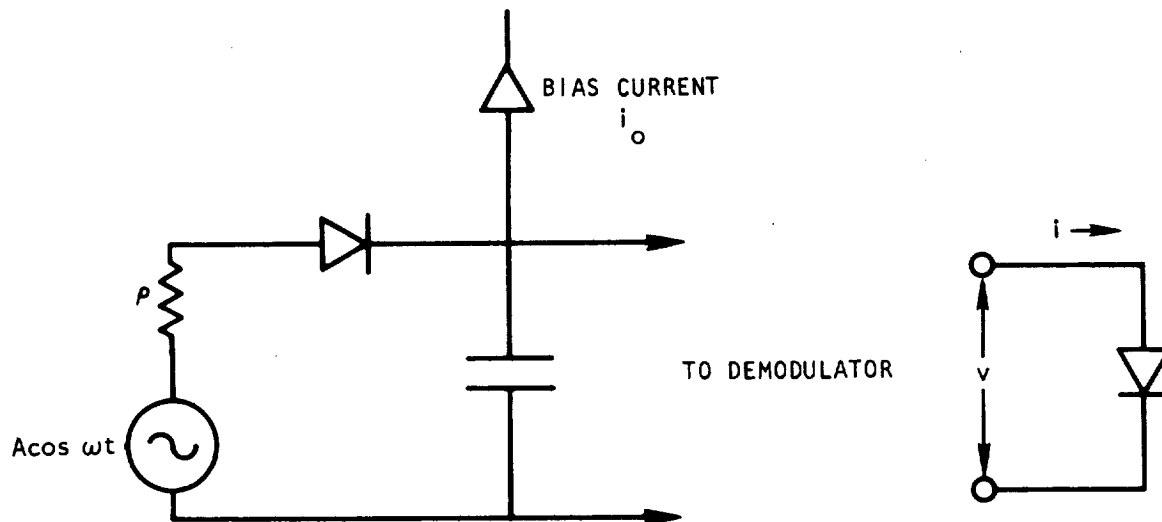


Figure 9.8 Detector Diode Circuit

$$i = I_s (e^{uv} - 1) \quad (9.24)$$

where

$$u = q/nkT$$

I_s is the saturation current

q is the electronic charge

T is the temperature in $^{\circ}\text{K}$

k is Boltzman's constant

n is the diode ideality factor (1.05 for Hewlett Packard silicon hot carrier diodes)

Putting $v = v_o + A \cos \omega t$ and expanding the exponential, i can be expressed as:

$$i = i_o + I_s e^{uv_o} \left[uA \cos \omega t + \frac{u^2 A^2}{2!} \cos^2 \omega t + \frac{u^3 A^3}{3!} \cos^3 \omega t + \frac{u^4 A^4}{4!} \cos^4 \omega t + \dots \right] \quad (9.25)$$

where A is the peak rf voltage, v_o the voltage across the diode due to the bias current i_o . Taking averages (the rf current cannot generate a voltage across the capacitor) and retaining terms up to the fourth power in A one obtains

$$\langle i \rangle = i_o + I_s e^{uv_o} \frac{u^2 A^2}{4} \left[1 + \frac{u^2 A^2}{16} \right] \quad (9.26)$$

The video impedance R_j is given by

$$R_j = \frac{dv}{di} = (u I_s e^{uv_o})^{-1} \quad (9.27)$$

so that the output voltage change Δv resulting from the rf voltage A is given by

$$\Delta v = R_j \Delta \langle i \rangle = \frac{u A^2}{4} \left[1 + \frac{u^2 A^2}{16} \right] \quad (9.28)$$

It is important to notice that the voltage sensitivity and the deviation from square law response (given by the factor $u^2 A^2/16$) are both independent of bias current.

Supposing for the moment that a deviation from square law response of 1 in 10^4 can be tolerated, the maximum rf voltage is obtained from

$$\delta = \frac{u^2 A^2}{16} = 10^{-4}$$

or $A = 4 \times 10^{-2} / u = 1.04 \text{mv}$ since $1/u = nkT/q = 26 \text{mv}$ for $T = 300^\circ \text{K}$. The corresponding output voltage is

$$\Delta v = \frac{4}{u} \frac{u^2 A^2}{16} = \frac{4 \times 10^{-4}}{u} = 10 \mu \text{volts.}$$

The mean square noise voltage $\overline{e_n^2}$ across the diode is given by

$$\overline{e_n^2} = 4 kT B_{1f} R_j t_d \quad (9.29)$$

where t_d is the noise temperature ratio of the diode. For a Hot Carrier diode t_d is closely approximated by

$$t_d = t_w + \frac{K_n I_d}{f} \quad (9.30)$$

where I_d is the diode current, f the frequency at which the noise is measured, and typical values of t_w and K_n are 0.8 and 1.8 Hz/ μ A respectively. The video impedance R_j is approximated by $1/uI_d$ for $I_d \gg I_s$ ($\approx 10^{-8}$ amps).

Therefore

$$e_n^2 = 4 kT B_{lf} \frac{1}{uI_d} \left[1 + \frac{K_n I_d}{f} \right] \quad (9.31)$$

which reaches a limiting value as I_d is increased of

$$e_n^2 \Big|_{\min} = 4 kT B_{lf} K_n / uf \quad (9.32)$$

or $(e_n^2)^{1/2} \approx 4\text{nV}$ in a 1 Hz bandwidth for $K_n = 1.8 \text{ Hz}/\mu\text{A}$ and $f = 50 \text{ Hz}$. The amplifier following the square law detector should therefore have an equivalent input noise of $4\text{nV}/\sqrt{\text{Hz}}$ or less. Without the use of a transformer this is achieved only with the very best low frequency, low noise junction field effect transistors. A transformer could be used, but would be quite bulky since the square wave demodulation demands very good low frequency response.

Combining Equation 9.32 with the result $\Delta v = 4 u^2 A^2 / u 16 = 4 \delta / u$ where δ is the fractional deviation from square law response, one obtains the relationship between signal/noise ratio and square law deviation:

$$\begin{aligned} \text{SN} &= \frac{\Delta v}{(e_n^2)^{1/2}} = \delta \left[\frac{4f}{kTB_{lf} K_n u} \right]^{1/2} \quad (9.33) \\ &= 26 \times 10^6 \delta \text{ for } (e_n^2)^{1/2} = 4\text{nV}. \end{aligned}$$

To summarize, for a Hot Carrier diode

- (1) The deviation from square law response of a diode fed by a constant RF voltage is independent of the dc bias current and is given by $\delta = u^2 A^2 / 16$.
- (2) The voltage sensitivity at constant rf voltage is also independent of bias current I_d .
- (3) The noise decreases as I_d increases until the $1/f$ noise dominates and a constant value is observed.
- (4) In the bias region of constant noise the signal/noise ratio S/N and fractional deviation from square law response δ are related by $S/N / \delta = \text{constant}$.

A practical procedure is, therefore, to increase the bias current until there is no further change in noise (if I_d is further increased the only effect is to lower the RF impedance). The RF and/or IF gain must then be carefully set to achieve the desired balance between S/N ratio and square law response. The very uniform characteristics of Hot Carrier diodes allows one to set δ simply by measuring the detected signal level and using $\delta = u \Delta v / 4$ where $u = 1/26 \text{mv}$.

The actual error in the radiometer reading caused by the non square law response of the diode depends on the relative closeness of the temperature to be measured and the temperature at which the radiometer was calibrated. Figure 9.9 shows the signal (referred to the input of the RF amplifier) presented to the square law detector during a portion of both parts of the modulation cycle. The voltage sensitivity of the diode can be rewritten as

$$e_{\text{out}} = C T_k (1 + \eta T_k) \quad (9.34)$$

where C is a constant, T_k the power input to the diode expressed in $^{\circ}\text{K}$ and referred to the input of the RF amplifier, and $\eta T_k = \delta$ the deviation parameter. Putting $T = e_{\text{out}}/C$, the quantities T_1 , T_2 , T_3 are defined as e_{out}/C for $T_k = T_n + T_A$, $T_n + T_A + T_D$ and $T_n + T_o$ respectively. T_n and T_A have been defined previously, and T_D represents the injected noise.

At null, one must have

$$T_3 - \left[(1-p)T_1 + pT_2 \right] = 0 \quad (9.35)$$

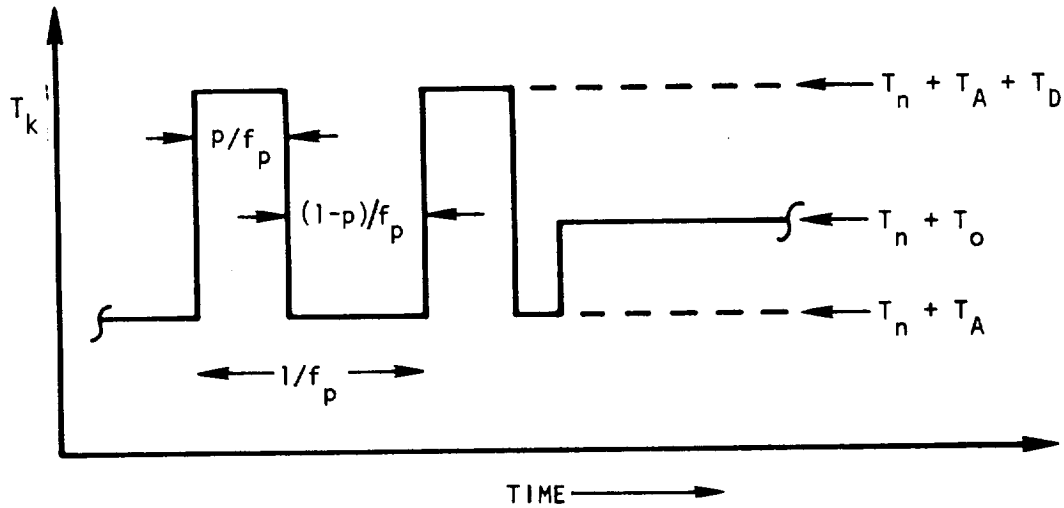


Figure 9.9 Effective Power Input to Square Law Detector

where p is the fraction of time the noise diode is turned on and is proportional to the pulse frequency f_p for constant width noise pulses.

If η were zero, this would translate to

$$T_o - \left[(1-p)T_A + p(T_A + T_D) \right] = 0 \quad (9.36a)$$

or
$$T_A = T_o - pT_D \quad (9.36b)$$

The calibration procedure is to replace T_A with a known temperature T_c :

$$T_c = T_o - p_c T_D \quad (9.36c)$$

Therefore, combining Equation 9.36b with 9.36c one has the radiometer equation (for $\eta=0$)

$$T_A = T_o - \frac{P}{p_c} (T_o - T_c) . \quad (9.37)$$

In practice η is always finite and it is desired to know the consequent error if Equation 9.37 is used, p and p_c now being determined by the exact null condition given by Equation 9.35:

$$p = \frac{T_3 - T_1}{T_2 - T_1} .$$

Now

$$\begin{aligned} T_1 &= (T_n + T_A) \left[1 + \eta (T_n + T_A) \right] \\ T_2 &= (T_n + T_A + T_D) \left[1 + \eta (T_n + T_A + T_D) \right] \\ T_3 &= (T_n + T_o) \left[1 + \eta (T_n + T_o) \right] \end{aligned}$$

so that with rearrangement

$$\begin{aligned} T_3 - T_1 &= (T_o - T_A) \left[1 + \eta (2T_n + T_o + T_A) \right] \\ T_2 - T_1 &= T_D \left[1 + \eta (2T_n + 2T_A + T_D) \right] , \end{aligned}$$

and therefore to first order in η

$$p = \frac{T_o - T_A}{T_D} \left[1 + \eta (T_o - T_D - T_A) \right] ,$$

and again to first order in η ,

$$\frac{p}{p_c} = \frac{T_o - T_A}{T_o - T_c} \left[1 - \eta (T_A - T_c) \right] . \quad (9.38)$$

In the NASA Convair 990 flights, operation of the radiometer at full band width ($2.69 \text{ GHz} \pm 50 \text{ MHz}$) was found to be too noisy. However, it was determined that radar interference could be minimized over the Northern Pacific Ocean by narrowing the bandwidth to $2.69 \pm 20 \text{ MHz}$. Radar interference even at a $\pm 10 \text{ MHz}$ bandwidth at a center frequency of 2.69 GHz began to be a serious problem within 100 n.m. of the Pacific Coast and Alaska.

After discussions with Dr. Blume regarding the operational and physical factors, the decision was made to use the frequency range 2.55 to 2.70 GHz for the NASA Airborne Radiometer.

9.6 RADIOMETER ANTENNA CONFIGURATION

In the following discussion the basic requirements for the radiometer antenna are developed and various antenna types are examined and compared. As a result of these studies, the horn antenna has been selected as the only candidate which best meets all the requirements. Two basically different kinds of horn radiators are discussed and the study concludes with an analysis of the multimode horn.

9.6.1 Fundamental Requirements

Field of View. The interrelationship between temperature resolution and spatial resolution for a satellite radiometric sensor has been definitively studied by Sherman (1969). His treatment is quite general and assumes that the sea surface is scanned in the flight path direction by the motion of the spacecraft, and transversely thereto by step-scanning the antenna. One general conclusion is that best temperature resolution is achieved with a small diameter antenna and a large surface resolution element.

Although antenna scanning is not contemplated at present, Sherman's conclusions are still generally valid. Ewing (1967), however, estimates that maximum acceptable resolution element size is about 200 miles on the sea surface. Footprint size (defined by the antenna's 3 db contour) is approximately given by H/D_λ where H is satellite altitude and D_λ is the aperture dimension in wavelengths. Thus, for a satellite at 500 miles altitude an aperture of at least $2\text{-}1/2$ wavelengths is needed.

If the footprint is to move no more than one-half its diameter during the course of a temperature determination, then $V\tau \leq H/2D_\lambda$ where V is the satellite's orbital speed (~ 5 miles per second) and τ is the radiometer's integration time (~ 4 seconds). This condition leads to an aperture not exceeding $12\text{-}1/2$ wavelengths. Applying the same reasoning to the case of an aircraft flying at 40,000 feet altitude and a speed of 800 feet per second (550 mph) leads to an antenna size of about 6 wavelengths or smaller.

Thus, it appears that an aperture size in the region of 2.5λ to 6λ is satisfactory for both satellite and aircraft flight test use. The surface resolution is approximately equal to the footprint size and will be from 80 to 200 miles for the satellite case. Assuming an aperture efficiency of 55 percent this requires an antenna having between 16 and 24 db gain.

Beam Efficiency. In light of the above, aperture efficiency is of considerably less importance than beam efficiency, the latter being a measure of how well the antenna concentrates its radiated power into its main lobe. From the radio astronomical viewpoint, high beam efficiency goes along with low "zenith noise temperature"; minor lobes which point earthward or to warm regions of the sky are very small and contribute little compared to the main beam.

Beam efficiency is formally defined by

$$\eta = \frac{\Omega_M}{\Omega_A} = \frac{\iint_{\text{main lobe}} P(\theta, \phi) d\Omega}{\iint_{4\pi} P(\theta, \phi) d\theta} \quad (9.41)$$

where $P(\theta, \phi)$ is the antenna power pattern and Ω_M is the solid angle of the main beam. The effective antenna solid angle Ω_A is related to the directive gain G by

$$\Omega_A = \frac{4\pi}{G} \quad (9.42)$$

Thus high beam efficiency will result only when the total integrated side lobe level is small. It is particularly important to ensure that all side lobes remote from the main beam be suppressed to very low levels.

Ohmic Efficiency. Ohmic loss in the antenna will modify the apparent temperature in accordance with the usual relation

$$T_a = tT_B + (1-t) T_h$$

where T_a is the apparent temperature of the source whose brightness temperature is T_B , T_h is the ambient temperature of the antenna, and t represents its transmission coefficient. When the loss is .01 db the value of $1-t$ is numerically .0023. At $T_h = 300^\circ\text{K}$, the second term above is then almost

0.7°K. Thus a very small amount of loss makes a significant contribution to the apparent temperature.

It is a practical impossibility to make the ohmic loss term negligible. Hence the only recourse is to make ohmic loss as small as possible, and then to apply a correction. To do this successfully it is imperative that the losses be stable with respect to time and environmental conditions and that they be measurable or otherwise calculable to within an uncertainty of less than .0015 db (i. e. 0.1°K in temperature).

Circular Polarization. A convenient way of measuring the average of the parallel and perpendicularly polarized components of thermal emission is to use an antenna responsive to circular polarization. The necessary averaging is then performed automatically, independently of the orientation of the antenna around its own axis.

In satellite use the antenna will point directly downward toward the sea surface; the angle of incidence, therefore, is zero for the beam axis. There is thus no unique plane of incidence and it is meaningless to distinguish between parallel and perpendicular polarizations. For other directions within the main beam, however, the two polarizations do exist independently. Consequently the antenna should be circularly polarized everywhere throughout its main beam. It is not sufficient simply to specify zero db ellipticity ratio on axis, though this is acceptable in many other applications.

Other Requirements. The antenna must operate over a bandwidth at least equal to that of the radiometer receiver. Although the latter should be narrow, to reduce interference, it may have to be as much as 100 MHz in order to meet temperature resolution requirements.

One final but important consideration concerns the size and shape of the antenna, for it clearly must be compatible with spacecraft mounting and deployment.

9.6.2 Comparison of Antenna Types

The desiderata discussed above will now be used to evaluate the potential applicability of various generic antenna types to satellite radiometer use.

Reflectors. This type of antenna can easily meet the gain requirement and, with care, will have very low ohmic loss. It will have reasonably good circular polarization characteristics over the main beam, but some off-axis ellipticity is inevitable, partly due to curvature of the reflector which creates cross-polarized radiation, and partly to ellipticity in the feed pattern. It is well adapted to packaging and deployment in a spacecraft.

The weakness of the reflector is in respect to beam efficiency, which is poor largely because of spillover. Spillover into the rear hemisphere can be reduced by use of a deep reflector (i. e. small F/D ratio) but spurious forward radiation scattered by the feed and its supports still degrades beam efficiency.

Cassegrain systems merely substitute forward spillover for rearward and are quite unattractive for small apertures; shadowing would be enormous in the case of an aperture size of $2-1/2 \lambda$ to 6λ .

Arrays. One of the main advantages of the array, namely its ability to scan electronically, is irrelevant in this application where antenna pointing direction is fixed.

The non-resonant array, using an element spacing which differs from one-half wavelength, does not generate a broadside beam, and the pointing angle scans with changing frequency. These are minor disadvantages compared to the fact that there must always be some power left over at the end of the feed line. If the line is short-circuited, reflection gives rise to a conjugate beam at angle $-\theta$ to the normal when the principal beam is at angle $+\theta$. The conjugate beam is just an unwanted sidelobe that degrades beam efficiency. It is usually suppressed by terminating the feed line in a matched load instead of a short circuit. The fractional power so absorbed then represents ohmic loss. In a short array it is not possible to ensure that less than 4 to 5 percent of the power is left over. This would represent intolerably high loss of about 0.2 db.

The above difficulties are overcome in the resonant array where element spacing is one-half wavelength measured in the feed lines, the latter being terminated in a short circuit at a quarter wave beyond the last element. A phase shift of π radians must be introduced between adjacent elements in order to obtain a broadside beam. The conjugate beam then coincides with the main beam. One way of obtaining the phase shift is by staggering longitudinal slots alternately on each side of the center line of the broad face of a waveguide. The orthogonal linear polarization can be produced by an array of inclined edge slots in the narrow wall, providing slot inclinations are alternated to yield the necessary π radians phase shift. In both arrangements the radiation pattern is degraded in the intercardinal planes; high side lobes occur for the staggered broadwall slots, and high cross polarization for the inclined edge slots.

The degradation in beam efficiency due to these effects can partially be overcome by fitting fins to the side of the guide to form a long narrow continuous aperture. Several such line sources must then be placed side

by side to form a two dimensional array, and a corporate power divider performace is used to feed the several line sources, thereby introducing matching difficulties and increased loss.

The production of circular polarization appears to require the interleaving of both kinds of array discussed above, i. e., the staggered broad wall slots together with the inclined edge slots. The need to excite the two in quadrature further complicates the power divider and the whole geometrical configuration becomes extremely complex. It is not at all certain that a satisfactory circularly polarized array could be designed in this manner.

Horn Antennas. Ohmic loss in waveguide decreases inversely with the transverse dimensions of the guide. The loss in a horn thus comes mainly from the throat area, not from the mouth. A horn which flares from typical waveguide dimensions to an aperture size between $2\frac{1}{2}\lambda$ and 6λ will have very low loss if well constructed of high conductivity metal.

The conventional horn cannot yield high beam efficiency nor good circular polarization over the whole of the main beam when excited in the dominant mode alone. This is a result of the fact that it has an aperture distribution which is tapered in the H plane, but uniform in the E plane. Two principal techniques have been developed by which the E plane distribution can be tapered to match that in the H plane; it is a fortunate fact that such techniques lead simultaneously to high beam efficiency and excellent polarization characteristics.

In one technique, transverse corrugations are cut into the horn walls, creating a capacitive surface when the depth is between $\lambda/4$ and $\lambda/2$. This has the effect of forcing the same boundary conditions upon both E and H. Rumsey (1966) has shown that this condition is sufficient to produce a radiation pattern (from a square or circular aperture) which is the same in all planes through the axis. Experimental results obtained with such horns are described in the literature (Minnett, et al, 1966 and Kay, 1962). The technique has also been successfully developed at Ohio State University (Lawrie, et al, 1966 and Bahret, et al, 1968), although from a different viewpoint, namely that of diffraction theory applied to the E plane edges of a pyramidal horn.

Another technique in wide use is exemplified by the multimode conical horn of Potter (1963), in which the E plane aperture distribution of the dominant TE_{11} mode is suitably modified by the introduction of the higher order TM_{11} mode. A modification of this approach has been emphasized in the present study in the belief that diagonal horn performance could be improved by using higher order mode excitation to suppress unwanted

Table 9.5 Antenna Comparison Chart

Antenna Type Desired Specification	Reflector	Array	Multimode Horn
Gain of 16 to 24 db (aperture size 2.5λ to 6λ) Beam efficiency	Easily achieved with prime focus feed. Cassegrain systems suffer too much blocking. Poor but special techniques can boost it somewhat.	Easily achieved, requiring square array of 5x5 up to 12x12 elements. Good in a non-resonant array. Resonant array requires use of fins to suppress unwanted lobes.	Easily achieved. Very high: estimated at 98%
Circular Polarization (low ellipticity over the main lobe)	Good. Some off-axis ellipticity is inevitable.	Poor. Very complex techniques and much development work needed.	Excellent. Very high purity can be achieved over the major part of the main lobe.
Ohmic Efficiency Satellite Packaging Compatibility	Very high. Losses are confined mainly to the feed and can be kept small. Good	Fairly high for a resonant array, but very poor in non-resonant arrays. Excellent	Very high. The horn is simply a low loss transmission line. Poor

cross-polarized radiation. For this reason attention was focused on square aperture horns fed by square waveguide. The dominant mode is thus the TE₁₀, and investigations have shown that excellent results can be obtained by exciting the proper amounts of the TM₁₂ and TE₁₂ modes. It turns out, however, that when this is correctly done there is no advantage to be gained by using a diagonal mode square horn. Diagonalization is worthwhile only for the dominant mode, in which case it suppresses principal plane side-lobes and equalizes beam widths at the expense of introducing cross polarized lobes in the inter-cardinal planes.

9.6.3 Antenna Selection

In the light of the above discussion, Table 9.5 has been prepared to summarize the merits and demerits of the various types of antennas which can be considered as serious candidates for satellite radiometer use.

Until means are found to improve significantly the beam efficiency factor it appears necessary to rule out the reflector antenna, although it is attractive on other counts.

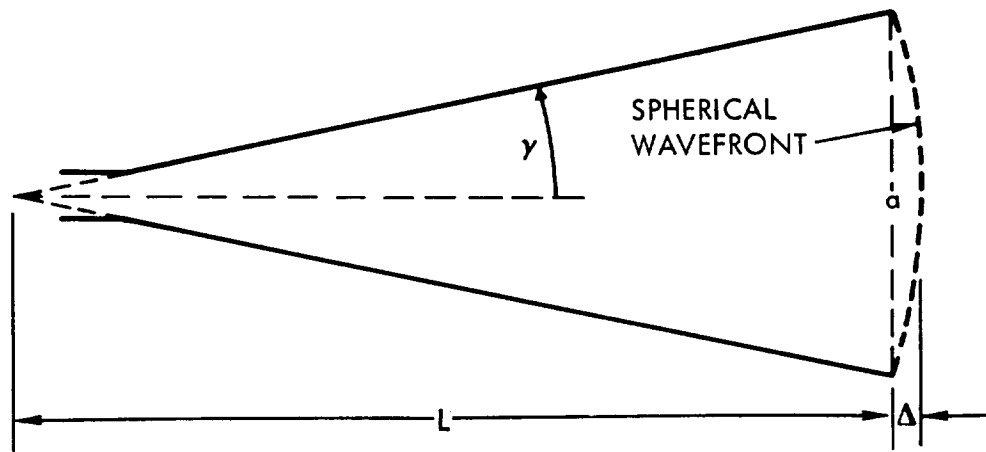
The non-resonant array falls far short of meeting the high ohmic efficiency requirement and is therefore summarily discarded. The resonant array has potential, but uncertainties exist in regard to the areas of beam efficiency and circular polarization. A large amount of development effort would be required to determine whether this potential is realizable in practice.

From the electrical point of view, the horn is unequivocally the right choice. Although there is little to choose between the multi-mode horn and the corrugated horn so far as electrical performance is concerned, the former appears to be somewhat simpler mechanically since it does not require thick walls to accommodate deep corrugations.

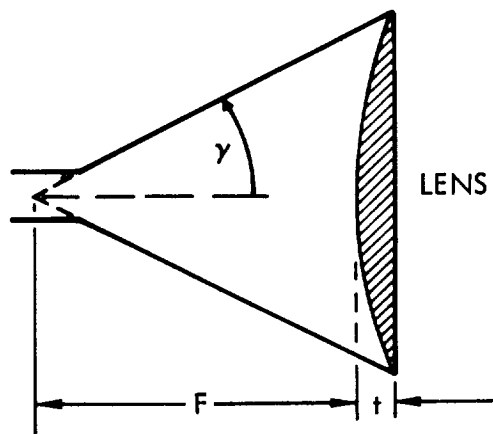
Horn Compensation. The one shortcoming of the horn is that it has a poor form factor for satellite packaging compatibility. Unless some of its electrical characteristics are compromised the flare angle must be small and the overall length long, or else compensation is required to correct phase error.

An uncompensated horn is shown in Figure 9.10A. The spherical wave front across the aperture implies the existence of quadratic phase error of magnitude $2\pi\Delta/\lambda$ radians, in which

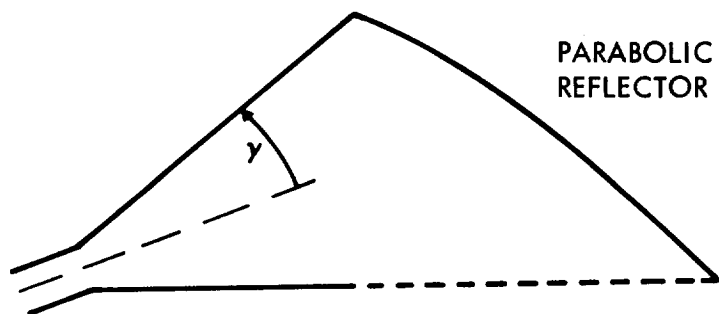
$$\frac{\Delta}{\lambda} \approx \frac{a^2}{8\lambda L} = \frac{a}{4\lambda} \cdot \tan^2\gamma \quad (9.43)$$



A. UNCORRECTED



B. LENS CORRECTED



C. HORN/REFLECTOR

Figure 9.10 Horn Compensation

where γ is the half-flare angle, a the aperture dimension and L the overall length from apex to aperture. Actual length is normally somewhat less than L . Using $a = 4.5\lambda$ as an average diameter, and taking $\lambda = 11.2$ cm ($f = 2690$ MHz), Table 9.6 lists phase error and length for various flare angles.

In the first two cases phase error compensation might possibly not be needed, but the horn is objectionably long. The last two cases lead to a compact horn, but phase error correction is certainly required. This can be accomplished in several ways, of which two are discussed below.

First, a horn reflector may be used, as in Figure 9.10C. Clearly, the reflector will remove all of the phase error and beam efficiency will remain high. Polarization characteristics will be somewhat degraded, however, due to loss of symmetry in the aperture, which is no longer square but trapezoidal.

Second, a lens may be fitted in the aperture, as in Figure 9.10B although it need not be plano-convex. This appears to be the preferred technique, even though a small amount of ohmic loss is thereby introduced. The loss is easily calculable, and a rough estimate will now be given. The lens thickness d depends on dielectric constant ϵ and is given by $d = \Delta/(\sqrt{\epsilon} - 1.)$

If the loss tangent of the dielectric is $\tan \delta$ then its attenuation constant is

$$\alpha = 1/2 k\sqrt{\epsilon} \cdot \tan \delta \text{ nepers/unit length.}$$

Table 9.6. Phase Error in Horns of Various Flare Angles

γ degrees	$\frac{\Delta}{\lambda}$	Error in degrees	L cm
8	0.16	57	178
12	0.24	86	119
16	0.32	116	88
20	0.41	147	69

Providing a is small the loss in a thickness d is approximately

$$ad \approx \frac{\pi d}{\lambda} \sqrt{\epsilon} \cdot \tan \delta \text{ nepers}$$

or

$$ad \approx 8.68 \frac{\pi \Delta}{\lambda} \frac{\sqrt{\epsilon}}{\sqrt{\epsilon} - 1} \cdot \tan \delta \text{ db} \quad (9.44)$$

Assuming the lens is of teflon, then $\epsilon = 2.05$ and $\tan \delta = 3 \times 10^{-4}$, so that loss in the lens is given by

$$ad = .027 \frac{\Delta}{\lambda} \text{ db.} \quad (9.45)$$

Table 9.7 lists the lens loss for the previous cases and also indicates the temperature contributed by this loss, based on the assumption that the lens is at 300°K ; 0.01 db then corresponds to 0.69°K in temperature.

Though the ohmic loss is extremely small, nevertheless the temperature contribution is significant and must be corrected for. The correction, fortunately, is small and it is a simple matter to calculate it to a precision of better than 0.1°K . The above estimate is clearly somewhat pessimistic, for it assumes that all paths have length d through the lens, whereas d is in reality the maximum path.

Recommended Configuration. These studies unequivocally point to some form of horn antenna as the preferred choice for radiometric use in remote sensing of ocean surface temperature. In this study emphasis has been placed on the multimode pyramidal horn, partly because it is somewhat simpler in construction and partly because corrugated horns are the subject of detailed study elsewhere (Lawrie, et al, 1966).

The recommended form of multimode horn employs a teflon lens for aperture phase compensation. It should be noted that lens compensation also should be used for a corrugated horn if optimum performance is to be realized.

Table 9.7. Lens Loss for Horns of Various Flare Angles

γ degrees	$\frac{\Delta}{\lambda}$	lens loss, db	temperature added, $^\circ\text{K}$
8	0.16	0.0043	0.30
12	0.24	0.0065	0.45
16	0.32	0.0087	0.60
20	0.41	0.010	0.69

9.6.4 Multimode Horn Analysis

Radiation Pattern. The dominant mode radiation field of a pyramidal horn is free of cross-polarization except in directions far from the beam axis. If higher mode radiation is to be introduced for purposes of pattern control then this radiation must likewise be free of cross-polarization. This is not the case for any higher order TM or TE mode alone, but the following analysis shows that certain combinations of TM and TE modes do effect suppression of cross-polarized radiation.

A square horn aperture of side a is assumed, lying in the xy plane with the z axis along the axis of the square waveguide which feeds the horn. It will be assumed that the aperture fields are just those of the exciting waveguide mode. Taking spherical coordinates R, θ, ϕ with origin at the center of the aperture, the radiated field has components (Silver, 1947),

$$\left. \begin{aligned} E_{\theta} &= w \cdot \frac{m^2 \sin^2 \phi - n^2 \cos^2 \phi}{\sqrt{m^2 + n^2}} \cdot \psi_{mn} \\ E_{\phi} &= w \cdot \sqrt{m^2 + n^2} \cdot \sin \phi \cos \phi \cdot \psi_{mn} \end{aligned} \right\} \quad (9.46)$$

for TE_{mn} mode excitation, while for the TM_{mn} mode the components are

$$\left. \begin{aligned} E_{\theta} &= w \cdot \frac{mn}{\sqrt{m^2 + n^2}} \psi_{mn} \\ E_{\phi} &= 0 \end{aligned} \right\} \quad (9.47)$$

where

$$\psi_{mn} = \epsilon_{mn} \frac{\sin\left(u + \frac{m\pi}{2}\right)}{u^2 - \left(\frac{m\pi}{2}\right)^2} \cdot \frac{\sin\left(v + \frac{n\pi}{2}\right)}{v^2 - \left(\frac{n\pi}{2}\right)^2} e^{i(m+n+1)\frac{\pi}{2}} \quad (9.48)$$

$$u = w \cos \phi \quad v = w \sin \phi \quad w = \frac{\pi a}{\lambda} \sin \theta \quad (9.49)$$

and

$$\left. \begin{array}{l} \epsilon_{mn} = 1 \quad \text{for } m \neq 0, n \neq 0 \\ \epsilon_{mn} = 1/\sqrt{2} \quad \text{if } m = 0 \text{ or } n = 0 \end{array} \right\} \quad (9.50)$$

The field expressions have been normalized in such a way that all modes carry the same power to the aperture. This is done by requiring that the integral of the Poynting vector over the aperture be constant.

In directions not too far from the beam axis (i. e., small θ) the rectangular components of field are

$$E_x = E_\theta \cos \phi - E_\phi \sin \phi$$

$$E_y = E_\theta \sin \phi + E_\phi \cos \phi$$

so that for TE modes

$$\left. \begin{array}{l} E_x = \frac{-n^2}{\sqrt{m^2 + n^2}} \cdot u\psi_{mn} \\ E_y = \frac{m^2}{\sqrt{m^2 + n^2}} \cdot v\psi_{mn} \end{array} \right\} \quad (9.51)$$

while for TM modes

$$\left. \begin{array}{l} E_x = \frac{mn}{\sqrt{m^2 + n^2}} u\psi_{mn} \\ E_y = \frac{mn}{\sqrt{m^2 + n^2}} v\psi_{mn} \end{array} \right\} \quad (9.52)$$

It now becomes clear that, by taking a linear combination of TE_{mn} and TM_{mn} modes, either E_x or E_y can be made to vanish. Thus, if the radiation field is to be entirely polarized in the y direction, then E_x is required to vanish and the proper combination is the hybrid

$$\frac{m \cdot \text{TE}_{mn} + n \cdot \text{TM}_{mn}}{\sqrt{m^2 + n^2}} \quad (9.53)$$

which gives

$$E_x = 0 \quad E_y = m v \psi_{mn} \quad (9.54)$$

Because of the normalization the powers carried by the TE and TM modes are respectively proportional to m^2 and n^2 , while the total power is unity.

The dominant mode field, given by Equations (9.51) with $m = 1$ $n = 0$, is

$$E_x = 0, \quad E_y = \frac{1}{\sqrt{2}} \frac{\cos u}{u^2 - \frac{\pi^2}{4}} \cdot \frac{\sin v}{v} \quad (9.55)$$

The E plane is the yz plane, for which $\phi = 90^\circ$ and $u = 0$. The E plane field pattern is thus

$$E_y = \frac{4}{\pi^2 \sqrt{2}} \frac{\sin w}{w} \quad (9.56)$$

With $\phi = 0$, $v = 0$, the H plane pattern becomes

$$E_y = \frac{4}{\pi^2 \sqrt{2}} \frac{\cos w}{1 - \frac{4w^2}{\pi^2}} \quad (9.57)$$

These are the familiar results for dominant mode horn radiation, in which the H plane pattern is about 35 percent wider and has side lobe levels about 10 db lower than the E plane, these facts being responsible for degraded beam efficiency and inability to radiate circular polarization over the whole of the main beam. Introduction of the hybrid mode discussed above effects not only E plane side lobe suppression but almost equalizes the pattern shape in all planes.

The proper hybrid mode for this purpose is that for which $m = 1$ $n = 2$ and is henceforth referred to as the TE/TM₁₂ hybrid. If the fractional power in this mode is β^2 relative to the dominant mode then the radiated field is, by combining (9.54) and (9.55) and dropping a numerical multiplier,

$$E_x = 0, \quad E_y = \frac{\cos u}{1 - \frac{4u^2}{\pi^2}} \cdot \frac{\sin v}{v} \cdot \left[1 - \beta\sqrt{2} \frac{v^2}{v^2 - \pi^2} \right] \quad (9.58)$$

The H plane pattern, for which $\phi = 0$ and $u = w$, $v = 0$, remains unchanged,

$$\text{H plane:} \quad E_y = \frac{\cos w}{1 - \frac{4w^2}{\pi^2}} \quad (9.59)$$

The E plane pattern, for which $\phi = 90^\circ$, $u = 0$, $v = w$, becomes

$$\text{E plane} \quad E_y = \frac{\sin w}{w} \left[1 - \beta\sqrt{2} \frac{w^2}{w^2 - \pi^2} \right] \quad (9.60)$$

Computer calculations of these patterns show that the interesting range for the parameter β is between 0.4 and 0.6. The former value leads to near equalization of the main beam shapes in all planes, whereas the latter results in almost total suppression of all side lobes in the E plane. Figure 9.11 shows the principal and intercardinal plane patterns for $\beta = 0.465$ and Table 9.8 lists the main features.

Table 9.8. Multimode Horn Pattern Characteristics; $\beta = 0.465$

Characteristic Feature	E Plane	H Plane	45° Planes
Full 3db beamwidth in radians	$1.16 \frac{\lambda}{a}$	$1.19 \frac{\lambda}{a}$	$1.19 \frac{\lambda}{a}$
Full 10db beamwidth in radians	$2.04 \frac{\lambda}{a}$	$2.04 \frac{\lambda}{a}$	$2.10 \frac{\lambda}{a}$
First sidelobe level in db	-45	-23	-64
Second sidelobe level in db	-31	-32	-68

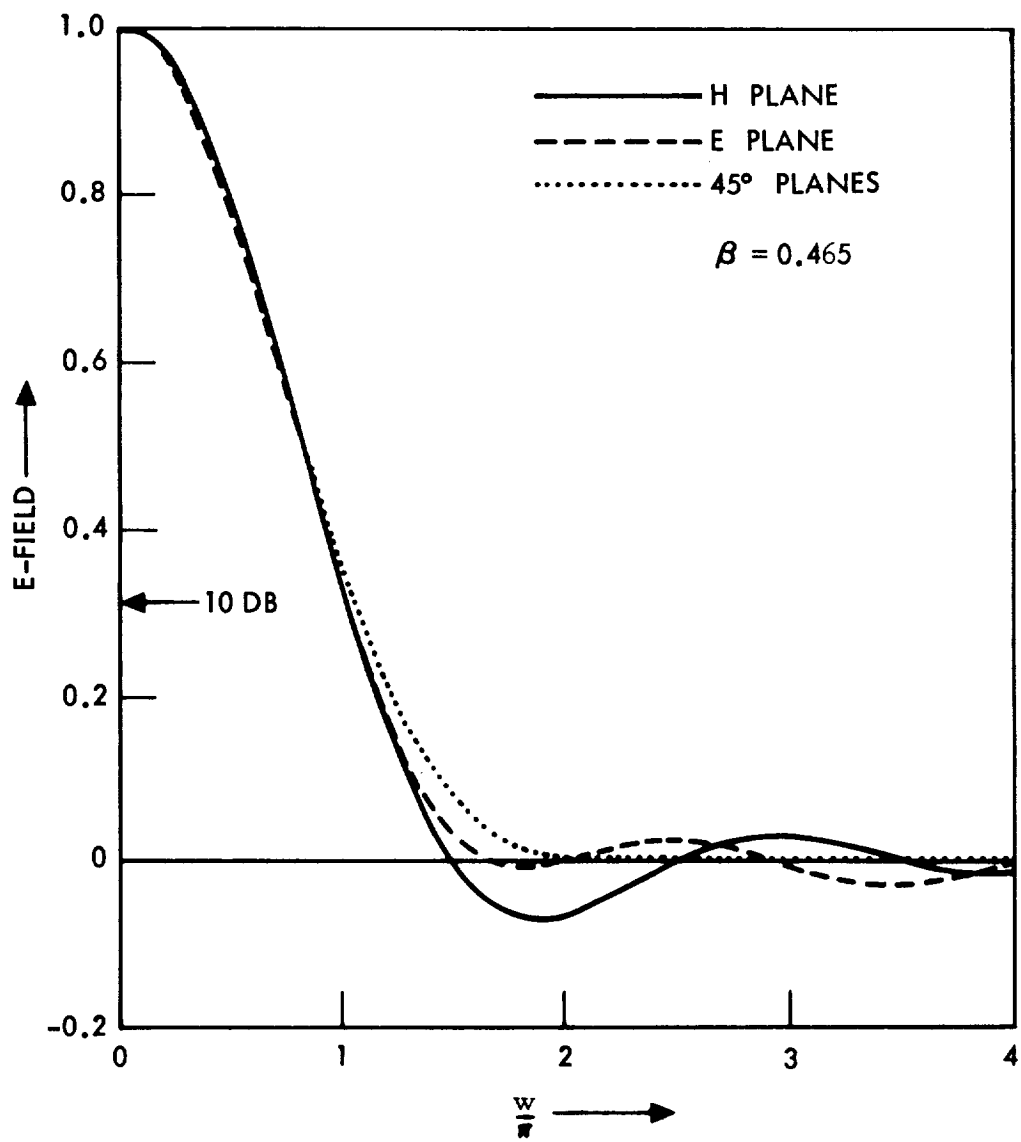


Figure 9.11 Multimode Horn Pattern

Mode Generation. One method of generating the required hybrid TE/TM₁₂ mode becomes apparent when the internal waveguide field for this mode is examined, along with that of the dominant mode. A qualitative picture of the transverse electric field in the aperture is shown in Figure 9.12. The dominant mode has no component E_x and it turns out that this component is vanishingly small for the hybrid mode also, when the guide cross-section becomes large, as it is in the aperture.

The sketches in Figure 9.12 show that the electric field can be made small, or even zero, at the E plane edges y = 0 and y = a. Thus a tapered field distribution is obtained in the E plane as well as in the H plane. Furthermore, conducting surfaces may be placed in the guide as indicated by the hatched areas without doing violence to the boundary condition that tangential E must vanish on a conductor. Conversely, therefore, it follows that when the dominant mode encounters such a pair of obstacles the boundary conditions will ensure generation of the desired hybrid TE/TM₁₂ mode. When circular polarized modes are required a similar, but orthogonal, pair of baffles will be needed. Of course such baffles will give rise to both forward and backward hybrid waves. If, instead of baffles, the guide cross-section is discontinuously increased then the backward wave can be suppressed by sizing the guide to be cut off for the hybrid mode (but not for the dominant) on the incident side of the step.

Flare angle changes in the horn can also be used to generate the TE/TM₁₂ hybrid as described by Cohn (1970). This method appears to be capable of yielding greater bandwidth and lower mismatch than that indicated above, but is unsuited for use in short horns having relatively large flare angles.

Beam efficiency. It is instructive to regard beam efficiency as a function of the polar angle θ , measured from the beam axis. This requires a slight modification of the definition given earlier, such that Equation (9.41) becomes

$$\eta(\theta) = \frac{\int_0^\theta \int_0^{2\pi} P(\theta, \phi) \sin \theta d\theta d\phi}{\int \int_{4\pi} P(\theta, \phi) d\Omega} \quad (9.61)$$

By this new definition, beam efficiency is simply the fractional power radiated within a cone whose axis coincides with the beam axis, and whose half-angle is θ .

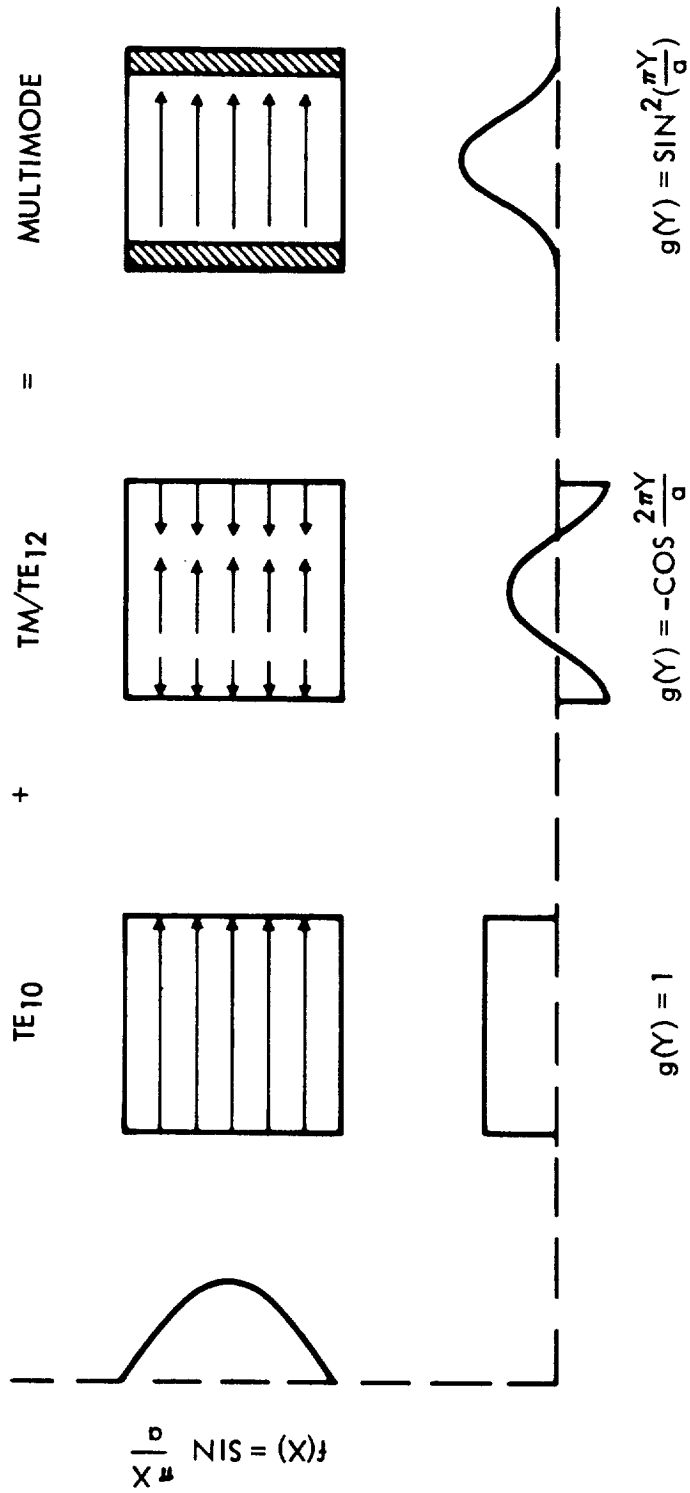


Figure 9.12 Multiple Modes in Square Aperture

To determine beam efficiency in this way for a multimode square horn the power pattern is obtained from

$$P(\theta, \phi) = \left| E_x \right|^2 + \left| E_y \right|^2$$

where E_x and E_y are given by Equations (9.58). When this $P(\theta, \phi)$ is substituted in (9.61) a numerical integration may then be performed to obtain $\eta(\theta)$.

This has been done for a multimode square horn having a full half-power beamwidth of 12° and the radiation patterns shown in Figure 9.11. The computed beam efficiency, as a function of θ , is shown in Figure 9.13. At the angle of the first H plane null ($\theta \approx 15^\circ$) the beam efficiency has reached almost 98 percent.

9.6.5 Effect of Change in Frequency

The optimum frequency for radiometric sensing of ocean surface temperature lies in the rather broad range 2 to 5 GHz. For reasons given in Section 9.5 the narrower range 2.55 to 2.70 GHz was selected for development effort in the immediate future. Should it later appear desirable to revise the operating frequency upward (perhaps as high as 5 GHz) then it is important to assess the effect this might have on the radiometer.

The radiation pattern characteristics of the antenna are entirely specified by the reduced angle variable $w = \pi a / \lambda \sin \theta$, given in Equation (9.49). Hence antenna dimensions scale inversely with frequency so that, for a given beamwidth, the antenna aperture becomes smaller as frequency increases. There is no frequency dependence elsewhere in the radiometer; the analyses and conclusions developed in Sections 9.1 to 9.4 are essentially frequency independent. It is true, however, that microwave component and transmission line losses will increase slightly, approximately as $f^{1/2}$. This is because the losses are mainly due to skin effect in conductors, rather than to dielectric loss.

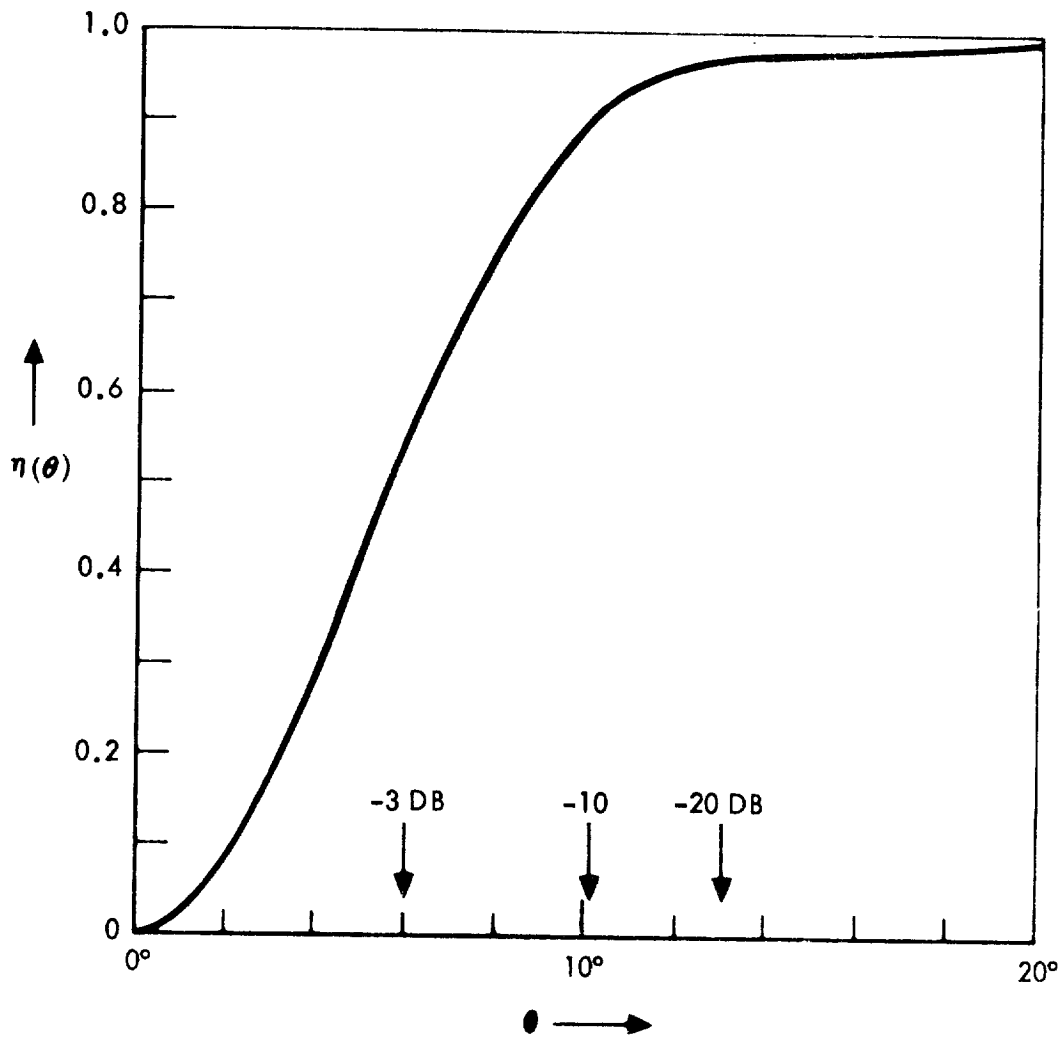


Figure 9.13 Beam Efficiency, Multimode Square Horn

REFERENCES

- Bahret, W.F., and L. Peters, Jr., 1968, "Small-Aperture, Small-Flare Angle Corrugated Horns", IEEE Trans. Vol. AP-16, pp 494-495.
- Cohn, S.B., 1970, "Flare Angle Changes in a Horn as a Means of Pattern Control", Microwave Journal, Vol. 13, pp. 41-46.
- Denson, C.I. and G.J. Halford, 1968, "Plasma Noise Sources of Improved Accuracy", IEEE Trans MTT, Vol. MTT-16, pp. 655-663.
- Dicke, R.H., 1946, "The Measurement of Thermal Radiation at Microwave Frequencies", Rev. Sci. Instr., Vol. 17, pp. 268-275.
- Drake, F.D., and H.I. Ewen, 1958, "A Broad-band Microwave Source Comparison Radiometer for Advanced Research in Radio Astronomy", Proc. IRE, Vol. 46, pp. 53-60.
- Ewing, Gifford C., 1968, "Useful Applications of Earth Oriented Satellites: Oceanography", Summer Study on Space Applications, Woods Hole, Mass.
- Fujimoto, K., 1964, "On the Correlation Radiometer Technique", IEEE Trans. Microwave Theory Tech., Vol. MTT-12, p. 203.
- Goggins, W.B., 1967, "A Microwave Feedback Radiometer", IEEE Transactions on Aerospace and Electronic Systems, Vol. AES-3, pp. 83-90.
- Graham, M.H., 1958, "Radiometer Circuits", Proc. IRE, Vol. 46, p. 1966.
- Hach, J.P., 1968, "A Very Sensitive Airborne Microwave Radiometer Using Two Reference Temperatures", IEEE Trans MTT, Vol. MTT 16, pp. 629-636.
- Haitz, R.H. and F.W. Voltmer, 1968, "Noise of a Self-Sustaining Avalanche Discharge in Silicon: Studies at Microwave Frequencies", J. Applied Phys. Vol. 39, pp. 3379-3384.
- Haroules, G.G., and W.E. Brown III, 1967, "Technique for Absolute Temperature Measurement at Microwave Frequencies", Review of Scientific Instrument, Vol. 38, No. 8, pp. 1093-1096.

- Hewlett Packard Co., "Solid State Devices", 1967.
- Kay, A. F., "The Scalar Feed", AFCRL Report No. 64-347, ASTIA Document AD 601609.
- Lawrie, R. E., and L. Peters, Jr., 1966, "Modifications of Horn Antennas for Low Sidelobe Levels", IEEE Trans. Vol. AP-14, pp. 605-610.
- Minnett, H. C., and B. MacA. Thomas, 1966, "A Method of Synthesizing Radiation Patterns with Axial Symmetry", IEEE Trans. Vol. AP-14, pp. 654-656.
- Orhaug, T., and W. Waltman, 1962, "A Switched Load Radiometer", Publ. Natl. Radio Astron. Obs., Vol. 1, pp. 179-204.
- Penzias, A. A., 1965, "Helium-Cooled Reference Noise Source in a 4-kMc Waveguide", Rev. Sci. Instr. Vol. 36, pp. 68-70.
- Potter, P. D., 1963, "A New Horn Antenna with Suppressed Sidelobes and Equal Beamwidths", Microwave Journal, pp. 71-78.
- Rumsey, V. H., 1966, "Horn Antennas with Uniform Power Patterns Around their Axes", IEEE Trans. Vol. AP-14, pp. 656-658.
- Sherman, J. W. III, 1969, "Passive Microwave Sensors for Satellites", Proc. Sixth International Symposium on Remote Sensing of Environment, Vol. 2, pp. 651-659.
- Silver, S., 1947, "Microwave Antenna Theory and Design", MIT Radiation Lab. Series, Vol. 12, Section 10.3, McGraw Hill Book Co., New York
- Sorenson, H. O., 1965, "Using the Hot Carrier Diode as a Detector", Hewlett-Packard Journal, Vol. 17 #4.
- Stelzreid, C. T., 1968, "Microwave Thermal Noise Standards", IEEE Trans. on MTT, Vol. MTT-16, pp. 646-655.
- Tiuri, M. E., 1964, "Radio Astronomy Receivers", IEEE Trans. Antennas Propagation, Vol. AP-12, pp. 930-938.
- Van Der Ziel, A., 1954, "Noise", Prentiss Hall, Inc., Englewood Cliffs, N. J.

10.0 SEA TRUTH PROGRAM

One of the most important and still unsettled problems in establishing the quantitative limitations and applicability of remote sensing to oceanography is an adequate sea truth program. In virtually all of the development programs under consideration the usefulness of the instrument system has not been tested satisfactorily by comparison with direct observations of relevant ocean surface and atmospheric properties. The work in microwave radiometry of the sea suffers from this fundamental inadequacy. In view of this critical problem, it is vital that future development of the S-Band Microwave Radiometer system give full consideration to a suitable sea truth facility to be incorporated in the early development and performance testing of this program.

This section of the report discusses the requirements for a sea truth facility required for establishing a quantitative relationship between antenna temperature as sensed by the radiometer and molecular sea temperature. It will be noted in the discussion that the requirements for this radiometer project closely parallel the needs of other remote sensor systems. Thus a flexible, multi-application facility should be considered for most economical usage.

10.1 Requirements for Radiometry Tests

Based on experience gained during this current study program, it would be desirable to measure several atmospheric parameters as well as surface properties with a supporting sea truth facility. In Table 10.1, a comprehensive list of observational parameters is presented. Certain parameters have emerged as being particularly important to evaluate because of the sensitivity of the radiometer to them. These are indicated by an asterisk, and should be measured as accurately as possible.

To permit evaluation of radiometer performance to $\pm 0.5^\circ\text{K}$ accuracy under a variety atmospheric and sea conditions, the measurements of sea parameters by the sea truth facility should be made ideally to the accuracies indicated in Table 10.1. In practice, however, it probably will not be possible under ordinary conditions at sea to achieve such accuracies, particularly under moderate to heavy conditions of sea state. Therefore, the last column in Table 10.1 has been added to suggest minimum accuracy requirements for the sea truth data. Under realistic conditions at sea, it

Table 10.1 Projected Needs for S-Band Radiometer Sea Truth Program

Phenomenon or Parameter	Potentially Significant Variables	Ideally Desirable Measurements	Minimum Required Measurements
*1. Sea Water Properties	Temperature within 0.5 cm of surface. ----- Salinity within 0.5 cm of surface.	Spatial distribution over footprint area. Temperature to $\pm 0.2^\circ\text{K}$ Salinity to $\pm 0.02\%$	Temperature to $\pm 0.5^\circ\text{K}$, salinity to $\pm 0.05\%$ at 3-4 points in footprint area.
*2. Surface Roughness	Spectrum of wave heights and slopes over wavelength range 10 meters to 1.0 cm	Two dimension spectrum over wavelength range in footprint area.	Continuous record of mean wave heights and slopes at 3-4 points over footprint area.
*3. Surface Disturbances	*Foaming Bubble size Distribution Bubble lifetime ----- Spray Formation	Extent of surface coverage. Depth of bubble formation.	Extent of surface coverage. (The other parameters are probably strongly correlated with this one, and a separate experimental program can be carried out to determine their most probably values.) Liquid water content within 3 m of surface.
4. Surface Contamination by Organic Materials	Oil Slicks	Droplet concentration within 0.5 m of surface. Droplet spectrum near surface. Composition Thickness Surface Coverage (for slicks thicker than 1 mm)	Oil slick thickness and extent of surface coverage. (for slicks thicker than 0.5 cm)
5. Atmospheric Effects	*Cloud cover and depth air temperature near surface (1 meter height). Humidity (1 meter height). Wind Speed (1 meter and 10 meters height). *Precipitation Rate	Satellite or high altitude aircraft photos of cloud cover; aircraft survey of cloud depth over footprint area. Air temperature at 1 meter to $\pm 0.5^\circ\text{K}$. Relative humidity at 1 meter height to $\pm 1\%$. Wind speed at 1 and 10 meters to ± 0.2 knot Rate of precipitation to an accuracy of 1 mm hr^{-1} , automatic recording	All sky camera measurement of cloud cover estimate of depth to 0.5 km (if possible?). Air temperature to $\pm 1^\circ\text{K}$. Relative humidity to $\pm 5\%$. Wind speed at 10 meters or arbitrary height to ± 1 knot. Rate of precipitation and nature to an accuracy of 1 mm/hr.
*Starred parameters appear to be most significant to Radiometer Interpretation at this time.			

may not be feasible to achieve even these minimum requirements. In any case, every effort should be made in the design of the sea truth facility to approach the minimum measurement requirements so that a meaningful evaluation of the microwave radiometer system performance can be determined.

10.2 Development of a Sea Truth Program

Like most programs aimed at accurate and useful observations of sea surface conditions, the sea truth facility can best be developed in stages with each stage providing experience of value to successive programs. In this way excessive costs of a highly sophisticated but inadequate facility can be avoided.

Three phases for a development and test program have been recommended by Woods Hole Oceanographic Institution; these are:

- Phase 1. Radiometer operation combined with direct sea truth observations of water properties from a fixed location such as a dock, a tower or a bridge.
- Phase 2. Airborne radiometer operation combined with a fixed sea truth facility for observing atmospheric and sea properties.
- Phase 3. Airborne and satellite radiometer operation combined with ship-buoy sea truth network available during a major scientific exploration or routine oceanographic exploration.

Phase 1 - Sea Truth Facility. The first phase of the sea truth test program provides the first milestone in an orderly development of the radiometer system test procedure. This phase, in effect, has already been initiated. The current multi-frequency radiometer study by Ewen-Knight Corp. and Woods Hole Oceanographic Institution on the Buzzards Bay Bridge is aimed at providing a useful set of radiometric observations documented with direct measurements of water properties (Ewen, 1971). The results obtained from the Buzzards Bay project will be a valuable supplement to the information derived from this study. However, the Buzzards Bay project suffers from some limitations that will require a more elaborate study program in time. The limitations include the fact that the water conditions are not representative of the open sea. And there are potential difficulties in data interpretation because of the need to account for the interference of neighboring solid objects in the field of view of the radiometer antennas.

Phase 2 - Sea Truth Facility. The second phase of testing in the S-Band radiometer should be planned around the combination of airborne flights with a suitable sea truth program in a region of reasonably

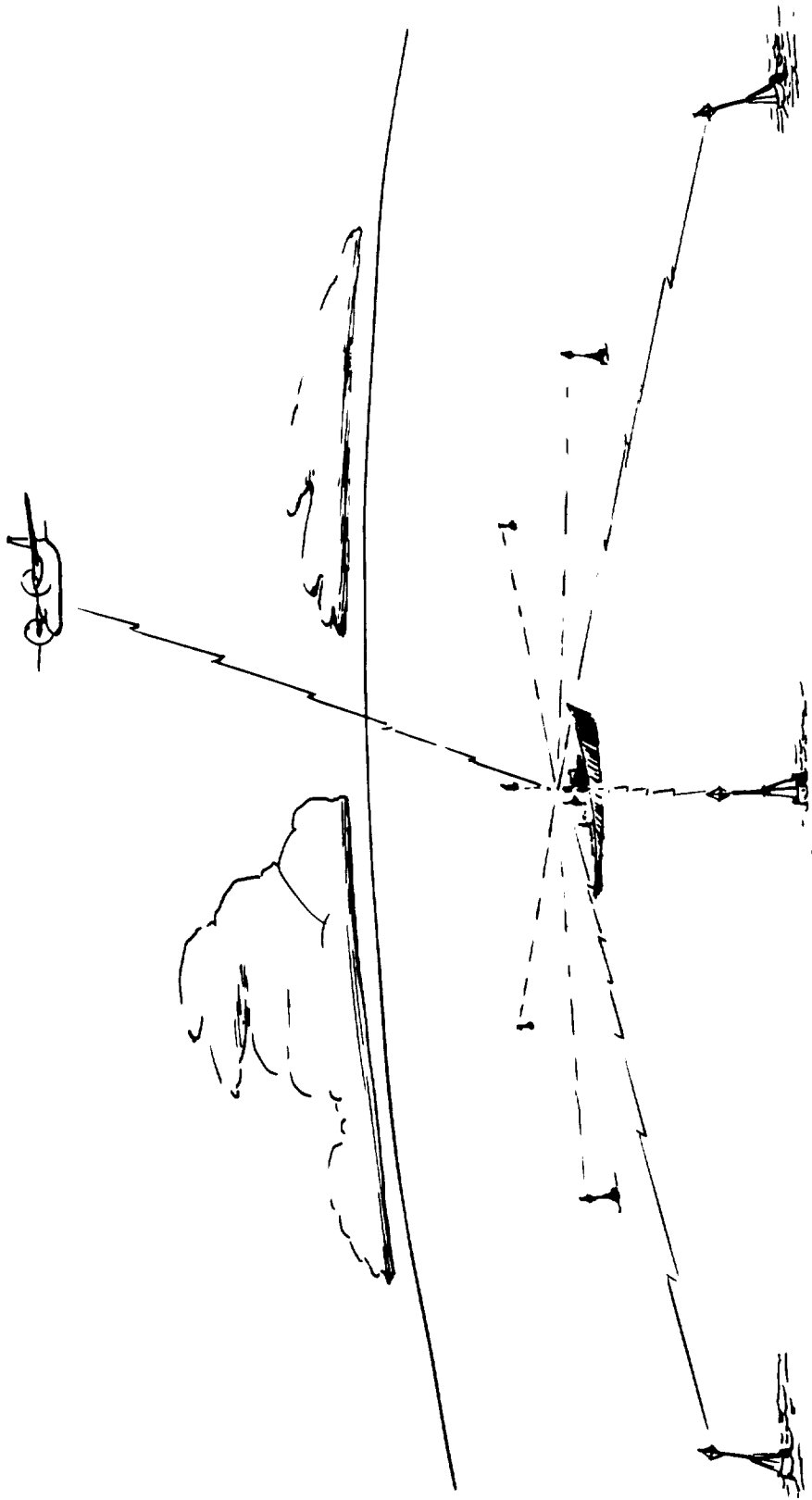


Figure 10.1 Conceptual Sea Truth Facility

open sea. An ideal combination for the sea truth facility in this phase would use a fixed instrumented ship or tower surrounded by a network of buoys placed several kilometers apart. A possible scheme is illustrated in Figure 10.1.

The ship or tower in the sea truth net should be well instrumented with high accuracy instrumentation to cover all aspects of the requirements in Table 10.1. In addition, it will be essential for meaningful comparisons to provide a radiometer system on the fixed station platform to compare with directly measured sea properties with the airborne radiometer being flown overhead.

Surrounding the main station, a network consisting of eight buoys would be moored in a pattern covering roughly 50 km on a side. These buoys would require a minimum of instruments to measure sea temperature, winds (magnitude and direction), salinity, and some measure of wave height or slope sensitive to water wavelengths as small as five centimeters. The choice of area coverage of fifty kilometers square is somewhat arbitrary. The coverage should be large enough to minimize the interference from the sea truth hardware in the received signal pattern of the airborne instrument. The coverage also should be large enough to obtain meaningful statistics of heterogeneities in sea surface properties over the observational pattern of the satellite-borne system. Yet the area should be small enough to be practical in maintenance by a single oceanographic vessel or station. Of course, it is recognized that a 50 kilometer square might not be very meaningful if located in the center of a strong current like the Gulf Stream, but would be expected to give representative data on spatial heterogeneities in a more homogeneous part of the ocean.

The proposed ideal sea truth facility for operation of an airborne radiometer system is very elaborate and would be very expensive to construct and maintain. A rough estimate of the cost to develop and operate a facility shown in Figure 10.1 could easily exceed a million dollars. Furthermore, the operation of an airborne system over a fixed sea truth facility negates the flexibility of the aircraft instrumentation by linking it to only a small fixed area of the ocean.

There is another serious practical limitation to any sophisticated network like that conceptualized in Figure 10.1. Under conditions of heavy seas where the testing of the radiometer performance is important it is extremely difficult to operate and maintain reasonably high precision equipment. Therefore, it seems that a less ambitious program using throwaway devices would prove more cost effective in practice than the more sophisticated project.

Investigators at the Woods Hole Oceanographic Institution have suggested that an alternate sea truth program utilizing air-expendable instruments

similar to the presently available sonobuoys and air-expendable bathythermographs. These throwaway devices could be released from aircraft over the area identified for testing. By retaining the flexibility of throwaway devices, the aircraft would be free to make scientific surveys at the same time the potential and usefulness of the remote system is being tested. Though the application of throwaway devices offers flexibility and more economic testing, limitations are imposed by the reduced accuracy of direct measurements of parameters like temperature and by the inherently smaller number of sea surface properties that can be observed in a spatial-array. It is likely, for example, that only temperature and conductivity could be measured by the throwaway devices. Wave properties would be difficult to instrument with any reasonable precision on throwaway devices. However, the use of photographic methods in combination with aerial observations over a test area where throwaway buoys have been deployed should provide a practical solution to the wave measurement problem in clear weather. Methods of deducing wave spectra from glitter photographs have been described in the literature. One example has been reported by Uberoi (1964) who derived the directional wave spectrum from stereophotographs of the ocean surface. Another innovative way of measuring wave spectra from low flying aircraft using a laser geodolite has been reported recently by Schule et al. (1971). These investigators showed that considerable information about the wave number-amplitude spectrum of wind waves can be derived from laser observations.

Phase 3 - Sea Truth Facility. The projection of an adequate sea truth program for the ultimate use with operational orbiting space vehicles and aircraft is difficult to define at this time. This is basically due to the uncertainty of the degree to which an adequate calibration system or test procedure can be designed into the radiometer system.

A practical operational calibration procedure may be to use a drifting buoy-ship network projected for general oceanographic-meteorological observations in current programs such as the World Weather Watch. Furthermore, internal consistency of retrieved data from a microwave system will undoubtedly be cross-checked with infrared radiometry as operationally used in Nimbus satellites currently in orbit.

Both the buoy system and the ship network suffer from the limitations that observation of ocean properties are made at fixed points, giving an indirect correlation with an orbiting satellite radiometer. Here the question of reliability of the remote sensor particularly as it averages properties over zones of stray surface gradients, remains ambiguous without an adequate model for statistically relating spatial averaged signals to point observations. However, the comparison could be checked routinely over certain identified ocean surface areas by instrumented aircraft over flights. Supplemental surveillance of this type would be a valuable operational check on satellite instrument performance.

The usefulness of an operational satellite instrument system will be linked closely with inputs to and outputs from such forecasting systems as presently available during climatological and available ship data. The forecasts from the U. S. Navy Environmental Data Network (NEDN), currently supplying daily weather and oceanographic maps in the Northern Hemisphere, will serve as an interactive element in the data messaging from a satellite instrument. In the same way, ship data are checked for reliability against climatological variations, and the satellite results can be evaluated for reliability as the remote sensor system is developed to an operational state.

10.3 Test Programs

Experience to date has indicated that a considerable amount of information can be obtained by modest test programs. For example, a great deal can be learned from experiments with the instrument fixed over a body of water under different conditions of surface agitation. Programs like the Buzzards Bay Bridge study continue to provide valuable and useful information on instrument performance. Flight programs over oceanographic vessels have been extremely useful, and it is anticipated that such flights will continue to provide useful data without great investment in a unique sea truth facility.

There has been some consideration given to the testing of a remote sensor fixed over a sea area in a tethered balloon platform. In the case of microwave measurements of thermal emission from the sea to accuracies of $\pm 0.1^\circ \text{K}$, it does not appear that the unattended operation of high precision S-band instrumentation during the development phase can be done at this time without considerable difficulty. Our experience to date has emphasized the need to carefully watch over airborne instruments to insure their proper performance during tests. It may be possible to use a blimp to fly over a fixed region of water with instrumentation on board. This approach would probably be more fruitful to consider as an initial flight program than an unattended balloon borne system until more confidence in instrument reliability and data retrievability can be obtained.

To make full use of the testing needs and the scientific opportunities afforded, it is recommended that every opportunity be taken to integrate the testing of the airborne microwave radiometer system with other planned oceanographic and meteorological experiments using shipboard instrumentation and other remote sensor systems. One of the most effective ways of determining the limitations of the applications of microwave radiometry to oceanography is to include the system in instrumented aircraft flights over areas projected for such experiments as GATE (GARP Atlantic Tropical Experiments) in 1974. In any case, an essential part of a successful sea truth program will require the comparison of data from a fixed near-surface downward-looking radiometer with data from an airborne instrument, as well as with direct observations of sea surface conditions.

10.4 Availability of Sea Truth Instrumentation

The practical constraints on any sea truth program considered for remote sensors are (1) the availability and reliability of oceanographic instrumentation to meet requirements outlined in Table 10-1, and (2) the costs of constructing and operating the facility at sea. The instrumentation is considered here only in the context of the needs for testing the S-band radiometer system to observe remotely sea surface temperature. There are several surveys of appropriate instrumentation available, the most current of which is the U. S. Coast Guard Buoy Program study (Texas Instruments, Inc., 1970), from which much of the data presented in Table 10.2 were extracted. This table presents a summary of instrumentation and techniques particularly suitable for meeting the needs of the proposed sea truth programs. Included are brief considerations of the present limitations of such instruments, as well as an estimated cost. An examination of the material in this table indicates that the cost of mounting a reasonably well instrumented fixed ship or tower combined with a buoy net such as that shown in Figure 10.1 would be exceedingly expensive.

Expendable bathythermographs are currently available for use in the Phase II program, but some development will be required to include a conductivity sensor in such a buoy package. While there is no known expendable device that can measure water conductivity in unattended operation to the precision required for this program, the problem of designing and constructing such a throwaway device is not outside the range of available technology (Ramsay, 1971). Therefore, a timely effort could be devoted to the development of inexpensive, expendable drifting buoys for measuring both sea temperature and electrical conductivity.

10.5 Summary and Conclusions

Based on this exploratory study, the development of a practical sea truth program involving aircraft or satellite observations of areas of the oceans being monitored is a critical requirement in the development testing for usefulness of the S-Band radiometer experiment. The current programs of fixing a radiometer or multi-frequency-radiometers from a platform over water should provide valuable results for interpretation of sensor data in terms of temperature, salinity and roughness. However, implementation of a second phase test program of aircraft operations is strongly recommended at this time.

It will be impractical to build a sea truth facility consisting of a broad network of elaborately instrumented, fixed buoys over an area roughly the size of a footprint expected to be viewed from a satellite. Instead, it is recommended, that a more moderate program consisting of instrumented aircraft flights over an instrumented fixed station mounted with a radiometer of the same type as flown in the aircraft. In addition, the detection of spatial heterogenities over a 50 kilometer square is recommended by use of inexpensive throwaway buoys released from the aircraft. As a minimum, these buoys should be designed to observe sea temperature to $\pm 0.5^{\circ}\text{K}$, and conductivity to a precision equivalent to $\pm 0.2\%$ in salinity.

Because of the large costs involved in implementing aircraft test programs, every effort should be made at this time to integrate the sea truth requirements for a variety of remote sensors into a multipurpose sea truth facility.

It is also recommended that future planning consider the simultaneous testing of remote sensors like the airborne S-Band radiometer in meteorological and oceanographic applications during major geophysical experiment projected for the next few years. For example, every effort should be made in early planning to meaningfully integrate these sensors into the initial Global Atmospheric Research Program (GARP) experiment, the GARP Atlantic Tropical Experiment (GATE). An active search for users in such experiments is initial to successful testing of the airborne sensors, while, at the same time, using their unique capabilities in spatial coverage of the ocean.

Table 10.2. Summary of Instrumentation and Techniques for
Sea Truth Program

Water Temperature	Ideal	Minimum	Existing Capability
Dynamic Range	0°C to 30°C	10°C to 30°C	0°C to 30°C
Measurement Accuracy	±0.1°C	±0.5°C	±0.02°C
Measurement Conditions	Within 0.5 cm of surface	Within 0.5 cm of surface	Within 10 cm of surface
Spectral Distribution	8 to 12 points in footprint area	1 to 4 points in footprint area	
Technique			<ol style="list-style-type: none"> 1. Thermister Sensor Est cost \$1000 2. Expendable bathythermograph (accuracy ±0.2°C) Ext cost \$30 per expendable unit
<p>Deficiencies: Measurement within 0.5 cm of surface not within state-of-the-art. Estimated cost for development of required system is \$20,000; additional units \$4,000 ea., on existing buoy.</p>			

Table 10.2. Summary of Instrumentation and Techniques for
Sea Truth Program (Cont)

Salinity	Ideal	Minimum	Existing Capability
Dynamic Range Salinity Conductivity	0 - 40 ppt 0 - 65 mmhos/cm	0 - 40 ppt 0 - 65 mmhos/cm	0 - 40 ppt 2 - 65 mmhos/cm
Measurement Accuracy Salinity Conductivity	±0.01 mmhos/cm	±0.025 mmhos/cm	±0.01 mmhos/cm
Measurement Conditions	Within 0.5 cm of surface	Within 0.5 cm of surface	Within ~10 cm of surface for in-situ measurement; within 0.5 cm of surface for manual sampling.
Spatial Distribution	8 to 12 points in footprint area	1 to 4 points in footprint area	
Technique			For manual sampling, Induction Salinimeter Est. cost: \$2500 Electrode Conductivity Est. cost: See Note
<p>Deficiencies: In-situ measurement or automatic sampling not within state-of-the art for measurements within 0.5 cm of surface. Development costs: Automatic sampler, \$25,000; bare electrode system ~\$100,000.</p>			

Table 10.2. Summary of Instrumentation and Techniques for Sea Truth Program (Cont)

Surface Roughness	Ideal	Minimum	Existing Capability
Spectrum of Wave Heights and Slopes	Range 1 cm to 10 M in footprint area, 2 dimensional		Direct measurement not within state-of-the art
Wave Height, Length		Wave height, slope measurement of 3-4 points in footprint area Resolution: 1 to 3 cm: 0.5 cm 3 to 30 cm: 1.0 cm 30 cm to 10 M: 5.0 cm	0 to 30 M with integrated system on ship or buoy 0.5 cm 1.0 cm 5.0 cm
Techniques			1. Wave Staff (10 cm to 10 M) Est. cost: \$2500 2. Acoustic (Pulse Repetition Rate) (1 to 30 cm) Est. cost: \$10,000
<p>Deficiencies: Existing systems give wave height and frequency; wavelengths and slopes must be calculated. Cost of developing buoy system for determination of wavelength, wave height, wave slope estimated at \$0.5 Million to 1 Million Dollars.</p>			

Table 10.2. Summary of Instrumentation and Techniques for
Sea Truth Program (Cont)

Foaming and Bubble Phenomena	Ideal	Minimum	Existing Capability
Extent of Surface Foam Coverage	Percent of surface coverage	Percent of surface coverage	Determination by observation (single point) Estimate from wind velocity
Bubble Formation	Bubble size distribution Bubble lifetime Depth of bubble formation		Laboratory studies to provide correlation with a) wind speed; b) extent of foaming; surface roughness
Techniques			Direct observation of surface Estimate from wind speed, etc.
Deficiencies: No technological deficiencies; a laboratory program is required to establish correlations between more readily observed phenomena and foaming mechanics.			

Table 10.2. Summary of Instrumentation and Techniques for
Sea Truth Program (Cont)

Spray Formation	Ideal	Minimum	Existing Capability
Spray Formation	Droplet concentration within 2 feet of surface Droplet spectrum near surface	Liquid water content within 10 feet of surface	Estimate from wind speed, wave height, surface roughness, based on existing laboratory and field data. As above, with limited shipboard sampling and analysis
Techniques			As noted above
Deficiencies: No technological deficiencies. Additional study required to establish correlations between easily observable phenomena and prediction of spray formation characteristics.			

Table 10.2. Summary of Instrumentation and Techniques for
Sea Truth Program (Cont)

Surface Contamination by Organic Materials	Ideal	Minimum	Existing Capability
Oil Slicks	<p>Surface Coverage (Slicks thicker than 1 mm)</p> <p>Thickness</p> <p>Composition</p>	<p>Surface Coverage (Slicks thicker than 0.5 cm)</p> <p>Thickness</p>	<p>Direct observation; Aerial photography; IR Radiometer mapping</p> <p>Direct observation; Surface sampling IR Radiometer mapping Aerial Photography</p> <p>Surface Sampling: IR Radiometer; UV Spectrometer</p>

Table 10.2. Summary of Instrumentation and Techniques for
Sea Truth Program (Cont)

Atmospheric Effects	Ideal	Minimum	Existing Capability
Cloud Cover and Depth	Satellite or High Altitude Aircraft Cloud Cover Survey	Sky camera and cloud cover estimate	Satellites (as available) High Altitude aircraft, color photography
Air Temperature near surface	Air Temperature of 1 M to $\pm 0.5^{\circ}\text{C}$	Air Temperature of 1 M to $\pm 1.0^{\circ}\text{C}$	Sky camera Automatic cloud cover radiometer
Relative Humidity	Humidity at 1 m height $\pm 1\%$	Humidity at 1 m height $\pm 5\%$	Platinum bulb; Thermister Dynamic Error 0.05°C
Wind Speed, Direction	Wind Speed to ± 0.2 knots. Wind Direction to $\pm 2^{\circ}$ at heights of 1 and 10 m	Wind Speed to ± 1 knot. Wind Direction to $\pm 5^{\circ}$ near surface	Dew Point Hygrometer Dynamic Error 0.5% 3 cup Anemometer: Dynamic error 1%
Precipitation	Measure, record amount, type of precipitation to 1 mm/hr		Tipping Bucket Rain Gauge, 0.025 cm, increments

REFERENCES

Ewen, H. I., 1971, User's Handbook, Buzzards Bay Measurement Instrument for Oceanographic Research, Ewen-Knight Corp., East Natick, Mass.

Ramsay, S. P., 1971, Personal Communication.

Schule, J. J., Jr., L. S. Simpson, and P. S. de Leonibus, 1971, "A Study of Fetch-Limited Wave Spectra with an Airborne Laser," J. Geophys. Res. 76, 4160-4171.

Texas Instruments, Inc., 1970, United States Coast Guard Oceanographic Sensor Study, Final Report, Contract DOT-GC-90505A. Dallas, Texas.

Uberoi, M. S., 1964, "Directional spectrum of wind generated ocean waves," J. Fluid Mech. 19, 452, 464.



11.0 FUTURE DEVELOPMENT PROGRAMS

The results of the investigations described in this report indicate that significant progress has been made towards the development of a satellite S-Band radiometer system for oceanographic applications. Progress has been made in two major classes of development, data interpretation and utilization, and instrument system configuration. The extensive theoretical analysis, laboratory testing, and preliminary aircraft flight experiments have revealed no limitations that ultimately will prevent achievement of our design and performance goals. However, there remain some important unresolved problems in both categories of development that require further study to complete plans for a useful operational instrument system. This last section is devoted to a brief discussion of the remaining development work vital to this program.

11.1 DATA INTERPRETATION AND UTILIZATION

To effectively use the S-Band radiometer for measurement of oceanographic properties such as surface temperature, the following areas should be studied further: (a) the roughness and foam influence on emissivity, (b) the relationship between instrument performance and design and viewing geometry (a master data and information retrieval program) and (c) the relation between the S-Band system and other sensors that might be carried on the same spacecraft. These problem areas require rather careful consideration at this stage of program development to insure maximum benefit to the user.

11.1.1 Roughness and Foaming

The level of understanding of these sea surface phenomena in relation to the projected radiometer application has been discussed in Sections 6, 7, and 8. Our conclusion is that the impact of surface roughness and foaming is the principal remaining critical problem in data interpretation and must be known empirically or theoretically to an accuracy compatible with the specification of all other effects on the signal received by the instrument. Therefore, it is essential to resolve the question of roughness and foam at the earliest possible stages of further program development.

11.1.2 Data Analysis and Interpretation

Our experience so far has indicated that the observations from an airborne S-Band radiometer can be interpreted only by using a rather

complicated analytical program. This program will require incorporation of the antenna geometry (e. g. beam angle and antenna pattern), the viewing angle, the location of the radiometer relative to the sun and other "hot" celestial objects, as well as information about the nature of the underlying atmosphere and the sea surface. To insure that such a program can be developed for satellite applications, a study should be initiated at this time. The initial computer program should be written for the prototype radiometer described in Section 11.2 so that it can be tested in airborne instrument experiments before continuing to a more elaborate generalized program for a satellite instrument.

11.1.3 Integration With Other Remote Sensors

For optimizing the usefulness of a particular sensor system such as the S-Band radiometer, independent data about the underlying atmosphere and the sea surface are needed. It is appropriate at this time to expend some effort to evaluate an optimum sensor package for oceanographic applications. Consideration should be given to the integration of microwave radiometers operating in the visible regime.

11.1.4 Oceanographic and Meteorological Utilization

The S-Band radiometer and related instrumentation should be evaluated for broader applications than measurement of sea temperature. For example, it may now be possible to obtain more information about sea state from the S-Band radiometer because of its apparent sensitivity to roughness. One way to achieve more information from the instrument would be to construct a system to measure both components of linear polarization simultaneously instead of using the circular polarization technique currently planned. The latter, of course, loses information by reducing the sensor sensitivity to roughness.

It is timely to consider in much more detail how one can relate directly the thermal emission to dynamical processes in the sea. Both meteorology and oceanography are "classical" sciences in that they continue to rely on interpretation of thermodynamic variables such as temperature and pressure to understand dynamical processes. Efforts should be made now to encourage oceanographers and meteorologists to try to initiate data analyses and studies relating geophysical fluid dynamical processes directly to the radiative properties of these fluids. Such research is recognized to be long range in nature but will undoubtedly produce important new considerations in the applications of remote sensing.

11.2 SATELLITE INSTRUMENT DEVELOPMENT

The following plan for instrument development is based on the results of the studies described in detail in Section 9 of this report, wherein a

conceptual design for a radiometer and its associated antenna has been formulated. The design is fully consistent with the goals of high absolute accuracy over long periods of time and, with practical development, can be made compatible with satellite operation.

An instrument should be constructed which is based on the system block diagram shown in Figure 9.7 and which uses one of the horn antennas described in Section 9.6.3. It should be designed for installation in a specific aircraft, so that operational testing may be carried out over wide areas of the ocean. At the same time, component selection, packaging, reliability considerations and operational features must reflect the eventual need for compatibility with unattended spacecraft operation. Careful attention should be given to the design of the RF portion of the radiometer in order to arrive at a configuration which will minimize size and weight without seriously increasing the RF losses and without compromising absolute measurement accuracy.

The planned design which appears best able to meet these requirements is based on the following considerations. The antenna will undoubtedly be the largest physical component in the system, and of necessity will utilize waveguide transmission line. This being so, the whole of the remainder of the RF portion should be made small and physically mounted in such a way as to be an integral part of the antenna - waveguide transmission line. It will be clearly impractical to attempt to include the antenna in the stabilized temperature enclosure. Therefore, the small RF package, which must be inside the stabilized enclosure, will require to be thermally insulated from the antenna.

A key element in this plan is the small RF package which will be maintained at the constant temperature T_0 . Thermal stabilization requirements will be eased if microstrip or stripline techniques are used to miniaturize the RF circuit and the further advantage of freedom from connector instabilities will be obtained.

Finally, packaging, construction and mounting should be such that the instrument may easily be removed from its aircraft location and re-mounted elsewhere; for example, on a tower overlooking a pool, or on a bridge above a river or estuary, to facilitate static testing under controlled conditions.

Although this plan is tailored to aircraft installation and testing of a radiometer system it will not be amiss to list the important development

requirements which will be needed when the instrument is to be tailored for use in a specific spacecraft. These are:

1. Size, weight and power reductions.
2. Miniaturization of the systems design by incorporating microstrip circuits for the active and passive microwave radiometer circuits.
3. Utilize miniaturized solid state components for the electronic subsystems.
4. Integrate the output of the radiometer with the onboard spacecraft data transmission and recording systems.
5. Space qualification of the operational hardware.
6. Coordination and integration of the ground data processing for interpretation by Principal Investigators and other users.
7. Antenna system, designed to be compatible with the orbital and satellite operational mission plans, spacecraft design and radiometer system requirements

In the last item, our studies have indicated that the antenna design represents a crucial factor in the instrument system. To minimize the error associated with receiving emission from the rough sea over a varying viewing angle and through a varying path in the atmosphere the narrowest possible beam width is required. However, high beam efficiency with very low side lobes also is necessary. To achieve such requirements horn antennas with large apertures appear to be needed for satellite applications. Thus, it would be desirable, at this time, to begin mechanical development efforts to provide foldable horn antennas at S-Band for use in spacecraft.

11.3 FLIGHT APPLICATIONS SURVEY

11.3.1 Aircraft

In the immediate future and possibly for long range applications, the microwave radiometer will probably be utilized most widely aboard aircraft in conjunction with other specialized remote sensors. It is felt that these applications will support the range of research and scientific programs. Little in-depth investigation has been done to identify these specific programs. This is primarily due to the present early state of development of the radiometer system and the short operational period of applicable programs. To

date, the NR S-Band Microwave Radiometer has been flown aboard two aircraft to collect sea surface temperature and related data:

1. Scripps Institution of Oceanography DC-3, Pacific Ocean Flights, October and November 1969
2. NASA-GODDARD, Arctic International Decade Joint Experiment (AIDJEX), utilizing the NASA-Ames Convair 990, February-March 1971.

There are many possible future aircraft programs where the radiometer system may have application. It should be planned to use the system aboard as many aircraft for various programs as possible in the next five years to demonstrate its capabilities.

There are several possible aircraft experiment programs where the S-Band radiometer may be integrated into a more elaborate instrument array. Some examples include:

1. NASA Convair 990 flight programs (Dr. Nordberg - Goddard)
2. Global Atmospheric Research Program (GARP) (particularly the GARP Atlantic Tropical Experiment)
3. National Center for Atmospheric Research (NCAR) Aircraft Surveys
4. U.S. Bureau of Fisheries, Project Little Window (Gulf of California Survey)
5. International Hydrological Decade, Great Lakes Study

It is expected that a limited demonstration flight program will be implemented for the NR prototype III radiometer currently being built for the AAFE program. Present plans call for a series of demonstration flights on the NASA, Wallops Island C-54 aircraft. The NR S-Band radiometer will be operated in parallel with several other remote sensing systems.

11.3.2 Satellite Applications

The development plan as currently projected cannot provide hardware for specific spacecraft application before the 1974-1975 period at the earliest. Under such circumstances, satellite launches for this period and later should be considered. There are a variety of unmanned satellite systems projected

for the late 1970's that might be large enough to accommodate the S-Band radiometer. Based on current NASA planning, the following vehicles should be considered:

1. NIMBUS G and later models
2. TIROS-N
3. ITOS-7
4. ERTS-E and later models

There may be application for the S-Band radiometer in the GARP-World Weather Watch (WWW) satellite series. Although some planning refers to such vehicles as separate entities, it is possible that the late NIMBUS-TIROS-ERTS satellite programs will be tailormade to support the GARP-WWW requirements.

Under the current planning it does not appear that the Small Applications Technology Satellites (SATS) will have large enough vehicles to support the S-Band radiometer. However, feasibility studies may indicate that such an application will be desirable.

For planning of manned space vehicles, there are at least three possible spacecraft that could carry the S-Band radiometer system. These include:

1. Post Skylab Series
2. Space Station
3. Space Shuttle

Since most of the planning for both unmanned and manned spacecraft for the late '70's is in early stages, it is too early to project definite engineering development programs to design and build a space rated S-Band radiometer. Therefore, no further considerations are given in this study.

APPENDIX

Major Users of Sea Surface Temperature Data

* Indicates Survey Contacts

U. S. Naval Oceanographic Office Oceanographic Surveys Dept.	Robert H. Randall, Jr. *Clifford H. Cline
Mauri Center for Oceanographic Research	*Dr. J. B. Hersey Capt. (Dr.) P. M. Wolff
Fleet Numerical Weather Central	*Dr. T. Laevastu
Naval Undersea Center	*Dr. E. C. LaFond *Mr. Owen Lee *Mr. Dale Good
Naval Facilities Engineering Command	*Mr. Michael Yachnis
Naval Weapons Research Facility	Cmdr. Glenn Hamilton
U. S. Coast Guard Hq. Washington, D. C.	*Capt. R. P. Dinsmore
National Weather Service Los Angeles	*Mr. Gordon C. Shields
La Jolla	Dr. Jerome Namais
Office of Naval Research La Jolla	Dr. Robert E. Stevenson
National Marine Fisheries Service La Jolla	*Dr. Merritt Stevenson *Dr. James A. Renner Dr. R. Michael Laurs *Dr. Paul E. Smith Dr. J. F. T. Sauer Dr. O. M. Sette
Stanford University	

NASA - Pacific Marine Laboratories	Capt. W. D. Barbee
National Environmental Satellite Service	Mr. E. Paul McClain Mr. L. F. Hubert Mr. V. Q. Wark Mr. H. L. Smith
Scripps Institute of Oceanography	*Dr. Joseph M. Reid *Dr. Margaret K. Robinson *Dr. Richard Born Dr. Warren S. Wooster Dr. Theodore Dr. E. C. MacAllister Dr. Walter H. Munk *Mr. James M. Snodgrass
Woods Hole Oceanographic Institution	*Dr. Gifford C. Ewing Dr. Nicholas P. Fofonoff Dr. Bruce A. Warren Dr. Paul M. Fye
Oregon State University	*Dr. June G. Pattullo Dr. William G. Percy Dr. George C. Anderson Dr. Wayne V. Burt
University of Washington	Dr. Gunnar I. Roden Dr. Joseph E. Henderson Dr. Maurice Raffray Dr. George C. Anderson
Nova University	*Dr. William S. Richardson
Univ. of California, Los Angeles	*Dr. Yale Mintz *Dr. Miohio Yanas
New York University	Dr. Gerhard Neumann
Bureau of Marine Sciences San Diego, California	*Dr. Glenn A. Flittner
Texas A & M University	Dr. Robert O. Reid Dr. John D. Cochrane
NAVOCEANO - Spacecraft Oceanography	*Mr. John W. Sherman, III *Mr. Lawrence Grubham





POSTMASTER: If Undeliverable (Section 158
Postal Manual) Do Not Return

"The aeronautical and space activities of the United States shall be conducted so as to contribute . . . to the expansion of human knowledge of phenomena in the atmosphere and space. The Administration shall provide for the widest practicable and appropriate dissemination of information concerning its activities and the results thereof."

— NATIONAL AERONAUTICS AND SPACE ACT OF 1958

NASA SCIENTIFIC AND TECHNICAL PUBLICATIONS

TECHNICAL REPORTS: Scientific and technical information considered important, complete, and a lasting contribution to existing knowledge.

TECHNICAL NOTES: Information less broad in scope but nevertheless of importance as a contribution to existing knowledge.

TECHNICAL MEMORANDUMS: Information receiving limited distribution because of preliminary data, security classification, or other reasons.

CONTRACTOR REPORTS: Scientific and technical information generated under a NASA contract or grant and considered an important contribution to existing knowledge.

TECHNICAL TRANSLATIONS: Information published in a foreign language considered to merit NASA distribution in English.

SPECIAL PUBLICATIONS: Information derived from or of value to NASA activities. Publications include conference proceedings, monographs, data compilations, handbooks, sourcebooks, and special bibliographies.

TECHNOLOGY UTILIZATION PUBLICATIONS: Information on technology used by NASA that may be of particular interest in commercial and other non-aerospace applications. Publications include Tech Briefs, Technology Utilization Reports and Technology Surveys.

Details on the availability of these publications may be obtained from:

SCIENTIFIC AND TECHNICAL INFORMATION OFFICE

NATIONAL AERONAUTICS AND SPACE ADMINISTRATION

Washington, D.C. 20546